Bergische Universität Wuppertal
Fakultät für Mathematik
und Naturwissenschaften
Fachgruppe Physik

Analog Hadronic Calorimeter for a Future Linear Collider

Dissertation by:
Amine Elkhalii

21th July 2020

Wuppertal

The PhD thesis can be quoted as follows:

urn:nbn:de:hbz:468-20201103-123225-7
[http://nbn-resolving.de/urn/resolver.pl?urn=urn%3Anbn%3Ade%3Ahbz%3A468-20201103-123225-7]

DOI: 10.25926/2jx6-f298
[https://doi.org/10.25926/2jx6-f298]

Gutachter/inner der Dissertation:	Prof. Dr. Christian Zeitnitz Dr. Katja Krüger
Zusammensetzung der Prüfungskommission	Prof. Dr. Christian Zeitnitz Dr. Katja Krüger Prof. Dr. Francesco Knechtli Prof. Dr. Karl-Heinz Kampert
Datum der Disputation	28.10.2020

Abstract

The work of this thesis is a part of the CALICE collaboration project, which develops calorimeters for a future e^+e^- linear collider. These calorimeters have a high granularity to allow Particle Flow Analysis and achieve a jet energy resolution of 3-4 %. One of these concepts is the Analog Hadronic Calorimeter (AHCAL) based on $3 \times 3 \times 0.3\ cm^3$ scintillator tiles with individual Silicon Photo-multiplier (SiPM) readout. A former physics prototype of the AHCAL has proven the performance and suitability of such a concept. A second generation technological prototype of 39 layers with a 1.7 cm steel absorber ($\sim 4\lambda$) has been constructed and commissioned by several institutes. A massive amount of components has been tested before the assembly, including the SPIROC ASIC developed by Omega. This chip provides the readout for 36 SiPMs, including individual bias voltages, self-triggering, timing measurements, and 12-bit signal resolution, while maintaining a low power consumption of 25 W per channel. A test stand has been designed and developed for testing the SPIROC2E, and around 625 working chips are assembled successfully to AHCAL Front-end Electronics. The test beam of the prototype has been performed during two periods in May and June 2018 in H2 beamline at the CERN SPS. Around 8 to 10 $\cdot 10^7$ events from muon, electron, and pion have been collected with different energy ranges. After a successful detector calibration, the electromagnetic response of the AHCAL is studied with electrons and a good electromagnetic energy resolution of $\frac{22.6\%}{\sqrt{E}} \oplus 1\%$ is achieved.

Contents

Introduction

The Standard Model is the most successful particle physics theory, which describes three out of four known fundamental forces, including the fundamental particles. The validity of this model has been confirmed after the latest discovery of Higgs boson at the CMS [1] and ATLAS [2] experiments at the Large Haron Collider (LHC) at CERN in 2012. The LHC is the highest energy particle accelerator to date, and the collision of protons at very high energy in the center of mass up to $\sqrt{s} = 14TeV$ makes it a perfect discovery machine. Nevertheless, since the protons are not elementary particles, only a fraction of the center-of-mass energy is achieved in each collision with a high background in the detector. These effects lead to complication in the measurement of the Higgs cross-section and, therefore, an inprecise measurement at LHC. One solution for these issues is the International Linear Collider (ILC) [3] which proposes a collision of electrons and positrons with a planned center of energy up to $\sqrt{s} = 500GeV$. The ILC promises a very high precision measurement, which can extend and complement the LHC physics program. Therefore, detectors with very high performance are needed to reach the desired results. Several detector concepts are in development by CALICE Collaboration and promise a high jet energy resolution of 3-4 % [3]. These concepts are optimized for the Particle Flow Algorithms [4], which require a high-resolution tracking system with a high granular calorimeter system.

This thesis's work is related to the development of the Analog Hadronic Calorimeter (AHCAL) detector, which is one of the concepts developed within CALICE Collaboration. The AHCAL is based on $3 \times 3\ cm^2$ scintillator tiles with individual Silicon Photomultiplier readout. A technological prototype of 39 layers with a 1.7 cm steel absorber has been constructed and commissioned by several institutes.

In the first chapter, a recapitulation of the particles and the three fundamental interactions described by the Standard Model is given. Afterward, the spontaneous symmetry breaking

in the Higgs mechanism is explained. Finally, the ATLAS and CMS results of the Higgs discovery are shown. The second chapter lies on the International Linear Collider (ILC), where the concept of e^+e^- linear collider is discussed and compared to the circular acceleration. Furthermore, the ILC project, including its acceleration technology and detector concepts, is described. Besides, the physics program as a function of the center of mass in the ILC is introduced. The third chapter firstly presents the different interactions of neutral and charged particles with matter. Subsequently, the simulation models of the electromagnetic and hadronic cascades are presented. Following this, the calorimeters' response is discussed, including the particle flow concept and its requirements. Eventually, a short description of the different calorimeters' concepts, developed by CALICE Collaboration, is presented. The fourth chapter lies on Analog Hadronic Calorimeter, where a description of the SiPM and plastic scintillator is given. Afterward, the AHCAL technological prototype is described, including its readout system, data acquisition, and operating mode.

The readout of the AHCAL is done by the SPIROC2E chip, which provides an individual readout of 36 SiPMs with time measurement. As part of the detector commissioning, the setup of the test stand designed for understanding the SPIROC2E behavior, and the results are discussed in chapter 5. A test beam campaign of the AHCAL technological prototype was performed at the CERN Super Proton Synchrotron (SPS) in June 2018 with different beam particles in a large energy range. In the last chapter, the test beam setup and the collected data are described, including the full chain to calibrate the energy deposited in the detector. The simulation is a fundamental tool to analyze and interpret the experimental results measured by the real detector. Therefore, the AHCAL prototype is simulated, including the implementation of all the geometry features. Towards the end of the chapter, the detector response to electron data is studied. This analysis consists of extracting a single electron event using a particle identification algorithm to understand the electromagnetic shower response and electromagnetic energy resolution of the AHCAL detector.

Chapter 1

Particle Physics

Particle physics is the field of studying the fundamental building blocks of matter and the interactions between them. In the 1930s, these studies led to understanding the atom, nuclei and their constituents: proton and neutrons, electrons and positrons, the neutrino and anti-neutrino. Consequently, particle physics became a field in its own right, addressing questions such as, how is the matter created in the initial creation of the universe and which interactions existed in the early universe? Particle physics is of particular interest since the conditions of high energy physics experiments approach the energy scale of the early universe. The science of particle physics advanced by building particle accelerators to accelerate protons and electrons to high energies and smash them into nuclei. Afterward, rich and surprising discoveries of many new particles were published. In the early 1960s, the accelerators started to reach higher energies, which led to a hundred discovered particles [5]. A new fundamental particle building block was defined after a very long series of experiments and theoretical studies. This block classified the particles into quarks and leptons, with their gauge bosons representing the fundamental forces of their interactions.

In this chapter, the Standard Model, including the particles and the fundamental forces of their interactions, are discussed briefly. Afterward, the mechanism of electroweak symmetry breaking is explained. Overall, the Higgs measurement in the e^+e^- collisions is introduced.

1.1 The Standard Model of Particle Physics

The Standard Model (SM) is a set of mathematical formulas and measurements describing all the known elementary particles and their interactions. These interactions are either strong,

weak, or electromagnetic. The description of these interactions is based on gauge theories that include the Quantum Electrodynamics (QED) and Quantum Chromodynamics (QCD). Massive or massless gauge bosons mediate the interactions between the elementary particles.

1.1.1 Particles

Particles are classified into leptons and hadrons, leptons interact weakly or electromagnetically, but never strongly. In Lepton family, electron (e), muon (μ), and tau (τ) are three particles with similar properties with the same charge -1 and same spin -$\frac{1}{2}$. Each of these leptons has its own neutrino ν_e, ν_μ, ν_τ. The properties of the six leptons are summarized in Table 1.1. Each lepton has a corresponding antiparticle, known as an anti-lepton, with the opposite charge and lepton number. The first observed lepton is the electron, and it was predicted in the mid-19 century by scientists and then discovered in 1897 by J.J. Thomson [6]. The second observed lepton is the muon, which was discovered by Carl D. Anderson in 1936 [7], and it was classified earlier as meson. The electron-neutrino was predicted to fulfill the characteristics of beta decay, then it was observed in 1956 by a neutrino experiment [8]. The muon-neutrino was observed afterward in 1962. The tau lepton was discovered in the 1970s [9], and 30 years later, its associated neutrino (ν_τ) was observed.

The leptonic number of each lepton family has to converse under the Standard Model if the neutrinos are massless. This conservation means when a particle is interacting, the leptonic number of the same type remains the same. However, the evidence for a tiny nonzero neutrino mass [10] has been observed recently, leading to a violation of these conservations laws. For the moment, there is no understanding of the neutrino mass hierarchy.

State	Q	Mass	L_e	L_μ	L_τ	Lifetime
e^-	-1	0.511 MeV	1	0	0	4.6×10^{26}years
ν_e	0	< 2 eV	1	0	0	Stable
μ_-	-1	105.7 MeV	0	1	0	2.197034×10^{-6} s
ν_e	0	< 0.19 MeV	0	1	0	Stable
τ^-	-1	1776.82±0.16 MeV	0	0	1	$(290.6 \pm 1.0) \times 10^{-15}$s
ν_τ	0	< 18.2 MeV	0	0	1	Stable

Table 1.1: Proprieties of leptons : charge (Q), mass, L_e, L_μ and L_τ are respectively the electron, muon and tau leptonic numbers to refer the lepton family of each particle [11].

In addition to leptons, bound of quarks and anti-quarks exist in $q\bar{q}$ (mesons) or qqq (baryons) combinations by the color-field of Quantum Chromodynamics (QCD). The quarks are the only elementary particles that can interact by all four fundamental interactions (electromagnetism, gravitational, strong and weak interactions). They carry a fractional electric charge, $\frac{2}{3}$e or -$\frac{1}{3}$e, where e is the charge of the positron. There are six types of quarks: up (u), down (d), strange (s), charm (c), bottom (b), and top (t). They are grouped in charge ($\frac{2}{3}$,-$\frac{1}{3}$) pairs: (d,u), (s,c), (b,t). The properties of the quarks are summarized in Table 1.2. The quarks u and d are the lightest of all quarks, and they are generally stable. However, s, b, c, and t are the heavier quarks and can decay to up and down quarks. Each quark particle has its anti-particle with an opposite charge, called anti-quark. Since the quarks are fermions, they are also subject to the Pauli Exclusion Principle, where two identical fermions cannot simultaneously occupy the same quantum state.

The Quark Model was invented by Gell-Mann [12] and Zweig [13] to explain the patterns of masses and interactions of light hadrons[1], and was extended to include heavier quark flavors. The evidence for their physical existence was provided by the deep inelastic scattering experiments at the Stanford Linear Accelerator Center in 1968. The last discovered quark was the top (t) quark at Fermilab [14].

State	Q	Mass	I	I_z
d	-$\frac{1}{3}$	4.1-5.8 MeV	$\frac{1}{2}$	-$\frac{1}{2}$
u	$\frac{2}{3}$	1.7-3.3 MeV	$\frac{1}{2}$	$\frac{1}{2}$
s	-$\frac{1}{3}$	80-130 MeV	0	1
c	$\frac{2}{3}$	1.18-1.34 GeV	0	0
b	-$\frac{1}{3}$	$4.19^{+0.18}_{-0.06}$ GeV	0	0
t	$\frac{2}{3}$	172.0 ± 1.6 GeV	0	0

Table 1.2: Proprieties of quarks : charge (Q), the (d,u) pair form a strong isospin doublet [11].

1.1.2 Forces

In principle, we have four fundamental interactions in nature: gravitation, weak, electromagnetic, and strong. However, in the Standard Model, gravitation remains unexplained.

[1]Light hadrons: composed of u and d quarks

The SM is a gauge theory based on the symmetry group $SU(3)_C \times SU(2)_L \times U(1)_Y$. The $SU(3)_C$ represents the gauge group for Quantum Chromodynamics (QCD), which describes the strong force. The $SU(2)_L \times U(1)_Y$ gauge group describes the electroweak interaction, which is discussed later in the following section.

1.1.2.1 Electroweak Interaction

The electroweak interaction is a unification of the electromagnetic and weak interactions, and it was postulated by Glashow-Weinberg-Salam theory [15] [16]. The electromagnetic and weak forces are independent at low energies, but they can merge into a single electroweak force on the order of 246 GeV. Four gauge bosons, $W^{\pm}$, Z^0, and γ are existing in the electroweak interaction. They are coupling to the three weak isospins (W^1_μ, W^2_μ, W^3_μ) and the B_μ boson of weak hypercharge, respectively. These mediators, listed in Table 1.3, are produced with the spontaneous symmetry breaking of the electroweak gauge symmetry $SU(2)_L \times U(1)_Y$ to the electromagnetic gauge symmetry $U(1)_{em}$. A detailed description of this symmetry breaking will be discussed in section 1.2.1. The massive charged gauge bosons $W^{\pm}_\mu$ are contracted as linear combinations of W^1_μ and W^2_μ.

$$W^{\pm}_\mu = \frac{1}{\sqrt{2}} \left(W^1_\mu + W^2_\mu \right) \tag{1.1}$$

The neutral gauge bosons (Z and photon field A) are defined as a linear combination of W^3_μ and B_μ:

$$\begin{aligned} A_\mu &= B_\mu \cos\theta_W + W^3_\mu \sin\theta_W \qquad && massless \rightarrow \gamma \\ Z_\mu &= -B_\mu \sin\theta_W + W^3_\mu \cos\theta_W \qquad && massive \rightarrow Z^0 \end{aligned} \tag{1.2}$$

where θ_W is the weak mixing angle of the weak interactions (or sometimes Weinberg angle). It is defined as $\tan(\theta_W) = \frac{g^{'}}{g}$, where g and $g^{'}$ are the coupling constants which are related to the electric charge with $e = g \sin\theta_W = g^{'} \cos\theta_W$.

1.1.2.2 Strong Interaction

The strong interaction is responsible for binding quarks together in hadrons such as protons and neutrons. At the quark scale, it is 100 times stronger than the electromagnetic force, a million times stronger than the weak interaction and 10^{43} times stronger than the gravitation.

The interaction between quarks is mediated by the exchange of eight massless particles called gluons, which carry three colored charges (red, green, blue) of the strong nuclear force. These colors are after the discovery of baryon Δ^{++}, which is composed of three identical quarks (qqq). These color quantum numbers are implemented to have a correct permutation symmetry of baryons and to satisfy Fermi-Dirac statistics.

Sector	Boson	Q	Colour charge	Mass	Strength
	γ	0	0	0	10^{-3}
EW	$W^{\pm}$	±1	0	80.399(23) GeV	10^{-8}
	Z^0	0	0	91.1876(21) GeV	10^{-8}
Strong	g (8 gluons)	0	r, g, b	0	1

Table 1.3: Forces carriers with their gauge bosons in the Standard Model [11].

1.2 Higgs Mechanism

In the electroweak interaction, the introduction of massive gauge bosons is prohibited under $SU(2)_L$ because the local principle of gauge variance under $SU(3)_C \times SU(2)_L \times U(1)_Y$ requires massless gauge bosons. Therefore, a spontaneous symmetry breaking in the electroweak interaction is needed to generate massive gauge bosons. Thus, the Higgs field is adopted while safeguarding the renormalization of the electroweak theory. It is postulated by the Higgs mechanism [17][18].

1.2.1 Spontaneous Symmetry Breaking

The generation of gauge bosons mass, by spontaneous symmetry breaking, needs a self-interaction of the field. This field is a complex scalar field $\phi = (\phi_1 + i\phi_2)/\sqrt{2}$. The gauge and self-interaction of the complex scalar fields are described by the Lagrangian [19].

$$L \equiv T - V = (\partial_\mu \phi)^* (\partial^\mu \phi) - V(\phi) \tag{1.3}$$

where T and V are the kinetic and potential energies of the system, the potential energy as a function of its associated field can be represented in Figure 1.1. As shown in Figure 1.1a, in the case of the non-existence of the field, the minimum potential is zero, and the potential variation function is V $\propto \phi^2$ or V $\propto \phi^4$. However, in the field theory, as shown in Figure 1.1b,

the minimum of the Higgs potential V(ϕ) has to be different than zero. The Higgs potential is described in the case of $\mu^2 < 0$ and $\lambda > 0$ and can be represented in the following equation:

$$\begin{aligned} V(\phi) &= \mu^2\phi^*\phi + \lambda(\phi^*\phi)^2 \\ &= \mu^2(\phi_1^2 + \phi_2^2) + \lambda(\phi_1^2 + \phi_2^2)^2 \end{aligned} \tag{1.4}$$

The Lagrangian (L) is invariant under $\phi \to e^{i\alpha}\phi$ and possesses a U(1) global symmetry. It can be represented in the following form:

$$L = (\partial_\mu\phi_1)^2 + (\partial_\mu\phi_2)^2 - \left(\mu^2(\phi_1^2 + \phi_2^2) + \lambda(\phi_1^2 + \phi_2^2)^2\right) \tag{1.5}$$

As shown in Figure 1.1b, the extremes $\phi_1 = 0$ and $\phi_2 = 0$ do not correspond to the potential minimum but to its local maximum. The potential minimum is located in the plan of radius v:

$$\phi_1^2 + \phi_2^2 = v^2 \qquad with \quad v^2 = -\frac{\mu^2}{\lambda} \tag{1.6}$$

The gauge bosons and fermions gain masses during their interaction with the Higgs field which can be represented by the following form :

$$\phi(x) = \frac{1}{\sqrt{2}} \begin{pmatrix} 0 \\ v + h(x) \end{pmatrix} \tag{1.7}$$

where $v = \sqrt{-\mu^2/\lambda}$ is called vacuum expectation value of the Higgs field $|\phi|$. $h(x)$ represents the quantum fluctuations of the Higgs field around the potential minimum. The vacuum expectation value of the scalar doublet can be represented as follows:

$$\phi(0) = \frac{1}{\sqrt{2}} \begin{pmatrix} 0 \\ v \end{pmatrix} \tag{1.8}$$

By replacing the Higgs field Eq. 1.7 in the Lagrangian Eq. 1.3, we obtain:

$$L = (\partial_\mu h)^2 + \mu^2 h^2 + ..terms(h) + const. \tag{1.9}$$

We know that the Lagrangian for a scaler field ϕ of a mass m with spin 0 is:

$$L = \frac{1}{2}(\partial_\mu \phi)^*(\partial^\mu \phi) - \frac{1}{2}m^2\phi^2 \tag{1.10}$$

Comparing to Eq. 1.9, the term $\mu^2 h^2$ of the higgs field has the same form as the mass term ($-\frac{1}{2}m^2\phi^2$). Thus, Higgs-mass can be defined as follows:

$$m_h = \sqrt{-2\mu^2} = \sqrt{2\lambda v^2} \tag{1.11}$$

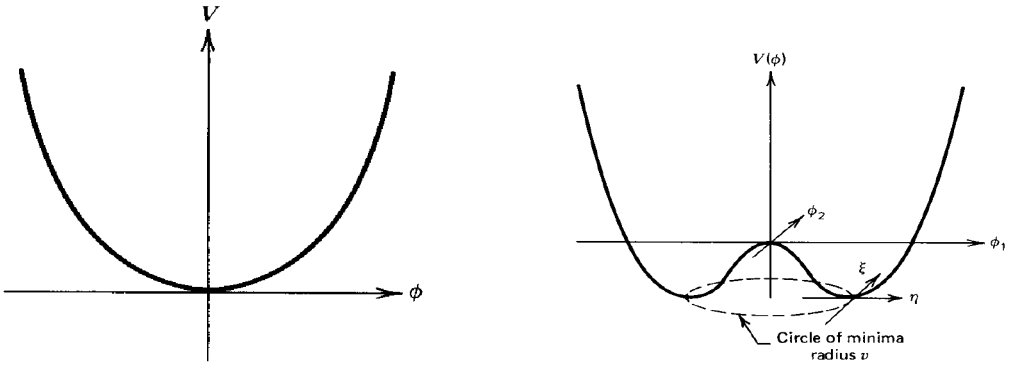

(a) (b)

Figure 1.1: The potential $V(\phi)$: a) with a scalar field for the case $\mu^2 > 0$ and $\lambda > 0$. b) with a complex scalar field for the case $\mu^2 < 0$ and $\lambda > 0$ [19].

The Higgs mechanism can be illustrated by the spontaneous breaking of a U(1) gauge symmetry and $SU(2)_L \times U(1)_Y$ gauge symmetry [19].

Spontaneous Breaking of a U(1) Gauge Symmetry

To illustrate the Higgs mechanism with the spontaneous breaking of U(1) gauge symmetry, the Lagrangian is required to be invariant under a U(1) local gauge transformation $\phi \rightarrow e^{i\alpha(x)}\phi$. In the Lagrangian Eq.1.3, ∂_μ is replaced by the covariant derivative $D_\mu = \partial_\mu - ieA_\mu$, where A_μ is the gauge field. The gauge-invariant Lagrangian is:

$$L = (D_\mu \phi)^*(D^\mu \phi) - \mu^2\phi^*\phi + \lambda(\phi^*\phi)^2 \tag{1.12}$$

By replacing $\phi(x)$ (Eq. 1.7) in the Lagrangian Eq. 1.12, we receive:

$$L = \frac{1}{2}(\partial_\mu - ieA_\mu)(v+h)(\partial^\mu + ieA^\mu)(v+h) - \frac{1}{2}\mu^2(v+h)^2 + \frac{1}{4}\lambda(v+h)^4 \tag{1.13}$$

we supersede $\mu^2 = -\lambda v^2$:

$$\begin{aligned} L = \quad & \underbrace{\frac{1}{2}\partial_\mu h \partial^\mu}_{\text{free Higgs particle}} + \underbrace{\left(\frac{h^2}{2} + vh\right) e^2 A_\mu A^\mu}_{\text{gauge-Higgs interaction}} + \underbrace{v^2 e^2 A_\mu A^\mu}_{\text{mass term for } A_\mu} \\ & \underbrace{-\frac{1}{4}\lambda h^4 - \lambda v h^3}_{\text{Higgs self-interaction}} - \underbrace{\lambda v^2 h^2}_{\text{Higgs mass}} + const \end{aligned} \tag{1.14}$$

The Lagrangian consists of many terms which describe the interaction of Higgs bosons and its mass. The term $\lambda v^2 h^2$ represents the Higgs mass term. The term $\left(\frac{h^2}{2} + vh\right) e^2 A_\mu A^\mu$ represents the interaction term between the Higgs and gauge boson field A_μ. The term $-\frac{1}{4}\lambda h^4 - \lambda v h^3$ represents the Higgs self interaction. The mass of gauge bosons ($M^2 \approx \frac{1}{2}e^2 v^2$) is described in the term $v^2 e^2 A_\mu A^\mu$.

Spontaneous Breaking of a Local $SU(2)_L \times U(1)_Y$ Gauge Symmetry

As mentioned previously, the procedure is repeated to study the spontaneous breaking in $SU(2)_L \times U(1)_Y$ gauge symmetry. Since the Higgs field is required to generate masses of the neutral (Z^0) and charged ($W^\pm$) bosons, the scalar field is represented as a complex doublet: neutral ϕ^0 and charged ϕ^+ scalars. In total, the doublet has four degrees of freedom illustrated with ϕ_1, ϕ_2, ϕ_3, ϕ_4.

$$\phi = \begin{pmatrix} \phi^+ \\ \phi^0 \end{pmatrix} = \frac{1}{\sqrt{2}} \begin{pmatrix} \phi_1 + i\phi_2 \\ \phi_3 + i\phi_4 \end{pmatrix} \tag{1.15}$$

The Lagrangian is invariant under global SU(2) phase transformations $\phi \to \phi' = e^{i\alpha_a(Y_\phi + T_a)}\phi$. ∂_μ is replaced with the covariant derivative D_μ:

$$D_\mu = \partial_\mu + ig' Y_\phi B_\mu + igT_a W_\mu^a \tag{1.16}$$

where $T_a = \tau_a/2$ and B_μ is the hypercharge gauge field. W_μ^a (with a = 1,2,3) represents

the three gauge fields. The mass of the gauge bosons of the electroweak interactions may be obtained as a function of weak coupling constants g of $SU(2)_L$, $g^{'}$ of $U(1)_Y$ and the vacuum expectation value v. The mass for $W^{\pm}$, Z^0 in the Standard Model are:

$$M_W = \frac{1}{2}gv \qquad M_Z = \frac{1}{2}v\sqrt{g^2 + g'^2} \tag{1.17}$$

The vacuum expectation value of Higgs field was calculated to be $v \sim 246GeV$, after measuring the M_W and the weak coupling constant g ($M_W = \frac{1}{2}gv$).

1.3 Higgs Bosons

The Higgs boson is the last elementary particle of the Standard Model, discovered in July 2012 by ATLAS and CMS collaborations [20] [21]. The integrated luminosity was $\int Ldt = 5fb^{-1}$ with $\sqrt{s}$= 7 TeV and $20fb^{-1}$ for $\sqrt{s}$ = 8 GeV for each experiment. The Figures 1.2a and 1.2b show the measurement of Higgs bosons from ATLAS and CMS, respectively. The Higgs mass was measured in the process $H \to \gamma\gamma$ which has a very small branching ratio, but was offering a clear signature at the LHC. The Higgs mass with combined ATLAS and CMS data is: $m_H = 125 \pm 0.21\,(stat) \pm 0.11\,(sys.)\,GeV$.

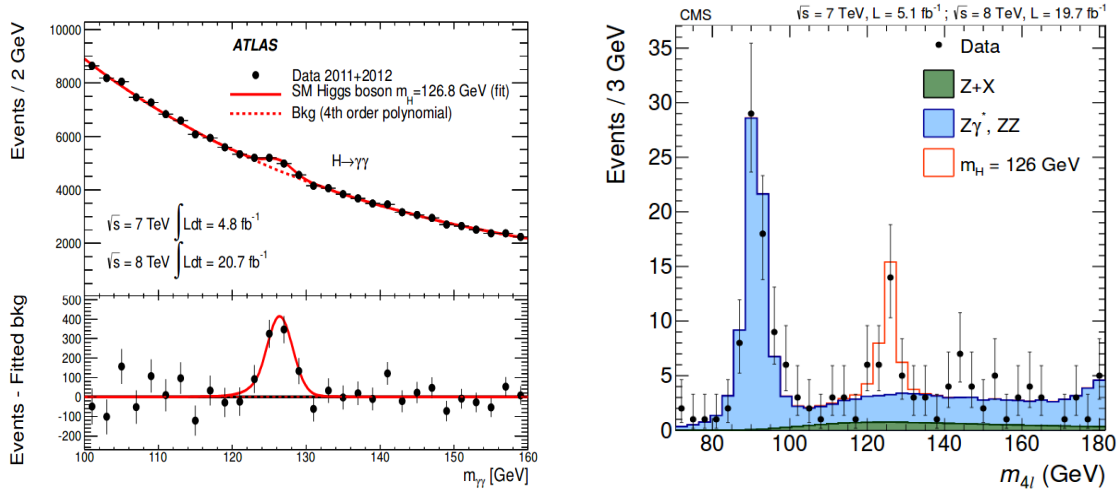

(a) (b)

Figure 1.2: a) The invariant mass distribution determined by the ATLAS collaboration for the diphoton channel. The Higgs-like particle appears at 126.5 GeV [20] b) The invariant mass distribution determined by the CMS collaboration in the four lepton channel [21].

Chapter 2

The International Linear Collider

The International Linear Collider could be a complement machine to the LHC physics program since it can provide a clean collision environment with low background. All these proprieties make the ILC a high precision collider experiment. The focus of this chapter lies in the description of the International Linear Collider (ILC). In this chapter, the concept of the e^-e^+ Linear Collider and general aspects of the linear and circular accelerators are discussed. Afterward, the ILC project with a brief description of the acceleration technology and the detectors' concepts are presented. At the end of this chapter, the ILC physics program as a function of the center-of-mass energy is illustrated.

2.1 The International Linear Collider Concept

2.1.1 e^-e^+ Linear Colliders

The Large Hadron Collider (LHC) is currently the highest energy collider experiment in the world, located at CERN in Switzerland and France. Its primary goal is to probe the Standard Model (SM) at high energy and discover new particles beyond the SM. The LHC is a circular collider that can accelerate protons to very high energy in the center of mass up to $\sim$14 TeV. Nevertheless, this machine can only reach a fraction of its' center-of-mass energy in each collision because the protons are not elementary particles. The collision of composite particles is very complex, but colliding elementary particles such as electrons or positrons can be a good alternative. However, the circular acceleration of electrons and positrons in the LHC is very wasteful due to the high synchrotron radiation. Therefore, the e^-e^+ collider, such as the ILC, can provide collisions with less QCD background and higher precision measurement

comparing to the LHC.

The ILC can be a prestigious machine to extend and complement the LHC physics program. It is designed to collide electrons and positrons at center-of-mass energy from 250 GeV to 500 GeV. The well-defined and clean collision, the high polarized beams, and the low background level at the ILC lead to an unprecedented precision on the measurement and provide the conditions needed to detect deviations from the SM. Other concepts for leptons' colliders are in progress, such as the Compact Linear Collider (CLIC) [22]. However, it is not as advanced as the ILC in terms of $R\&D$ development.

2.1.2 Linear Collider vs Circular Collider

In particle accelerators, there are two concepts of colliders, either circular or linear. In the circular collider, the particles are accelerated in a closed ring, and they can reach very high energy by repeated acceleration. However, the particles lose their energy by synchrotron radiation, due to the transverse acceleration of the particles. The energy loss is illustrated in the follows:

$$P_{sync} = 4 \cdot \frac{\pi \alpha \hbar c}{3} \cdot \frac{E^4}{m_0^4 c^8 R} \propto \frac{E^4}{m^4 R} \tag{2.1}$$

where E is the energy of the accelerated particle, R is the ring radius, and m is the particle's mass. The synchrotron radiation is proportional to the fourth power of the particle energy E^4 and inversely proportional to the ring radius R and the particle's mass m. Therefore, using massive particles, such as protons, can minimize this radiation. The energy loss for lepton in a circular collider can be compensated by increasing the radius of the ring, leading to a higher cost.

The best option to avoid the high electrons' synchrotron radiation is to use the linear collider. However, the beam particle can pass the accelerator module only once. Therefore, the linear acceleration path will be made of many accelerator modules to reach the desired beam energy. Besides, looking at the cost optimization of both accelerators, the cost for the circular collider is growing quadratically with the beam energy ($\propto E^2$) [23]. While in the linear collider case, the cost is linearly increasing with the beam energy ($\propto E$). The low cost and the clean environment of the linear lepton collider make it the ideal collider for electrons.

2.2 The ILC Accelerator

The International Linear Collider is one of the most advanced concepts for linear electron-positron collider experiments. Figure 2.1 shows the layout of the ILC with the major subsystems with a total length of 31 km. It is planned to collide electrons with positrons at center-of-mass energy from 250 GeV to 500 GeV, with an upgrade to 1 TeV.

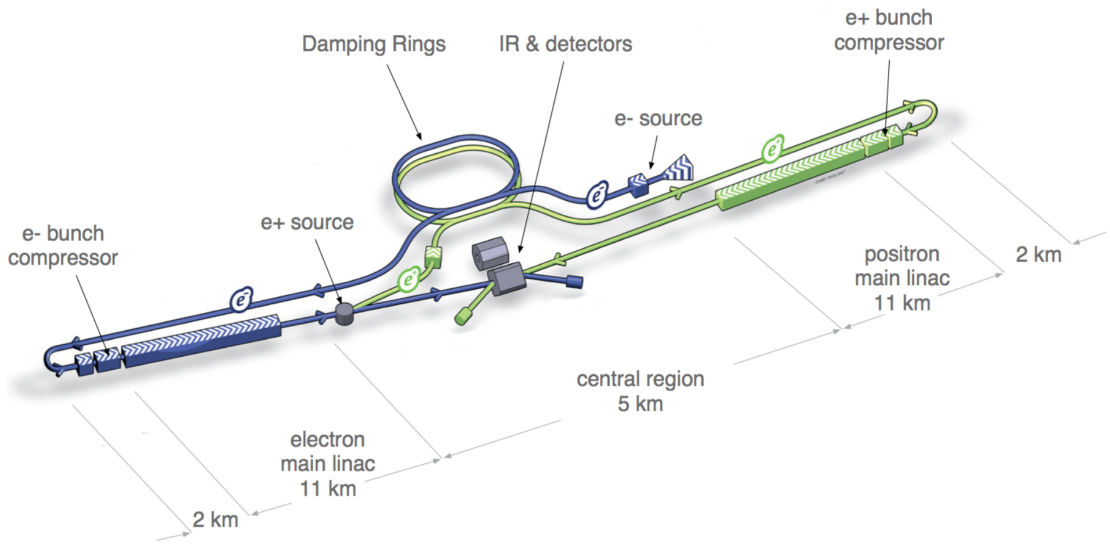

Figure 2.1: Layout of the International Linear Collider with the major subsystems [3].

The baseline of the ILC provides polarized electron and positron beams ($P_{e^-} = 80\,\%$, $P_{e^+} = \geq 30\,\%$). The electrons are generated by illuminating GaAs target with a laser light that uses a wavelength of 790 nm and pre-accelerated to 76 MeV. They are subsequently pre-accelerated to 5 GeV in the main linac with a Radiofrequency (RF) acceleration with super-conducting magnets.

The extraction of positrons is more complicated than the extraction of polarized electrons. The electron beams are passing through a helical undulator, generating polarized photons. These photons hit a thin target, producing polarized e^-e^+ -pairs. Afterward, the positrons are separated from the electrons and pre-accelerated to 5 GeV in the main linac.

The pre-accelerated electrons and positrons enter their corresponding damping ring (DR). The DRs have a circumference of 3.2 km and operate at a beam energy of 5 GeV. They reduce

the high emittance of the generated electrons and positrons and store the full bunch length. Each full bunch contains approximately 1312 merged bunches to acquire the needed luminosity. The transition from the DRs to the main linac is done by Ring to Main Linac (RTML). During this transition, the bunch length is compressed, the polarized beam orientation is adjusted, and the two beams are accelerated up to 15 GeV.

In the main linacs, the electrons and positrons are accelerated to the required energy up to 250 GeV. The linac consists of 7400 nine-cell niobium cavities, and each one operates with 1.3 GHz to reach an average accelerating gradient of 31.5 MeV/m. A picture of one cavity is shown in Figure 2.2. The two accelerated beams pass through the beam delivery system (BDS) of a length of 3.5 km from the interaction point. The BDS's primary role is to focus the beams on the smallest size necessary for the desired luminosity. Two different detectors technologies are planned for the ILC with one interaction point with a push-pull configuration, as illustrated in Figure 2.3.

Figure 2.2: Picture of a nine-cell cavity. Each main linac consists of 7400 cavities [24].

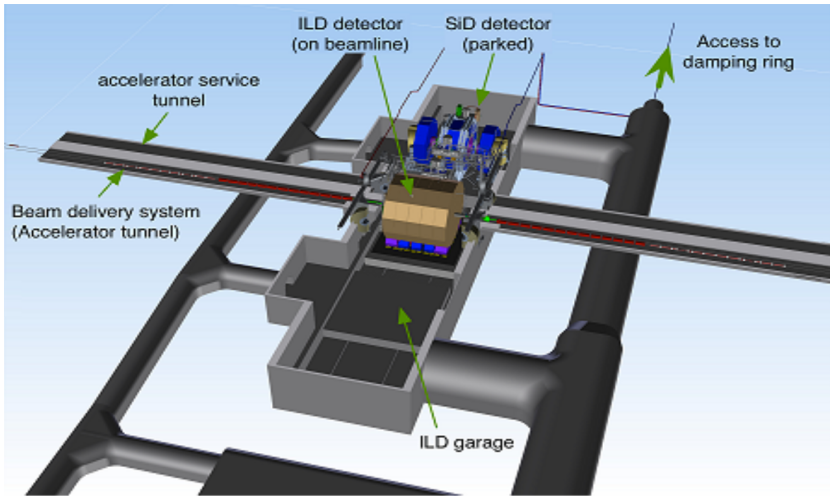

Figure 2.3: Push and pull configuration of the ILD and SID [25].

2.2.1 Luminosity for ILC

The luminosity L is one of the significant parameters of the colliders, and it is defined by the number of collisions per area unit per second. The luminosity for the ILC is defined as follows:

$$L = \frac{n_b N_1 N_2 f_{rep}}{A} \cdot H_D \tag{2.2}$$

n_b is the number of bunches, f_{ref} represents the frequency of the bunch trains. N_1 and N_2 are the numbers of particles per bunch for each beam. H_D is the beam-beam enhancement factor. A is the cross-section at the interaction point (IP), for a Gaussian beam profiles $A = 4\pi\sigma_x\sigma_y$ with σ_x and σ_y are the horizontal and vertical bunch sizes, respectively. The bunch sizes at the IP can be expressed by the horizontal and vertical emittance $\epsilon_{x,y}$ and the $\beta_{x,y}$ function:

$$\sigma_{x,y} = \sqrt{\epsilon_{x,y} \cot \beta_{x,y}} \tag{2.3}$$

The luminosity can also be expressed as a function of the beam size and the energy in the center-of-mass, and defined as follows:

$$L = \frac{\sqrt{s} n_b N^2 f_{rep}}{4\pi\sigma_x\sigma_y\sqrt{s}} \cot H_D \;\propto \frac{N}{4\pi\sigma_x\sigma_y\sqrt{s}} \cdot P_{beam} \tag{2.4}$$

where P_{beam} is the beam power ($P_{beam} = \sqrt{s} N f_{rep}$). It is proportional to the provided radio frequency power during the acceleration $P_{beam} = \eta_{RF} P_{RF}$. η_{RF} is the factor of transferring radio frequency power into beam power.

The luminosity in the ILC is estimated in the order of $L = 0.75\text{-}1.8 \times 10^{34} cm^{-2} s^{-1}$ for 250 GeV and $L = 3.6\text{-}4.9 \times 10^{34} cm^{-2} s^{-1}$ in case of an upgrade [26]. To reach this required luminosity, the beam needs to have a very small vertical emittance at the IP as well as a vertical bunch size of nanometer range.

2.2.2 Bunch Structure in the ILC

The beam structure in the ILC has a specific structure, as shown in Figure 2.4. It consists of bunch-trains with a repetition rate of 5 Hz, roughly 200 ms between two successive bunch-trains. One bunch-train contains 1312 bunches separated by 554 ns and with a population of 2×10^{10} particles. In case of an upgrade to 1 TeV, the number of bunches increases to 2450 per bunch train with a population of $1,74 \times 10^{10}$ particles [27]. Since the length of each

bunch-train is 727 μs, most parts of the detector components are running in idle during almost 199 ms. Therefore, a power pulsing concept is used where a part of the detector hardware can be switched off between the two bunch-trains. A detailed description of the power pulsing concept is discussed in (chapter 4) section 4.2.4.

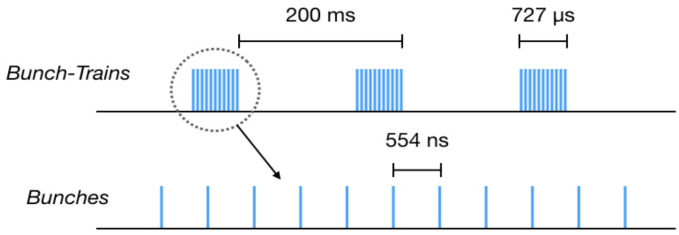

Figure 2.4: Schematic of the ILC bunch structure [28].

2.2.3 Detector concepts for the ILC

At the ILC, two detector experiments are planned to fulfill the four-eyes principle, which requires at least two detectors to confirm a discovery. These two concepts are the Silicon Detector (SID) and the International Large Detector (ILD).

2.2.3.1 The International Large Detector (ILD)

The ILD concept is a combination of two detectors concept, the LDC [29] and GLD [30]. The structure of the ILD is typical for collider experiments. Like many high energy physics detectors, it has a sandwich structure. A schematic view of the ILD detector is shown in Figure 2.5a. The current ILD design has a shape of the closest cylinder with a length of 13 m and a radius of 7.8 m. The different parts of the sub-detectors are shown in the 2D projection in Figure 2.5b. The vertex detector is the closest part of the interaction point, and the main tracker cylinder surrounds it. Both are, in turn, surrounded by the electromagnetic (blue) and hadronic (green) calorimeters. All the previous sub-detectors are located within a superconducting solenoid coil with an inner radius of 3.4 m. A magnetic field of 3.5 T will be used and oriented in parallel to the beam axis. A detailed description of all sub-detectors of the ILD starting from the IP is presented in the following paragraphs:

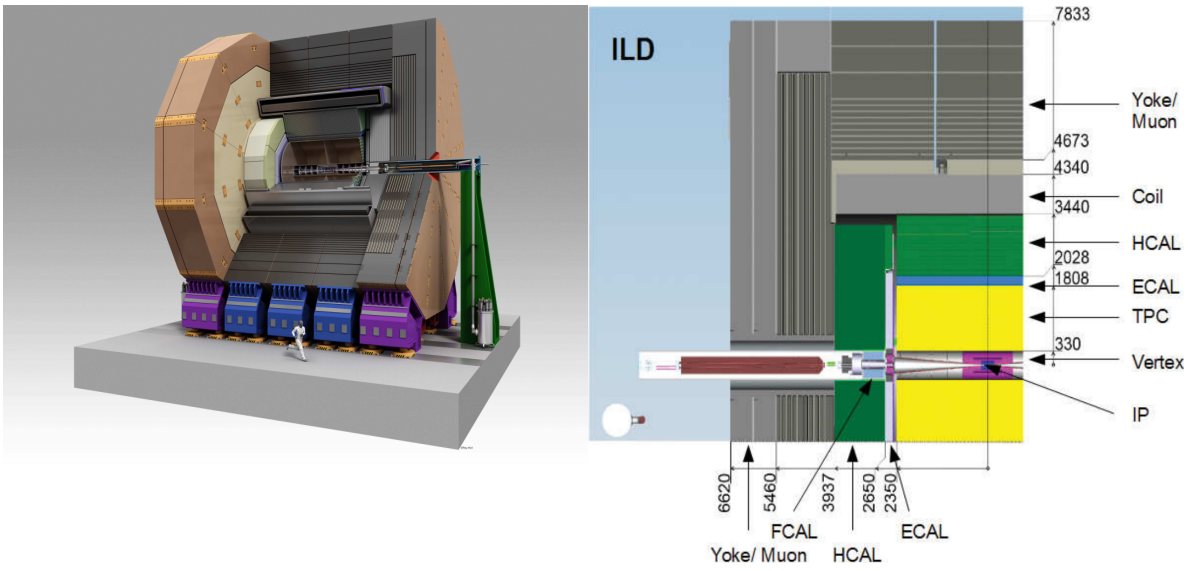

(a) (b)

Figure 2.5: a) 3D schematic of the International Large Detector. b) 2D projection of the ILD profile, the picture shows the interaction point with the different sub-detectors. The dimensions are given in mm [3].

Vertex Detector (VTX) : The Vertex detector consists of a multi-layer pixel surrounding the interaction point. There are two alternative geometries for the VTX, either three double-layers of a thin pixel sensor or five outdistance single layers of silicon pixel. The VTX provides a very high hit position resolution over 3 μm with a minimized material thickness of less than 0.0015 X_0 per layer. Therefore, a high track reconstruction of the short-lived particles, which does not reach the main tracking system, can be achieved.

Tracking System : The ILD tracking system combines a high-resolution Time Projection Chamber **(TPC)** with a few silicon tracking layers placed before and after the TPC. The TPC covers a volume of ∼4.6 m in length and 33 to 180 cm in radius. This large volume can provide up to 224 three dimensional points per track, leading to an excellent reconstruction of the charged particle, the secondaries, long-lived particle, kinks. Also, the TPC can offer the identification of the particles through the energy loss measurement ($\frac{dE}{dx}$). The combination of the TPC with the silicon layers can provide a high momentum resolution of $2 \times 10^{-5}\ GeV^{-1}c^{-1}$ in the complete tracking system.

Calorimeters : The calorimeter system is placed after the TPC and subdivided into two calorimeters. The Electromagnetic Calorimeter (ECAL) is optimized to measure the energy

deposit of electrons and photons, whereas the Hadronic Calorimeter (HCAL) is responsible for the hadronic shower measurement. They are designed for the Particle Flow approach with very high granularity to achieve the required energy resolution. The high granularity leads to a challenge of the readout system of 10^8 channels for HCAL and 10^{10} for the ECAL. A segmentation of $1{\times}1$ cm^2 and $3{\times}3$ cm^2 is required for the ECAL and HCAL, respectively. Different technologies are in development for both calorimeters with different active materials and absorbers. A detailed description of both detectors is discussed in section 3.5.

Magnet Coil and Yoke (muon system) : The calorimeter system is surrounded by a superconducting coil to generate an axial magnetic field of 3.5 Tesla. The high magnetic flux is returned by an iron yoke used as a muon system and a tail-catcher for the shower leakage in the HCAL.

2.2.3.2 The Silicon Detector (SiD)

The SiD concept is similar to the ILD with a difference in the size and the tracking system. The SiD is smaller than the ILD with a length of 11 m and a radius of 6.6 m, but it has a stronger magnetic field of 5 T. Besides, the SiD uses a full silicon tracking system, but the calorimeters technologies are the same as for ILD.

2.3 Physics of the ILC

The ILC machine plans an ambitious physics program. The aspects of its physics program are the measurement of the Higgs boson and the top quark properties with very high precision and the search for new particles at the TeV energy scale. In addition to the previous aspects, the ILC plans broader physics research by including the precision of the electroweak measurement and the study of the W and Z bosons couplings. An overview of the most relevant processes at the ILC for different center-of-mass energies are shown in Table 2.1.

2.3.1 Higgs Physics

At the ILC, they are three main processes in which the Higgs can be produced: $e^+e^- \rightarrow ZH$ (Higgsstrahlung), $e^+e^- \rightarrow \nu\bar{\nu}H$ (W-fusion) and $e^+e^- \rightarrow e^+e^-H$ (Z-fusion). Figure 2.6a shows the Higgsstrahlung process with Higgs Boson production in association with a Z

Boson. While in vector boson fusion processes the Higgs is in association with either neutrino-antineutrino pair or electron-positron pair, as shown in Figures 2.6b and 2.6c.

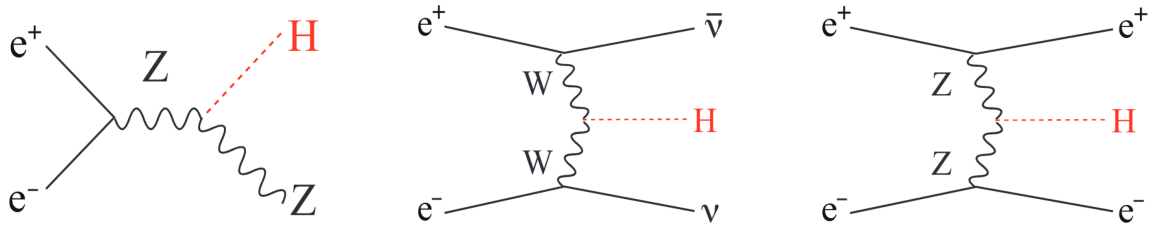

(a) Higgsstrahlung (b) W-fusion (c) Z-fusion

Figure 2.6: Feynman diagrams of the three major Higgs production processes at the ILC [26].

$\sqrt{s}[GeV]$	Processes	Physics goal
250	$e^+e^- \to Z$	utra-precision electroweak
	$e^+e^- \to WW$	utra-pracision W boson mass
	$e^+e^- \to ZH$	precision Higgs couplings
350-400	$e^+e^- \to t\bar{t}$	top quark mass and couplings
	$e^+e^- \to WW$	precision W boson couplings
	$e^+e^- \to \nu\bar{\nu}H$	precision Higgs couplings
500	$e^+e^- \to f\bar{f}$	precision search for Z'
	$e^+e^- \to t\bar{t}H$	Higgs couplings to top
	$e^+e^- \to ZHH$	Higgs self-coupling
	$e^+e^- \to \tilde{\chi}\tilde{\chi}$	search for supersymmetry
	$e^+e^- \to AH, H^+H^-$	search for extended Higgs states
700-1000	$e^+e^- \to \nu\bar{\nu}HH$	Higgs self-coupling
	$e^+e^- \to \nu\bar{\nu}VV$	composite Higgs sector
	$e^+e^- \to \nu\bar{\nu}t\bar{t}$	composite Higgs and top
	$e^+e^- \to \tilde{t}\tilde{t}*$	search for supersymmetry

Table 2.1: Major physics processes to be studied by the ILC at different center-of-mass energies. The table taken from [26].

Figure 2.7 shows the cross-section of the Higgs production processes with the left-hand polarization ($P(e^-, e^+) = (-0.8, +0.3)$) as a function of the energy in the center of mass ($\sqrt{s}$). At $\sqrt{s} = 250\,GeV$, the Higgsstrahlung process attains its maximum cross-section, while the W-fusion process becomes dominant above $\sqrt{s} = 450$ GeV. The Z-fusion process is possible, but it is suppressed by W-fusion, due to the small coupling of the Z boson to electrons. For

each of these processes, the decay modes of the Higgs can be separately identified, as shown in Table 2.2. The most dominant decays of the Higgs are into a pair of bottom quarks ($H \to b\bar{b}$) and a pair of W bosons ($H \to WW^*$) with a branching ratio of 57.7% and 21.5%, respectively. The Higgs can also decay into a pair of Z bosons, but with a branching ratio that is an order of magnitude lower than the W pairs. Other decays with low branching ratio are possible such as $H \to gg$, $H \to \tau^+\tau^-$, $H \to \gamma\gamma$, and $H \to \mu^+\mu^-$.

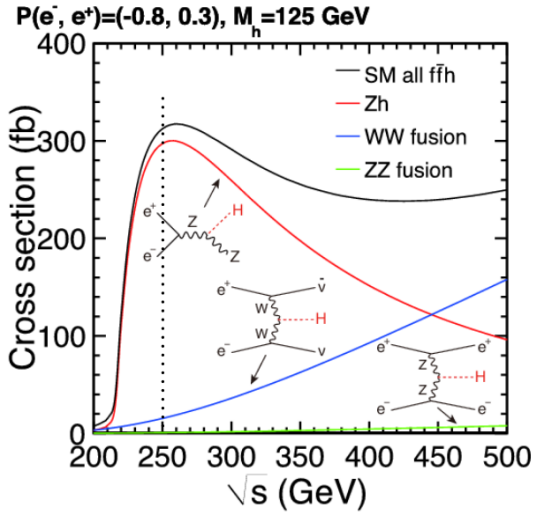

Figure 2.7: Standard Model cross-section of the dominant Higgs production channels at different collision energies at the ILC. The polarization is assumed to be 80% for the electron beam and 30% for the positron beam [31].

Decay modes	Branching Ratio
$H \to b\bar{b}$	57.7 %
$H \to WW^*$	21.5 %
$H \to ZZ^*$	2.6 %
$H \to gg$	8.6 %
$H \to \tau\bar{\tau}$	6.3 %
$H \to c\bar{c}H$	2.9 %
$H \to$ others	$< 1\%$

Table 2.2: Branching Ratio for decays modes of Higgs Bosons for $m_H = 125GeV$. Other decays represent: $\mu\mu$, $\gamma\gamma$, Zγ and invisible [32].

Higgs recoil mass measurement

At the ILC, the four-momentum of the initial state (p_{CM}) is well defined, leading to an inclusive measurement of the cross-section via the Higgsstrahlung process $e^+e^- \to ZH$. Since we can reconstruct the four-momentum of the Z boson (p_Z), it is possible to calculate the invariant mass of the Higgs without looking into its decays. The Higgs mass can then be calculated by the recoil technique $M_X = \sqrt{p_{CM}^2 - p_Z^2}$. The measurement of the leptonic decay of Z ($Z \to l^+l^-$ with $l = e, \mu$) provides a very precise determination of the Higgs boson mass. The mass of the particle recoiling against the lepton pair is calculated as follows:

$$M_X = \sqrt{p_{CM}^2 - (p_{l^+} + p_{l^-})^2} \tag{2.5}$$

where p_{CM} is the four-momentum of the annihilating electron-positron, and $p_{l^\pm}$ is the four-momentum of Z decay products. Figure 2.8 shows the measurement of recoil mass of Higgs of $e^+e^- \to ZH$ where four-momentum of Z is measured by its leptonic decay $Z \to \mu^+\mu^-$. With this measurement, the Higgs mass can be determined precisely with a mass resolution of $\Delta m_H \sim 30 MeV$.

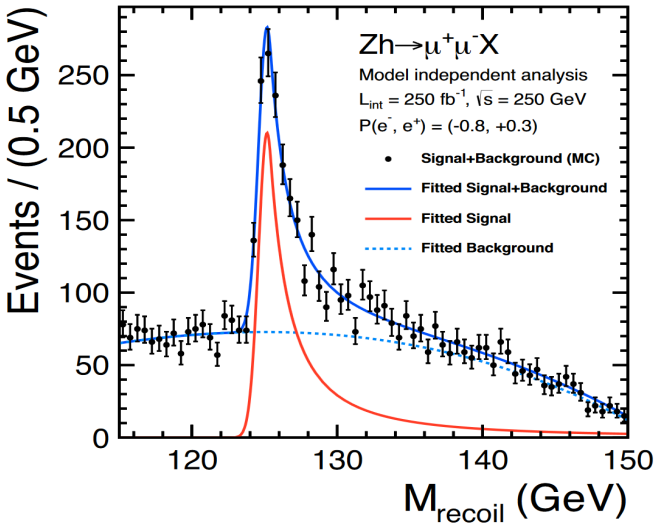

Figure 2.8: Recoil mass distribution of $e^+e^- \to ZH$ followed by $Z \to \mu^+\mu^- H$. Simulated for $m_h = 125$ GeV with an integrated luminosity L = $250 fb^{-1}$ at 250 GeV [33].

There is also the possibility to reconstruct the p_Z from the hadronic decay of $Z \to q\bar{q}$. However, the Higgs mass resolution won't be easy since the reconstruction of Z from the two

jets can be affected by the Higgs decay products. Furthermore, the branching ratio of the hadronic decay $Z \to q\bar{q}$ is much larger than the leptonic decay. Therefore, efforts are ongoing to improve the event selection. Additionally, the Z and Higgs bosons can be better separated at 500 GeV, since they are sufficiently boosted at high energy.

Higgs Couplings

In the Standard Model (SM), the couplings of the Higgs boson to SM particles can be calculated once the masses of the particles in question and the Higgs boson mass are measured. Therefore, one of the highest interest is the precision of the Higgs boson coupling strengths. The Higgs boson rate measurement is proportional to the cross-section for Higgs production multiplied by the branching ratio (BR). The BR of a decay channel is expressed as follows:

$$BR(h \to A\tilde{A}) \;=\; \Gamma(h \to A\bar{A})/\Gamma_h, \qquad\qquad with \qquad \Gamma(h \to A\bar{A}) \propto g^2_{hAA} \tag{2.6}$$

where $\Gamma(h \to A\bar{A})$ is the partial width into the observed channel, g_{hAA} is the coupling of Higgs to a given particle and Γ_h is the total width of Higgs boson. The determination of the Γ_h gives information about the absolute sizes of the Higgs boson couplings. At the LHC, all determinations of Γ_h require model-dependent assumptions. However, the ILC measurements provide a model-independent determination of Γ_h. As already discussed, it is possible to identify all Higgs decay modes in the Higgsstrahlung process using the recoil technique. Therefore, the full inclusive Higgsstrahlung production cross-section $\sigma(e^+e^- \to hZ)$ and the hZZ coupling (g_{hZZ}) can be measured. The hWW coupling can be defined as the event rate of the W fusion process ($e^+e^- \to h\nu_e\nu_e \quad with \quad h \to b\bar{b}$) divided by the branching ratio $BR(h \to b\bar{b})$, this BR is determined with Higgsstrahlung. Therefore, the measurements of g_{hZZ} and g_{hWW} determine the $\Gamma(h \to ZZ)$ and $\Gamma(h \to ZZ)$.

The measurement of the Higgs total with Γ_h can be determined by the equation 2.6, using the W fusion process since its branching ratio is roughly ten times larger than the Z fusion process. The measurement uncertainty of Γ_h lies on the precision of each absolute coupling measurement. Therefore, all the inclusive cross sections are included in the global fit to minimize the uncertainty of Γ_h. A comparison of the uncertainties in Higgs coupling expected from the High-Luminosity LHC and the two phases of the ILC program with the possible combination is shown in Figure 2.9a. A precise measurement of the Higgs coupling,

below 1%, can be provided by the ILC with an improvement of one order of magnitude compared to the LHC. The estimated uncertainties from the ILC using the model-independent fit to the Higgs boson couplings are shown in Figure 2.9b. In this model-independent analysis, all the Higgs couplings are considered separately, including the invisible and the exotic modes.

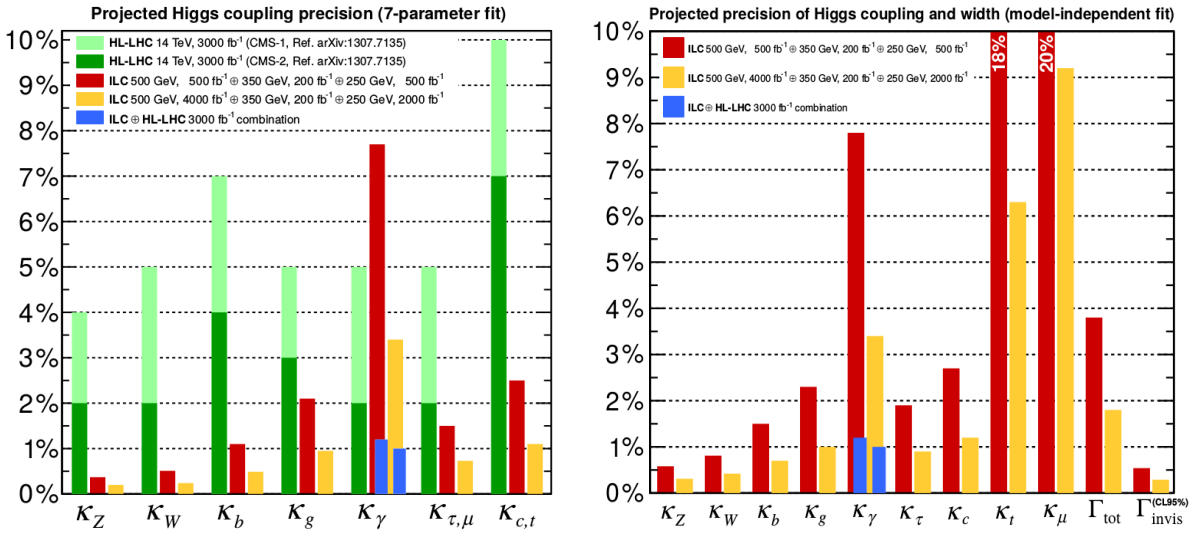

(a) Model-dependent (b) Model-independent

Figure 2.9: Relative precisions on the ratio of the measured Higgs couplings to the Standard Model expectations for the ILC, using both model-dependent (a) and model-independent (b) analysis. In the model-dependent assumptions, the projection of the achievable precision for the HL-LHC are shown in a pessimistic (CMS-1) and optimistic (CMS-2) case on the systematic uncertainties [31].

Higgs Self-Couplings

The studies of the Higgs self-coupling are an important key for improving our understanding of the symmetry breaking in the electroweak sector as well as the CP violation in the Higgs sector. The trilinear Higgs self-coupling λ can determine the shape of the Higgs potential, as already shown in Figure 1.2. A precise measurement of Higgs self-coupling can be done in the ILC either by Higgsstrahlung ($e^+e^- \to ZHH$) or W-fusion ($e^+e^- \to \nu\bar{\nu}HH$) processes. The cross-section of these processes depend strongly on the center-of-mass energy, where the Higgsstrahlung process is dominant at $\sqrt{s} = 500$ GeV and W-fusion process dominant at higher energies [34]. Simulations have been done for two Higgs decay modes $HH \to b\bar{b}b\bar{b}$ and $HH \to b\bar{b}WW$ at $\sqrt{s} = 500$ GeV with an integrated luminosity of 4 ab^{-1}. By combining the results of these two channels, a precision of 27% on the Higgs self-coupling can be predicted and a precision improvement to 10% at $\sqrt{s} = 1$ TeV for 5000 fb^{-1} is expected [34, 35].

2.3.2 Top Physics

The top quark is the heaviest and latest discovered quark in the Standard Model of particle physics. The mass of the top is $m_t = 173.34 \pm 27(Stat.) \pm 0.71(\text{Syst.})$ GeV with a short lifetime of $10^{-25}s$ [36]. Comparing to other particles, the top quark has the strongest coupling to the Higgs field because of its large mass. It has been studied in the hadron collider, so the International Linear Collider would be the first machine to study the top quark in its leptonic initial state.

At the ILC, two major top physics programs can be studied. The first consists of studying the threshold of the $t\bar{t}$ production at $\sqrt{s} = 350\ GeV$. This study provides the measurement of the top quark mass with a precision below 10^{-3}. Besides, the detailed properties of the top quark can be studied, such as its total width Γ_t. The second is to study the top quark coupling to the Higgs at $\sqrt{s} = 500\ GeV$. The precise measurement of top quark coupling to electroweak interactions can be a major key to search for physics beyond the Standard Model. At $\sqrt{s} = 500$ GeV with an integral luminosity of 2500 fb^{-1}, the ILD expects to measure the top quark coupling to Higgs with a statistical uncertainty of 11%. This precision can be improved to 6.4% with a higher integral luminosity of 4000 fb^{-1} [37]. Furthermore, a 4-5% precision is expected at $\sqrt{s} = 1$ TeV [38].

Chapter 3

Calorimetry and Particle Flow Concepts

The Calorimeters are the only tool to measure particles' energy by measuring the energy they deposit while interacting with matter. In this chapter, different interactions of particles with the matter are discussed, as well as detection methods of their interaction products. Subsequently, a description of the calorimetry response and energy resolution is given. Toward the end of the chapter, the Particle Flow Algorithm (PFA) used to improve the performance of jet reconstruction, is described in detail. Finally, the different concepts of high granularity calorimeter developed by CALICE Collaboration are presented.

3.1 Particle Interaction with Matter

Generally, when a particle traverses matter, it deposits a fraction of its energy via different interaction processes, depending on the nature and the energy of the particles. In this section, the interaction processes of particles with matter are presented, including the characteristics of the development of the electromagnetic and hadronic showers.

3.1.1 Electromagnetic Interactions

Electromagnetic interactions describe the interactions of charged particles while traversing the matter. These particles can be classified into electrons, positrons, heavy particles (muons), and charged hadrons and can lose their energy in different processes.

3.1.1.1 Energy Loss of Charged Particles

The electromagnetic interaction of electrons or positrons can manifest in different processes, depending on their initial energies. The fraction of energy loss per radiation length in lead as a function of electron or positron energy is shown in Figure 3.1. At low energies ($< 10\,MeV$), the ionization process is dominant, whereas, at energies above 100 MeV, domination by bremsstrahlung is visible. The photons emitted by Coulomb interaction carry a relatively small fraction of the incident particle, and their energy spectrum falls off as $1/E$. The energy loss for bremsstrahlung increases roughly linearly with the initial particle energy, as shown in following Eq. 3.1 [39]:

$$-\left[\frac{dE}{dx}\right]_{brems} = \frac{E}{X_0} \tag{3.1}$$

where E is the energy of the incident electron, X_0 is the radiation length. It corresponds to the distance over which a high energy electron or positron loses around 63.2% of its energy by bremsstrahlung. As shown in Eq. 3.2, X_0 depends on the atomic number Z and the mass number A of the material [39].

$$X_0 = \frac{716.4\ A}{Z(Z+1)\cdot ln(287/\sqrt{Z})}[g.cm^{-2}] \tag{3.2}$$

The concept of radiation length can also be applied to photons. When high energy photons lose energy in matter via e^+e^- pair production, the mean free path (l) for pair production is [39]:

$$l = \frac{9}{7}\cdot X_0 \tag{3.3}$$

The critical energy E_c is the energy at which the ionization loss is equal to the radiation loss. It is material-dependent and can be parametrized in Eq. 3.4 and Eq. 3.5 [40] for solids (or liquids) and gases, respectively. Figure 3.2 shows the electron critical energy of different chemical elements for gases and solids.

$$E_c = \frac{610\ MeV}{Z + 1.24} \tag{3.4}$$

$$E_c = \frac{710\ MeV}{Z + 0.92} \tag{3.5}$$

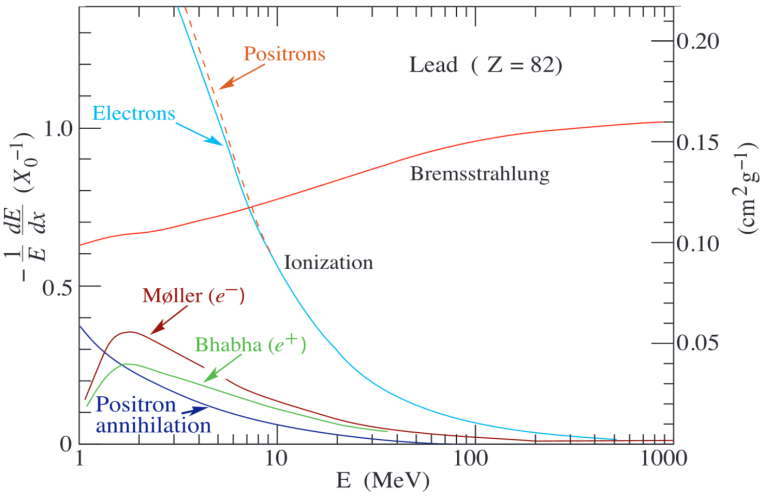

Figure 3.1: Fractional energy loss per radiation length in lead as a function of electron or positron energy [41].

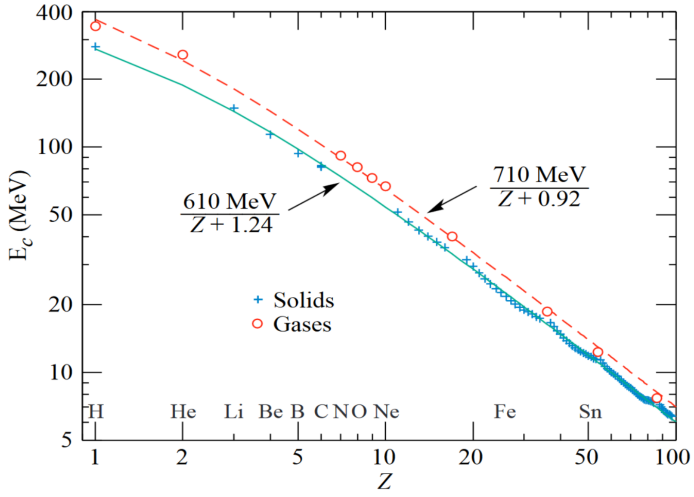

Figure 3.2: Electron critical energy for chemical elements for solids (liquids) and gases. For solids and liquids, the fit is in solid line while it is a dashed line for gases [42].

3.1.1.2 Energy Loss of Photon

Photons mainly interact in four processes: The photoelectric effect, coherent (Rayleigh) scattering, incoherent (Compton) scattering, and electron-positron pair production. In **photoelectric effect**, the photon ejects an electron from the atomic shells by transferring all its energy. The kinetic energy of the ejected electron equals the photon energy minus the binding energy. The **Rayleigh scattering** occurs at low photon energies, where the photon scatters in the medium without a significant energy loss. The **Compton effect** occurs when

the incident photon energy is much higher than the electron's binding energy. In this process, the photon interacts with an electron by transferring a part of its energy. The remaining photon energy is emitted in a different direction from the original. In **electron-positron pair production**, it is necessary for the photon to carry an energy twice larger as the electron rest mass ($\zeta = E_\gamma / m_e c^2$). The incident photon interacts in the matter very close to the nucleus and converts its total energy to $e^- e^+$ pair production.

Figure 3.3a shows the domination region for the photoelectric effect, Compton scattering and pair production, and its dependence on the photon energy and the Z value of the absorber material. At the highest Z value, the Compton scattering is the dominant process in a limited energy range between a few hundred keV and ~ 5 MeV. At high energies, the pair production process dominates. While at low energies, the domination of the photoelectric effect increases with the Z of the absorber material. The contribution of the photon cross-section in a heavy absorber (lead) is illustrated in Figure 3.3b. At low energies up to the pair production threshold, a domination of the photoelectric effect is seen.

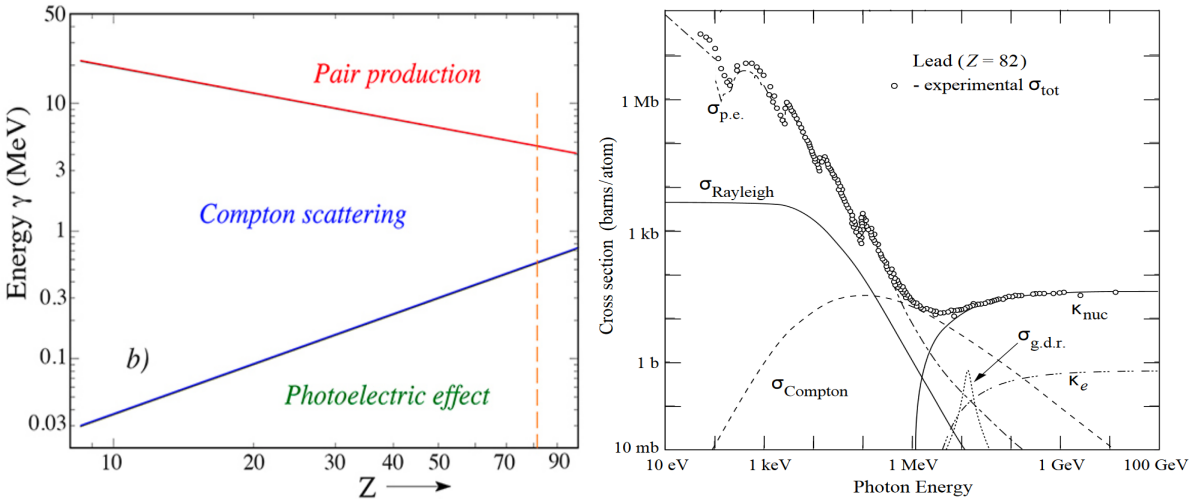

(a) (b)

Figure 3.3: a) The energy domains in which photoelectric effect, Compton scattering and pair production are the most likely processes to occur, as a function of the Z value of the absorber material [43]. b) Photon total cross-section as a function of photon energy in lead. $\sigma_{p.e}$ is the photoelectric cross-section, $\sigma_{Rayleigh}$ is the coherent scattering cross-section, $\sigma_{Compton}$ incoherent scattering cross-section, σ_{Ke} is the pair production cross-section in electron field, σ_{nuc} is pair production cross-section in nuclear field and $\sigma_{g.d.r.}$ is the photo-nuclear cross-section [42].

3.1.1.3 Electromagnetic Cascades

For high energy electrons, the primary source of energy loss is Bremsstrahlung. When a multi-GeV electron traverses the material, it may radiate thousands of photons, mostly very soft. They are then absorbed due to Compton scattering and the photoelectric effect. The photons with an energy more than ~1.1 MeV create a $e^- e^+$ pairs. The repetition of pair production and bremsstrahlung processes generate more electrons, positrons, and photons with lower energy leading to a formation of an electromagnetic shower. Figure 3.4 diagrams the development of electromagnetic cascade. The number of the generated particles is approximately $N \approx E/E_c$ with E_c being the critical energy. The electromagnetic cascade development stops when the electron energy is around the critical energy.

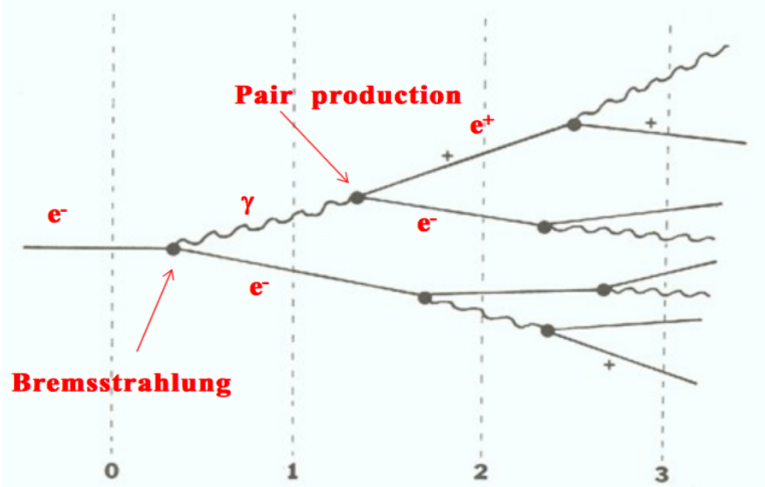

Figure 3.4: Sketch illustrating the development of electromagnetic cascade.

The Molière radius The Molière radius ρ_M describes the transverse development of electromagnetic showers. On average, the electromagnetic shower deposit 90% of its energy within a cylinder of 1 Molière radius, and 99% in a cylinder of ~3.5 ρ_M. It is parameterized as a function of radiation length X_0 and critical energy E_c, as follows [44]:

$$\rho_M = 21.2\, MeV \cdot \frac{X_0}{E_c} \tag{3.6}$$

Electromagnetic shower profiles The development of electromagnetic showers is almost material independent since it is expressed in X_0 and ρ_M units. The longitudinal development of 10 GeV electron showers in aluminum, iron, and lead are shown in Figure 3.5a. The shower

profile dependence on the atomic number of the absorber material can be seen. By increasing the Z value of the absorber, either the shower maximum shifts to a greater depth or the shower profile decays slowly beyond the shower maximum. The mean maximum shower t_{max} is parametrized by:

$$t_{max} = \frac{x}{X_0} = ln\left(\frac{E_0}{E_c}\right) + C_j \qquad with\ j = e, \gamma \tag{3.7}$$

with C_e = - 0.5 for cascades induced by electrons and C_e = 0.5 by photons. Figure 3.5b illustrates the energy deposit in copper as a function of the depth for electrons with different energies from 1 to 1000 GeV. The shower maximum for 1 GeV is roughly 5 cm, and then it increases by ∼3.5 cm for every order of magnitude in energy. The shower maximum of 1 TeV is ∼16 cm.

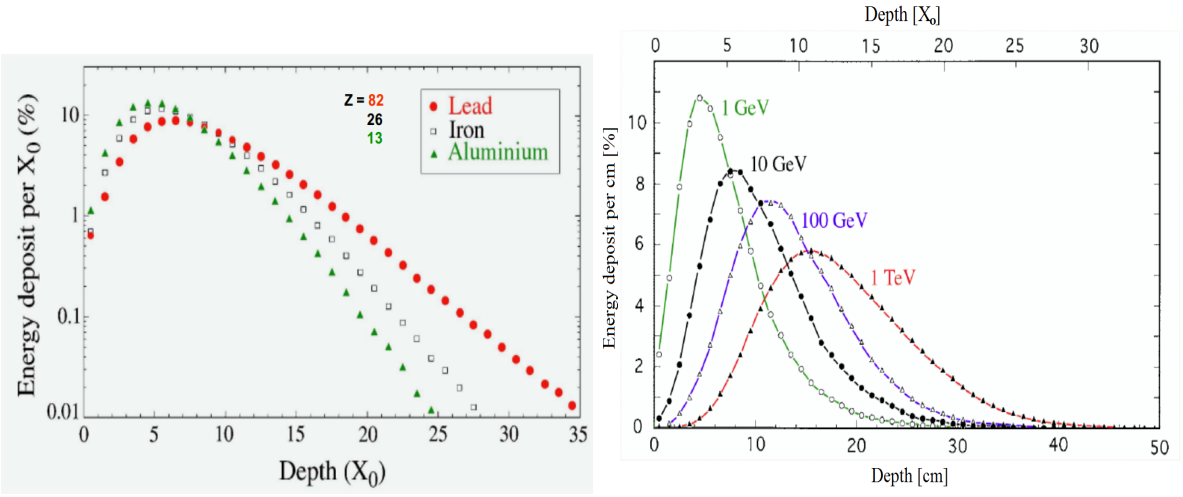

(a) (b)

Figure 3.5: a) Energy deposit as a function of the depth, for 10 GeV electron showers developing in aluminum, ion and lead. The plot shows an approximate scaling of the longitudinal shower profile. Results of EGS4 calculations [44]. b) Energy deposit as a function of depth, for 1, 10, 100 and 1000 GeV electron showers developing in a block of copper. The curves are normalized to the same value. The vertical scale gives the energy deposit per cm of copper, as a percentage of the energy of the showering particle, Results of EGS4 calculations [45].

3.1.2 Heavy Charged Particles Interactions

The major process in the energy loss of charged particles is bremsstrahlung, and it depends on the mass of the particle, as shown in the following equation:

$$-\left[\frac{dE}{dx}\right]_{brems} \approx \frac{1}{m^4} \tag{3.8}$$

Therefore, the bremsstrahlung process is suppressed for the massive charged particles. The heavy charged particles ionize the medium and release electrons from the Coulomb field if their energy is higher than the atom's binding energy. The energy loss via ionization is described by the Bethe-Bloch formula [46]:

$$-\left[\frac{dE}{dx}\right]_{brems} = Kz^2\frac{Z}{A}\frac{1}{\beta^2}\left[\frac{1}{2}ln\left(\frac{2m_ec^2\beta^2\gamma^2T_{max}}{I^2}\right) - \beta^2 - \frac{\delta(\beta\gamma)}{2}\right] \tag{3.9}$$

where the proportionality constant K equals $4\pi N_A {r_e}^2 m_e c^2$ (≈ 0.307 MeV $cm^2 mol^{-1}$). A and Z are the atomic mass and the atomic number of the material, and z is the projectile charge. T_{max} represents the maximum kinetic energy transferred in a single collision, it is defined as $T_{max} = \frac{2m_ec^2\beta^2\gamma^2}{1+2\gamma m_e/M+(m_e/M)^2}$ where M is the incident particle mass. I is the mean excitation energy of the absorber material and δ is the density correction at higher energies which depends on $\beta\gamma$.

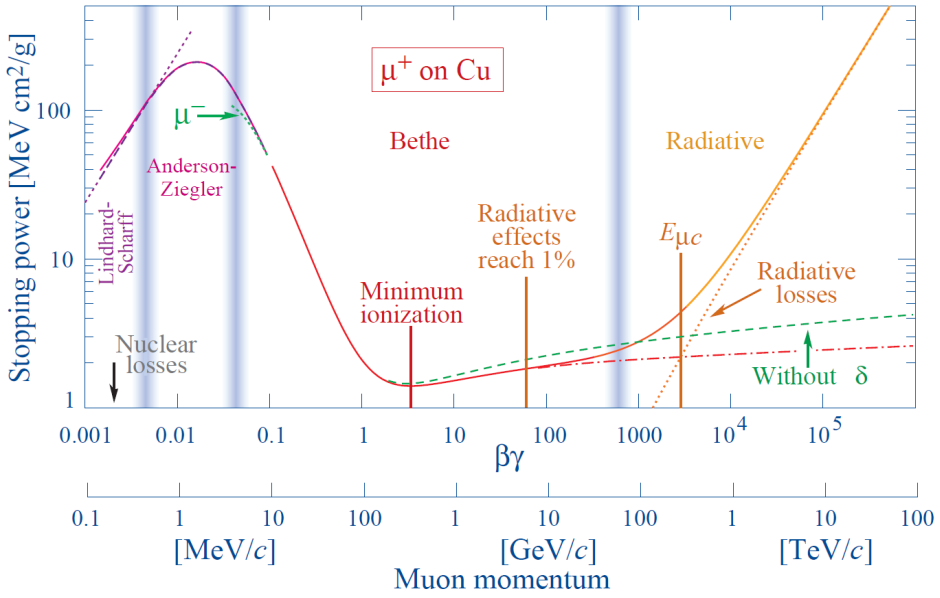

Figure 3.6: Stopping power($-dE/dx \cdot 1/\rho$) for positive muons in copper as a function of muon momentum and $\beta\gamma = p/Mc$ over nine orders of magnitude in momentum. The solid curves indicate the total stopping power [42].

Figure 3.6 represents the average energy loss of positively charged muons in copper as a function of muon momentum. At low momentum, the energy loss is inversely proportional to the square of its velocity $1/\beta^2$, and it decreases to a shallow minimum located approximately at $\beta\gamma \approx 3-4$. In this range, the particles deposit a minimum amount of their energy leading

to deep penetration in the material. These particles are called Minimum Ionizing Particles (MIPs) and are excellent candidates for the calibration measurements. Beyond the minimum ionization, dE/dx increases slightly with $ln(\beta^2\gamma^2)$, but above 100 GeV, the radiation effects are strongly dominating.

The total energy deposition in a sampling calorimeter $\Delta E/\Delta x$ with a thin active layer may differ from the calculated $< dE/dx >$, due to the low number of collisions with the atomic electrons and the large fluctuations of the transferred energy that occur in such collisions. The distribution of energy loss measured in a single layer of a sampling calorimeter is described by the Landau-Vavilov distribution, as shown in Figure 3.7. This distribution is skewed, because of the tail at high energy produced by the large fluctuations. The mean value of this distribution is not well defined, so the most probable energy deposition of a single charged particle is used to handle the energy deposit.

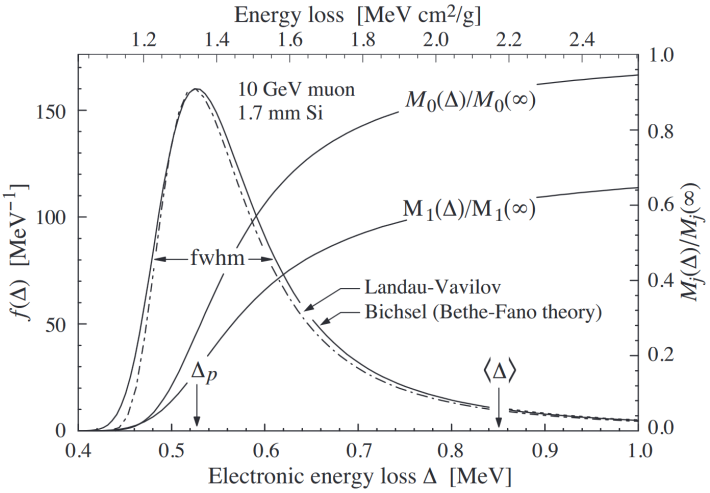

Figure 3.7: Energy deposit distribution for a 10 GeV muon traversing 1.7 mm of silicon. The Landau Vavilov function (dot-dashed) uses a Rutherford cross section and the solid curve was calculated using a different approach in deriving the distribution [42].

3.1.3 Hadronic Interactions

The hadronic interactions describe the strong interaction of neutral and charged hadrons. The hadrons can interact with the medium via two processes. Depending on their energies, they can scatter either elastically or inelastically. In the elastic process, the hadrons deflect at some angle from their initial trajectories without changing their nature. However, in the inelastic process, the incident hadron interacts strongly with the nucleus and can change its

identity by generating several secondary particles. Usually, the struck nucleus can also change its identity in such a reaction. As in the case of the electromagnetic interaction, the formation of a hadronic cascade can also be described by a series multiple strong interactions, as shown in Figure 3.8. The nuclear interaction length λ_{int}, shown in the Eq. 3.10 characterizes the longitudinal evolution of the hadronic shower. It is the average distance over which a high energetic hadron can travel through the matter before having the first strong interaction with a nucleus.

$$\lambda_{int} = \frac{A}{N_A} \cdot \frac{1}{\sigma_{inelas} \cdot \rho} \tag{3.10}$$

where A is the atomic mass, N_A is the Avogadro number, $\sigma_{inelas.}$ is the cross-section of the inelastic scattering, and ρ is the density of the traversed medium. In a medium with relatively high atomic number Z, the length of the hadronic shower is more extended than the electromagnetic shower. The probability that a hadron traverses a distance z in the medium without having a nuclear interaction is defined as follows:

$$P = \exp\left(\frac{-z}{\lambda_{int}}\right) \tag{3.11}$$

In the hadronic cascade, most of the generated secondary particles are η mesons or pions ($\pi^{\pm}$, π^0). Therefore, the electromagnetic component is always taking part in the hadronic shower, due to the electromagnetic decays of π^0 and η ($\pi^0, \eta \to \gamma\gamma$). On average, one-third of the mesons produced in the first interaction are neutral pions π^0. This means that for each collision, one-third of the energy deposit is originally from electromagnetic showers. Besides, the remaining hadrons from the second generation of nuclear interactions can also produce neutral pions if they are sufficiently energetic. Therefore, the fraction of π^0 produced from the initial hadron is gradually increasing with energy. After n generations the electromagnetic fraction of hadronic showers is defined as follows:

$$f_{em} = 1 - \left(1 - \frac{1}{3}\right)^n \tag{3.12}$$

In the example of a shower induced by 20 GeV pions in lead, the electromagnetic fraction is $< f_{em} >= 0.389$. While this fraction increases to $< f_{em} >= 0.678$ for 700 GeV pions [47].

In addition to the produced mesons, protons and neutrons can also be released after the nucleus's de-excitation via spallation, fissions, and evaporation processes. Spallation is the

most dominant process, and it is described as a two-stage process: a fast intranuclear cascade and slow nuclear evaporation. In the first stage, the strong interaction of the incoming hadron with the stuck nucleons leads to a ejection of nucleons. These particles travel through the medium and interact with other nucleons, forming a cascade of fast nucleons. The second stage of the spallation consists of a de-excitation of the nucleus by evaporating nucleons. This reaction takes place until the excitation energy is less than the binding energy of the nucleon. After spallation, the remaining energy of the nucleons is released by the emission of gammas. The fission reaction is also possible for very heavy nuclei like Uranium. In the hadronic cascade, only few hard interactions occur with a large number of secondary particles, leading to large event-to-event fluctuations.

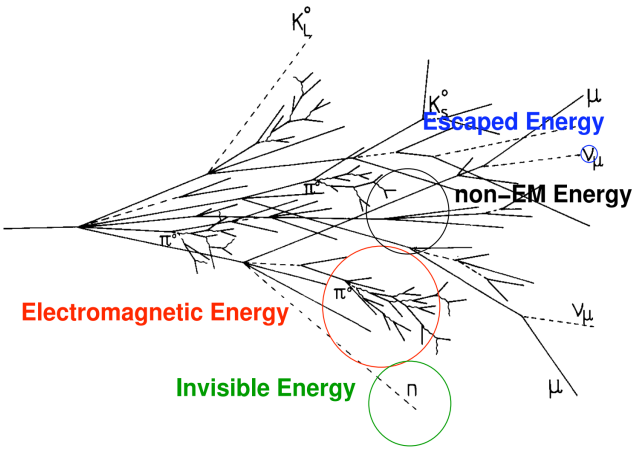

Figure 3.8: Components of hadronic shower. Different colors are representing the different energies calculated in different processes [48].

3.1.4 Invisible and Escaped Energies

In a hadronic calorimeter, around 30% of the energy deposited by the hadronic shower is not measurable as it is either invisible or escaped. In the nuclear reaction, the energy used to release the nucleons is invisible and does not contribute to the calorimeter signal. Additionally, the stable neutral and long-lived particles like neutrons, K_L^0, or neutrinos can escape from the calorimeter, leading to missing energy. Consequently, these processes that occur in the hadronic cascade, including the large fluctuations and the non-measurable energy, have a significant effect on the degradation of the hadronic energy resolution.

3.2 Particle Shower Simulation

Simulation is a major key to develop and optimize new detector technologies. In the calorimeter, it helps to understand the shower development and the dependence on the energy and nature of particles and the traversed medium. Several models are provided to simulate all the processes that occur in the electromagnetic and hadronic showers. Besides, the simulation can also be used as a tool for the event selection of the collected data.

The GEANT4 offers various tools and models to simulate both electromagnetic and hadronic cascades. described in more detail in the following sub-sections.

3.2.1 Electromagnetic shower

The electromagnetic showers are mainly composed of the interactions of the electrons, positrons, and photons with the matter, which are generally well understood. The simulation of EM cascades is done by the EM package [49], which can reproduce observables in a sampling calorimeter with a precision of less than 1% [50]. Different EM sub-packages and processes are used to simulate the electromagnetic interactions of charged particles, gammas. The validity range of these models is from the threshold up to 10 PeV. The standard Geant4 approaches in electromagnetic physics are optimal for high and medium energy applications. However, a low energy electromagnetic package is implemented to cover all processes in low-energy applications.

The EM physics list is introduced to GEANT4 with `_EMY` suffix, to improve the description of the ionization processes in the active material. The purpose of this implementation is to simulate thin active layers where detection methods are sensitive to the first ionization.

3.2.2 Hadronic shower

The simulation of hadronic showers is more complicated than the electromagnetic ones, because of the internal composition of the incoming hadron and the nuclei target. Analytically, it is impossible to calculate an individual process of a strong interaction between projectile and target, due to the broad phase space of the final state. Several models are provided by GEANT4 to describe the strong interaction of hadrons with the matter. These models use some approximations and assumptions which are valid in a limited energy range. Therefore, these different models are combined into a physics lists to cover a wide energy range. A

detailed description of the physics lists is discussed in section 3.2.3.

The hadronic interaction is modeled differently, depending on the deBroglie wavelength of the projectile $\lambda_{dB} = \frac{h}{p}$. The nucleus can be modeled as a collection of nucleons at low energies or as a collection of quarks at higher energies. Therefore, different models describe the interactions in different energy ranges.

3.2.2.1 Cascade Models

In the hadronic interaction of particles up to a few GeV, the λ_{dB} is approximately the distance between nucleons. Therefore, the intra-nuclear models simulate only the interactions between nucleons. The free path length between individual interactions within the nucleus is calculated from the modeled densities and parametrized cross-sections. The secondary particles are modeled similarly as the incident particle. Figure.3.9 illustrate the schematic of the cascade models. This process stops when the secondary particles are either absorbed or leave the nucleus, while the remaining nuclear fragments are transferred to the equilibrium state and de-excited.

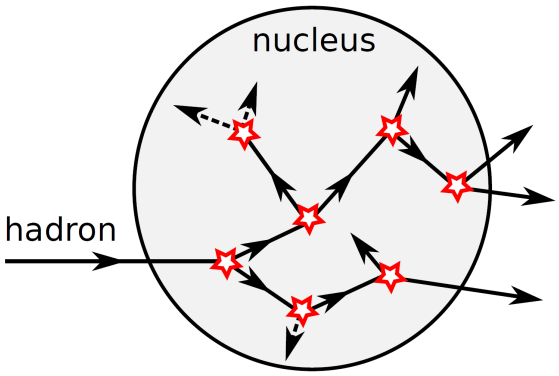

Figure 3.9: Sketch of an intra-nuclear cascade models implemented in GEANT4 [51].

Two different models are provided by GEANT4, Bertini cascade [52], and Binary cascade [53]. In **Bertini Cascade**, the nucleus is modeled as spherical shells of a constant nucleon density. Inside each shell, the model assumes the nucleons to habe a Fermi-gas momentum distribution. As long as the tracked nucleon's energy is greater than 2 MeV, the model keeps calculating the momentum of the struck hadron, reaction type, the reaction products, and the four-momenta. Furthermore, the Bertini model includes the pre-equilibrium evaporation (protons and neutrons emission). Additionally, a full de-excitation is simulated, including

Fermi breakup of the light nucleus ($A < 17$), a simple explosion model, where all nucleons are ejected from the nucleus, a phenomenological fission model and an evaporation model at equilibrium. The **Binary Cascade** models the nucleus as a 3-dimensional spheric and isotropic nucleus with a defined position and momentum of the nucleons. The nucleons position is sampled differently for heavy and light nuclei, using nuclear density distributions while remaining consistent with Pauli's exclusion principle. The nucleons carry momentum randomly chosen between 0 and Fermi momentum such that the vector sum of all momenta is 0. The cascade stops if the kinetic energy of all participants is below 70 MeV. The remaining pre-fragments are modeled by pre-equilibrium and de-excitation models.

3.2.2.2 String Parton Models

The string parton models [54] simulate the inelastic scattering of high energy particles (> 5 GeV) with a nucleus. These models take into account the interaction between quarks using the string excitation model. Figure 3.10.a shows the sketch of the string models, where a string is formed between the projectile quark and nucleus quark. As shown in Figure 3.10.b, this string is excited after multiples interactions leading to a fragmentation of the target nucleon with quark-antiquark production and a new string formation.

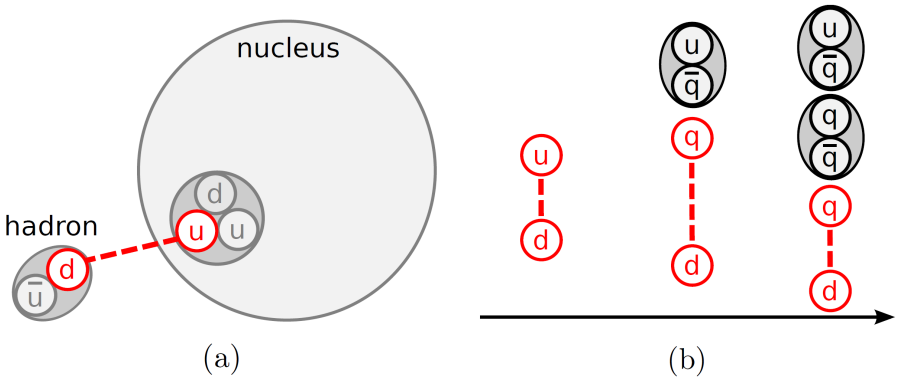

Figure 3.10: Sketch of string models: a) String formation between one parton of incident hadron with one parton from the target nucleon. b) illustrate the strong fragmentation via the generation of quark-antiquark pairs and harmonization [51].

Geant4 provides two different string excitation models, the Fritiof model (FTF) and the quark-gluon string model. These models differ in modelling string formation and fragmentation. In the Fritiof models, only the momentum exchange between projectile and nucleon

in diffractive hadronic interactions is considered [55]. While in the quark-gluon string model, the inelastic scattering process mediated by pomerons is considered [56, 57]. The cascades models also include the propagation of the secondary particles. Additionally, the de-excitation is calculated using the standard GEANT4 de-excitation model [58].

3.2.3 Physics Lists

Several Physics Lists are provided by GEANT4 to simulate the hadron interaction with matter. As shown in Figure 3.11, the physics lists are combining different models which are valid for different energy ranges with a smooth energy transition. In the overlap region, one model is chosen randomly for each incident particle, but some models describe only specific particles. For electromagnetic cascades, the modeling is the same for all these physics lists since there are no differences in the prediction of electromagnetic physics. In this thesis, the physics list used is QGSP_BERT_HP in GEANT4 version 10.03. The QGSP_BERT physics list uses the Bertini cascade model in the energy range up to 10 GeV, and in high energy ($>$ 12 GeV), it uses the Quark-Gluon String Precompound (QGSP) modeling. It also uses a parametrized LEP model to cover the gaps between the transition of cascade models and string parton models. The _HP versions of the QGSP_BERT list improve the high precision neutron tracking at low energies.

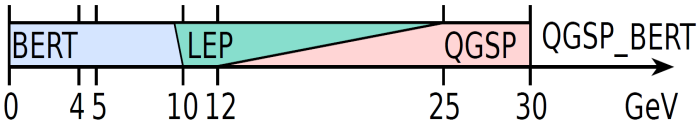

Figure 3.11: Schematic of the physics list which can be used in GEANT4 [59].

3.3 Calorimeters

In high energy physics, the calorimeter is a block of matter used to measure the energy deposited by incident particles. This energy is converted into an electrical signal that is proportional to the energy loss. As already discussed in sections 3.1.3 and 3.1.1, the longitudinal development scales with the energy of the incident particles. Therefore, dense material in the calorimeters is necessary for the full absorption of the particle shower. The calorimeter classifies into homogeneous and sampling calorimeters.

Homogeneous calorimeters: In Homogeneous calorimeter, the whole detector volume is sensitive to particles and can contribute to the generated signals. To restore the total energy of an incident particle, a material with high density and high atomic number is required. In this calorimeter, the charged particle of the shower has the same response in the whole detector. Thus, high statistical precision and good linearity can be achieved. However, their disadvantages are the high cost and limited segmentation. An example of homogeneous calorimeter is used by CMS as an electromagnetic calorimeter with scintillating crystals $PbWO_4$ ($\rho = 8.2\frac{g}{cm^3}$) [60].

Sampling calorimeters: The sampling calorimeter consists of passive absorber layers with high-density alternated with active layers such as silicon, scintillator, or liquid argon. Consequently, a good transverse and longitudinal segmentation can be archived. However, only the energy deposited in the active material is measured and used to extrapolate the full shower energy deposited in the whole detector. Therefore, the energy resolution is worse than the homogeneous calorimeter, due to the fluctuations in the fraction of the total energy measured in the sensitive layers. This fraction can be quantified by the sampling fraction factor f_s. It is defined as the fraction of the full shower energy measured by the active layers divided by the energy deposited in the whole detector. Its is parametrized as follow:

$$f_s = \frac{d\_layer_{sens.}\,[X_0]}{d\_layer_{abs.}\,[X_0] + d\_layer_{sens.}\,[X_0]} \tag{3.13}$$

where $d\_layer_{sens.}$ and $d\_layer_{abs.}$ are the layer thickness expressed in X_0 for the sensitive material and the absorber, respectively.

Two different calorimeter systems are dedicated to measure the energy deposit by electromagnetic and hadronic showers. The electromagnetic calorimeters (ECALs) are optimized to

measure the electromagnetic showers and can be either homogeneous or sampling calorimeters with a high-density absorber and a sampling fraction of at least 5% [61]. The hadronic calorimeters (HCALs) are developed to measure particles that interact strongly and commonly designed as sampling calorimeters with a steel plate absorbers. The depth of the HCALs is significantly larger than the ECALs, due to the larger longitudinal development of hadronic showers. For a 100 GeV charged pion, a depth of 160 cm with Fe absorber is needed to contain 95% of its hadronic showers [44]. The HCALs can also measure the electromagnetic showers but with a worse energy resolution than the ECALs [44].

3.3.1 Calorimeter Response

The response of a calorimeter is defined as the average calorimeter signal divided by the incident particle's energy. In principle, the calorimeter response for the electromagnetic showers is linear since the electrons and photons are visible and measurable particles. However, the response of the hadrons shower is non-linear, due to the invisible energy and the large event to event fluctuations of the electromagnetic fraction of the shower yield, as explained in section 3.1.4. The response ratio of the hadronic calorimeter is expressed by e/h, where e is the electromagnetic response, and h represents the non-electromagnetic response. If a ratio response of $\frac{e}{h} = 1$ is achieved, the calorimeter is called compensating. Whereas, the calorimeters are called non-compensating when the ratio response is $\frac{e}{h} \neq 1$.

The compensation of the calorimeter response can be done either by reducing the electromagnetic response or boosting the non-electromagnetic response. As discussed previously in section 3.1.3, the em response can be reduced by using an absorber material with high-Z, e.g., lead or uranium. Uranium is an ideal absorber to catch the neutrons and, therefore, to reduce the invisible energy. Besides, increasing the hydrogen content in the active material boosts the non-em response, due to the high momentum transfer between particles. Additionally, an off-line compensation can be done by applying a weight factor to the portion of the signals generated by the electromagnetic showers. The calorimeters with a ratio response of $\frac{e}{h} > 1$ and $\frac{e}{h} < 1$ are under-compensated and over-compensated, respectively. Generally, the sampling calorimeters can be compensated ($e/h \sim 1$), whereas the homogeneous calorimeters are always under-compensated because of the invisible energy.

3.3.2 Energy Resolution of Calorimeters

In principle, as shown in equation 3.14, the number of generated particles in the showers is proportional to the energy of the incident particle. Thus it is also proportional to the measured energy deposit in the calorimeter. The statistical error of the generated particles N follows a Poisson distribution with $\sqrt{N}$, so the following equation represents N:

$$N \approx E \Rightarrow \sigma_E \approx \sqrt{E} \Rightarrow \frac{\sigma_E}{E} \approx \frac{1}{\sqrt{E}} \tag{3.14}$$

From this relation, the energy resolution is better for higher energies. The relative energy resolution σ_E/E is parametrized as follows:

$$\frac{\sigma_E}{E} = \frac{A}{\sqrt{E}} \oplus \frac{B}{E} \oplus C = \sqrt{\left(\frac{A}{\sqrt{E}}\right)^2 + \left(\frac{B}{E}\right)^2 + C^2} \tag{3.15}$$

where $A/\sqrt{E}$ is the stochastic term which describes the sampling fluctuations, B/E represents the electronic noise caused by pedestal fluctuations of the individual channel readout. The C term is constant and represents the mis-calibration, calorimeter inhomogeneities, and leakage effects. At high energies, the energy resolution is limited by the C term. However, at low energies, it is limited by the noise and stochastic terms.

Examples of calorimeters energy resolution

Examples of energy resolution obtained by some operating calorimeters. The ECAL of CMS is an homogeneous crystal calorimeter of fine grained lead tungsten ($PbWO_4$) with an energy resolution of $\frac{\sigma_E}{E} = \frac{2.8\%}{\sqrt{E}} \oplus 0.3\%$ [62]. The ATLAS ECAL is a sampling calorimeter of lead-liquid argon which could reach an energy resolution of $\frac{\sigma_E}{E} = \frac{9.2\%}{\sqrt{E}} \oplus 0.2\%$ [63][64]. The HCAL of CMS achieves an energy resolution of $\frac{\sigma_E}{E} = \frac{84\%}{\sqrt{E}} \oplus 0.7\%$ [65].

The best hadronic energy resolution, of $\frac{\sigma_E}{E} = \frac{35\%}{\sqrt{E}} \oplus 2\%$ [65], was achieved by the hadronic calorimeter of ZEUS experiment. This HCAL is a compensating sampling calorimeter with Uranium absorber plates of 3.2 mm and interleaved with 3 mm plastic scintillator tiles.

3.4 Particle flow Approch

3.4.1 Particle Flow Algorithm

The Particle Flow Algorithm (PFA) is a concept that allows reaching a good jet energy resolution, which is better than the traditional calorimetry approach. A jet is a bundle of high energetic particles produced in high energy particles collisions from the hadronization of (final state) quarks. In the traditional approach, the jet energy is measured exclusively in the ECAL and HCAL. Therefore, the measurement of the jet energy resolution of the whole detector is degraded, due to the poor hadronic energy resolution ($\sim 60\%/\sqrt{E}$). However, in the Particle Flow Algorithm, the reconstructed jet is measured using the calorimeters and the tracking detector. The reconstruction of each particle is done in the sub-detector, which gives the best resolution by employing pattern recognition algorithms [66] [67]. A typical jet consists of $\sim 60\%$ charged particles, $\sim 30\%$ photons and $\sim 10\%$ of neutral hadrons. As shown in Figure 3.12, the PFA reconstructs photons and electrons in the ECAL and neutral hadrons in the HCAL. While charged hadrons are measured in the tracker since its momentum resolution is much better than the calorimeters resolution. Consequently, the jet energy resolution significantly improves, due to the excellent momentum resolution of the tracker.

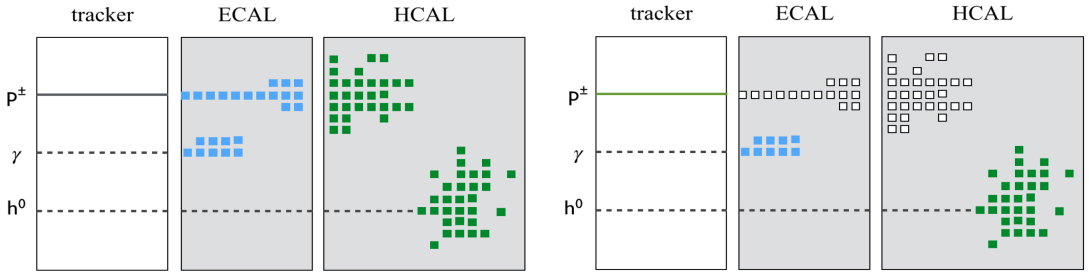

(a) (b)

Figure 3.12: Reconstruction principles: a) traditional calorimeter : charged particles $p^{\pm}$ and neutral hadrons h^0 are measured in ECAL and HCAL. b) Particle Flow approach: $p^{\pm}$ are measured by the tracker and only neutral hadrons h^0 are measured in the HCAL [59].

For the ILD detector, the resolution for each sub-detectors is assumed to be as follows:

- tracking : $\frac{\sigma}{p} \approx 5.10^{-5} \times p[GeV/c]$
- ECAL : $\frac{\sigma}{E} \approx \frac{17\%}{\sqrt{E[GeV]}}$

- HCAL : $\frac{\sigma}{E} \approx \frac{60\%}{\sqrt{E[GeV]}}$

This estimation represents the ideal case, where the energy deposited is associated with the right particle, which is not that easy in reality. Therefore, a very high longitudinal and transversal segmentations are required in calorimeters by the PFAs, to separate between neutral and charged hadrons and associate them to the corresponding particles. The PFA at the ILC can achieve a jet energy resolution of 3-4% for jet energies in the range of 40 GeV to 400 GeV [68]. The jet energy resolution can be calculated as follows:

$$\sigma_{jet} \approx \sigma_{Det.} \oplus \sigma_{Conf.} \oplus \sigma_{loss} \tag{3.16}$$

where $\sigma_{Conf.}$ is the confusion term that corresponds to the wrong assignment of the deposited energy to the corresponding particle. $\sigma_{loss.}$ corresponds to the geometric inefficiencies, which lead to an energy leakage in the calorimeter. $\sigma_{Det.}$ is the energy resolution of all sub-detectors parts: tracker, ECAL and HCAL. it is defined as follows:

$$\sigma_{Det} = f_{h^{\pm}} \cdot \sigma_{tracker} \oplus f_{\gamma} \cdot \sigma_{ECAL} \oplus f_{h^0} \cdot \sigma_{HCAL} \tag{3.17}$$

$f_{h^{\pm}}$, f_{γ}, f_{h^0} represent the fraction of total energy carried by charged particles, photons and neutral hadrons, respectively. $\sigma_{tracker}$, σ_{ECAL} and σ_{HCAL} are the jet energy resolutions of the different sub-detectors (tracker, ECAL and HCAL).

The performance of the PFA depends strongly to the confusion part that takes place in two different cases:

- Cluster Splitting: the reconstruction considers a part of the charged hadron energy as a neutral hadron, which leads to double counting of the deposited energy. The sketch of Cluster Splitting is illustrated in Figure 3.13.

- Cluster Merging: The neutral cluster merges into the charged cluster due to the mis-separation between charged and neutral particles. Therefore, the energy of the neutral particles is missing since it is reconstructed by the tracker. Figure 3.13 illustrates the cluster merging.

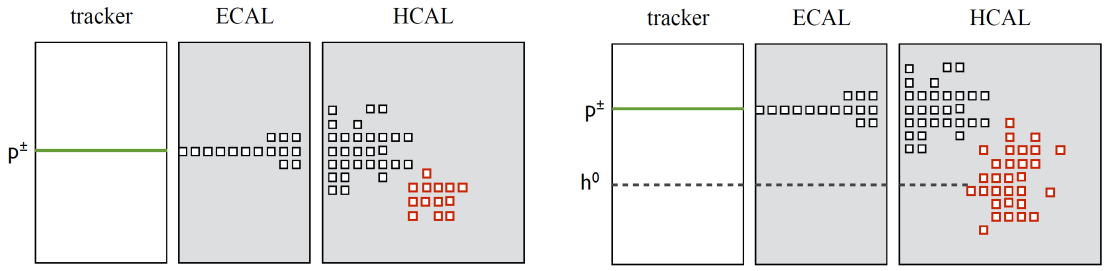

(a) (b)

Figure 3.13: PFA confusion: a) cluster splitting: reconstruction of a fraction of charged particle cluster as a cluster of neutral particle (red cluster). b) cluster merging: merging the neutral cluster into a very close charged cluster [59].

3.4.2 Requirement for Particle Flow

The performance of the PFA is related strongly to the minimization of the confusion term, which in turn requires a high granularity calorimeters. Simulation studies are done for the optimization of transverse segmentation in the ECAL (silicon pixel size) and the HCAL (scintillator tile size) [68]. Figure 3.14 shows the jet energy resolution as a function cell size of the ECAL (left) and the HCAL (right) for a range of jets energies between 45 GeV to 250 GeV. In order to reach a jet energy resolution of 4%, a maximum cell sizes of 1×1 cm^2 and 3×3 cm^2 are required for the ECAL and the HCAL, respectively.

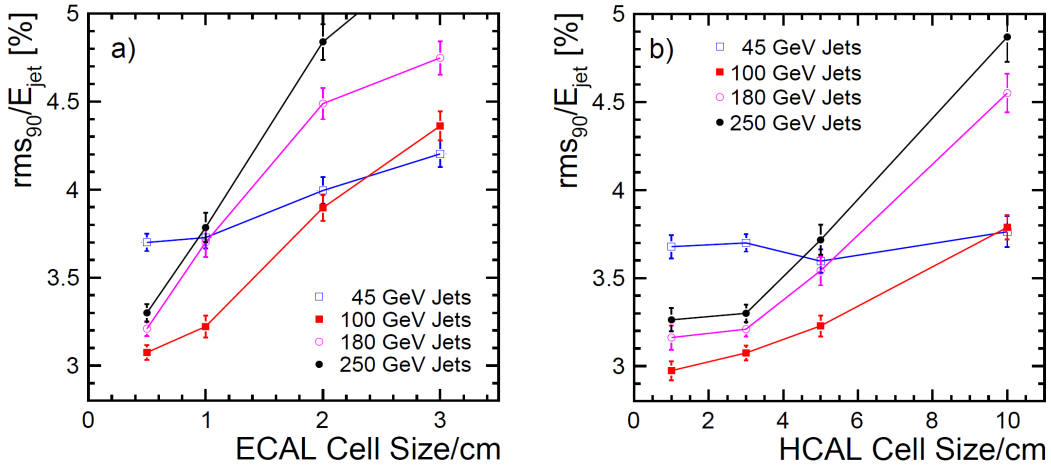

Figure 3.14: The dependence of the jet energy resolution on the ECAL (a) and the HCAL (b) transverse segmentations in the LDCPrime model [68].

These high granular calorimeters require a large number of readout channels, roughly 10^8 for the ECAL and 10^7 for the HCAL. Therefore, this large number of readouts leads to a big challenge on the calorimeter calibration and the integration of the electronic readout.

3.4.3 Implementation in PandoraPFA

PandoraPFA is a software framework developed for the implementation of the Particle Flow algorithm for the ILD. This concept can provide the required jet energy resolution to achieve the goals of the ILC physics program. The reconstruction in this framework uses the reconstructed tracks and the list of digitized hits from the ECAL and HCAL as an input. Figure 3.15 shows the jet energy resolution calculated in a realistic simulation of the full ILD detector. Using PandoraPFA, a jet energy resolution of 3-4% is achieved in a broad energy range, which is much better than the traditional approach (Calorimeter only (ILD)). At high energy, the energy resolution of the ILD using PFA is limited by the confusion term.

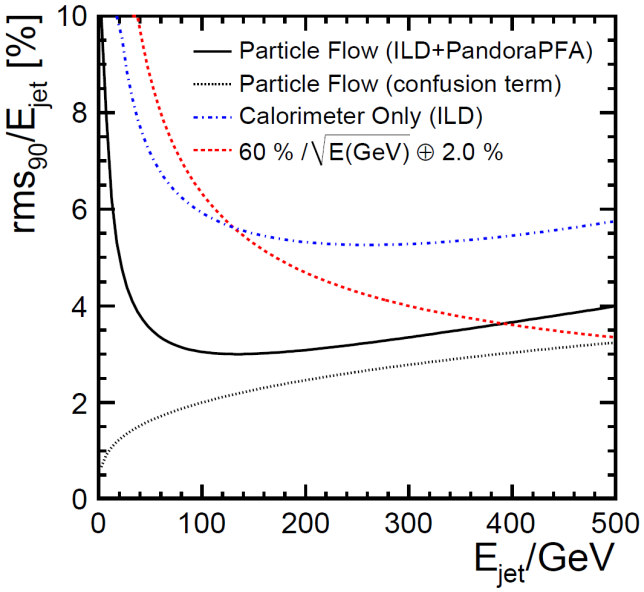

Figure 3.15: The empirical functional form of the jet energy resolution obtained from Particle Flow calorimetry (PandoraPFA and the ILD concept). The estimated contribution from only the confusion term is shown (dotted). The dot-dashed curve shows the parameterization of the jet energy resolution obtained from the total calorimetric energy deposition in the ILD detector. The dashed red curve, $60\%/\sqrt{E(GeV)} \oplus 2.0\%$, shows the jet energy resolution achieved by the traditional calorimetric approach [68].

3.5 CALICE Detector Concepts

3.5.1 CALICE Collaboration

CALICE Collaboration constitutes of 57 institutes from 17 countries, around 300 scientists and engineers are developing highly granular electromagnetic and hadronic calorimeters optimized for Particle Flow at a future e^+e^- collider experiment. Beside the Analog Hadronic Calorimeter (AHCAL), which is the detector behind the work of this thesis, several other calorimeters are in development with different absorbers and readout systems. For each technology, the design of the physics prototype is essential to prove the performance of the calorimeter response. Afterward, the engineering prototype is developed to improve the calorimeter design, which consists of integrating the front-end electronics. Recently, CALICE collaborates with the LHC to develop calorimeters that fulfill the required granularity needed for the High Luminosity Large Hadron Collider upgrade (HL-LHC).

3.5.2 Electromagnetic Detectors

For the moment, two different technologies of the electromagnetic calorimeter (ECAL) are in development. The Silicon ECAL uses silicon as an active material, while the Scintillator ECAL is based on the scintillator tiles with individual SiPM readout. Both technologies are discussed in the following sub-sections.

3.5.2.1 Silicon-Tungsten ECAL

The Silicon-Tungsten ECAL physics prototype, shown in Figure 3.16, consists of 30 active and absorber layers based on silicon and tungsten, respectively, with a depth of 24 X_0. Each silicon layer has an active zone of 18×18 cm^2 with a segmentation of 1×1 cm^2 [69]. In the Very-Front-End (VFE) board, the ASICs (FLC-PHY3) is used to read out the silicon modules. The prototype is tested in various test-beam at DESY, FNAL, and CERN and an energy resolution of $\frac{16.53\%}{\sqrt{E}} \oplus 1.07\%$ is achieved [70].

The SiW-ECAL technological prototype is based on sensors with high resistivity silicon wafers with a size of 9×9 cm^2. Each sensor is divided into an array of 256 PIN diodes of 5×5 mm^2, to improve the pattern recognition of the calorimeter. The silicon wafers are read out by the SKIROC2 chip of 64 channels [71]. The technological prototype of 7 layers inside the aluminum stack is shown in Figure 3.16.b.

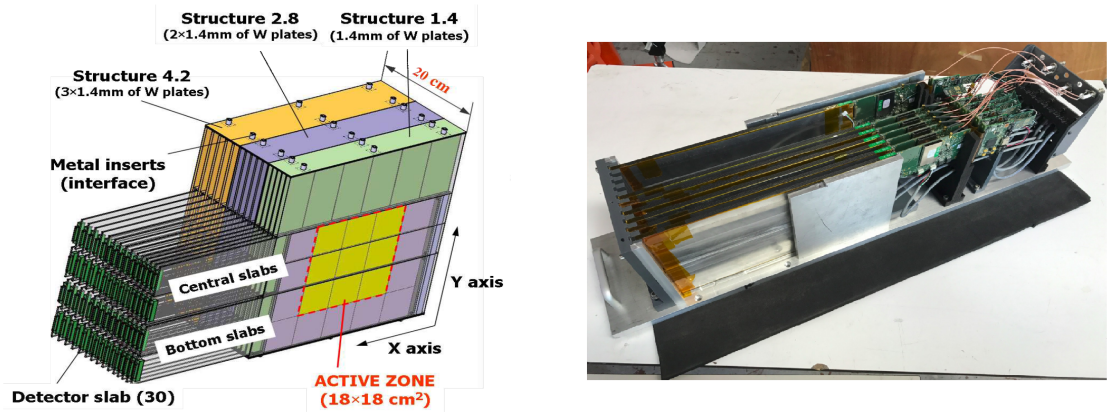

Figure 3.16: a) Schematic 3D view of the SiW-ECAL physics prototype [70]. b) Picture of SiW-ECAL technological prototype with 7 layers inside the aluminum stack [72].

3.5.2.2 Scintillator Strip-Tungsten ECAL

The ScECAL physics prototype, shown in Figure 3.17, consists of 30 layers based on scintillator strips and tungsten absorber plates with a total depth of ∼266 mm (21.5 X_0) and transversal area of $180 \times 180\ mm^2$. A test beam of this prototype is done at the FNAL with the AHCAL and a tail catcher muon tracker (TCMT) prototypes and an energy resolution of $\frac{12.6\%}{\sqrt{E}} \oplus 1.6\%$ is achieved [73]. The ScECAL technological prototype, shown in Figure 3.17.b, is optimized with full front-end electronics integration in the layer. Each ECAL Base Unit (EBU) has 144 scintillators strips of dimension $45 \times 5 \times 2\ mm^3$ with a transversal dimension of $180 \times 180\ mm^2$.

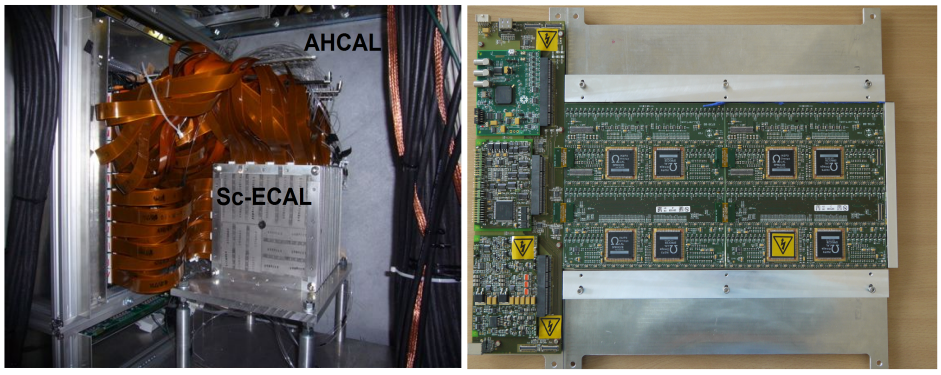

Figure 3.17: a) Picture of the ScECAL physics prototype front of the Fe-AHCAL. b) Picture of one layer of the technological ScECAL prototype [48].

3.5.3 Hadronic Detectors

As for the ECAL, several HCAL prototypes with different technologies are built and thoroughly tested by the CALICE collaboration. The primary goal is to develop a HCAL with very high granularity which varies from 3×3 cm^2 to 1×1 cm^2, for the separation of particles within the hadronic jets. In addition to the AHCAL, described in the next Chapter 4, two other technologies are described in the following subsections.

3.5.3.1 Digital Hadron Calorimeter (DHCAL)

The DHCAL [74] is a digital sampling calorimeter based on Resistive Plate Chambers (RPCs) as active elements with one single-bit readout system [75]. In this calorimeter concept, the deposited energy of an incident particle is proportional to the number of hits. The schematic of an RPC is shown in Figure 3.18, where the readout anode of the RPC is segmented into 1×1 cm^2. The DHCAL consists of 38 layers inserted in steel absorber stack into a gap width of 1.4 cm. A test beam campaign of this prototype is done at CERN and Fermilab with positron and pion beams. An electromagnetic energy resolution of $\frac{35.1\%}{\sqrt{E}} \oplus 12.4\%$ and a hadronic energy resolution of $\frac{64\%}{\sqrt{E}} \oplus 4\%$ are achieved [76].

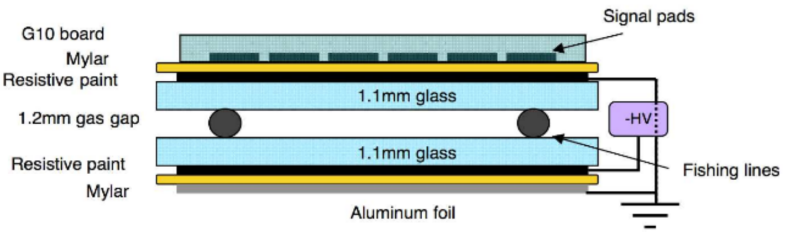

Figure 3.18: Schematic of the cross section of an RPC on the DHCAL prototype [75].

3.5.3.2 Semi-Digital Hadron Calorimeter (SDHCAL)

The Semi-Digital Calorimeter prototype is based on Glass Resistive Plate Chambers and consists of 48 layers with a size of 1×1 m^2. The readout is done by the HARDROC chip [77] of 64 channels with 3-bit readout system which corresponds to three thresholds. As shown in Figure 3.19, a test-beam campaign is performed at the CERN SPS in 2012 with various beam particles (muons, electrons and pions). More detail about the SDHCAL can be found in [78].

Figure 3.19: Picture of the SDHCAL technological prototype during the test beam at SPS, CERN 2012 [48].

Chapter 4

AHCAL Technological Prototype

The Analog Hadronic Calorimeter (AHCAL) is one of the calorimeter technologies developed for more than 15 years. The AHCAL is a sampling calorimeter based on scintillator tiles read out by Silicon Photomultipliers (SiPMs) as an active material. The AHCAL physics prototype is built, operated, and tested successfully in many test-beam campaigns [79]. Based on the physical prototype, a technological prototype is developed with new hardware and readout system to demonstrate the feasibility of mass production for the ILD detector.

In this chapter, the description of SiPM and plastic scintillator tiles is given. Subsequently, the Analogue Hadronic Calorimeter technology, with its readout system and operating modes, is presented in detail. At the end of this chapter, a brief explanation of the AHCAL calibration procedures is discussed.

4.1 Measurement of the energy deposition in the AHCAL

4.1.1 Silicon Photomultiplier

The Silicon Photomultiplier (SiPM) is a semiconductor photo-detector used for measuring the light amplitude down to a single photon. A gain of 10^5-10^6 electrons per detected photon can be archived by the SiPMs, which is similar to the gain of a photomultiplier tube (PMT). The advantages of using SiPMs instead of PMT are their small size in the range of mm^2, low required bias voltage (less than 100 V), a low cost, and insensitivity to a strong magnetic field [80] [81]. A Microscope picture of a SiPM is shown in Figure 4.1.

The SiPM integrates a dense array of small single avalanche photo-diodes (SAPD) connected in parallel to a common cathode and anode. Theses diodes operate in Geiger mode if the bias voltage U_{bias} applied to each pixel is larger than its breakdown voltage U_{bd}. As

shown in Figure 4.1.b, each micro-cell is connected to a quenching resistor R_Q, to limit the current drawn by the diodes during the breakdown. When a micro-cell fires after photon absorption, a photo-current is generated by Geiger avalanche and flows through the micro-cell. Therefore, the voltage drop across the quenching resistor reduces the bias voltage lower than the breakdown voltage. After this current quenching, the voltage across the diode recharges to the nominal bias value, and further Geiger avalanches can be realized. The recovery time ($\tau = R_Q * C_{px}$) needed to recharge the diodes is around hundreds of nanoseconds and depends on the quenching resistor and pixel capacitance C_{px}. The cycle of breakdown, avalanche, quench, and recharge of the bias voltage is shown in Figure 4.2. The charge Q of a fired pixel depends on the over-voltage U_{ov} and its capacitance C_{px}. It is defined as follows:

$$Q = U_{ov} \cdot C_{px} \qquad with \qquad U_{ov} = U_{bias} - U_{bd} \tag{4.1}$$

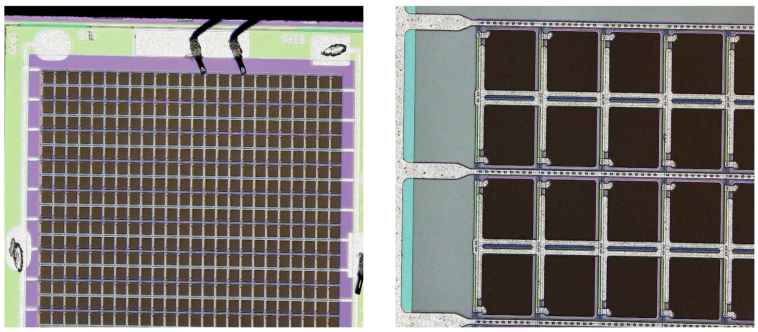

(a) SiPM Surface (b) SiPM Pixel Detail

Figure 4.1: Microscope pictures of a SiPM. a) Picture shows the grid of pixels, ground and bias voltage distribution traces. b) Picture of the individual pixel structure, polysilicon quenching resistor is in green [82].

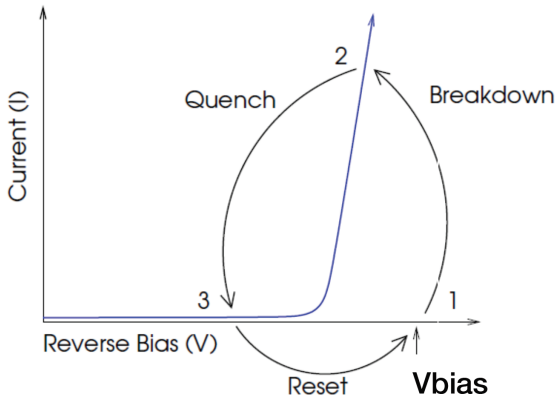

Figure 4.2: Breakdown, quench and reset cycle of the SPAD operated in Geiger mode [83].

4.1.1.1 Photomultiplier Performance Parameters

The performance of the SiPM response is related to many parameters. Therefore, the understanding of these parameters and their correlation to the SiPM performance is essential.

Gain: The gain of one micro-cell of a SiPM is the amount of charge generated by the fired pixel divided by the electron charge e. It is defined as follows:

$$G = \frac{Q_{pixel}}{e} \tag{4.2}$$

The total generated signal (Q_{tot}) is the sum of charges produced by all fired pixels:

$$Q_{tot} = N_{fired} \cdot Q_{pixel} = N_{fired} \cdot G \cdot e \tag{4.3}$$

Photon Detection Efficiency and Responsibility: The photon detection efficiency is one of the most important parameters of the SiPMs. As defined in Eq. 4.4, it depends on the geometry efficiency ($\epsilon_{geo.}$), the quantum efficiency (ϵ_Q) and the Geiger efficiency (ϵ_G). $\epsilon_{geo.}$ is the fraction of active space in the SiPM defined as the ratio of the active area by the total surface of the SiPM. ϵ_Q is the probability that a photon generates an e/h pair in the active region. ϵ_G is the probability that a carrier (electron/hole) traversing a high field region triggers a Geiger avalanche.

$$\epsilon_{SiPM} = \epsilon_{geo.} \cdot \epsilon_Q \cdot \epsilon_G \tag{4.4}$$

Dark Count Rate: The dark count rate (DCR) is the primary source of the SiPM noise due to thermal electrons that trigger a Geiger avalanche. The electric pulse generated by dark events is indistinguishable from the absorbed photon's signal, and it depends strongly on the size of the active area, over-voltage, and the temperature. Minimizing these dark counts is possible by cooling the SiPMs.

Optical Crosstalk: In addition to the dark rate, the optical cross-talk also contributes to the SiPM noise. It depends on the over-voltage and the size of the active area in the SiPM. The optical cross-talk is defined as the probability of generating a second avalanche in the neighbor micro-cell from the active micro-cell. Figure 4.3 illustrates the cases of multiple photons generated by a single incident photon in the neighboring micro-cells.

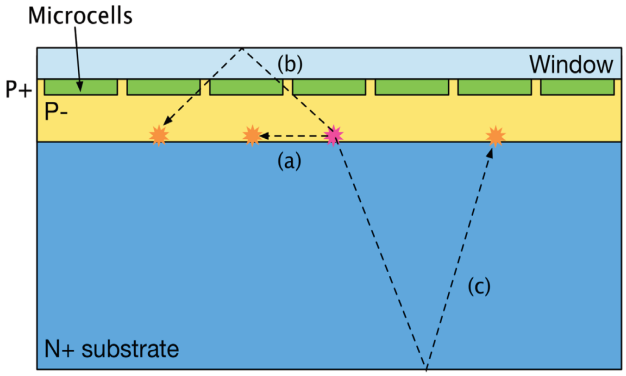

Figure 4.3: Sketch illustrating the various case where secondary photons can travel and generate a signal in the neighboring micro-cells. a) a photon travels to neighboring micro-cell. b) a photon is reflected by the material window in the top of the sensor and generates an avalanche in one of the micro-cell. c) a photon is reflected by the bottom to the silicon substrates and generates as well a Geiger avalanche [83].

After Pulsing: The after-pulsing effect can happen when a carrier gets trapped by a defect in the silicon lattice. These carriers can be released after a delay of few ns up to several μs and then trigger an avalanche generating an after-pulse in the same micro-cell. The after-pulse depends on the delay time and can be negligible if it is lower than the pixel recovery time. Studies of the after-pulse measurements for three HAMAMATSU Multi-Pixel Photon Counters (MPPCs) are shown in Figure 4.4. An increase in the after-pulse probabilities with the over-voltage is observed.

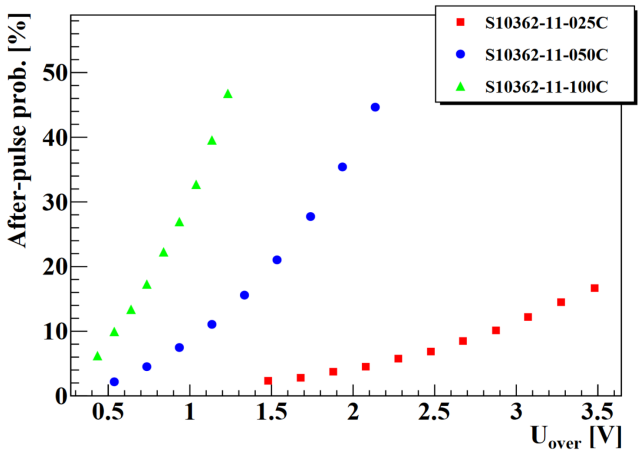

Figure 4.4: After-pulse probability as a function of the over-voltage measured for three different HAMAMATSU MPPCs [84].

Dynamic Range and Linearity: The dynamic range of SiPM is defined as the range where the number of the fired pixels correspond exactly to the generated photo-electrons. In principle, the response of SiPM is linear at a low number of generated photo-electrons while it is non-linear at a high number of photons, due to the finite number of pixels. This effect is called the saturation of the SiPM. The number of fired pixels is defined as follows:

$$N_{fired} = N_{tot} * \left[1 - e^{\left(-\frac{N_{pe}}{N_{tot}}\right)}\right] \tag{4.5}$$

where N_{fired} is the number of fired pixels, N_{tot} is the total number of pixels that can fire and N_{pe} is the number of generated photo-electrons. Figure 4.5 shows the measurement of the SiPM (MEPhI/Pulsar) response for different pixel numbers [85]. A non-linear SiPM response is observed for the high number of photo-electrons, and the dynamic range increases for SiPM with a large number of pixels. Nevertheless, this saturation can be corrected offline, as described in section 6.7.1.

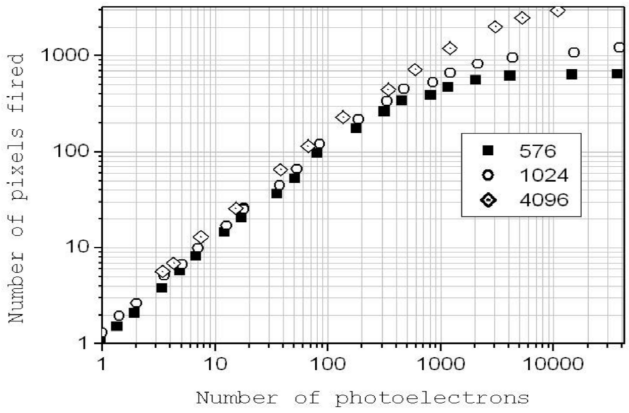

Figure 4.5: Non-linear response of MEPhI/PULSAR SiPMs with different pixel numbers. The light signal is produced by a fast laser (40 ps) [85].

Temperature Dependency: The temperature has a significant effect on the SiPM response due to its breakdown voltage dependence. A study of the SiPM characterization for magnetic resonance compatible positron emission tomography (PET) is done in a cooling chamber with controlled temperature from $0°C$ to $40°C$ [86]. As shown in Figure 4.6, a linear increase of the breakdown voltage with temperature by $\sim 25mV/°C$ is observed. Therefore, this temperature rise leads to a 50% increase of the DCR for every $10°C$. According to this result, the cooling of the SiPM can significantly reduce the growth in breakdown voltage.

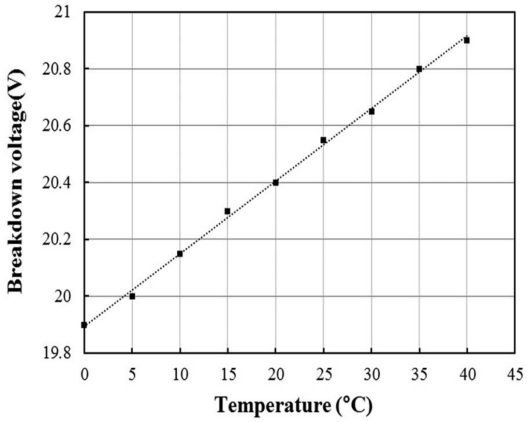

Figure 4.6: Temperature dependence on breakdown voltage for the SiPM [86].

4.1.1.2 Silicon Photomultiplier for the AHCAL

A new SiPM generation (Hamamatsu MPPC S13360-1325PE) is assembled in the AHCAL technological prototype. It has an area of 1.3×1.3 mm^2 of 2668 pixels with a pixel pitch size of 25 μm. It is sensitive to blue light, which was not the case in the old SiPM generation used in the AHCAL physics prototype. As shown in Figure 4.7a, this generation SiPM has a dark count rate of 20-60 kHz with a cross-talk smaller than 0.1%. While in the old SiPM generation shown in Figure 4.7b, the dark rate is around 500 kHz with a cross-talk of 20%. This improvement increases the photon detection efficiency and the signal to noise ratio. Therefore, the new SiPMs have excellent uniformity in the operating voltage and gain.

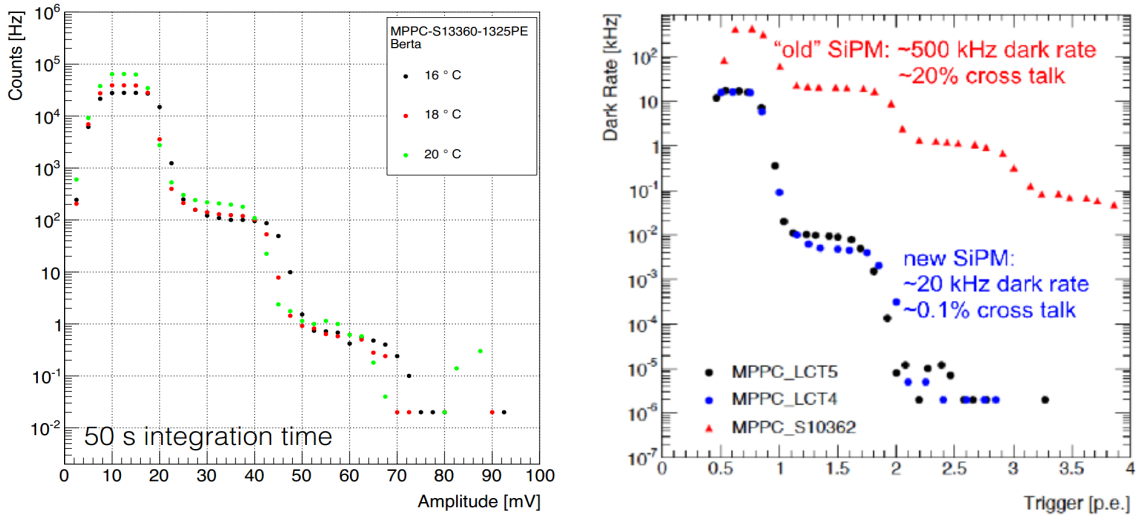

(a) (b)

Figure 4.7: a) The rate of signals from the SiPM MPPC_S13360_1225PE above the trigger value for different temperatures [87]. b) Comparison of the rate for the old SiPM MPPC_S10362 and the a new SiPM generation (MPPC_LCT5 and MPPC_LCT4) [88] [89].

4.1.2 Plastic Scintillator Tiles

The AHCAL technological prototype is based on scintillator tiles as an active material with SiPM readout. Each tile has a dimension of $30 \times 30 \times 3\ mm^3$, required by the high granular calorimeters [68]. As shown in Figure 4.8, the tile is directly mounted on the Printed Circuit Board (PCB) and over the SiPM. A dimple cavity is designed in the tile center in the bottom surface, to place the SiPM and improve light collection produced by incident particles passing through the tile at different positions. A test stand is performed to measure the uniformity response of the SiPM inside the cavity of the scintillator tile. As shown in Figure 4.9, a good agreement to the full simulation is seen, with a global mean response across the tile area of 22.0 p.e. (photon equivalents) in simulation and 20.6 p.e in measurement. More than 97% (80%) of the tile area is within 10% (5%) deviation from the mean value of the measured and simulated studies. As shown in Figure 4.10, the single-MIP response for scintillator tiles with the cavity design, measured using cosmic rays, reaches a mean response of 23.2 p.e [90].

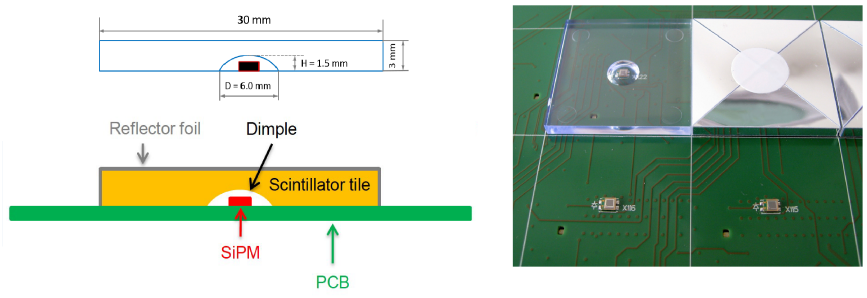

Figure 4.8: a) Schematic and sketch of the scintillator tile with an optimized dimple and a SMD-SiPM (red) completely inside the cavity [90]. b) Picture of the CALICE AHCAL scintillator tiles with central dimple mounted over the SiPM on the HBU.

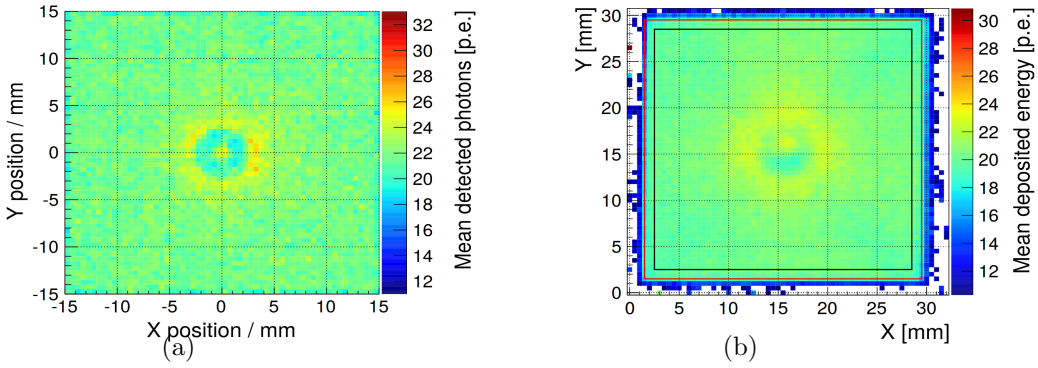

Figure 4.9: a) Simulated uniformity using the optimized cavity design with 2.28 MeV electrons perpendicularly penetrating the tile [90]. b) The uniformity of a scintillator tile with the cavity design is measured by electrons selected from a beta source ^{90}Sr [90].

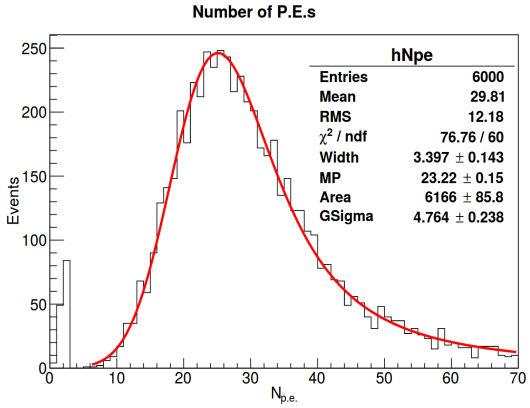

Figure 4.10: Cosmic-ray measurement: single-MIP responses of a scintillator tile with a Hamamatsu SMD-SiPM coupled inside the optimized cavity [90].

4.2 The AHCAL Technological Prototype

The AHCAL technological prototype is the first large scale particle physics detector using the SiPMs. It is based on a steel-scintillator sandwich structure with a fully integrated electronic readout system. As shown in Figure 4.2, the AHCAL prototype of 72×72 cm^2 size consists of 38 layers with a tile size of 3×3 cm^2 and an additional layer with a tile size of 6×6 cm^2 [91]. All the layers are inserted in a stack of 40 steel absorber plates with a thickness of 17.4 mm each. The total depth of this hadronic calorimeter prototype is roughly four nuclear interaction lengths ($\sim 4\lambda$).

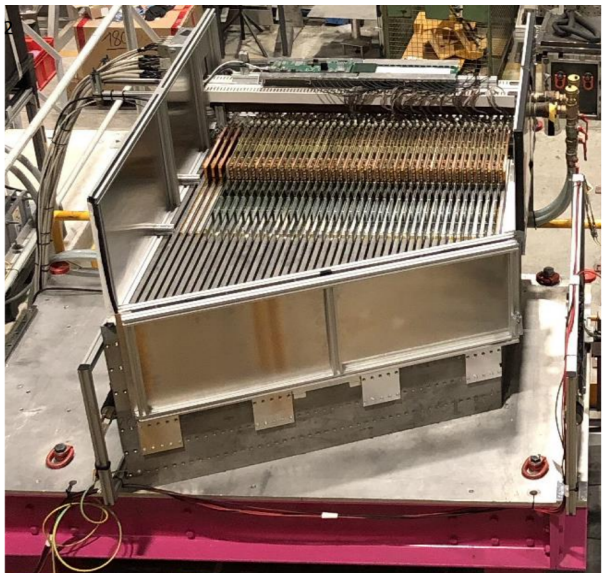

Figure 4.11: Picture of the AHCAL technological prototype.

4.2.1 Layout of the AHCAL Technological Prototype

The AHCAL layer is subdivided into several boards to control the production and the maintenance of each layer. Each layer consists of two slabs with 2 Hadron Base Units (HBUs) with a size of $36 \times 36\ cm^2$. As shown in Figure 4.12, the readout of each HBU is done by 4 SPIROC2E ASICs for a total of 144 SiPMs. Additionally, the HBU hosts Light Emitting Diodes (LEDs) that inject light pulses into the scintillator tiles for the calibration of the SiPMs. The main slab is connected to the Data Acquisition Interface (DAQ) via the Central Interface Board (CIB), while the side slab is attached to the CIB via the Side Interface Board (SIBs). Figures 4.13 and 4.14 show the layer top side with the integrated electronic readout system and bottom side with the mounted scintillators tile, respectively. As shown in Figure 4.15, both slabs are inserted in a steel cassette of 0.5 mm thickness then into the steel absorber stack.

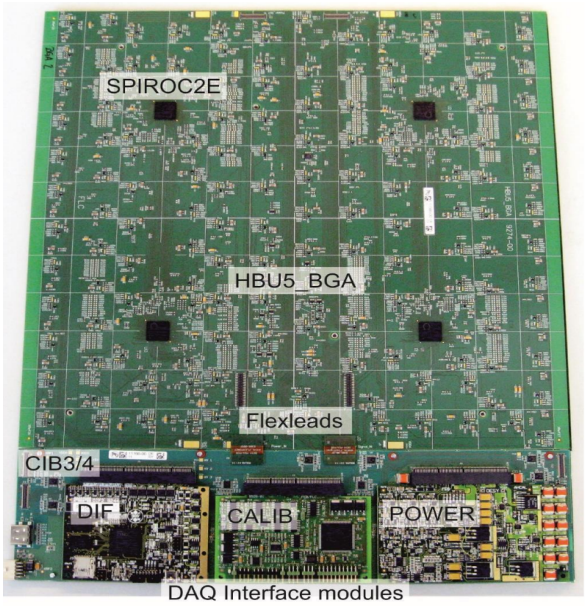

Figure 4.12: HBU top view with SPIROC2E.

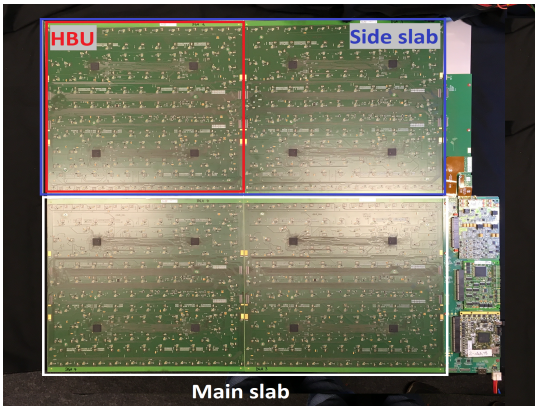

Figure 4.13: Layer top view with 4 HBUs.

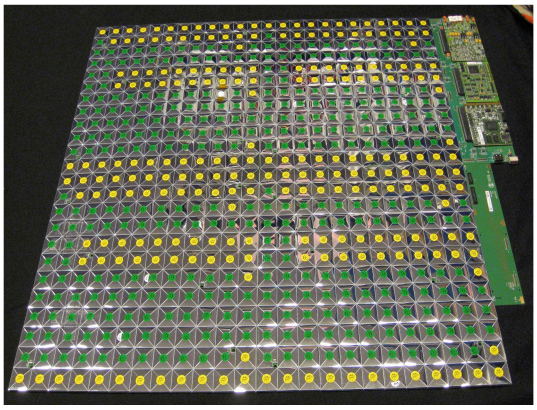

Figure 4.14: Layer bottom view with mounted scintillators tiles.

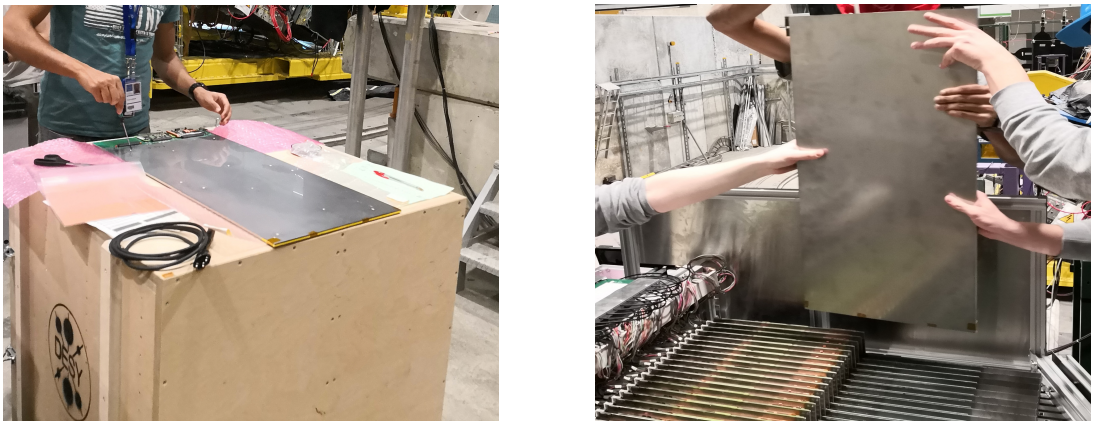

(a) (b)

Figure 4.15: a) Picture of the slab insertion inside the steel cassette. b) Picture token while the insertion of the slab inside the steel absorber stack.

4.2.2 Readout Chips: SPIROC2E

The SPIROC2E ASIC [92] (Silicon Photomultiplier Integrated Read-Out Chip) shown in Figure 4.16, is the latest generation of the SPIROC ASIC family. It is designed by the OMEGA group [93] for the ILC to read out the Silicon Photomultipliers of the AHCAL detector. This chip matches the requirements of large dynamic range, low noise, low consumption, high precision, and a large number of read-out channels. It provides individual bias voltage and read-out of 36 SiPMs, including self-triggering with variable gain to achieve charge and time measurements. It has the advantage of operating in the power pulsing mode, where each channel consumes around 25 μW per passing beam.

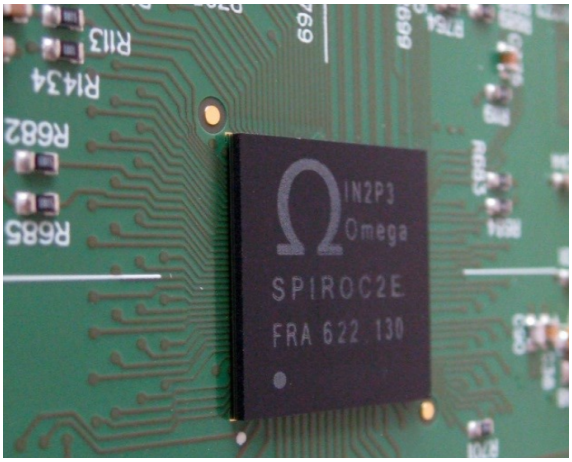

Figure 4.16: SPIROC2E BGA package with a size of 15×15 mm^2.

The schematic of the signal path of a single channel in the SPIROC2 ASIC is illustrated in Figure 4.17. The chip can be operated either with the external trigger (ET) or the auto-trigger (AT) modes. In each channel, the input signal splits into a high gain (HG) and low gain (LG) pre-amplifiers with a ratio of 1:10 for low and high amplitudes, respectively. These pre-amplifiers can be configured with a feedback capacitance from 0.1-1.5 pC to cover a high dynamic range of up to several thousand photoelectrons. Both HG and LG signals are shaped with the slow shaper. In ET mode, both signals are sampled synchronously on the external signal. Alternatively, in AT mode, the HG signal is shaped by a fast shaper and continuously compared to an internal configured threshold to provide the auto-trigger. Both HG and LG signals are sampled after the trigger, but depending on the gain-threshold, only one of them is digitalized by the 12-bit Wilkinson ADC converter.

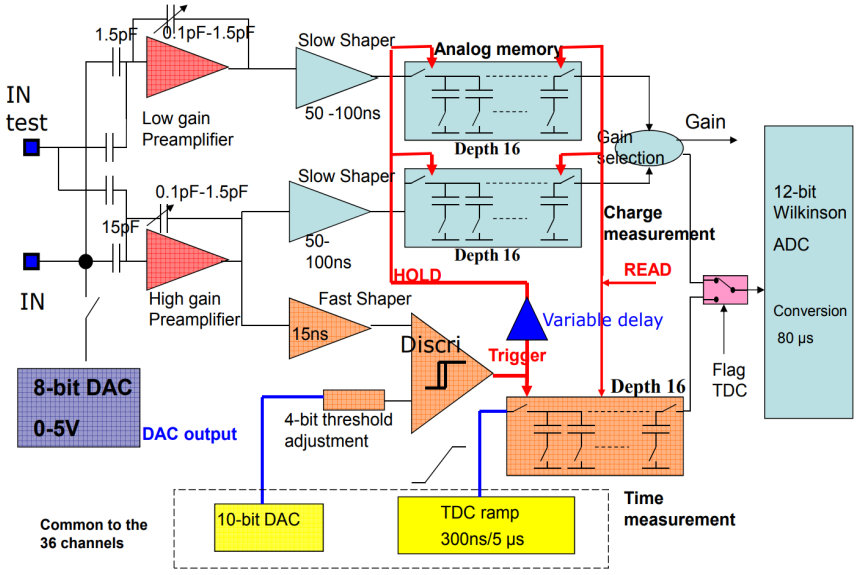

Figure 4.17: Schematic of the signal path of the SPIROC2 family for a single channel [94].

In parallel to the input signal, the corresponding timing is stored in the 16 TDC memory cells. The time measurement is digitized by a 12-bit Time to Digital Converter (TDC). As shown in Figure 4.18, the SPIROC2E has two multiplied TDC voltage ramps to avoid dead time between each clock cycle. The TDC voltage ramp has a designed time resolution of 100 ps under ILC-like conditions, which corresponds to a length of 200 ms. The time resolution in the test beam is 1.9 ns, which corresponds to a ramp length of 4 μs.

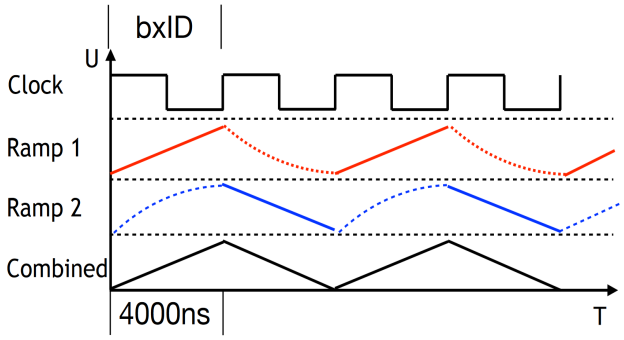

Figure 4.18: Schematic TDC ramps in the SPIROC2E generation [95].

The chip can measure HG and LG signals, but depending on the operating modes, either one signal or both signals can be digitalized. These modes are listed as follows:

- Auto-Trigger and Auto-Gain (**ATAG**): the chip uses a self-triggering and auto-gain selects either HG or LG signal, depending on signal amplitude.
- Auto-Trigger and Inter-Calibration (**ATIC**): It is a calibration mode where the chip uses a self-triggering, and both HG and LG signals are read out.
- External-Trigger and Inter-Calibration (**ETIC**): It is a calibration mode where the chip uses the external trigger, and both HG and LG signals are read out.

4.2.3 Data Acquisition Interface

Each layer is connected to the Data Acquisition (DAQ) system via the Central Interface Board (CIB) [96]. As shown in Figure 4.12, the DAQ consists of three modules: Power board (POWER), Calibration board (CALIB), and Detector Interface board (DIF).

The **Power board** operates by 5V and 12V and provides all the voltages of the front-end electronics of each layer. It can also be operated by a high voltage between 40 to 400 V for the bias voltage of the SiPMs. Further, the POWER board can enable the power pulsing mode (see section 4.2.4). The **CALIB board** is a steering board used for the LED gain calibration system, which consists of the calibration of the SiPM gain and monitoring the SiPM saturation behavior. The **DIF board** manages and monitors the communication between SPIROCs, POWER, CALIB, and data processing. It can communicate and control up to 3 slabs, which corresponds to 18 HBUs with 72 ASICs. The DAQ hardware is a chain of devices with a tree hierarchy, as shown in Figure 4.19. On the top, the Clock and Control

Card (CCC) provides the master clock to the AHCAL and manages the starts and stops of the acquisition according to the spill level and readiness of all ASICs. The DIF mainly controls and collects the data from all ASICs and sends the packets of the collected data to the Link Data Aggregator (LDA). The LDA merges the ASICs packets coming via the DIF, then decodes and adds the headers to the packets. Afterward, this data is sent to the PC via the TCP connection.

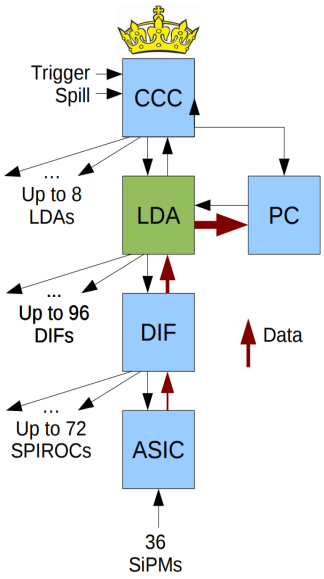

Figure 4.19: Sketch of the DAQ hardware hierarchy of the AHCAL [97].

4.2.4 Power Pulsing Mode

The ASICs concept with low power consumption is developed to avoid the active cooling of the detection gap while preserving high-performance calorimetry. A power pulsing operating mode is a solution that promises a low power dissipation of the front-end electronics. It consists of switching off the parts of the readout chip not used between the ILC bunch trains. In this mode, the ASIC's analog preamp power is off for 99.5% of the time. As shown in Figure 4.20, the chip powering is done separately for each electronic part. The *pwr_a* delivers the power to the analog part of the ASIC, consisting of preamplifiers and shapers. These analog parts are switched on only during 1 ms with an extra short activation time T_{on} that the electronics are ready for data taking. The *pwr_adc* supplies the A/D converter during ~3.2 ms to digitize the analog signals. The *pwr_*d is supplied during the digitization and readout of the whole slab. The *pwr_dac* powers an additional analog and digital part, and it

is turned on during the bunch train and the A/D conversation (∼4.2 ms).

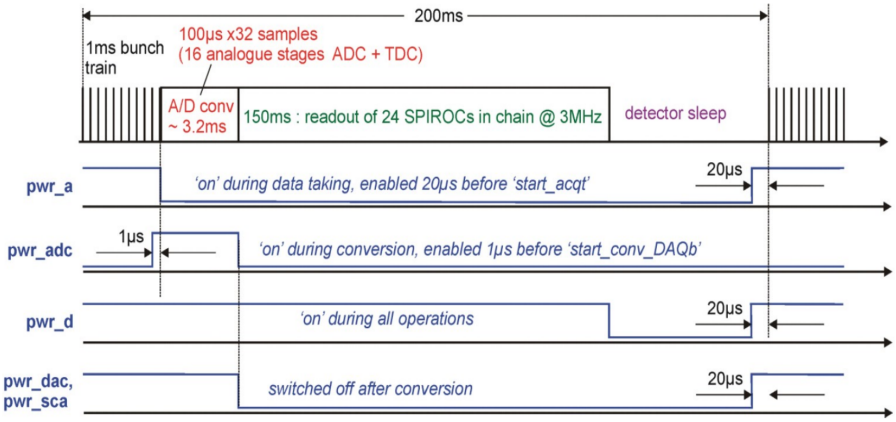

Figure 4.20: Sketch of the power pulsing cycling with the time structure, subdivided into time periods with different power consumption [98].

4.3 Calibration of the AHCAL

The signal recorded by the SiPM is measured in Analog to Digital Converter (ADC) counts. Therefore a conversation of the measured amplitude to a common physics unit is essential. For each channel i, the amplitude is calibrated to the energy in the Minimum Ionization Particle (MIP) unit, following this equation:

$$E_i[MIP] = (f^i_{sat})^{-1} * \frac{(A_i[ADC] - P_i[ADC]) * IC_i}{A^{MIP}_i[ADC]} \tag{4.6}$$

where A_i is the amplitude of channel i measured in ADC counts. P_i is the extracted pedestal for each channel. IC_i is the high gain - low gain inter-calibration factor (discussed in subsection 4.3.3). A^{MIP}_i is the MIP amplitude of channel i in ADC counts, which corresponds to the amplitude measured for the minimum ionization particle. $f^i_{sat}(A_i[pixels])$ is the correction function of the non-linear response of the SiPMs, applied on the amplitude $A[pixels]$ expressed in the number of pixels. The amplitude in pixels is defined as the amplitude with the pedestal subtraction divided by the SiPMs Gain, as follows:

$$A_i[pixels] = \frac{(A_i[ADC] - P_i[ADC])}{Gain_i[ADC]} \tag{4.7}$$

The extraction of all the constants needed for the energy calibration is done via several

procedures, as described briefly in the following sub-sections.

4.3.1 Pedestal extraction

The pedestal is an effective ADC offset extracted from channels with no physical signal (flagged by Hitbit=0). The pedestal spectrum and its width can be used to determine the broken channels, where the cells with narrow or very wide pedestal distribution are considered dead or noisy channels. For this analysis, a high gain and a low gain pedestal are extracted per channel using LED and muon runs. A detail study is done (chapter 6) section 6.5.1.

4.3.2 Gain Calibration

The SiPM gain is the average signal from a single fired pixel. The gain is an intrinsic SiPM scale needed to express the amplitude in the number of pixels. It can be measured per channel using the LED runs, where the single-photon spectra token at low intensity LED light is fitted with a multi-Gaussian function. Therefore, the difference between the means of two consecutive single-photon peaks corresponds to the gain value of this specific channel. The gain calibration study for the AHCAL is presented in (chapter 6) section 6.5.2.

4.3.3 High gain and Low gain inter-calibration

As discussed in section 4.2.2, the measured amplitude of the SiPMs is read by HG and LG preamplifiers with a configured ratio of ∼1:10. However, this ratio is not exactly 10, and it is variating from channel to channel due to the uneven quality of capacitance and the parasitic capacitance. Therefore, extraction of the inter-calibration factor is needed to calibrate the LG signal for all cells using the LED runs. A detailed study of the HG/LG inter-calibration is illustrated in (chapter 6) section 6.5.3.

4.3.4 MIP Calibration

The extraction of the MIP constant is done using 40 GeV muons data because they are considered as a Minimum Ionizing Particle. For each channel, the MIP constant is defined by fitting the ADC spectrum of a muon after pedestal subtraction with the convolution of Landau and Gaussian function [99]. The most probable value of this fit corresponds to the MIP constant. However, the uncalibrated channels take the mean value of the MIPs of the corresponding chip. The MIP extraction study is presented in (chapter 6) section 6.5.4.

Chapter 5

Test of the SPIROC2E ASICs

The testing of the SPIROC2E (Silicon Photomultiplier Integrated Read-Out Chip) is an essential part of the development of the Analog Hadronic Calorimeter (AHCAL) technological prototype. It consists of the characterization and the understanding of the readout chip SPIROC2E needed for the commissioning and the operation of the AHCAL detector. Furthermore, the SPIROC2E ASICs test is a part of the detector production quality control to ensure that only well-known and characterized ASICs are used for the detector readout. Therefore, a test-board is designed and produced with a special BGA-socket to test and characterize the SPIROC2E chips before their assembly to the PCBs. A test stand is developed and automatized by LabVIEW [1] [100] for the configuration and control of the setup. The test of each chip lasts approximately eight to ten minutes, including the data analysis that is done automatically after each subtest. A brief result is stored in the AHCAL database for a quick check, while the detailed data is saved for further analyses. Around 1000 ASICs are characterized and tested using the test stand that is also optimized to test the chips of the whole detector (∼230 000 working ASICs).

In this chapter, a description of the test-board and test stand with its different components are presented. Subsequently, the procedure of the chip testing and the analysis results of each test are discussed.

[1] LabVIEW version 15.01.f2 is used for the test-stand

5.1 Test-board Design

The test-board, shown in Figure 5.1, is developed and produced with the help of the electronic department of Deutsches Elektronen-Synchroton (DESY) [101]. It is designed similarly to the AHCAL Base Unit (HBU, see section 4.2.1), to test the chip behaviour in similar conditions as in the real AHCAL using the same Data Acquisition system (DAQ). This allows us to understand and characterize the functioning of the SPIROC2E ASICs and ensures the production of the HBUs and the data taking quality. In the middle of the test board, a socket is specially designed for the SPIROC2E ASIC in its BGA-372 package. On the left side, two connectors of 40 pins are used to measure the input DAC voltage of all the ASIC channels with reference to +5 V, since they are connected to pull up resistance and not to the ground. A fast pulse is injected into the chip channels with a pulse generator via the Lemo cable and distributed simultaneously to all channels via 36 amplifiers. Each amplifier can be disabled by jumper to test one channel or a group of channels. On the right side of the board, eight SiPMs are assembled to measure their real pulse-shapes. The test-board connects to the DAQ interface via flex-leads connectors, which transmit all communications between the chip and the DAQ. The test board has two powers, ∼12.6 V for powering the test board and the DAQ via the data acquisition interface, and ∼4.9 V for powering the chip. Furthermore, the board communicates with the rest of the setup via an HDMI cable.

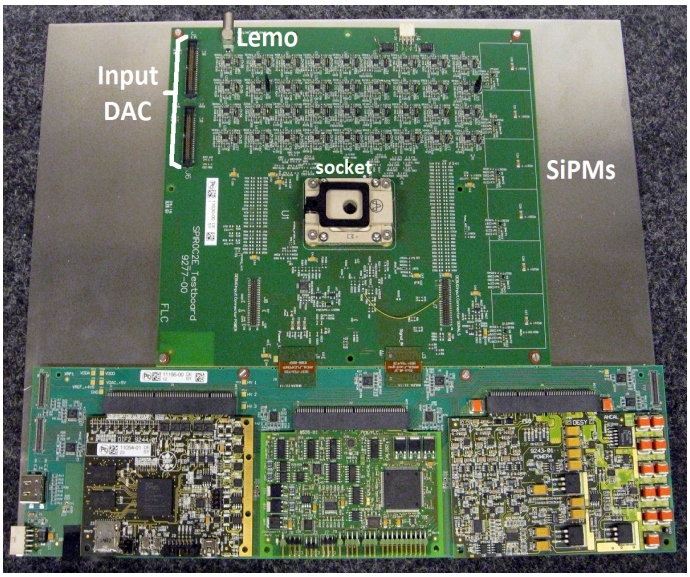

Figure 5.1: Picture of the test board for testing the SPIROC2E ASICs. The test-board is connected to the DAQ interface via flex-leads connectors.

5.2 Charge Injection

As illustrated in Figure 5.2, the chip test consists of injecting a fast pulse with a leading edge of 10 ns and a trailing edge of 100 ns, at the same time to all the 36 channels. For each test measurement, a configuration of 16 triggers with 500 readout cycles is set, and the chip triggers after receiving a start acquisition signal from the DIF board (see section 4.2.3). For each channel, the ADC and TDC signals are stored, digitized, and then transferred to the PC via the Link Data Aggregator (LDA) (see section 5.3.2), which is in turn connected to the PC via an Ethernet cable.

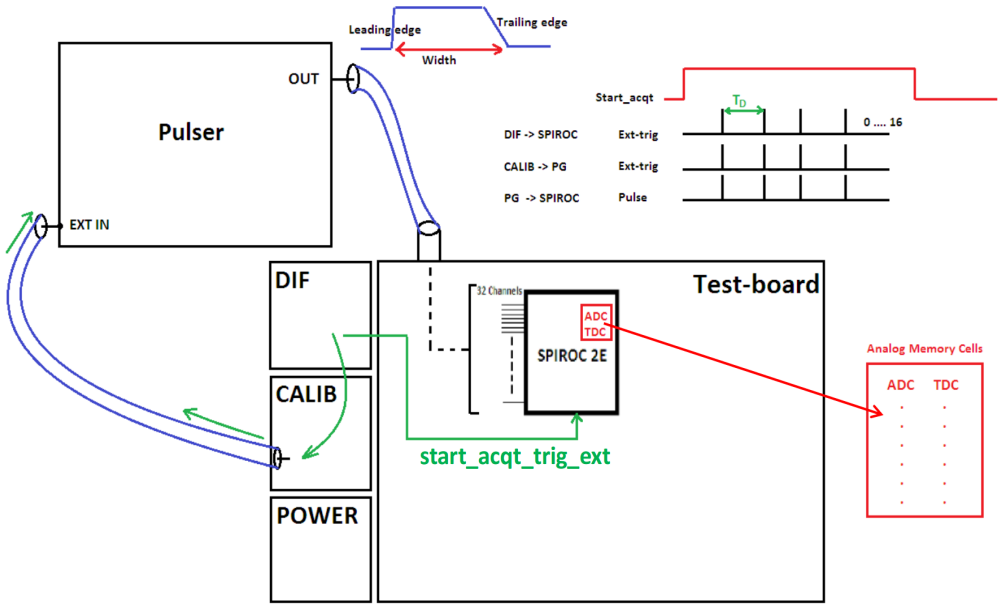

Figure 5.2: Sketch of the charge injection procedure.

5.3 Setup of Chip Testing

The chip testing setup is established in a compatible way to the AHCAL prototype, using the same communication components and data collection. Figure 5.3 shows the test stand of the chip testing with all the components, powered by two power supplies. The first power supply uses two voltages, ∼12.6 V for the test-board and ∼5 V for the chip. The second supply of ±5 V is used as the bias voltage reference. Automation of the chip testing is done by LabVIEW code with a graphical user interface, where he can enter the chip number and start the test, as shown in Figure 5.4. The procedure of chip testing consists of different tests

described in section 5.4. The list of all tests with the configuration parameters is transmitted to the LabVIEW code as an input text file, where each test can be enabled or disabled. The Boolean LEDs shown in the LabVIEW interface are used to check the components' powering and configurations status. The test stand is ready for testing the chip once the LEDs are green. A follow-up of each test is possible via the status windows with a printed status message. A full analysis runs after each test, and the data is stored in the specific test folder. After the end of the tests, a window pops up with the status of the chip.

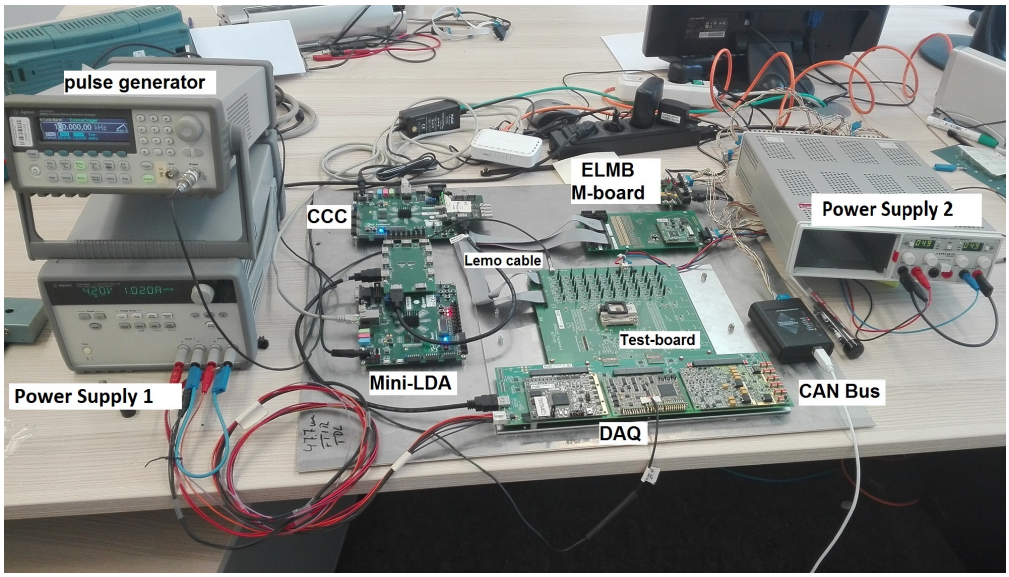

Figure 5.3: Setup of the chip testing.

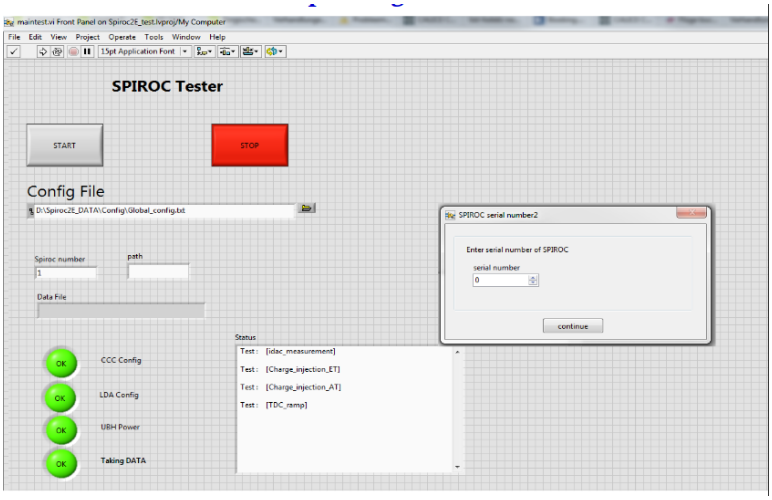

Figure 5.4: LabVIEW user interface for the chip testing.

5.3.1 The Embedded Local Monitor Board (ELMB)

The Embedded Local Monitor Board (ELMB) [102], shown in Figure 5.5, is a plug-on board designed by the ATLAS experiment and can be used for a range of different front-end control and monitoring tasks. It is designed with a low-power, low-cost, and high I/O-channel density, and it can run at 4 MHz clock speed. The ELMB contains an 8-bit micro-controller, a CAN-controller, and a CAN-BUS driver, additionally it is insensitive to the magnetic field. Furthermore, the ELMB is equipped with a 16-bit ADC (Crystal CS 5523) and a multiplexer circuitry for 64 analog inputs. It can measure the voltage from $-5\,V$ to $5\,V$ and temperature from $-5\,°C$ to $> 100\,°C$.

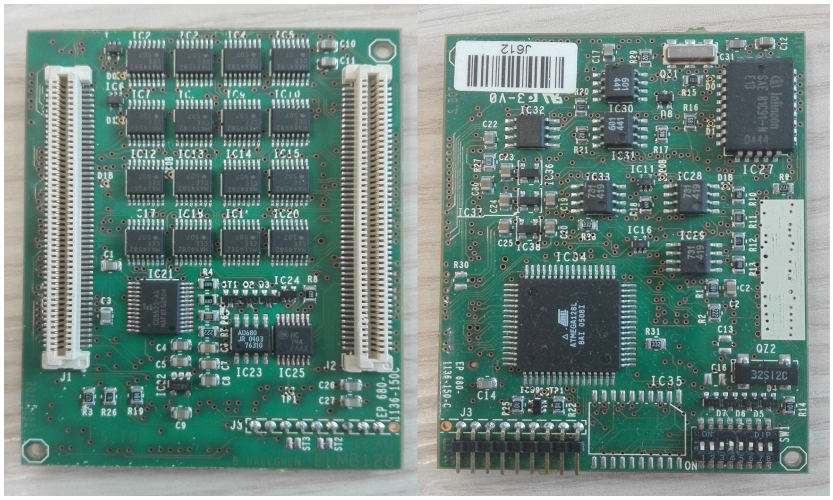

Figure 5.5: The Embedded Local Monitor Board: the left picture is the backside of the ELMB printed circuit board and the right one is the front side.

In this test stand, the ELMB is used to measure the input DAC bias voltage for all the 36 channels. Therefore a motherboard is designed by Wuppertal University with adapters to read out the output of the ELMB. Two 100-pins SMD connectors are available for the ELMB connection, and an additional four connectors of 20 pins to measure the bias voltage of each channel. The measured voltages of all the channels are transferred to the PC via the USB CAN-BUS, using a LabVIEW code. Figure 5.6 shows a picture of the ELMB motherboard where the ELMB is plugged in and connected to the test-board via flat cable connectors.

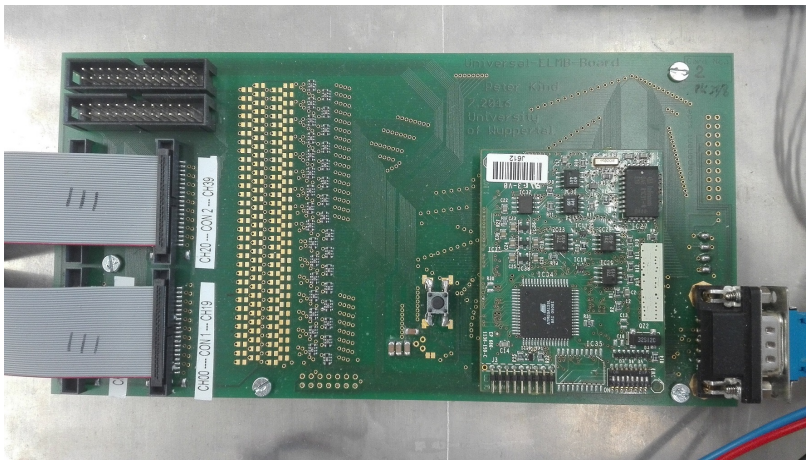

Figure 5.6: The ELMB motherboard designed by Wuppertal University.

5.3.2 Link Data Aggregator (LDA)

The Link Data Aggregator (LDA) board provides the interfaces to detector layers, the processes, and routes data packets exchanged between various sub-systems. Two LDA boards are available for different setups but with the same functionality. The Wing-LDA is intended for large setups like the AHCAL detector geometry with 96 micro-HDMI ports, which can communicate with up to 96 layers. The Mini-LDA hardware, shown in Figure 5.7, is designed for small setups. It is a custom FMC-LPC (FPGA Mezzanine Card - Low Pin Count) with 10 HDMI connectors, where two connect to DIFs and the Clock and Control Card (CCC). The mezzanine is attached to a Zedboard, a commercial development board hosting a Zynq-7020 SoC [103]. For the chip testing setup, the Mini LDA is decoding and merging each data package collected by the DIF from the SPIROC2E ASIC. Then, all the packets are transferred to DAQ PC via the TCP.

5.3.3 Clock and Control Card (CCC)

The Clock and Control Card (CCC), shown in Figure 5.8, provides a global clock to all detector layers via the LDA. It starts and stops the acquisition according to the spill level and the readiness of all the ASICs. It also guarantees the synchronous operation of all detector layers. The CCC is realized using a custom mezzanine card attached to a commercially available ZedBoard, and it has three HBMI ports. Depending on the CCC file configuration, one or more HDMI ports can communicate with the LDA. The CCC board communicates with

the PC via the Ethernet cable.

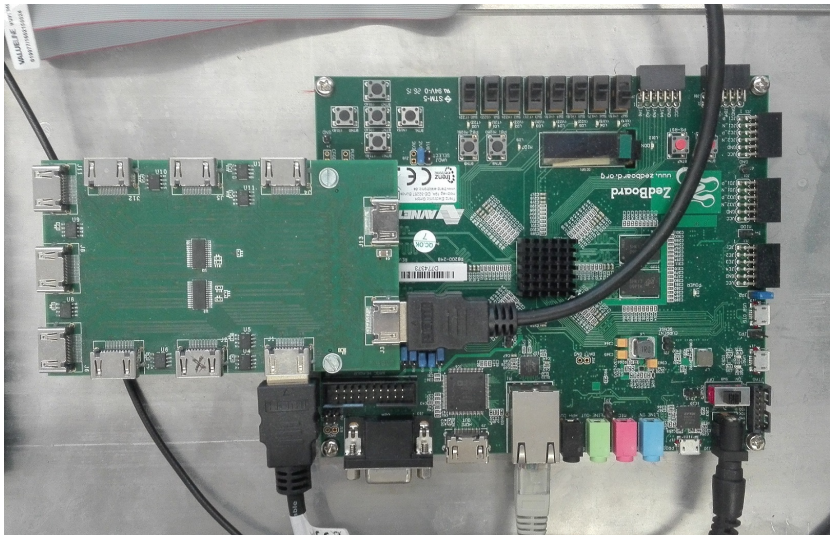

Figure 5.7: A custom Mini-LDA mezzanine card attached to a ZedBoard.

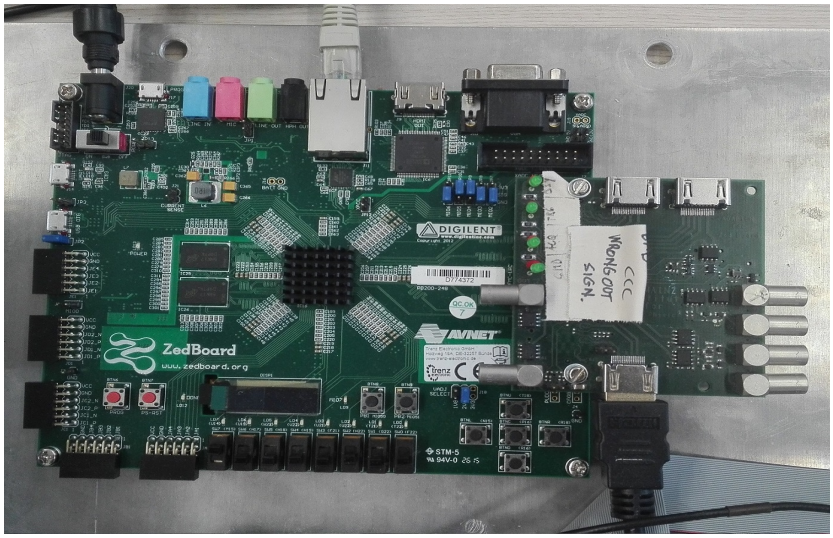

Figure 5.8: A custom CCC mezzanine card attached to a ZedBoard.

5.4 Procedure for the SPIROC2E Chip Testing

For the large AHCAL technological prototype, around 1000 chips need to be tested. The procedure of testing consists of several tests with a specific ordering and is optimized with a compromise between short time and quality. Here only a brief overview of tall the test is given. More details follow in the indicated sections.

1. **Hold scan:** It consists of injecting a fixed charge of 3 pC into all channels and measuring the amplitude of the output signal for the hold time range from 20 ns to 160 ns. The hold scan is done with the external and auto triggers for different preamplifier feedback capacitors setting: 100 fF, 200 fF, and 600 fF. The purpose of this test is to define the right time for sampling the signal (see section 5.5.1).

2. **Input DACs:** This test consists of measuring the bias voltage of all the 36 channels for six input DACs values (0, 50, 100, 150, 200, 255). The voltage measurement is within the range of 0 V to 2.5 V.

3. **Gain measurement (external-trigger):** Several charges Q_{inj} are injected into all the channels using a pulse generator with external trigger mode. The amplitude is measured with different feedback capacitors (C_{FB}).
   a. C_{FB}= 100 fF, 200 fF, 600 fF. $Q_{inj}[pC] = 1, 3, 5, 7, 9, 11, 13, 15, 17$.

4. **Gain measurement (auto-trigger):** Several charges Q_{inj} are injected and measured using auto-trigger mode. The amplitude is measured using a configured auto-gain threshold (AG) for each feedback capacitor.
   a. $C_{FB} = 100$ fF, $Threshold_{AG} = 360$, $Q_{inj}[pC] = 1, 2, 3, 4, 5, 6, 7, 8, 9, 10, 11, 12, 13, 14, 15$.
   b. $C_{FB} = 200$ fF, $Threshold_{AG} = 310$, $Q_{inj}[pC] = 1, 2, 3, 4, 5, 6, 7, 8, 9, 10, 11, 12, 13, 14, 15$.
   c. $C_{FB} = 600$ fF, $Threshold_{AG} = 280$, $Q_{inj}[pC] = 1, 2, 3, 4, 5, 6, 7, 8, 9, 10, 11, 12, 13, 14, 15$.

5. **TDC measurement**: This test consists of injecting a fixed charge of 1 pC and measuring the corresponding time in TDC units using the auto-trigger mode. The time is measured for different delays between the injected charge and auto-trigger, which correspond to the falling and rising TDC ramps. A chip configuration with a feedback capacitor of C_{FB} = 200 fF and an auto-gain threshold of 230, is used.
   a. Falling ramp: delay[μs]=0, 1, 2, 3, 3.5, 3.7 .
   b. Rising ramp: delay[μs]=4, 5, 6, 7, 7.5, 8 .

5.5 Results of Chip Testing

5.5.1 Hold Scan Timing

The hold time consists of defining the optimal time to sample the signal. The sampling point corresponds to the maximum region of the amplitude. The hold time is the delay time between the trigger and sampling point and can be set in two different ways, depending on the trigger mode. In the external-trigger (ET) mode, the hold time corresponds to the time between the external trigger of the pulse generator and the start acquisition signal. While in auto-trigger (AT) mode, the hold time can be set as a configuration parameter of the ASICs and corresponds to the delay between the trigger generated by the fast shaper and the signal's sampling time, as shown in Figure 5.9. Therefore, proper optimization of this delay leads to a good separation between signal and noise.

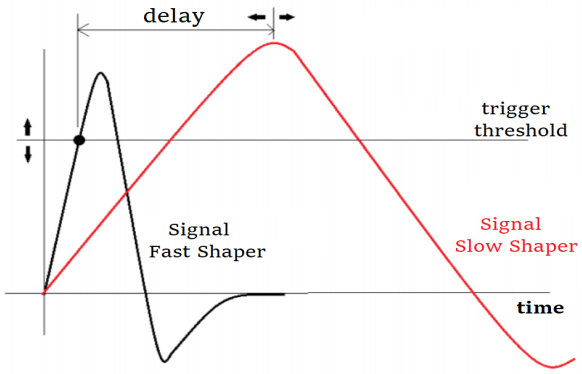

Figure 5.9: Hold time of the ASICs corresponds to the delay time between trigger threshold and sampling point of the signal. [104].

The hold time measurement consists of injecting a fixed input charge of 3 pC into all the 36 channels for different delay times. Figures 5.10a and 5.10b show the hold time measurement with the ET mode for different pre-amplifiers setting: 100 fF, 200 fF, and 600 fF, and for high gain (HG) and low gain (LG) signals. The hold time is variated from 10 ns to 120 ns for external-trigger and from 10 ns to 180 ns for auto-trigger. For both HG and LG signals, the hold time depends strongly on the pre-amplifier feedback capacitors. For both measurements, the filled and the empty triangle correspond to HG and LG signals, respectively. A difference in the optimal hold time can also be observed between HG and LG for both trigger modes. Therefore, as shown in Table 5.1, a compromise is optimized for a better sampling of the signal. The hold time depends on trigger modes and pre-amplifiers' setting. It is set as an

ASIC configuration parameter for the AT mode and a delay time in the pulse generator for the ET mode. The optimal hold time is used afterward during all steps of the chip testing.

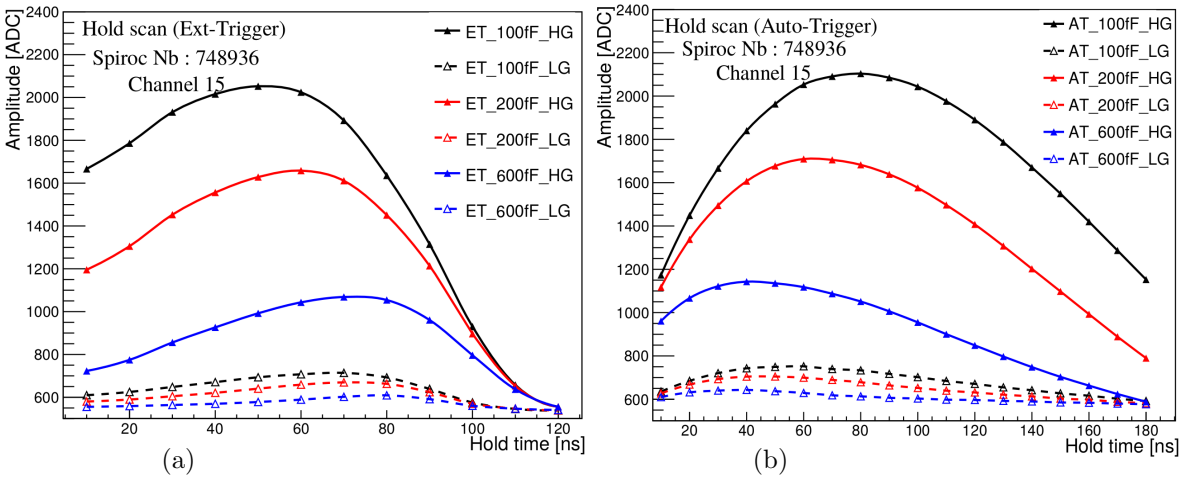

Figure 5.10: Amplitude measurement with a fixed charge injection for different delays of both trigger modes: ET (a) and AT (b). The colors correspond to different feedback capacitors (100 fF, 200 fF and 600 fF). The filled and empty triangle correspond to high gain and the low gain signals, respectively. These measurements correspond to channel 15.

Trigger Modes	Pre-amplifier[fF]	hold time [ns]
Auto-trigger	100	90
	200	70
	300	50
Ext-trigger	100	50
	200	60
	600	75

Table 5.1: Hold time for auto and external triggers for different feedback capacitances 100 fF, 200 fF and 600 fF. The scan of the hold time is from 10 to 120 ns for ET and from 20 to 180 ns for AT. The scan is done for high gain and low gain signals, the optimal hold time depends on the feedback capacitance.

5.5.2 Input DACs measurement

The linearity of the input DACs (IDACs) defines how accurate the working point of the photomultiplier can be set. This test consists of measuring the bias voltage of each channel and check its stability for the 8-bit Input DAC, where only five IDAC points (0, 50, 100, 150, 200, 255) are chosen to check the IDAC linearity. The bias voltage measurement as a

function of the IDAC points is shown in Figure 5.11a, and the multiple graphs represent the measurement of all the 36 channels. For each channel, the linear fit slope is used to check the IDACs linearity, and a reliable linearity region is defined to select the chip with non-broken IDAC and optimized by the mean of the slope over all channel ±1.5 mV, as shown in Figure 5.11b. This selection consists of discarding the chip if at least one of the channel slope is out of the reliable range. If the chip passes the test successfully, the next test starts automatically by following the testing procedure described in section 5.4.

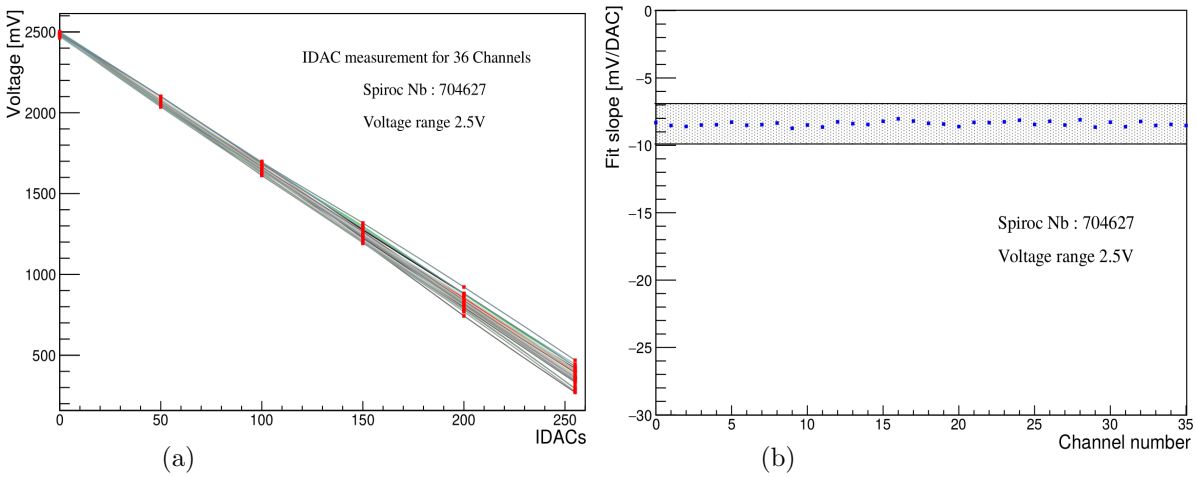

Figure 5.11: a) Input IDAC performance of all the 36 channels of the SPIROC. The output voltage measurement (mV) for different input DAC values. The voltage is fitted with a linear function. b) The slope of the linear fit as function of channel number.

5.5.3 Gain and Linearity

The SPIROC2E has an input DACs of 8 bits, limiting the dynamic range to ∼48 dB, but various pre-amplifiers are used for LG and HG signals to increase the dynamic range. In principle, the gain is higher for small feedback capacitance, but the dynamic range is short. Therefore, a compromise between the high gain and the large dynamic range is essential. This test consists of checking the linearity of the dynamic range by measuring the gain for different pre-amplifier feedback capacitors. This gain is measured with three feedback capacitances 100 fF, 200 fF, and 600 fF for all memory cells of the 36 channels, using external and auto triggers. This measurement consists of injecting several charges from 1pC to 15 pC (AT) or 17 pC (ET) and measuring the amplitude of the output signal in ADC counts. However, after testing several chips, a lower charge injection region up to 11 pC is optimized to reduce the time of testing by 30% while keeping the quality of the test. An automatic channel and

memory cells wise analysis is done with LabVIEW, and it consists of fitting the dynamic range with a linear fit for LG and HG signals. A chip is rejected or badly classified if one of the channels or memory cells has an unstable gain.

5.5.3.1 External Trigger

The amplitude of the output signal measured with several charge injections up to 17 pC, using the external trigger for channels 26 and 35, is shown in Figure 5.12. The various colors correspond to different pre-amplifiers' feedback capacitors. The filled and empty triangles correspond to HG and LG signals, respectively. The linearity of the dynamic range is checked with a linear fit function from 1 to 7 pC for each memory cell. Comparing the gain measurement of HG and LG signal, an early saturation of the HG signal can be seen. A higher gain is observed for a small capacitor of 100 fF, while the dynamic range increases significantly for 600 fF.

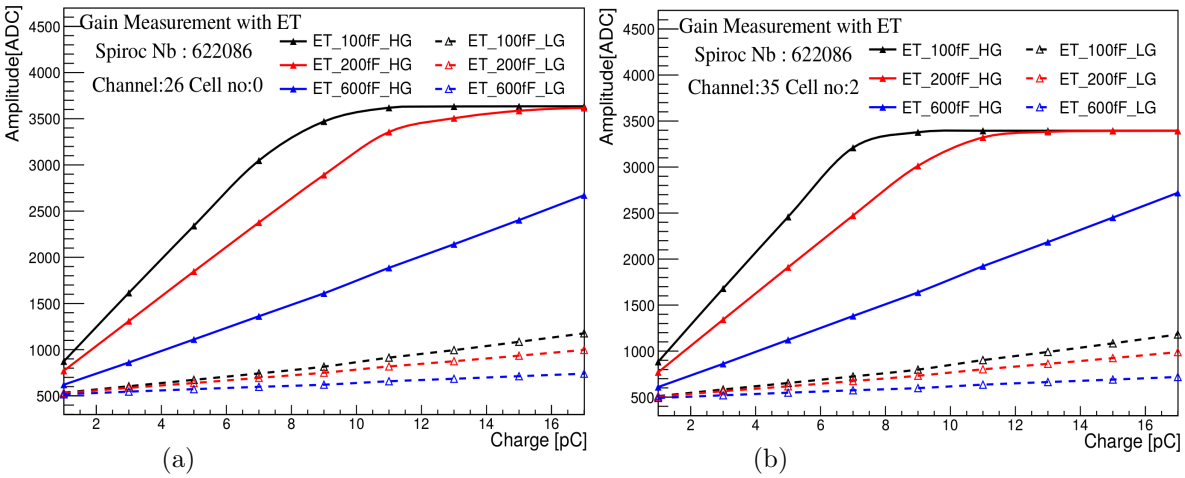

Figure 5.12: Amplitude measurements as a function of injected charged for channels 26 (a) and 35 (b) with the Ext-trigger for HG and LG are represented with filled and empty triangles, respectively. The different colors represent various pre-amplifiers' feedback capacitors.

The gain extracted from the fit slope of the dynamic range linearity of all memory cells for HG and LG signal as a function of the channels number is shown in Figure 5.13. The three plots correspond to the measurement for different feedback capacitors: 100 fF, 200 fF, and 600 fF. No gain variation from memory cell to memory cell is observed. For each channel, a reliable gain region is defined by the mean gain over all memory cells with a variation of ± 10 ADC/pC for 100 and 200 fF and ± 3 ADC/pC for 600 fF. The chip is badly categorized if one of the memory cells' slope is not within the reliable region.

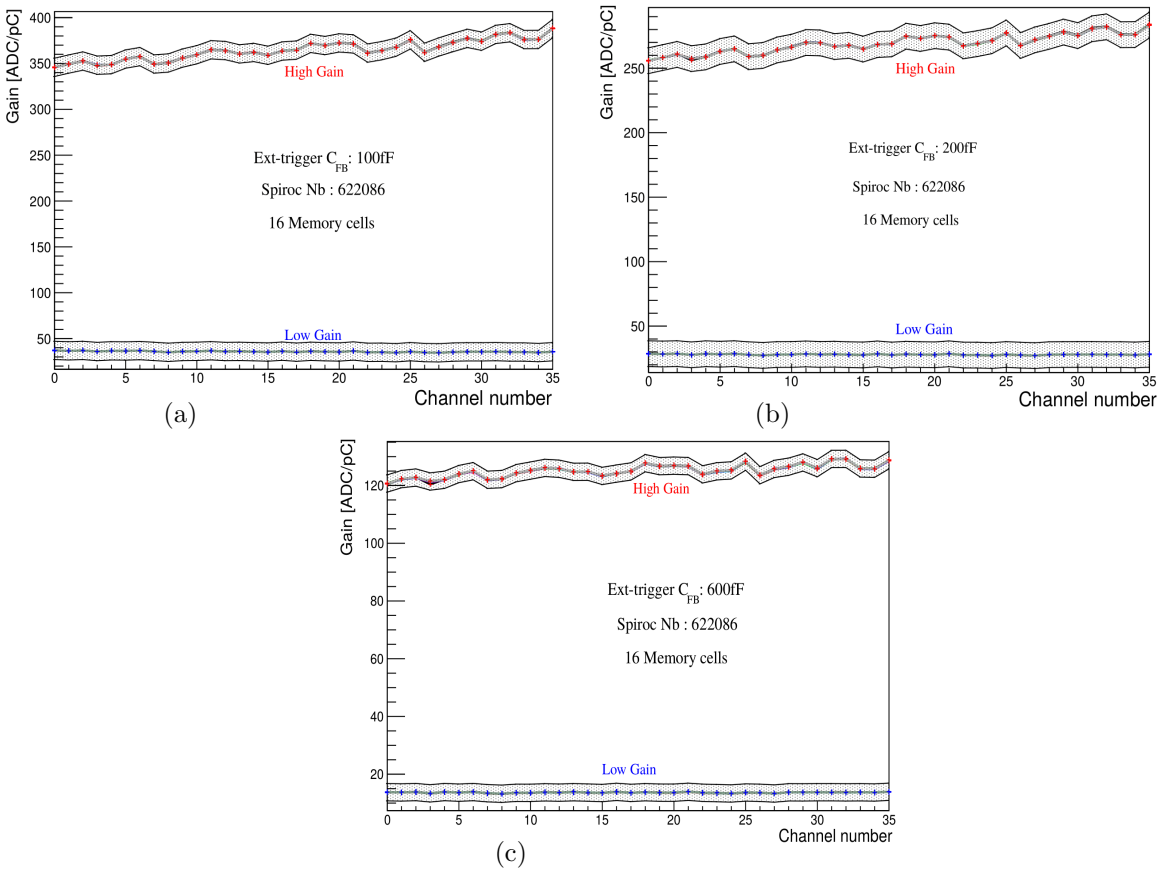

Figure 5.13: Gain measurements with ET mode extracted from the linear fit slope of the dynamic range for HG (red) and LG (blue). Figures a, b and c represent the results for different feedback capacitors 100 fF, 200 fF and 600 fF. The filled area represents the reliable region defined by the mean of the gain over all memory cells with a symmetric variation.

5.5.3.2 Auto trigger

Similarly to the external trigger, the chip is also tested with auto-trigger mode, by measuring the gain and checking the linearity of its dynamic range. Figure 5.14 shows the amplitude measurement with different pre-amplifiers feedback capacitors for HG and LG signals as a function of injected charges for one memeory cell of channels 26 and 35 number. Excellent linearity of the dynamic range up to 8 pC is seen for 100 fF with an offset that corresponds to the HG and LG pedestals. Additionally, an ADC saturation is present with capacitors 100 fF and 200 fF at an injected charge of 9 pC, whereas it is not for 600 fF up to a charge of 17 pC. As shown in Figures 5.14a and 5.14b, the ADC saturation depends also on the channel numbers. The gain measurements as a function of channel number are shown in Figure 5.15 with no variation in memory cells wise. The working chips' categorization is made similarly

to the external trigger mode by defining the reliable gain region for each channel. This region is defined for each channel as the mean gain over all the memory with a variation of ± 10 DAC/pC for 100 and 200 fF and ±3 ADC/pC for 600 fF.

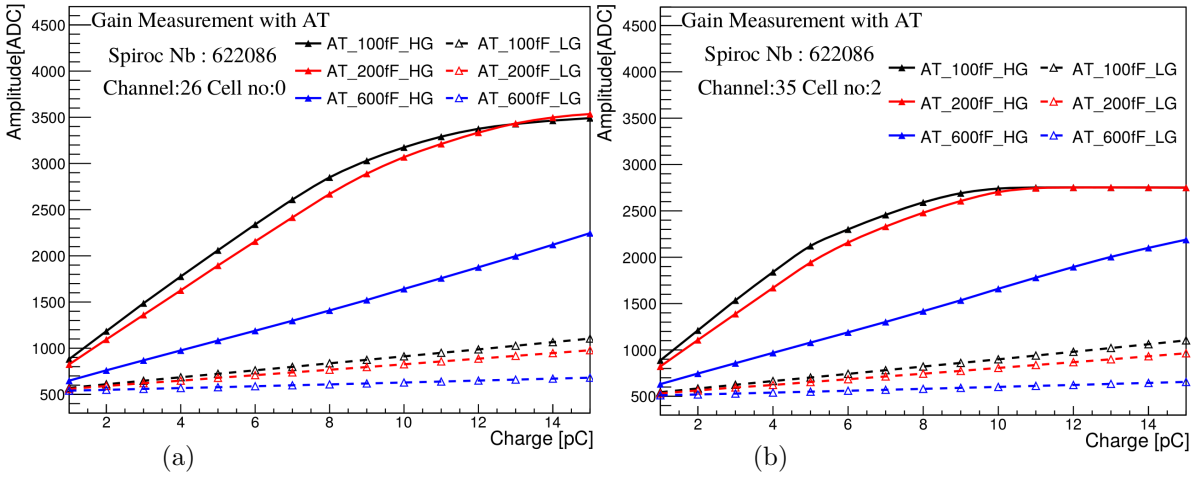

Figure 5.14: Amplitude measurements as a function of injected charged for channels 26 (a) and 35 (b) with the Auto-trigger for HG and LG are represented with filled and empty triangles, respectively. The different colors represent various pre-amplifiers' feedback capacitors.

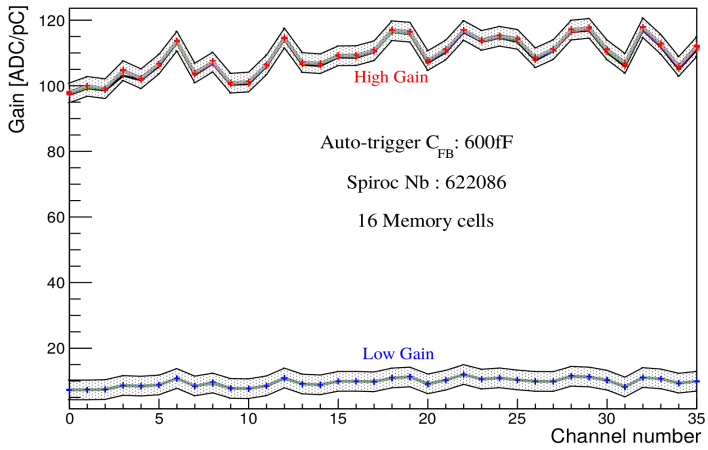

Figure 5.15: Gain measurement with the AT mode extracted from the linear fit slope of the dynamic range for HG (red) and LG (blue) for $C_{FB} = 600fF$. The filled area represents the reliable region defined by the mean of the gain over all memory cells ±3 ADC/pC.

Figure 5.16 shows the maximum amplitude in ADC counts for AT and ET as a function of channel numbers for two chips. Comparing the Figures 5.16a and 5.16b, the saturation level depends strongly on the channel number, which can be observed earlier for higher channels. Additionally, the saturation using the AT mode is much stronger than the ET mode. Therefore, further studies are discussed in the following section to understand the ADC saturation

thoroughly.

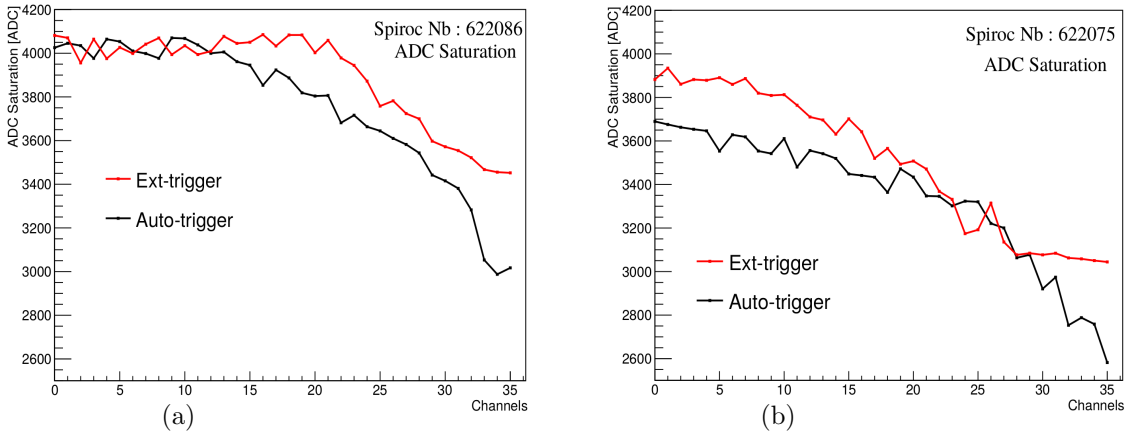

Figure 5.16: Variation of the ADC maximum as a function of channels for chips 622086 and 622075. It is defined as the maximum amplitude over all the memory cells.

5.5.4 ADC Saturation

As discussed previously in the gain measurement, an ADC saturation is observed only with feedback capacitor 100 fF. In order to reach the saturation level of high pre-amplifiers' feedback capacitors, high fast pulses are injected up to 30 pC using several feedback capacitors: 100fF, 200fF, 600fF, 850fF, 1000fF, and 1200fF. This measurement is done only for the HG signals since no ADC saturation is present for LG signals by injecting charges up to 30 pC. Figure 5.17 shows the measured amplitude of the HG signal with AT mode as a function of the charge injection for channels 0 and 35. An ADC saturation is seen for all the pre-amplifiers' feedback capacitors, but a saturation difference of $\sim$ 1000 ADC counts is observed for channel 35 comparing to channel 0. The dynamic range increases for a large feedback capacitor, while the linearity degrades for feedback capacitance higher than 1000 fF.

In the global level, a chip to chip variation of the ADC saturation is studied for a feedback capacitor of 100 fF. The saturation level is defined, for each ASIC chip, as the maximum amplitude over all the memory cells and channels. Figure 5.18 shows the ADC saturation level as a function of the chips, which variates between 2200 ADC to 3200 ADC. The purpose of these studies is to define the saturation level over all the ASICs, so the ADC saturation in the readout of the AHCAL technological prototype could be avoided. Therefore, the precision of the saturation level is essential for defining the pre-amplifier feedback capacitors used to read out HG and LG signals. The ADC saturation results are helpful for the ASICs configuration

used in the June test beam 2018 at the SPS, where 600 fF and 1200 fF are used for HG and LG signals.

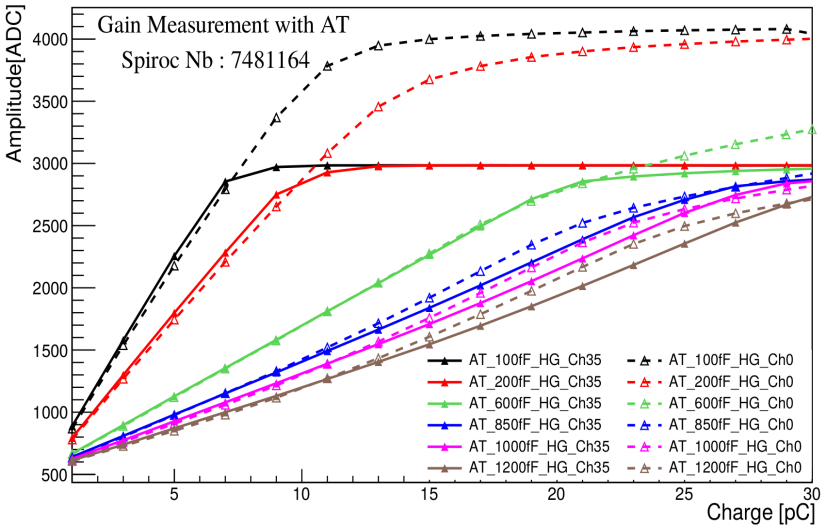

Figure 5.17: Gain measurement for channels 0 and 35 for different pre-amplifiers' feedback capacitors. The filled and empty triangles represent the channels 35 and 0, respectively. The different colors correspond to different pre-amplifiers' feedback capacitors.

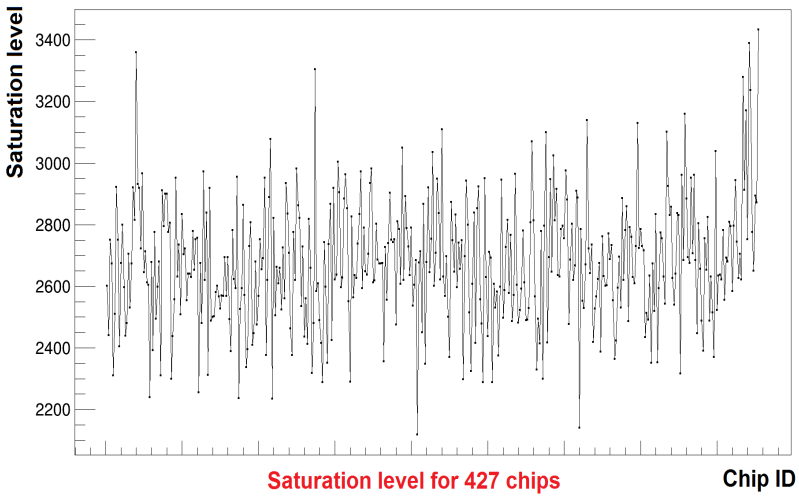

Figure 5.18: ADC saturation level over all channels and memory cells for 427 chips.

5.5.5 Gain Measurement with and without Power Pulsing

As discussed in section 4.2.4, the SPIROC2E ASIC operates with power pulsing mode. Therefore, the stability of gain measurement is checked with and without the pulsing power mode. This test consists of injecting several charges from 1 pC to 30 pC and measuring the

gain for several pre-amplifiers' feedback capacitors (100 fF, 200 fF, and 600 fF). Figure 5.19a shows the measured amplitude in ADC counts with and without the power pulsing mode using the auto-trigger. The graphs with different colors correspond to different feedback capacitors for high and low gain signals. The empty and the filled triangles represent the power pulsing on (PP_ON) and power pulsing off (PP_OFF). The power pulsing does not affect the dynamic range, whereas a slight gain variation of 1 to 2% is seen in the ratio plot. Additionally, as shown in Figure 5.19b, no difference is observed while using the external trigger mode. The validity of the power pulsing operating mode, used in the test beam of the AHCAL technological prototype, could be tested earlier with our test stand.

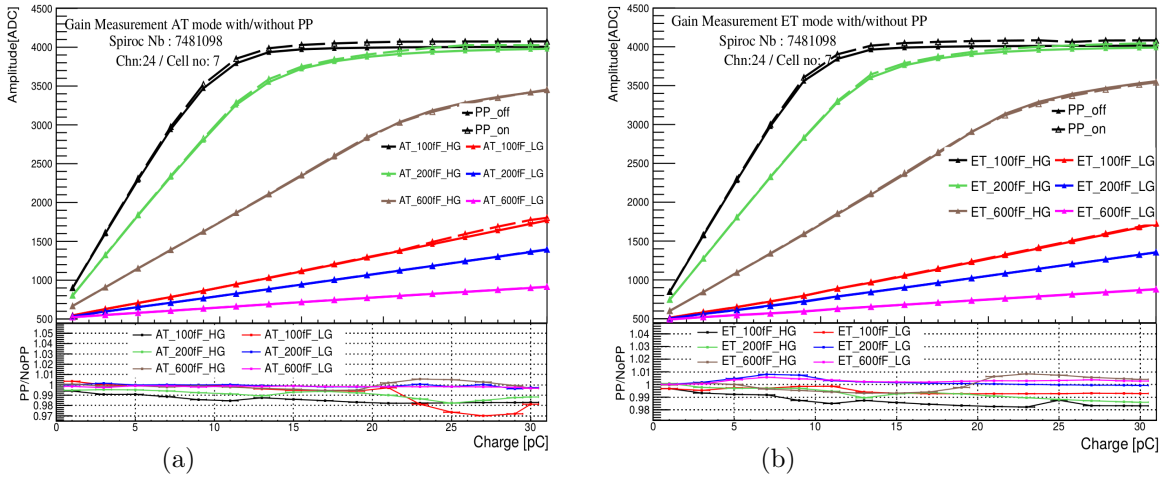

Figure 5.19: Gain measurement with and without power pulsing for different pre-amplifiers setting with the external-trigger (a) and auto-trigger (b).

5.5.6 TDC Ramp measurement

As explained in section 4.2.2, the SPIROC2E provides the time information in the form of two ramps in TDC units, the falling ramp from 0 to 4 μs and the rising ramp from 4 to 8 μs. The purpose of this test is to check the TDC's linearity of these two ramps, by injecting a fixed charge of 1 pC into all the 36 channels using the auto-trigger mode with a feedback capacitor C_{FB}= 200 fF and a gain threshold of 230. The timing is measured with a variable delay between the injected pulse and the internal trigger from 0 to 8 μs. Figure 5.20a shows the timing measurement as a function of the delay time for channel 21. This measurement is done per channel, and the linearity is checked by fitting the ramps with a linear function fit. As shown in Figures 5.21 and 5.20b, the slopes and χ^2 of the linear fit are extracted for all the 36 channels. A validation slope region is optimized to check the linearity of TDC ramps and

defined by the slopes' mean over all channels with a variation of $\pm 15\ TDC/\mu s$. Additionally, an extra cross-check is done using the χ^2 fit parameter to ensure the fit quality. The chip is good if the χ^2 is lower than 200; otherwise, it is classified in different categories.

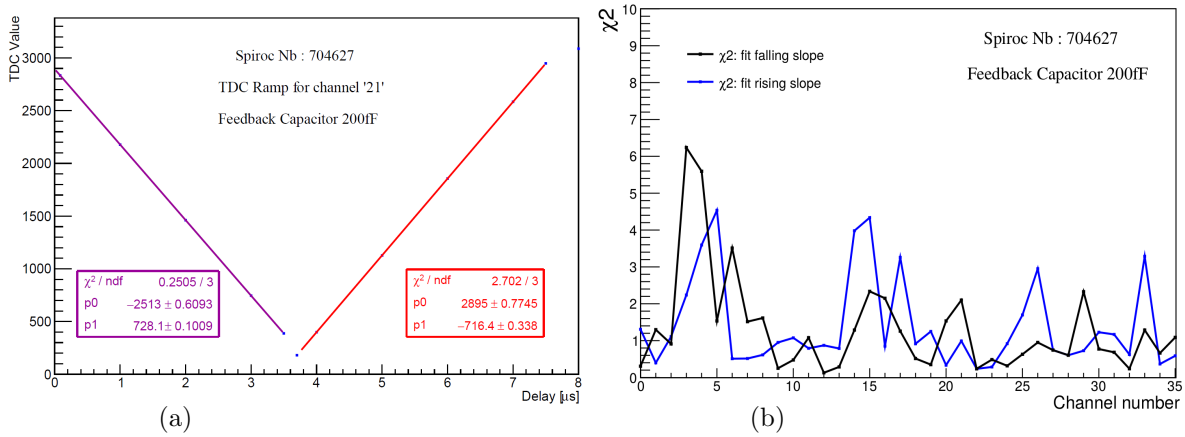

Figure 5.20: a) TDC measurement for falling and rising ramps of channel 21. A linear fit for each ramp is done to check the TDC linearity. b) Plot of the χ^2 of linear fit for the falling and rising ramps.

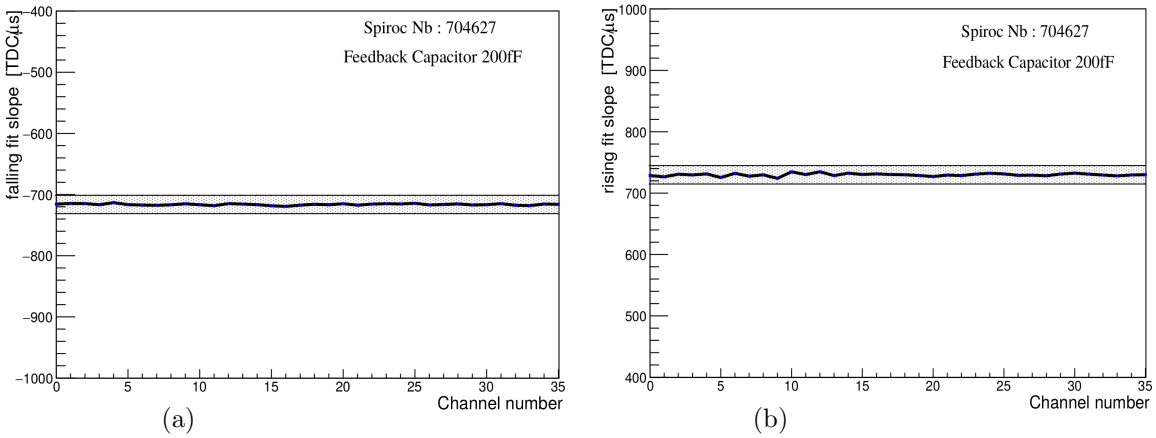

Figure 5.21: The fit slope of falling (a) and rising (b) ramps as a function of channel number. The filled band represents the reliable region defined by the mean slope $\pm 15\ TDC/\mu s$

5.5.7 Pedestal for low gain and high gain

An additional test is performed to check the variation of HG and LG pedestals for different charge injections, by injecting five pulses: 1, 2, 3, 4, and 5 MIP, into one channel, and extracting the pedestal from other channels with Hitbit = 0. The different plots in Figure 5.22 show the pedestal distribution for HG and LG for various charge injections. A slight increase of the HG pedestal is observed compared to the LG pedestal for all the injected

charges. Figure 5.23 shows the HG and LG mean pedestal extracted by the Gaussian fit for several injected charges, where the variation is less than 1% from 1 MIP to 5 MIP. In the ratio plot, a difference of 1 to 2% is seen between the HG and LG pedestals.

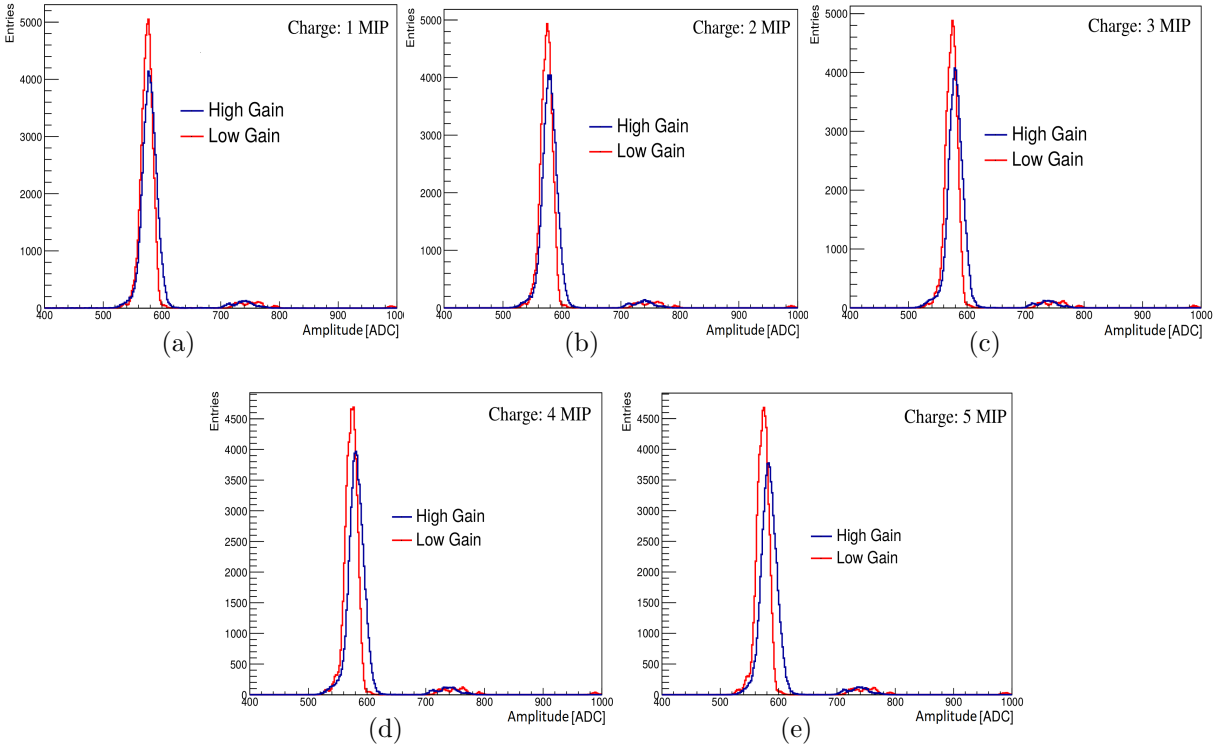

Figure 5.22: The high-gain and low-gain pedestal measurements for different injected charges of 1 MIP (a), 2 MIP (b), 3 MIP (c), 4 MIP (d), 5 MIP (e).

Additionally, pedestal jumps to higher ADC values can be observed in Figure 5.22, leading to several small peaks in the right of the pedestal distributions. Therefore, the pedestal variation is studied per channel and memory cells to understand the reason for these jumps. Figure 5.24b shows the LG pedestal for three cases, memory cells from 0 to 7 in green, cells from 8 to 15 in red, and memory cell 9. As shown in Figure 5.24a, the HG pedestal jumps happen mainly in memory cells from 8 to 15. However, no pedestal jump is present for memory cells 0 to 7. The same case is observed for the LG pedestal, as shown in Figure 5.24b. Besides, it is essential to check if these jumps are taking place in the signals. Therefore, the signal from channels with Hitbit = 1 is extracted for the same three cases. Figure 5.25 shows the amplitude distribution of signals for various memory cell ranges. Luckily, no ADC jump is observed for memory cells from 8 to 15, ensuring the quality of the measured signal.

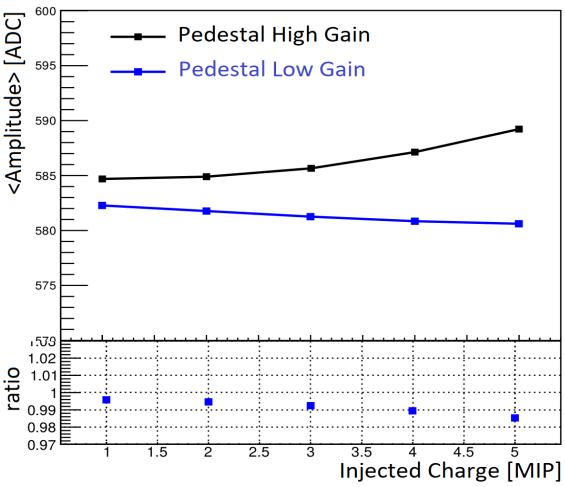

Figure 5.23: The mean pedestal for high gain and low gain as a function of injected charges. The mean is defined by Gaussian fit of the pedestal distributions.

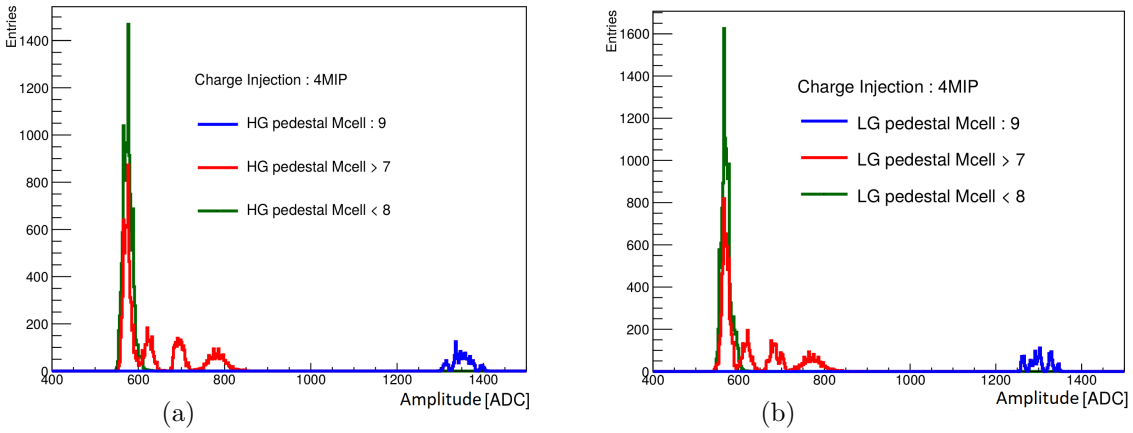

Figure 5.24: Pedestal distributions of HG (a) and LG (b) for memory cell 0 to 7 (red), 8 to 15 (green) and memory cell 9 (blue)

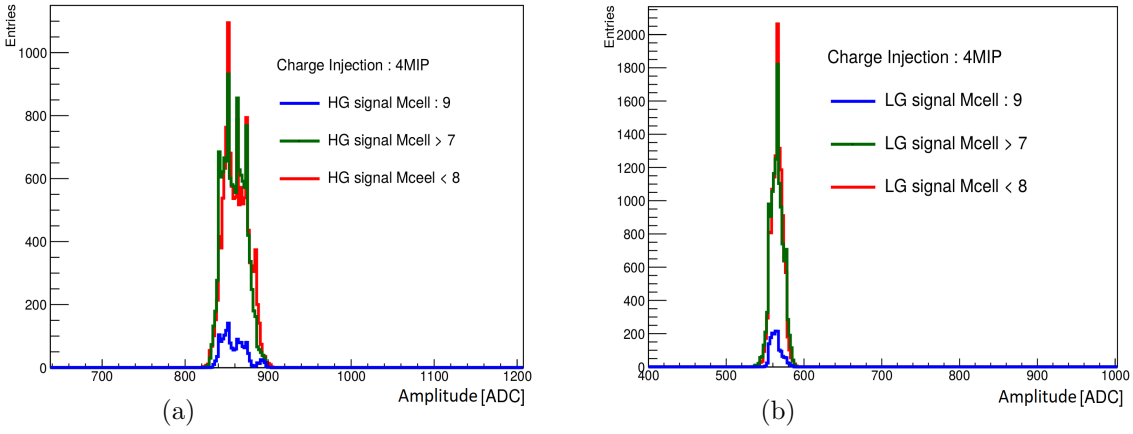

Figure 5.25: Signal distributions of HG (a) and LG (b) for memory cell 0 to 7 (red), 8 to 15 (green) and memory cell 9 (blue)

5.5.8 Summary of the selection criteria of the chip

The full procedure of the chip testing with the analysis is done successfully with an automatic test stand in a reasonable time of 8 to 10 min, which compromises between the minimum time and quality of the test. After each test, an automatic analysis helps to classify the chip in different classes, where different selection criteria are optimized. The selection criteria for the chip classification are summarized in Table 5.2, where slope and χ^2 are the fit parameters of each test. The chips of Class A are the fully working chips assembled in the AHCAL technological prototype with a yield of ∼85%. Around 10% of the chips of Class C are utterly or partially broken, while the 5% of Class B could be used in an emergency case since they only have a broken input DAC. The data and the analysis results of each test are stored with the chip serial number for further analysis. Additionally, some extra checks are performed to understand the chip behavior, such as the gain stability in the power pulsing mode and the variation of the HG and LG pedestals. All the observed problems are reported to the developers of the SPIROC2E to improve its features and production.

Tests	Slope range	χ^2	Class A	Class B	Class C		
IDAC	$< slope >_{chn}$ ±1.5 mV/DAC	✗	✓	—	✗	✓	✓
Gain	$< Gain_{100fF} >_{M.cell}$ ±10 ADC/pC $< Gain_{200fF} >_{M.cell}$ ±10 ADC/pC $< Gain_{600fF} >_{M.cell}$ ±3 ADC/pC	✗	✓	✓	✓	✗	✓
TDC	$< slope_{(ris.,fal.)} >_{chn}$ ±15 TDC/μs	$\chi^2 < 200$	✓	✓	✓	✓	✗

Table 5.2: Table of the selection criteria of the chip classification defined for different tests. For the IDAC test, the reliable region is defined by the mean slope $< slope >_{chn}$ over all the channels with a variation of ±1.5 mV/DAC. For the Gain test, the reliable region is defined by the mean gain $< Gain_{C_{FB}} >_{M.cell}$ over all memory cells of each channel with the variation corresponding to each feedback capacitor. For the TDC test, the reliable region is defined by the mean slope $< slope_{(ris.,fal.)} >_{chn}$ of the rising and falling TDC ramps calculated over all channels with a variation of ±15 $TDC/\mu s$, and $\chi^2 < 200$ is required.

Chapter 6

Testbeam Measurement with Electrons

In the previous chapter, the AHCAL technological prototype developed for the ILD detector has been presented. After the construction and commission of the AHCAL detector, it has been installed in the test beam at CERN Super Proton Synchrotron (SPS) to study its electromagnetic and hadronic response. Different beam particles were collected: 40 and 120 GeV muons, 10 to 100 GeV electrons, and 10 to 160 pions. The electron particles are the primary data set used for the analysis of this thesis.

In this chapter, the beamline setup of the test beam campaign and the collected data are presented. Afterward, the energy calibration is explained in detail with the extraction procedures of all the calibrations constants. Subsequently, a detailed description of the AHCAL geometry features implemented in the simulated detector model is illustrated. Furthermore, the full analysis of electrons is studied and compared to the simulation for the validation of the AHCAL detector. This analysis aims to have a thorough understanding of the electromagnetic response of the calorimeter by measuring the energy deposited by the electron shower, the linearity, the energy resolution, and studying the longitudinal shower profile. Towards the end of this chapter, the systematic uncertainties are calculated for the calibration factors using simulated event samples. Finally, the summary of this analysis with the final comparison of linearity and energy resolution for data and simulation are discussed.

6.1 Beamline Setup of the H2 at SPS, CERN

The test beam of the AHCAL detector is performed in the North Area of the SPS in the H2 beamline [105], which is a high-energy and high-resolution secondary hadrons beam. It provides a primary beam of protons of up to 400 GeV or secondary mixed hadrons with a wide energy range of 10-400 GeV. The electrons can be selected from secondary beams using the Cerenkov counter, which leads to a momentum-dependent purity of 10-99.5%. Figure 6.1 shows the vertical plan of the momentum selection. In the beamline, the particle selection is made by two large spectrometers according to their magnetic rigidity R = $B\rho$ [Tesla-meters] $\sim 3.33\, p_b/Z$, where B is the magnetic field, and ρ [m] is the bending radius of particle motion in the magnetic field. p_b [GeV/c] represents the momentum of beam particle, and Z corresponds to the charge of the particle in proton charge units. Each spectrometer consists of six dipoles to deflect the beam by a total angle of 41 $mrad$, and a collimator to define the beam trajectory. The intrinsic resolution of the beam spectrometer is about ∼0.13% with a maximum rapidity acceptance of ±1.7 %.

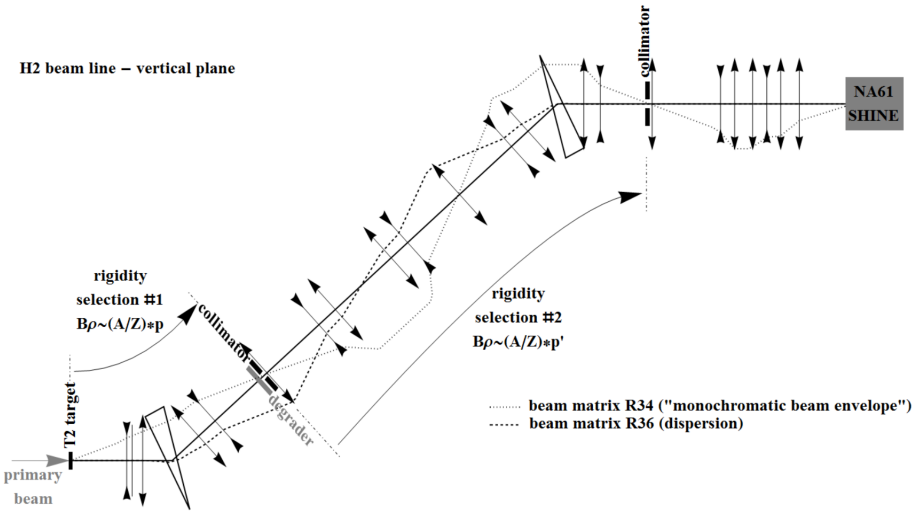

Figure 6.1: Vertical plan of the H2 beamline at SPS, CERN. The dimensions are not to scale, e.g., the beamline is more than 600 m long, the heigh difference between T2 and the Hall is ∼12 m [106].

The H2 beamline can deliver positively or negatively charged secondary hadrons produced after the interaction of the primary proton beam with the target T2. The secondary hadrons are generated with a mixture of muons and electrons, and tertiary hadrons produced from interactions with the collimators. A Cerenkov threshold counter detector is installed in the

beamline and used for online particle selection and reduction of the contaminations in the recorded beam data. The beamline is also equipped with many beam instrumentation detectors as wire chambers and scintillators to provide the beam position.

6.2 Testbeam Campaign at CERN: June 2018

The AHCAL was installed in the H2 beamline at the SPS facility in CERN during two test beam campaigns for testing the performance of the new SiPMs, tile, and readout system. The first test beam, in May 2018, [107] aimed to validate the operation of the AHCAL in the pulsing power mode by collecting the data with and without power pulsing. The second test beam was performed in June 2018 with the same prototype where muons, electrons, and pions were collected only with power pulsing mode.

The AHCAL detector, described in detail in section 4.2, consists of 39 layers inserted in a steel absorber stack with scintillator plastic tiles as an active material. In front of the detector, one HBU layer is placed to reject early showering particles. Besides, a tail catcher is located behind the AHCAL to measure the hadronic shower leakage, and it consists of 15 HBU layers of 36×36 cm^2 inserted in a steel absorber stack with a layer thickness of 1.76 cm. As shown in Figure 6.2, the detector is positioned on a movable stage capable of placing the calorimeter to any desired position with respect to the incoming particles.

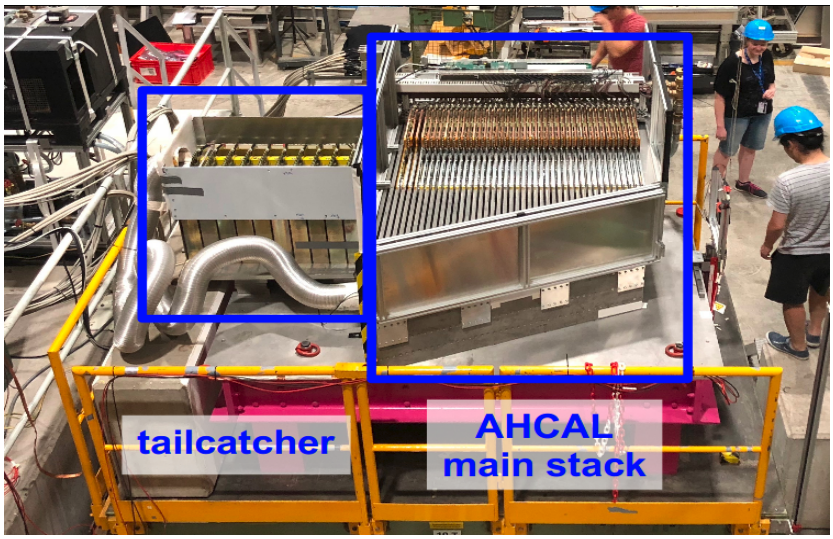

Figure 6.2: Picture of the AHCAL technological prototype during the June test beam in the H2 beamline at the SPS. The AHCAL is placed on a movable stage (pink) with a tail catcher in the back and pre-shower layer in the front.

The beamline is instrumented with wire chambers for tracking, scintillators for the triggering, and a Cerenkov detector for the particle identification, as shown in Figure 6.3. Out of 6 wire chambers and 7 scintillators, only 4 and 6 are used, respectively.

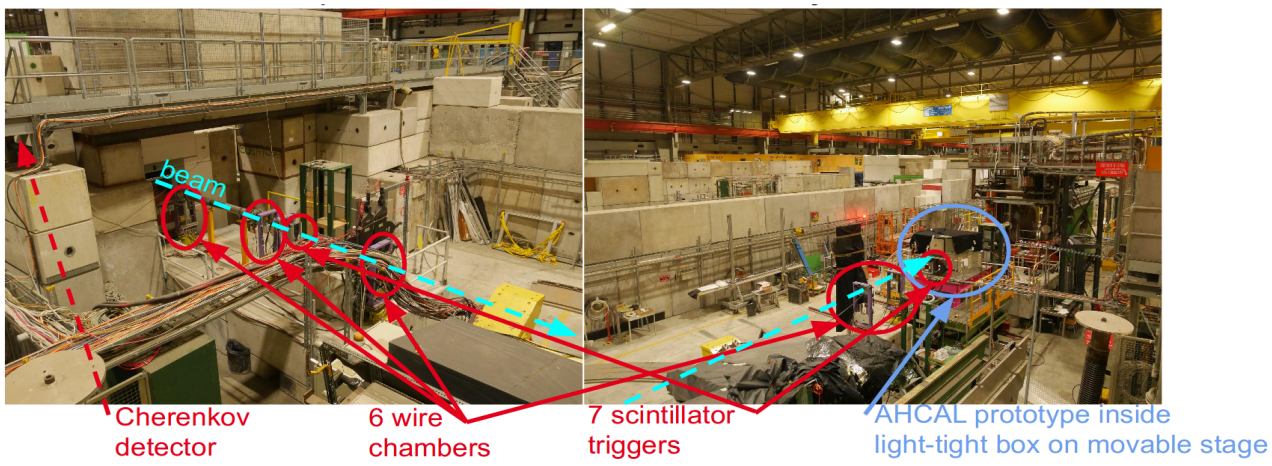

Figure 6.3: Picture of the beamline H2 during the test beam of the AHCAL in June 2018. The visible components in the beamline are: 6 wire chambers and 7 scintillator triggers [108].

6.3 Data Taking

During the test beam campaign in June 2018, several beam particles were taken in different energy ranges. Additionally a long LED runs used for the gain calibration of the SiPMs and the extraction of High Gain (HG) - Low Gain (LG) inter-calibration (IC). The muon data were collected with energies of 120 GeV and 40 GeV with a scan of more than 16 positions to extract the calibration constants for the maximum number of channels. Many electron runs were taken with an energy range from 10 GeV to 100 GeV with 10 GeV steps. This data set was collected to check the calibration constants (Pedestal, MIP, Gain, and HG/LG inter-calibration), study the detector's electromagnetic performance, and tune the parameters of Monte Carlo (MC) simulation. The last data set was pions at an energy range from 10 GeV to 200 GeV with 10 GeV steps, which allowed us to study the hadronic response of the calorimeter. The event displays of muons, electrons, and pions are shown in Figure 6.4.

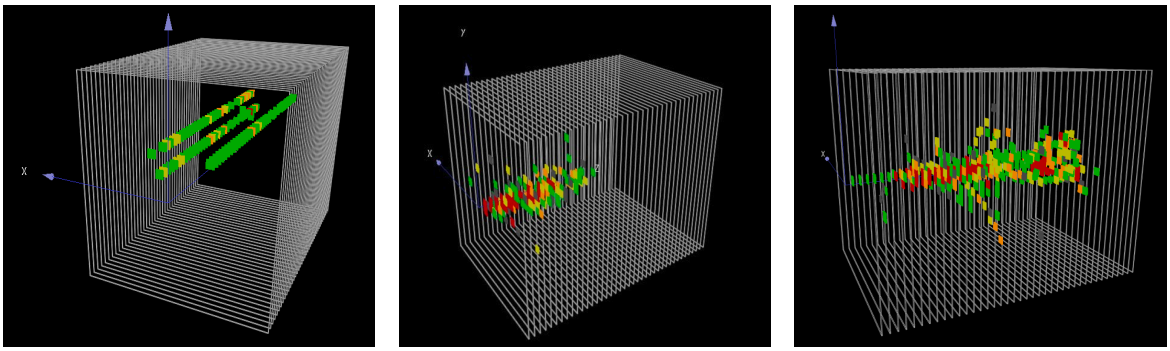

(a) (b) (c)

Figure 6.4: Event-display of the data taking during June SPS testbeam at CERN: a) three parallel muons crossing the detector, b) a contained electromagnetic shower, c) an extended hadronic shower with a visible first hadronic interaction around the 8th layer.

6.4 Event Selection

In the beamline H2, as explained in section 6.1, it is possible to provide a high beam rate of different particles for a wide energy range. In principle, a pre-selection is made in the beamline using the Cerenkov threshold-counter filled with Helium gas. The Cerenkov can provide a good selection efficiency of the momentum and particle type utilizing the difference between the set pressure and threshold pressure. However, contamination of unwanted particles can always exist due to wrong particle selection.

In this analysis, an event selection is essential to select either muons, electrons, or pions. Firstly, a selection of all signals above a threshold of 0.5 MIP is required to reject empty events that occur from random triggers. The muons generally travel through the whole detector without generating any shower, and the number of hits equals roughly to the layer number. Therefore, a pre-selection of muons is based on the number of hits and the center of gravity defined in Eq. 6.4. Additionally, a muon track selection is made by the track finding algorithm to reconstruct only the MIP-like particles for the MIP calibration. This algorithm identifies the muons which travel straight through the whole detector, by searching for consecutive hits in the z-direction and layer-wise with a maximal deviation in x and y directions and a minimum hits of 30 in each track. Besides, one hit per layer is required to reject double muon and pion contaminations. The electrons usually interact in the first layer by producing a dense shower in the first layers of the AHCAL. However, the pions can generate showers, but they often deposit a MIP-like track before their first hadronic interaction. In

extreme cases, the pion can look like an electron if the first hadronic interaction is happening in the first layer, or like a muon when no interaction occurs in the calorimeter.

The event selection of electrons is the essential aspect of this analysis, where the rejection of muons and pions contamination is necessary. Therefore, a Particle Identification (PID) algorithm is used to select the electron events and discard the contamination of other particles (see section 6.7.2).

6.5 Detector Calibration

In this section, the different procedures of the energy calibration discussed in section 4.3 are illustrated in detail. This calibration consists of extracting the following constants for each detector channel:

- Pedestal values
- Gain Calibration
- High Gain - Low Gain Inter-Calibration
- MIP Calibration

6.5.1 Pedestal Extraction

As explained in section 4.3.1, pedestal extraction is important for reliable energy calibration. The procedure of the pedestal extraction belongs to the work done by D. Heuchel and Y. Sudo [109]. For this analysis, the pedestal is extracted from muon runs, collected at the test beam campaign, by looking only to the channels without signal (flagged by HitBit=0). The pedestal distribution is shown in Figure 6.5 with a mean value of 555 ADC counts. Besides, a tail is visible on the right side of the pedestal distribution, which comes from pedestal jump in memory cells higher than 7. This pedestal jump to high ADC value is also observed during the chip testing in chapter 5 (section 5.5.7). Therefore, the pedestal of the memory cells higher than 7 corresponds to the average pedestal over the memory cells 0 to 7. The pedestals' intrinsic widths are shown in the right plot of Figure 6.5 with the mean intrinsic width of $\sim$6.4 ADC.

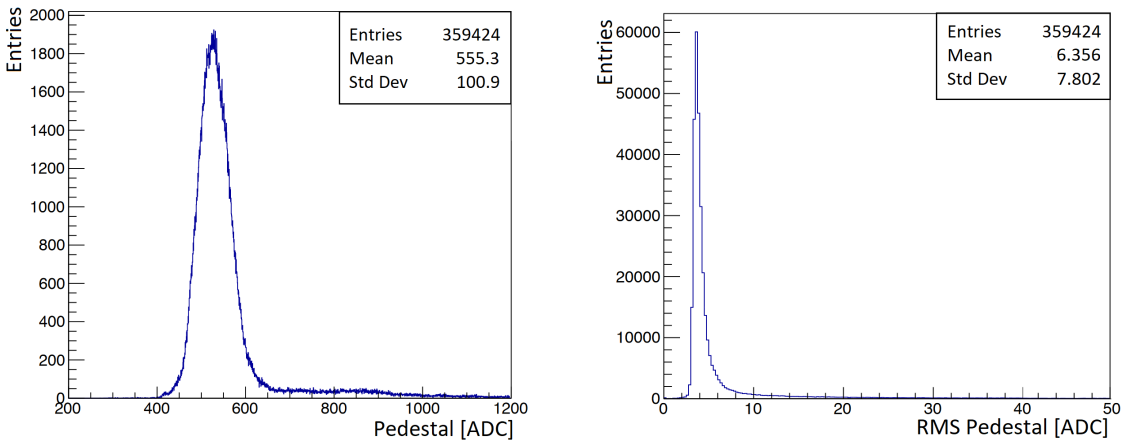

(a) (b)

Figure 6.5: a) Pedestal distribution in ADC extracted from muons runs. b) The distribution of the intrinsic width of the pedestal spectrum [109].

In the first phase, the pedestal is extracted only from the high gain mode, but a difference between high gain (HG) and low gain (HG) pedestals is observed. Therefore, a correction from HG to LG pedestal is essential. Figure 6.6 shows the HG and LG pedestals extraction method from collected data with Hitbit=0 (upper table) and Hitbit=1 (lower table) for different data-taking modes explained in section 4.2.2. In the ATAG mode, the chip reads out either the HG or the LG signal, but the pedestal can be extracted only for HG memory cells. For the ATIC, both HG and LG signals are read out, and the pedestal extraction is possible for both signals. In the ETIC, the trigger mode is external and used for the LED runs.

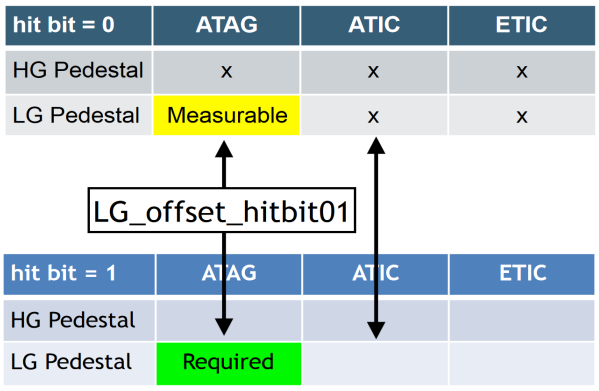

Figure 6.6: Sketch of the LG pedestal and LG offset calculation from data with Hitbit=0 to Hitbit=1 [109].

The HG to LG pedestal difference is corrected with the following equation:

$$Ped0_{(LG,ATAG)} = Ped0_{(HG\,,\,ATAG)} + \underbrace{Ped0_{(LG\,,\,ATIC)} - Ped0_{(HG\,,\,ATIC)}}_{HG\ to\ LG\ pedestal\ correction} \tag{6.1}$$

where $Ped0$ is the pedestal extracted from channels with Hitbit=0. Since the LG pedestal is not accessible in ATAG mode, a pedestal correction is obtained with the difference between HG and LG pedestals in the ATIC mode. Afterward, the MIP and pedestal spectra for HG and LG output are extracted separately in ATIC mode using muon data, as shown in Figures 6.7a and 6.7b. However, a MIP signal shift is seen in the LG output due to the LG pedestal shift from Hitbit 0 to 1. Therefore, a second correction of the LG pedestal offset is essential:

$$\begin{aligned}
Ped1_{(LG\,,\,ATAG)} &= Ped0_{(LG\,,\,ATAG)} + \underbrace{Ped_ofst_{(LG\,,\,Hitbit\,0\to1)}}_{LG\ pedestal\ offset\ from\ Hitbit\ 0\ to\ 1} \\
with: \quad Ped_ofst_{(LG\,,\,Hitbit\,0\to1)} &= Ped1_{(LG\,,\,ATIC)} - Ped0_{(LG\,,\,ATIC)} \\
with: \quad Ped1_{(LG\,,\,ATIC)} &= \underbrace{MIP_meas_{(LG\,,\,ATIC)}}_{measured\ LG\ MIP\ signal} - \underbrace{MIP_exp_{(LG\,,\,ATIC)}}_{expected\ LG\ MIP\ signal} \\
&= MIP_meas_{(LG\,,\,ATIC)} - MIP_{(HG\,,\,ATIC)}/IC
\end{aligned} \tag{6.2}$$

$Ped1_{(LG\,,\,ATAG)}$ is the LG pedestal extracted from Hitbit=1 in ATAG mode, and it is equal to the LG pedestal in Hitbit=0 ($Ped0_{(LG\,,\,ATAG)}$) with an offset correction from Hitbit $= 0 \to 1$ ($Ped\_ofst_{(LG\,,\,Hitbit\,0\to1)}$). This offset is the LG pedestal difference between Hitbit 0 and 1 in the ATIC mode. The $Ped1_{(LG\,,\,ATIC)}$ is measurable, whereas the $Ped1_{(LG\,,\,ATIC)}$ is calculated by the difference of the measured and the expected LG MIP signals. The expected LG MIP signal ($MIP\_exp_{(LG\,,\,ATIC)}$) is the HG MIP signal ($MIP_{HG\,,\,ATIC}$) divided by the IC factor extracted by the LED runs in ATIC mode. The corrected LG pedestal, shown in Figure 6.8, is done per channel and memory cell with a mean value of ∼515 ADC and a standard deviation of ∼33 ADC. Compared to the HG pedestal, the LG pedestal is smaller by ∼15 ADC counts with a variation of 5 ADC in memory cells within one channel, as shown in Figure 6.9a. While the variety from channel to channel within one chip is about 8.5 ADC, as shown in Figure 6.9b. Therefore, the LG pedestal variation is dominated by the chip to chip variation.

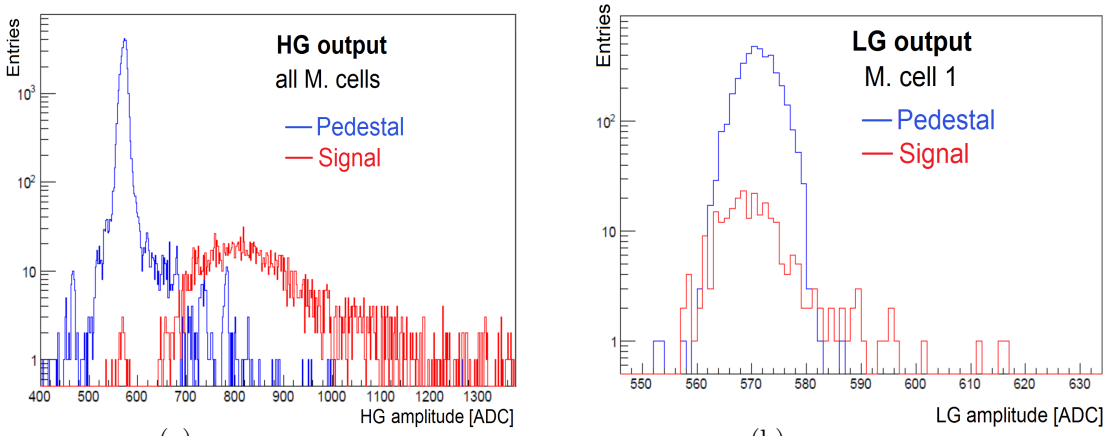

(a) (b)

Figure 6.7: a)MIP and Pedestal spectra extracted from the HG (a) and LG (b) outputs using muon data in ATIC mode [109].

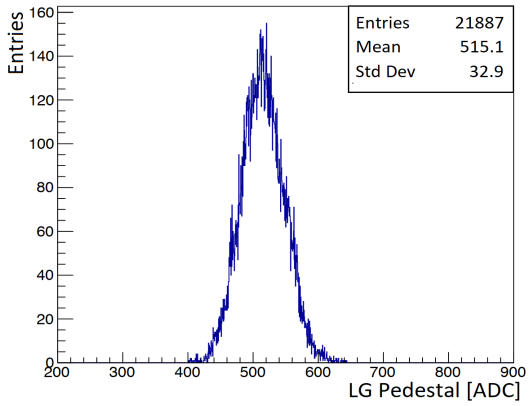

Figure 6.8: Distribution of the corrected LG pedestal in ADC counts, the mean is about 515 ADC with a standard deviation of 33 ADC which mainly comes from chip to chip variation [109].

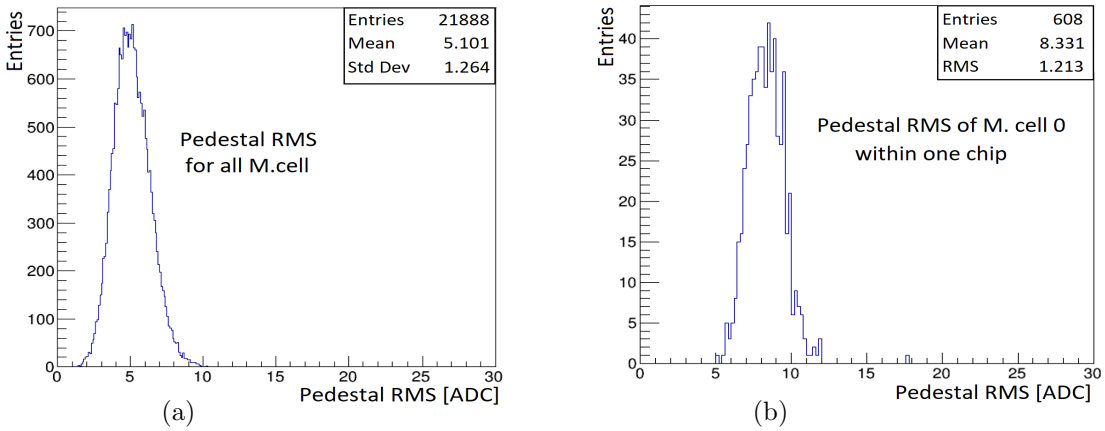

(a) (b)

Figure 6.9: Distribution of the pedestal RMS for all memory cells (a) and over all channels (b) within the chip. The standard deviation is ∼5 ADC from M.cell to M.cell variation and ∼8 ADC from channel to channel variation [109].

6.5.2 Gain Calibration

As explained in section 4.3.2, the gain calibration consists of converting the measured amplitude in ADC counts into the number of fired SiPM pixels. The SiPM gain is the charge produced for one fired pixel with ADC count units. As explained in section 4.2.1, the gain is measured using LED runs where light pulses with short and low amplitude illuminate the SiPMs. The results of the gain calibration are based on the work done by O. Pinto [110]. Figure 6.10 represents a single photon spectrum of one channel fitted with a multi-Gaussian function, and each peak corresponds to the number of photoelectrons in one SiPM. The gain corresponds to the distance between the means of two consecutive single-photon peaks, where the width of the fitted peaks does not increase with a higher number of fired pixels.

The LED runs are performed periodically during the whole test-beam campaign for checking the gain stability. The total number of calibrated channels is 22013 over 22032, while the remaining channels acquire the mean gain value of the corresponding chip. Figure 6.11 shows the gain distribution of all the channels with a Gaussian fit, where the mean value is $\sim$ 16.62 ADC with a standard deviation of $\sim$ 1.1 ADC that corresponds to the chip to chip variation. Besides, the gain is stable within the period of the test beam due to the temperature compensation. The latter consists of adjusting the bias voltage of the SiPMs according to temperature in the layers. A detailed explanation is illustrated in [111].

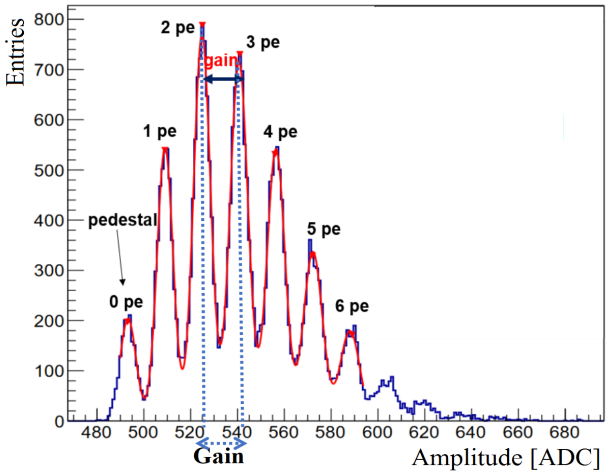

Figure 6.10: Single Photon Spectrum acquired with MPPC S13360-1325PE, read out by a SPIROC2E ASICs. The first peak corresponds to the pedestal, the other peaks correspond to the number of photoelectrons in one SiPM. The spectrum is fitted with multi-Gaussian function and the gain corresponds to the mean distance between two consecutive peaks [110].

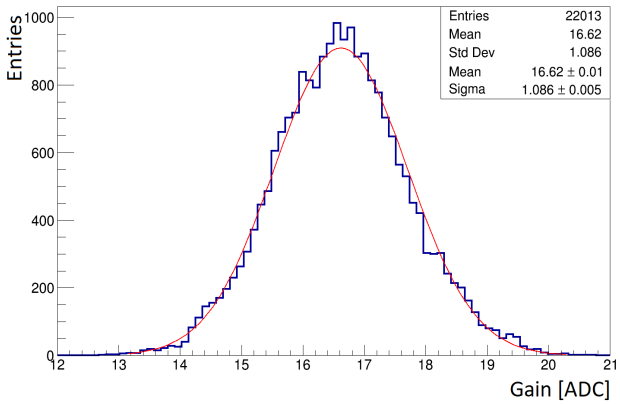

Figure 6.11: Gain distribution in ADC counts for all the channels, the gain is the charge produced for one fired pixel extracted from the LED runs [110].

6.5.3 High Gain and Low Gain Inter-Calibration

As explained in section 4.2.2, the input signal splits into HG and LG pre-amplifiers, which correspond to low and high amplitudes. Depending on the gain threshold, only one signal is digitized. The LG signal supposes to have a fixed ratio of 1:10, but it fluctuates slightly due to variations in the amplifier feedbacks capacities produced by the production process. Therefore, a high gain - low gain inter-calibration is calculated per channel in the ETIC mode where both signals are read out.

The extraction of the HG-LG inter-calibration factor is done by Y. Sudo [111]. This study uses the LED runs with a calibration voltage from 5000 mV to 7000 mV in steps of 20 mV. As shown in Figure 6.12, for each channel, the amplitudes in ADC counts of HG signal versus the LG signal is plotted, and each point corresponds to one calibration voltage. The IC factor for each channel is calculated in the linear region with two different methods. In the first method, as shown in Eq 6.3, the IC factor is the difference of HG amplitude for two LED voltages divided by the difference of LG signal. In the second method, the IC factor corresponds to the slope of the linear region fitted from 30 ADC to 100 ADC counts.

$$IC = \frac{Signal_{HG}}{Signal_{LG}} = \frac{HG_{i+1}[ADC] - HG_i[ADC]}{LG_{i+1}[ADC] - LG_i[ADC]} \tag{6.3}$$

where the HG_i and LG_i correspond to high gain and low gain signals for a specific LED voltage i. Figures 6.13a and 6.13b represents the distribution of the IC factor extracted from both methods. The mean IC factor is ∼19.4, with a standard deviation of ∼0.66 that comes from channel to channel variation. The IC factor is extracted for ∼80% of channels, and the

mean IC factor over all channels is used for the remaining channels.

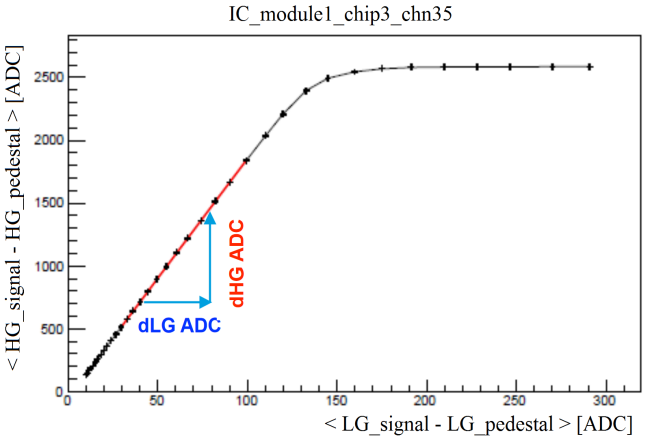

Figure 6.12: The mean amplitude of HG signal vs LG signal after the pedestal subtraction for one channel. Each point corresponds to one LED voltage [111].

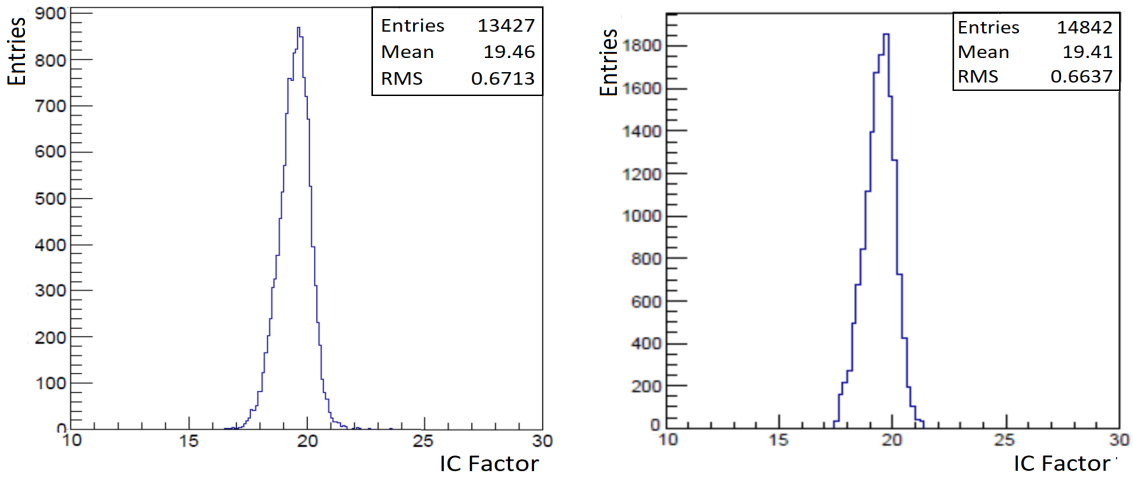

(a) (b)

Figure 6.13: Distribution of the HG - LG inter-calibration factor calculated by the first method (a) and by the slope of the linear region fitted from 30 ADC to 100 ADC (b) [111].

Additionally, the IC factors' reliability is checked with electron data by inspecting the hit energy distributions for HG and LG signals. In principle, after applying the extracted IC factors to all the channels, the HG and LG spectra has to be connected smoothly in the intersection region. Figure 6.14 shows the hit energy distribution of HG and LG and the total amplitudes. The left plot represents the hit energy deposited in the whole detector, and the right plot corresponds to layer 2. As expected, the total hit energy for both levels shows a smooth transition between HG and LG spectra.

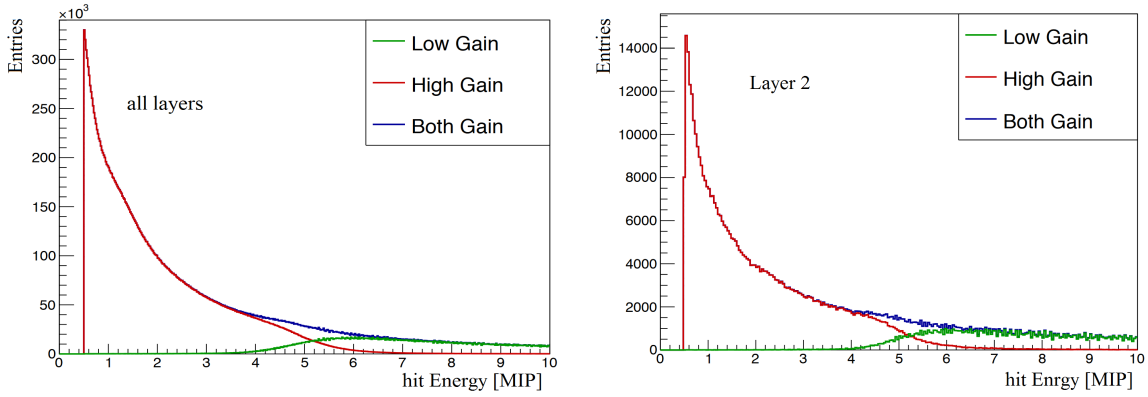

(a) (b)

Figure 6.14: Hit energy distribution of electron data for LG (green), HG (red) and the total (blue) deposited in the whole detector (a) and in layer 2 (b) [109].

6.5.4 MIP Calibration

As explained in section 4.3, the amplitude measured by the AHCAL readout system is normalized to physical energy in the MIP scale. The MIP calibration factor corresponds to the most probable value of the signal deposited by the Minimum Ionizing Particles (MIPs) in a single channel. Therefore, the calorimeter's response is calibrated using 40 GeV muons with high statistics. Before extracting the MIP factor of each channel, an offline cut at 0.5 MIP is applied during the energy reconstruction for the noise rejection. The MIP calibration study belongs to the work of D. Heuchel [109].

As explained in section 6.4, the extraction of the MIP factor consists of selecting the muon using a track selection procedure with a rejection of pion contamination. After the pedestal subtraction, the distribution of muons amplitude in ADC counts is fitted by the convolution of a Landau and Gaussian function. The MIP calibration factor is given by the most probable value of the fit. Figure 6.15a shows the distribution of the MIP factor of all the calibrated channels with a mean of 218 ADC and a standard deviation of 31 ADC. Around 99,9 % of the channels are calibrated with muons scan data over 16 positions in the detector face. The MIP uniformity of the whole AHCAL (MIP_{mean}/MIP_{RMS}) is $\approx$ 14%. The MIP variation from channel to channel is shown in Figure 6.15b with a standard deviation of 18.4 ADC. The MIP uniformity within a chip ($MIP_{mean}/MIP_{RMS(within\,a\,chip)}$) is $\approx$ 8.1%, while it is $\approx$ 14% from chip to chip variation.

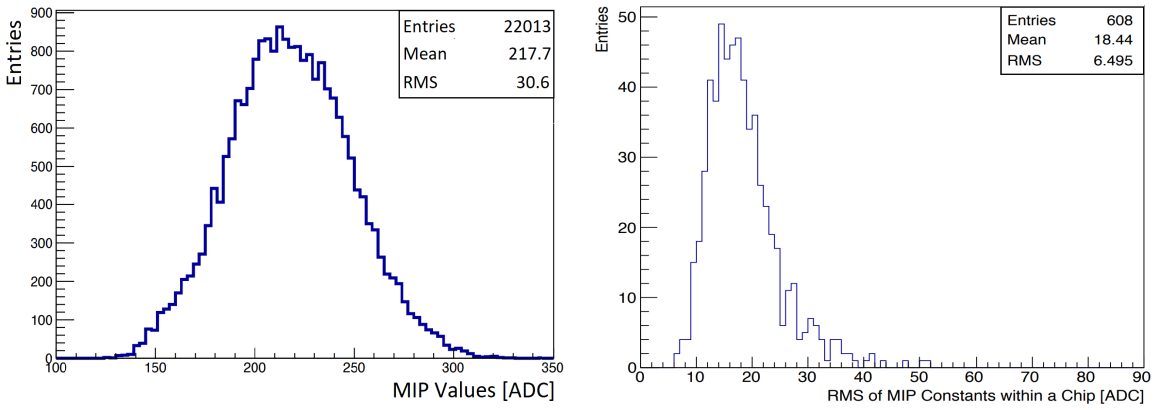

(a) (b)

Figure 6.15: a) The MIP factor distribution of all the channels with a mean value of $\sim$ 218 ADC. b) The standard deviation distribution within one chip is $\sim$18.4 ADC [109].

The hit energy is calibrated to the MIP units using the equation 4.6 after extracting all the calibration constants. Figure 6.16a shows the hit energy spectra with the most probable value of the fit peaks at 1 MIP. The reliability of the MIP calibration factor for all channels is seen in Figure 6.16b, where the distribution of the MPV is narrow and peaks at 1 MIP.

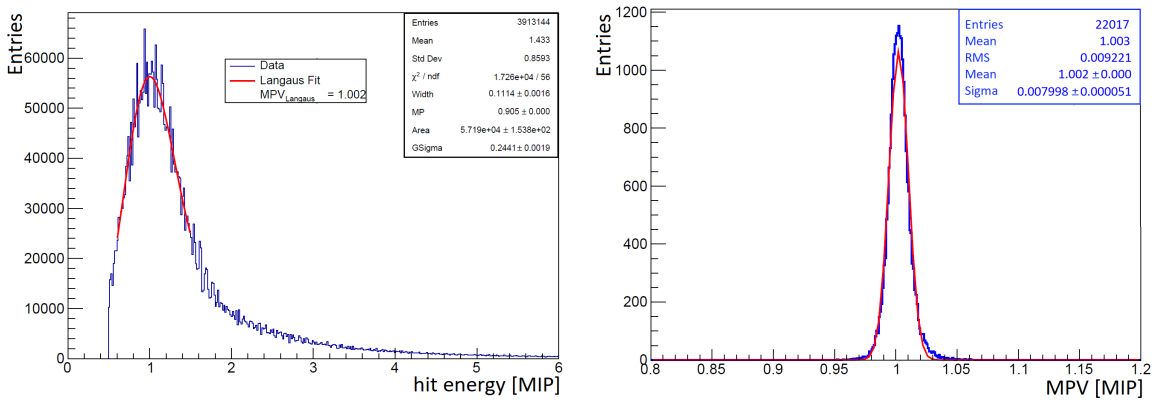

(a) (b)

Figure 6.16: a) The hit energy distribution of muon data after the MIP calibration, fitted with Landau convolution Gaussian function and the MPV is $\sim$1 MIP. b) The MPV distribution over all the channels with a Gaussian fit function, the mean of the fit is $\sim$1 MIP [109].

6.6 Simulation

The AHCAL detector is simulated with the Detector Description Toolkit for High Energy Physics Experiments (DD4Hep[1]) [112]. This toolkit implements a modular and flexible approach to the simulation activities using GEANT4[2] [113]. DD4hep is a software framework that provides a full description of the detector (geometry, materials, visualization, readout, alignment, calibration, etc.).

6.6.1 Simulation Setup

As shown previously in Figure 6.3, the H2 beamline is very complex, and it is not easy to implement all these elements in the simulation. Figure 6.17 shows the simulation setup of our beamline in DD4hep geometry, which contains three scintillators and the Cerenkov counter. The AHCAL is located in the reference of the beamline at 0 m, and the three trigger scintillators, with the dimensions of $10 \times 10\ cm^2$, $10 \times 10\ cm^2$ and $50 \times 50\ cm^2$, are placed right before the detector. The Cerenkov detector is filled with Helium gas with a density of $0.0001663\ g/m^3$ and positioned at - 40 m. The rest of the components is simulated by placing an upstream material at - 47 m from the AHCAL. The tuning of the beamline is done to define the thickness of the upstream material, as discussed in the next sub-section.

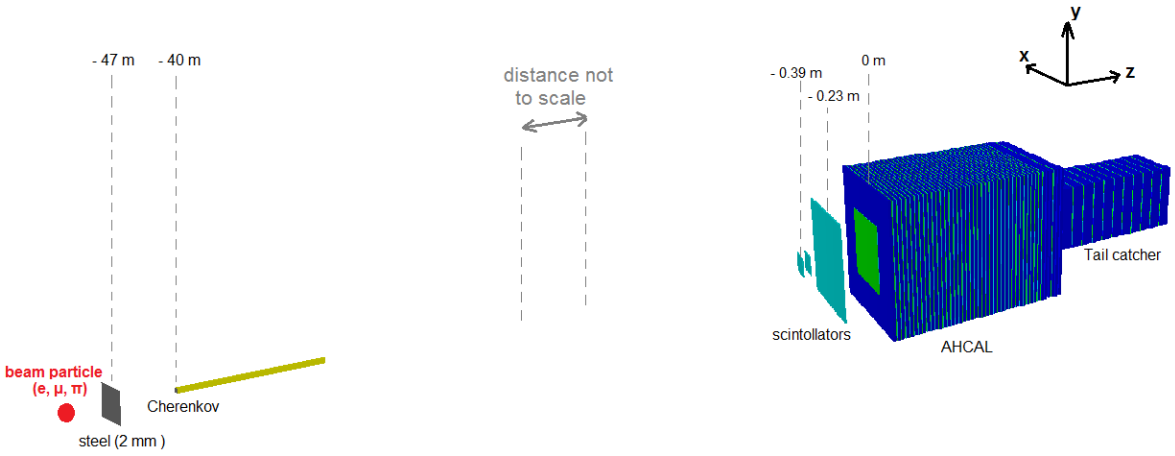

Figure 6.17: Sketch of the simulated beamline. The dimensions are not to scale. Positions: AHCAL at 0 m, beam particles at - 50 m and the additional steel material at - 47 m.

[1] DD4hep version used for this simulation: v01-10
[2] GEANT4 version used is v-10-03

6.6.2 Beam Line Tuning

The upstream material, used to cover the missing beamline elements, is simulated, and its thickness is tuned by looking at the center of gravity of the shower in the beam direction Z. The center of gravity (cog_Z) is defined as follows:

$$cog\_Z = \frac{\sum_i E_i x_i}{\sum_i E_i} \tag{6.4}$$

where E_i and x_i are the deposited energy and the position of each hit, respectively. The sum is over the number of hits in each event. For 60 GeV electrons, the comparison of the center of gravity in the beam axis direction Z for data and simulation is shown in Figure 6.18 with no upstream material in the beamline. Due to the missing elements in the beamline, a slightly late showering in the simulation compared to data is observed.

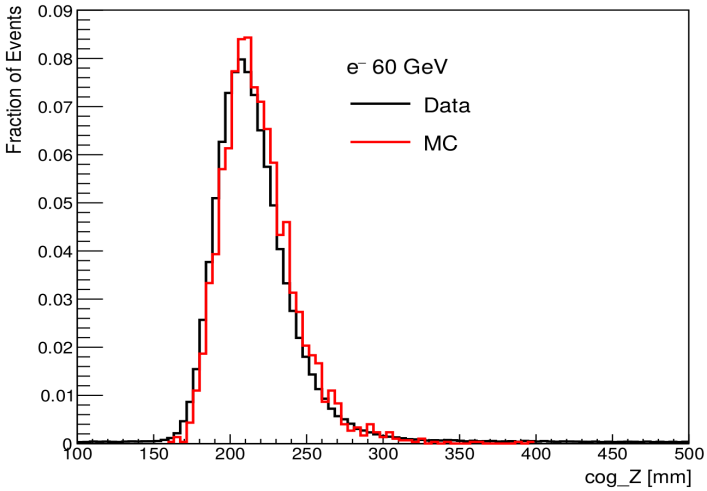

Figure 6.18: Center of gravity distribution in Z direction of 60 GeV electrons for data (black) and simulation (red).

As shown in Figure 6.19, the beamline is simulated with various thicknesses of a steel plate. Comparing the cog_Z of data with simulation, 2 mm seems to be the optimal thickness. However, it is essential to check the independency of the upstream material's thickness for the beam energy. Therefore, a comparison of the center of gravity in Z is made for electrons 30 GeV, 40 GeV, and 90 GeV, as shown in Figure 6.20, and no thickness dependence to the beam energies is seen.

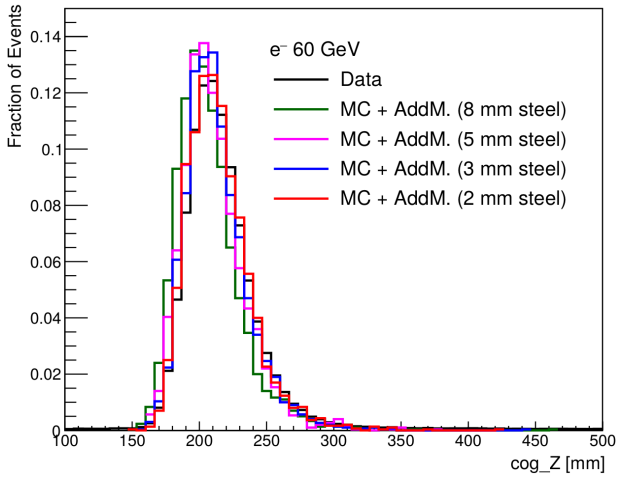

Figure 6.19: Center of gravity distribution in the Z direction for 60 GeV electrons. Data in black and simulation are in various colors for different thicknesses of upstream material.

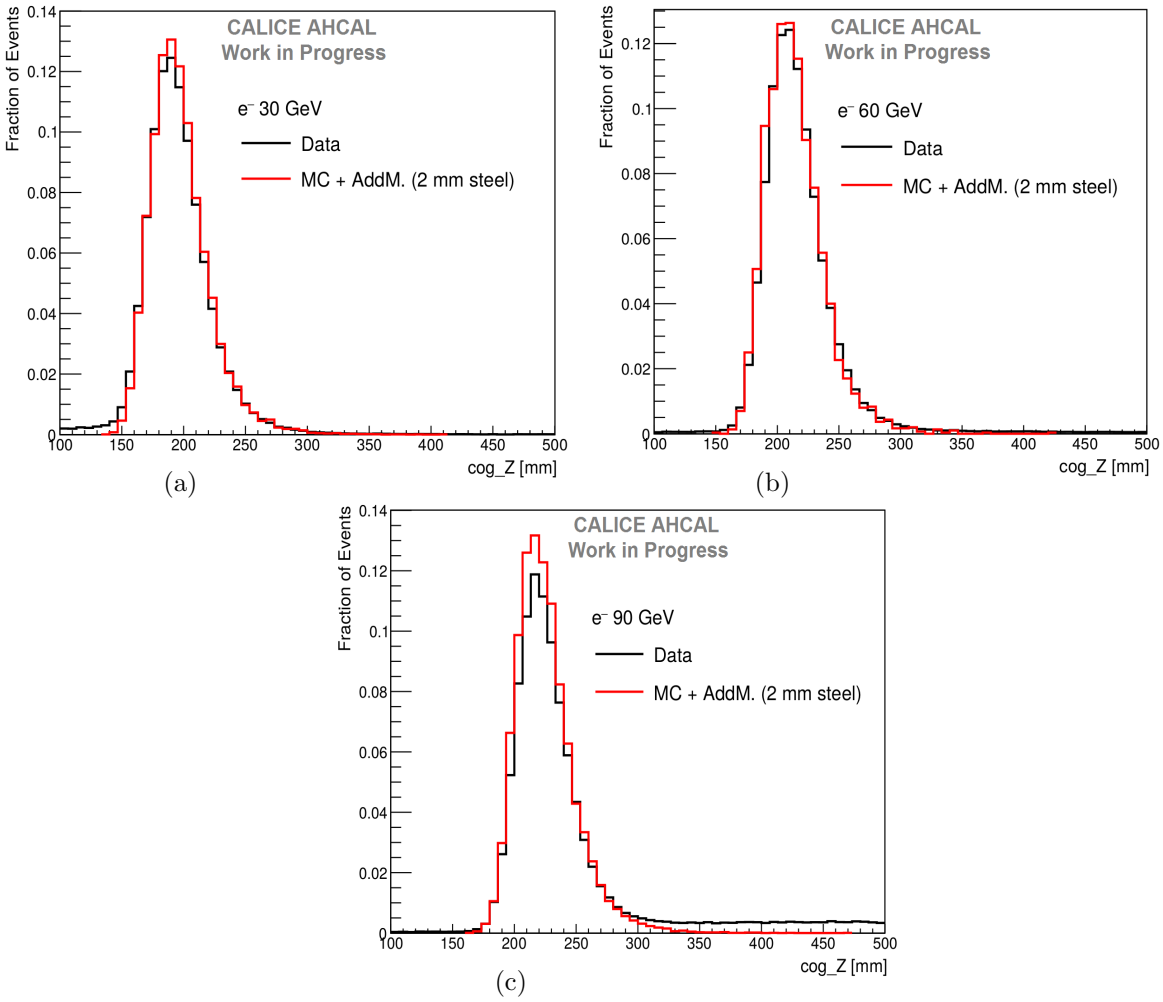

Figure 6.20: Center of gravity distribution in the Z direction for 30 GeV (a), 60 GeV (b) and 90 GeV electrons. Data in black and simulation in red.

6.6.3 Geometry Implementation

6.6.3.1 Gap between the slabs

As described in section 4.2.1, each AHCAL layer consists of two slabs with a gap in between produced by flex-lead connectors. This gap is measured for all the layers using the wire chambers located in the beamline and implemented in the AHCAL simulation model. As shown in Figure 6.21a, the measured gap varies from 1 to 4 mm [114]. The 3D display of the simulated detector is shown in Figure 6.21b, where the implemented gap is scaled by 20 for better visualization.

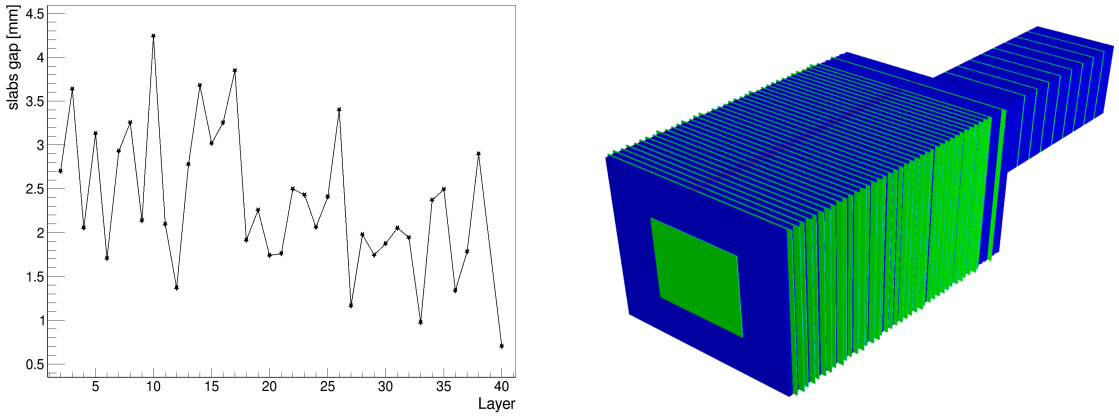

(a) (b)

Figure 6.21: a) The slabs' gap is measured per layer using wire chambers [114]. b) 3D display of the AHCAL detector model with the implemented gap between slabs. The green color represents the active layer, and the gap is scaled by 20 for better visualization.

The gap implementation in the detector geometry is cross-checked by illuminating the detector with 50 GeV electrons in two positions. The first beam position is very close to the gap's area, whereas the second one is far from it. A significant effect of the gap on the total number of hits and the total deposited energy is visible, as shown in Figure 6.22. When the beam position is in the gap, the total number of hits decreases, and a tail appears in the left of the energy sum distribution.

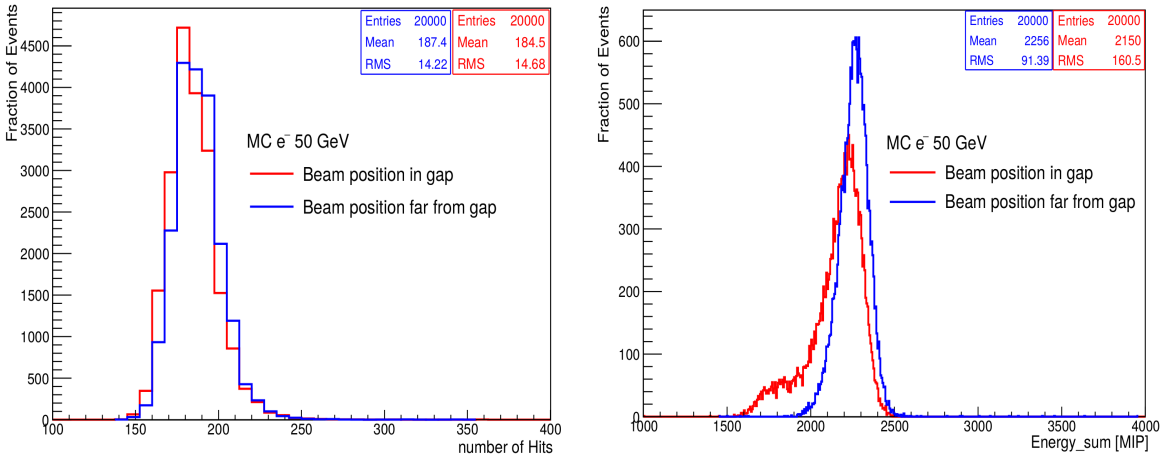

(a) (b)

Figure 6.22: The distributions of hits (a) and energy sum (b) for two-beam positions, red: beam close to the gap space, blue: beam far away from the gap.

6.6.3.2 Layers offset in X and Y

The offset position of each detector layer in x and y coordinates is calculated with the wire chambers. As shown in Figures 6.23a and 6.23b, an offset in x and y directions is observed for all layers. From the variation of these offsets, a slight inclination of the detector is visible in both directions. Figure 6.24 shows the 2D projection of the AHCAL in x and y plans after the implementation of the offsets. In this projection, the offsets of x and y are scaled by 30 for clear visualization. Finally, a good agreement of the center of gravity's distribution in x and y directions is seen between MC and data for 80 GeV electrons, as shown in Figure 6.25.

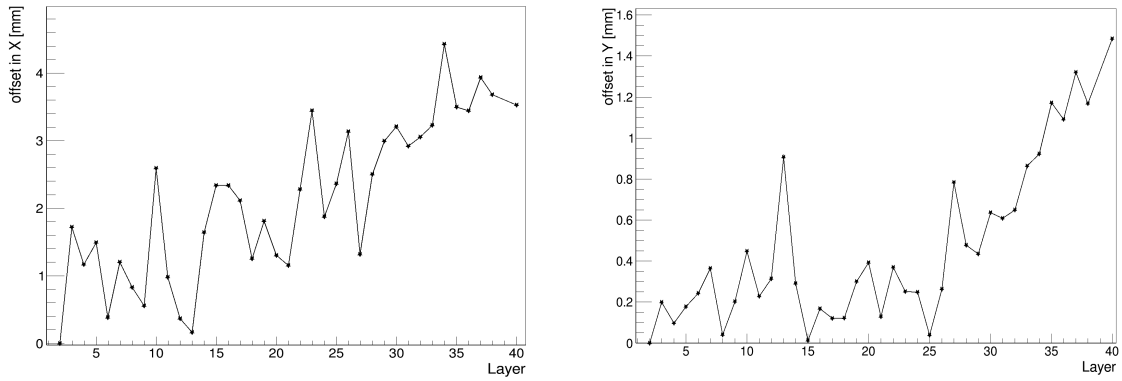

(a) (b)

Figure 6.23: The offset position of all the detector layer in x (a) and y (b) directions. They are calculated with the wire chambers placed in the beamline [114].

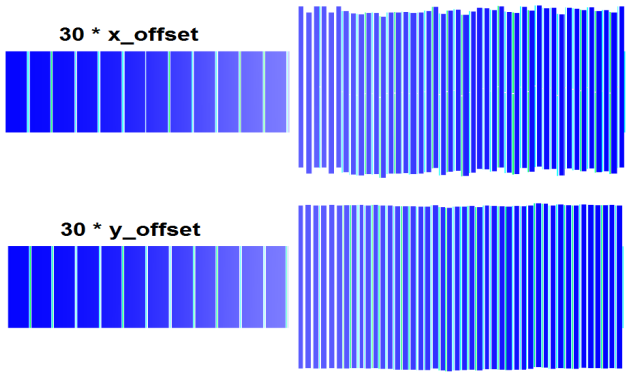

Figure 6.24: Display of the AHCAL model in 2D projection with the implementation of the layers offsets in x and y directions. The offsets are scaled by 30 for better visualization.

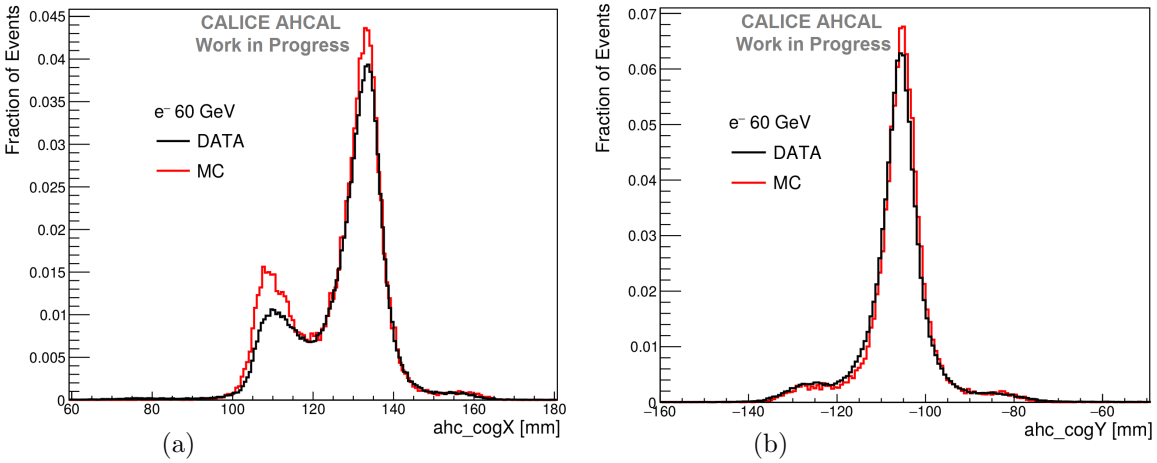

Figure 6.25: Center of gravity distribution in x (a) and y (b) directions for DATA and MC for 60 GeV electrons.

6.6.3.3 Ganging Processor for Tokyo Layer

As illustrated in section 4.2, the segmentation of the Tokyo layer differs from the other layers of the AHCAL. In the detector geometry description, a ganging of cells for the Tokyo layer is essential due to the limitation of the segmentation readout in DD4hep. Therefore, a ganging MARLIN [115] processor is developed and implemented in the digitization stage of simulation. The purpose of this processor is ganging four cells of size $3 \times 3\ cm^2$ into one cell of $6 \times 6\ cm^2$. Each cell is uniquely identified by the three indices I (row of a cell), J (column of a cell), and K (layer of a cell). The ganging of I and J is calculated as follows:

$$I_{ganged} = Int\left(\frac{I_i - offset}{div_{size}}\right) + offset \qquad J_{ganged} = Int\left(\frac{J_i - offset}{div_{size}}\right) + offset \quad (6.5)$$

where Int is the integer part of the division, the offset is 1, which corresponds to the cell's starting point. div_{dize} is the ratio of the new ganged size (6 cm) by the real cell size (3 cm) ($\frac{ganged_{size}}{cell_{size}}$). Figure 6.26 shows a sketch of the ganging process, where the energy and time of the ganged cell correspond to the energy sum and the shortest time of the four cells.

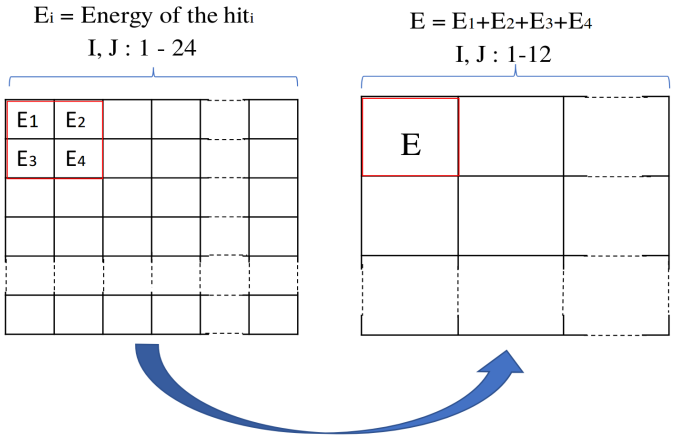

Figure 6.26: Sketch of ganging processor, every four cells are ganged to one cell. The energy and the time of the ganged cell is the energy sum and the shortest time over the four cells.

The ganging processor's reliability is checked by illuminating the whole detector with a rectangular beam profile to have enough statistics in all the tiles. Figure 6.27 shows a 2D profile histogram of the energy deposited in each cell in I and J indices for all detector layers in the left and Tokyo layer in the right, where a correct ganging of the I and J and energy is seen.

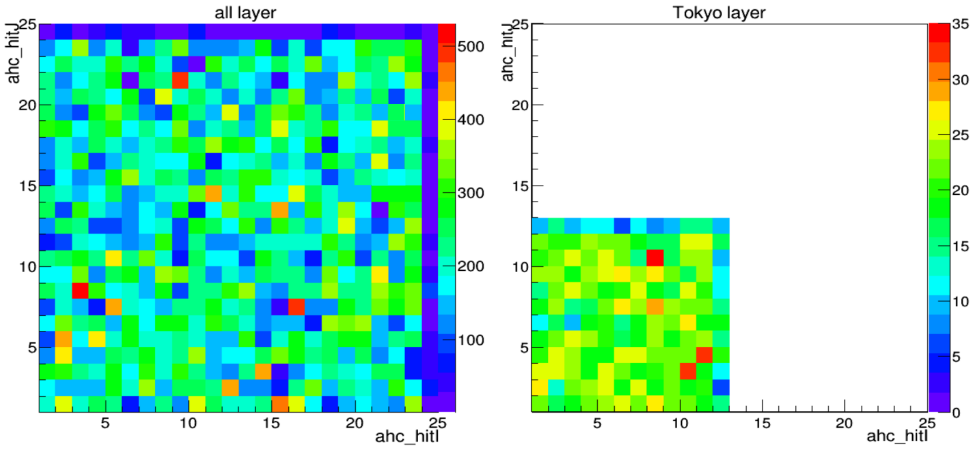

Figure 6.27: Mean energy deposited in I and J indices for all detector layers (left) and Tokyo layer (right).

6.7 Analysis of electron data

This analysis consists of measuring the electromagnetic response of the AHCAL to electron runs between 10 to 100 GeV with 10 GeV steps. All the electron runs are simulated with the same profile and statistics. Comparing the electromagnetic response of the AHCAL prototype between data and simulation is essential to check the detector calibration and accurize its simulation description. Therefore, a selection of single-electron events is vital, with a rejection of muons and hadrons contamination. The list of electron runs and the beam profile of simulated data used for this analysis is given in Appendix Table 3. The reconstructed energy spectra of 10 to 100 GeV electrons for data and simulation are shown in Figure 6.28.

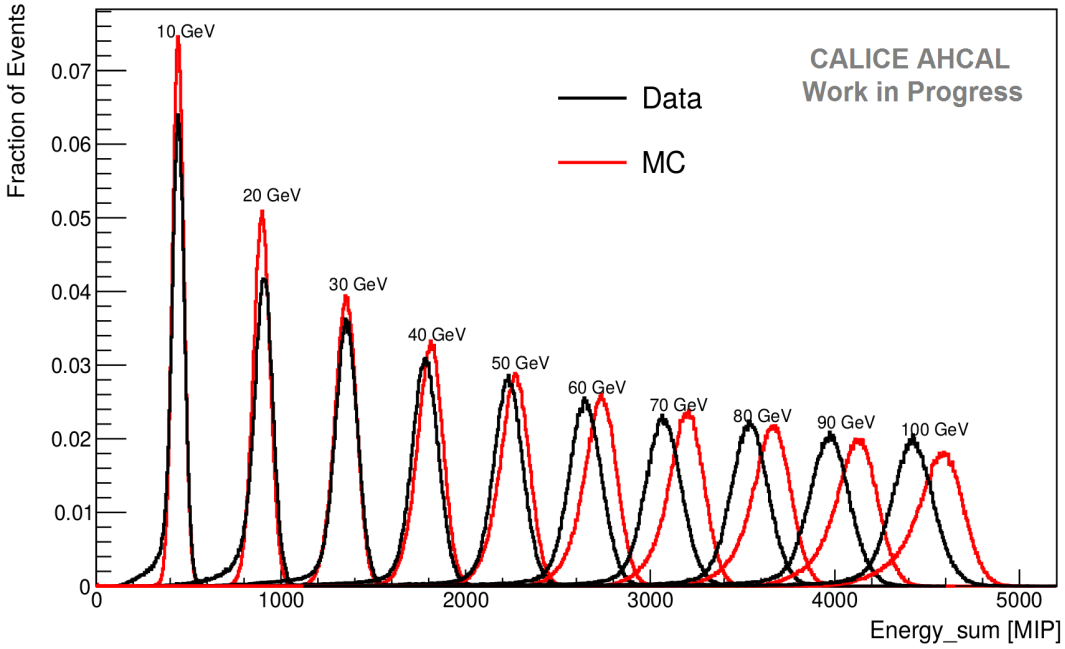

Figure 6.28: The distribution of the energy deposited in the whole detector for all beam energies, data in black and simulation in red.

6.7.1 SiPM Saturation

As explained in section 4.1.1, the response of the silicon photomultiplier is not linear for a high number of incident photons due to its finite number of pixels. During the data reconstruction, a saturation correction function is applied to the measured hit energy. The saturation correction function [116] is defined as follows:

$$A_i^{unsat}[pixels] = -N_{eff} \cdot ln\left(1 - \frac{A_i^{sat}[pixels]}{N_{eff}}\right) \tag{6.6}$$

where A_i^{unsat} and A_i^{sat} represent the unsaturated and saturated amplitude in pixels for channel i, and N_{eff} is the number of effective pixels. Before applying the saturation correction, the measured amplitude in ADC is divided by the gain to represent it in pixel numbers. The saturated amplitude is corrected using the Eq. 6.6 and then calibrated to the energy in MIP. These steps are done in the reconstruction as follows:

- $A_i[ADC]$: The measured amplitude in channel i.
- $A_i^{sat}[pixels] = A_i[ADC]/gain$: Amplitude conversion from ADC to pixels number.
- $A_i^{unsat}[pixels] = f_{sat}^{-1}(A_i^{sat}[pixels])$: Saturation correction f_{sat} applied to the amplitude
- $Energy = (A_i^{unsat}[pixels] \cdot gain)/A_i^{MIP}$: Energy calibration to MIP unit.

The response of the SIPM (MPPC S13360-1328 PE) is measured at the University of Mainz using laser light, and a simple exponential response function Eq. 4.5 is used for modeling the SiPM saturation. The result of this measurement is shown in Figure 6.29, where the calculated number of effective pixels N_{eff} of 2553 is 10% less than the nominal number of pixels 2668.

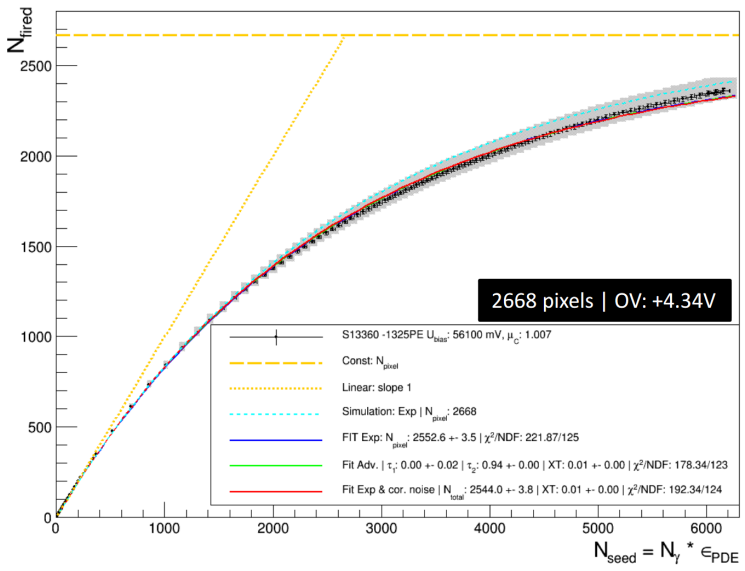

Figure 6.29: Measurement of SiPM response for MPPC S13360-1325PE at Mainz University using laser beam with uniform intensity. The nominal number of pixels is 2668 [117].

In the first step of our analysis, the saturation correction of the energy is done with the N_{eff} of 2553. The hit energy distributions for data and MC for 40 GeV and 80 GeV are

shown in Figures 6.30a and 6.30b. A large tail at higher hit energy can be seen in data for 80 GeV electrons, representing the under-saturation of the high energy hits due to the lower number of effective pixels. Since our understanding of the SiPM saturation is limited, further study is essential to define the optimal number of effective pixels. Therefore, a saturation correction is applied to the reconstructed data with a different number of effective pixels, and the hit energy distribution is compared to MC, as shown in Figure 6.31. The form in the hit energy distribution for data depends strongly on the N_{eff}, where the large tail appears only for a low number of effective pixels. For N_{eff} 2668 pixels, the upper edge of the hit energy is nearly equal for data and simulation, while the shape is still different for hits with high energy. However, for N_{eff} of 2778 pixels, the hit energy high edge is much lower than MC, due to the over-saturation correction in data.

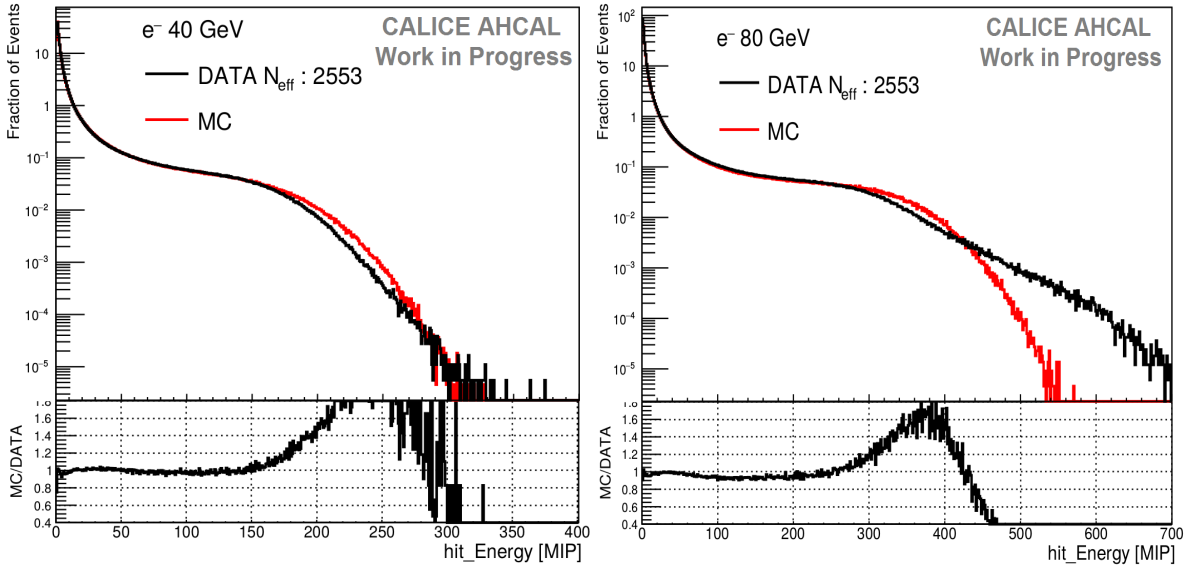

(a) (b)

Figure 6.30: Hit energy distribution for data and simulation for 40 GeV (a) and 80 GeV (b) electrons. The number of effective pixels used in the saturation correction is 2553.

A more detailed study is done by O. Pinto [110] to understand the saturation correction of the SiPM. For this study, the saturation function is applied to the MC in the digitization for two numbers of effective pixels 2553 and 2668, while no saturation correction is applied to data and MC. Afterward, a tiny tower of $1 \times 1\ cm^2$ is selected within one tile and through the detector. Figure 6.32 shows the hit energy distribution deposited within the selected tour for layers 6, 7, 8, and 9. By comparing layers 6 and 9, an agreement in the upper edge of the hit energy distribution between DATA and MC for N_{eff} 2553 can be seen. However,

for layers 7 and 8, the DATA agrees with MC when the saturation function uses the N_{eff} 2668. In conclusion, the SiPM saturation variates from SiPM to SiPM, making the saturation correction difficult since a fixed number of effective pixels is used for all detector channels. Theoretically, an individual study of the saturation for each SiPM can be an option. However, it is not possible due to the lack of statistics of all the channels.

Before choosing the number of effective pixels used for the saturation correction, a global study of the SiPM saturation for three different values of N_{eff} is essential. Figure 6.33a shows the reconstructed energy as a function of beam momentum for MC with data, where a various number of effective pixels 2500, 2668, and 2778 are used in the saturation correction in data. The reconstructed energy E_{reco} is the mean of the Gaussian fit function in the central region of the energy sum within a range of $\pm 2\ \sigma$. Higher energy deposition in MC comparing to data can be seen. The ratio plot in Figure 6.33b shows a better agreement of data with simulation while using the N_{eff} pixels of 2500. In the same way, the energy resolution of data, defined by the width over the mean of the Gaussian fit within a range of $\pm 2\ \sigma$, is compared to MC. Figure 6.34a shows the resolution plots for all cases, where the energy resolution improves for a higher number of effective pixels. However, for N_{eff} of 2500, the resolution gets worse at high energies. From the ratio plot in Figure 6.34b, a better agreement of DATA and MC with 2668 and 2778 can be seen.

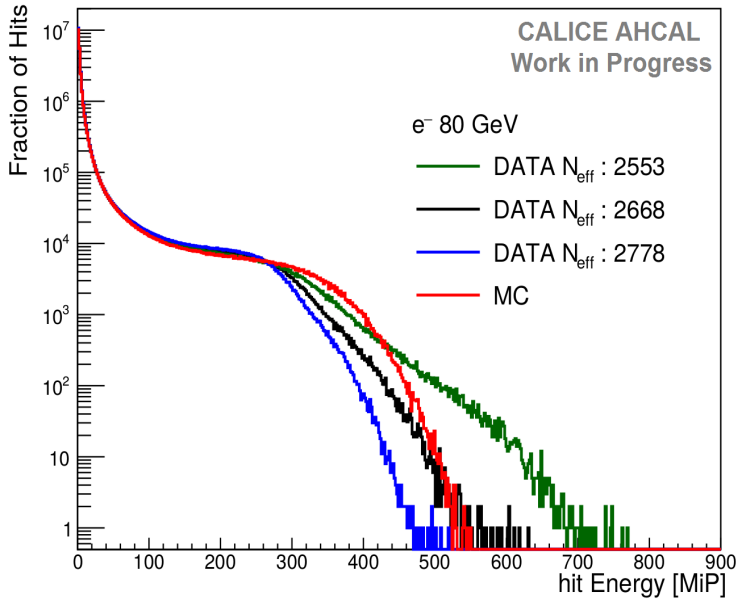

Figure 6.31: Hit energy distribution of MC (red) and DATA with saturation correction using different numbers of effective pixels: 2553 (green), 2668 (black) and 2778 (blue).

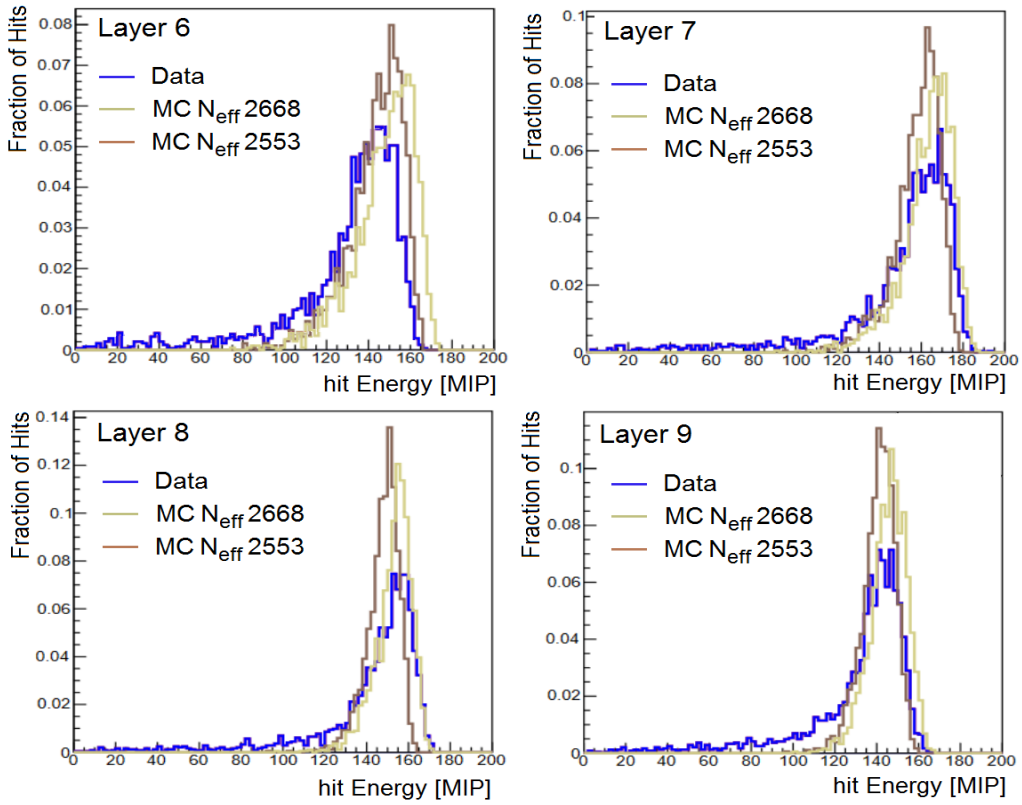

Figure 6.32: Hit energy distribution of data and MC deposited in a tower of $1\,cm^2$ through layers 6, 7, 8 and 9. A saturation function for different N_{eff} 2553 and 2668 is applied in MC digitization, but no saturation correction is used in the reconstruction of data and simulation [110].

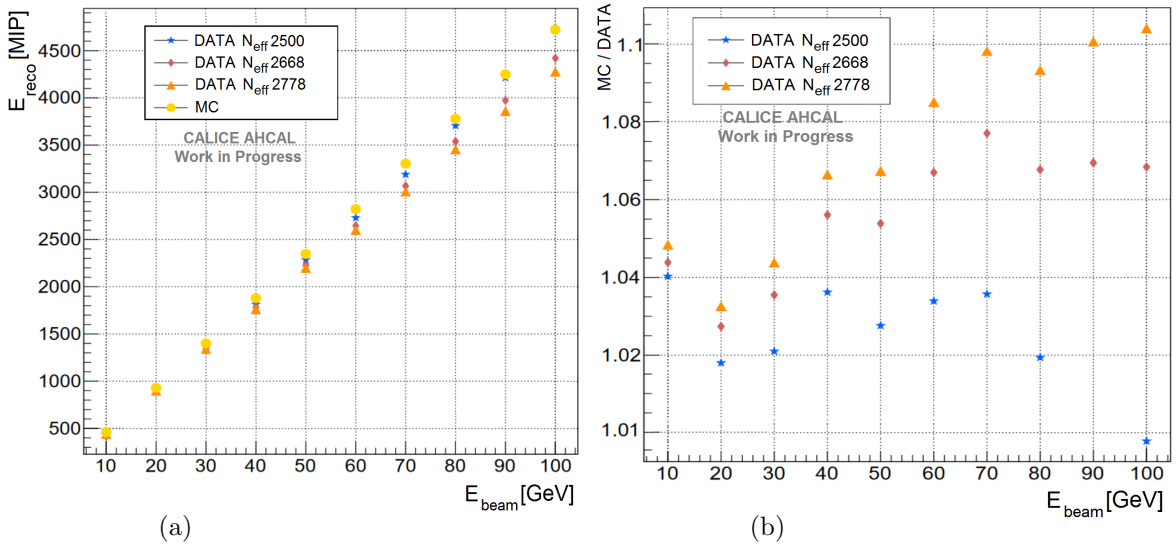

Figure 6.33: a) The reconstructed energy as a function of the beam energy for MC and data with a saturation correction using different numbers of effective pixels. b) Ratio plot of MC and DATA for different N_{eff} [110].

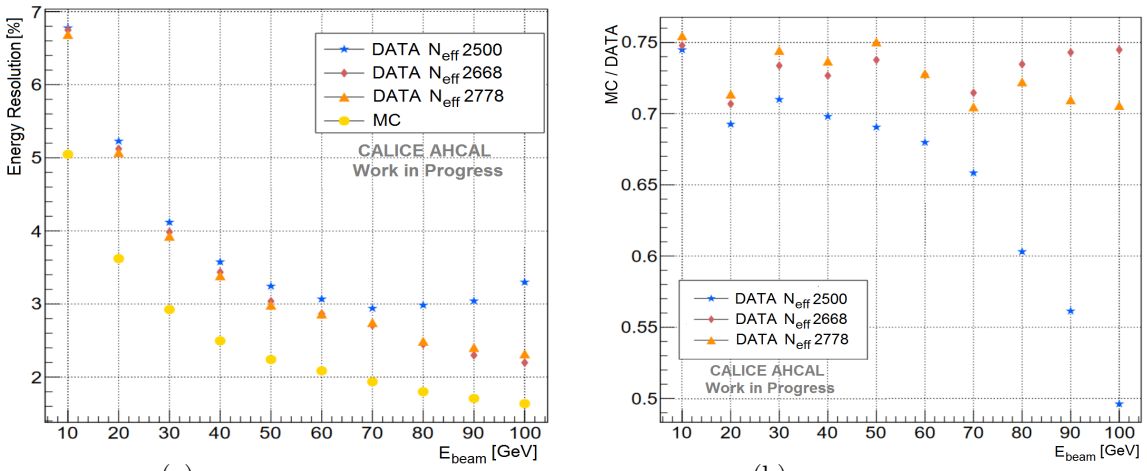

(a) (b)

Figure 6.34: a) Energy resolution comparison of MC and data with the saturation correction using different N_{eff}. b) Ratio plot of MC and DATA [110].

After all these studies, our knowledge of SiPM saturation is still limited; therefore, it is included in the systematic uncertainties. Figure 6.35 shows the MIP factor as a function of the upper edge of the hit energy in pixels, where each MIP factor corresponds to one channel. With the available statistics, only the upper hit edge of five channels per layer is extracted, which variates by 100 pixels. This variation is used to calculate the systematic uncertainties of SiPMs saturation. For this analysis, in the digitization of simulated data, the saturation function is applied using random Gaussian smearing of N_{eff} 2668 within $\pm$100 pixels to be consistent with the variation of the SiPM saturation in data. However, the reconstruction of data and MC uses a fixed N_{eff} 2668 in the saturation correction for all channels.

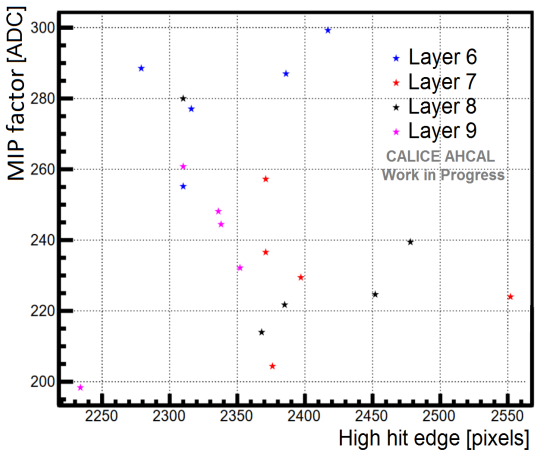

Figure 6.35: MIP factor in ADC counts as a function of the high hit edge (upper edge of the hit energy) deposited in $1 \times 1\ cm^2$ in pixels unit for layers 6, 7, 8 and 9 [110].

6.7.2 Event Selection

6.7.2.1 Selection of electrons events

The event selection consists of extracting a single electron shower contained in the AHCAL, providing a reliable comparison of the electromagnetic detector response between data and simulation. A pre-selection for electrons is done in the beamline using the Cerenkov detector, where only the particles that generate a signal above the threshold are selected. However, contamination from other particles can always exist. Figure 6.36 shows the number of hits versus the center of gravity of the shower along the beam axis z for 60 GeV electrons, where the contamination of muons and hadrons can be seen. In principle, the showers of electrons have a low depth in the calorimeter with a relatively narrow hits distribution, while the hadrons are characterized by a large number of hits and a deep showers along the beam axis. The muon events appear as a narrow band in half depth of the detector with hits number roughly equal to the number of layers.

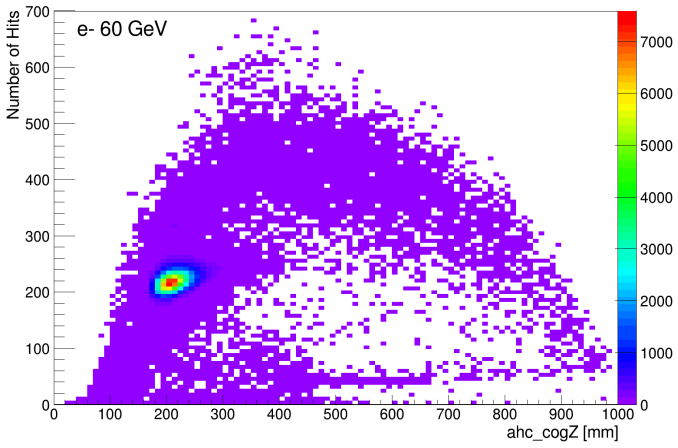

Figure 6.36: Number of hits versus center of gravity in beam line axis z for 60 GeV electrons.

In this analysis, the selection of desired particles is performed with a particle identification (ParticleID) algorithm [118], which provides a classification and selection of the particles with an efficient event filtering. This algorithm is implemented in the CALICE software as a MARLIN processor and uses several hits and events observables listed as follows:

- Number of hits
- Shower radius
- cog_Z
- Shower start: layer in where the particle start showering
- $fracE\_layers\_22$: fraction of energy in the first 22 layers
- $fracCore$: fraction of hits in shower core.

The selection of electron events with PID firstly consists of an event filtering that uses a minimum number of hits to reject the multi-particle and early shower particles. Then a selection on the number of hits and *cog_Z* is made since electrons are characterized with relatively narrow hits and *cog_Z* distributions. Afterward, a cut-off on the shower start variable is applied to select electrons that interact in the first layers and reject pions that start showering later and particles without interaction such as muons or muon-like. A cut-off in the shower radius is applied to reject hadrons events with a wide shower radius. Furthermore, a cut-off on the energy fraction in the first 22 layers is done since the maximum depth of the electromagnetic electron shower is optimized up to layer 22. Finally, after calculating the fraction of hits in the shower core, the events with a low fraction are rejected. Figure 6.38 shows the distribution of all the Particle ID variables for data and simulation. Besides the PID selection, an extra-selection on the center of gravity of the shower in X (CoG_X) and Y (CoG_Y) is performed to reduce the transverse leakage. The event selection on these variables is estimated by simulation and applied to data, as summarized in Table 6.1. Figures 6.37a and 6.37b show the energy sum distributions for 10 GeV and 80 GeV with different event selection. A total rejection of muons with a reduction of hadrons contamination is visible after the event selection, improving the width of the energy sum distribution. However, the events from the tail in the left side of the energy sum are not fully discarded.

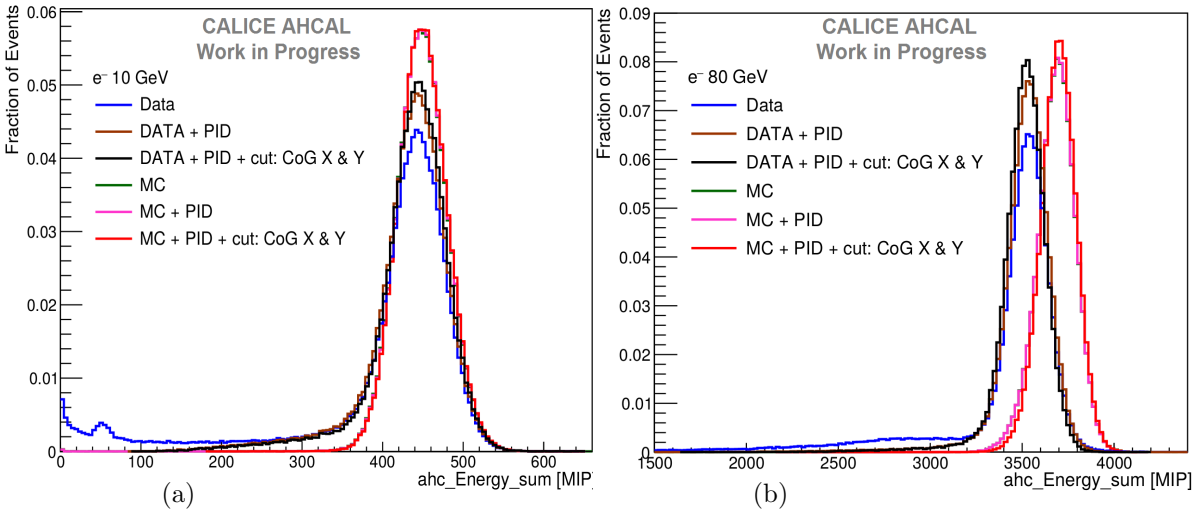

Figure 6.37: Energy sum distribution for data and simulation with different event selection for 10 GeV and 80 GeV electrons. The first event selection is made only with the Particle ID processor (brown and pink). The second selection is made by Particle ID with an additional cut-offs in the center of gravity in the X and Y axis (black and red).

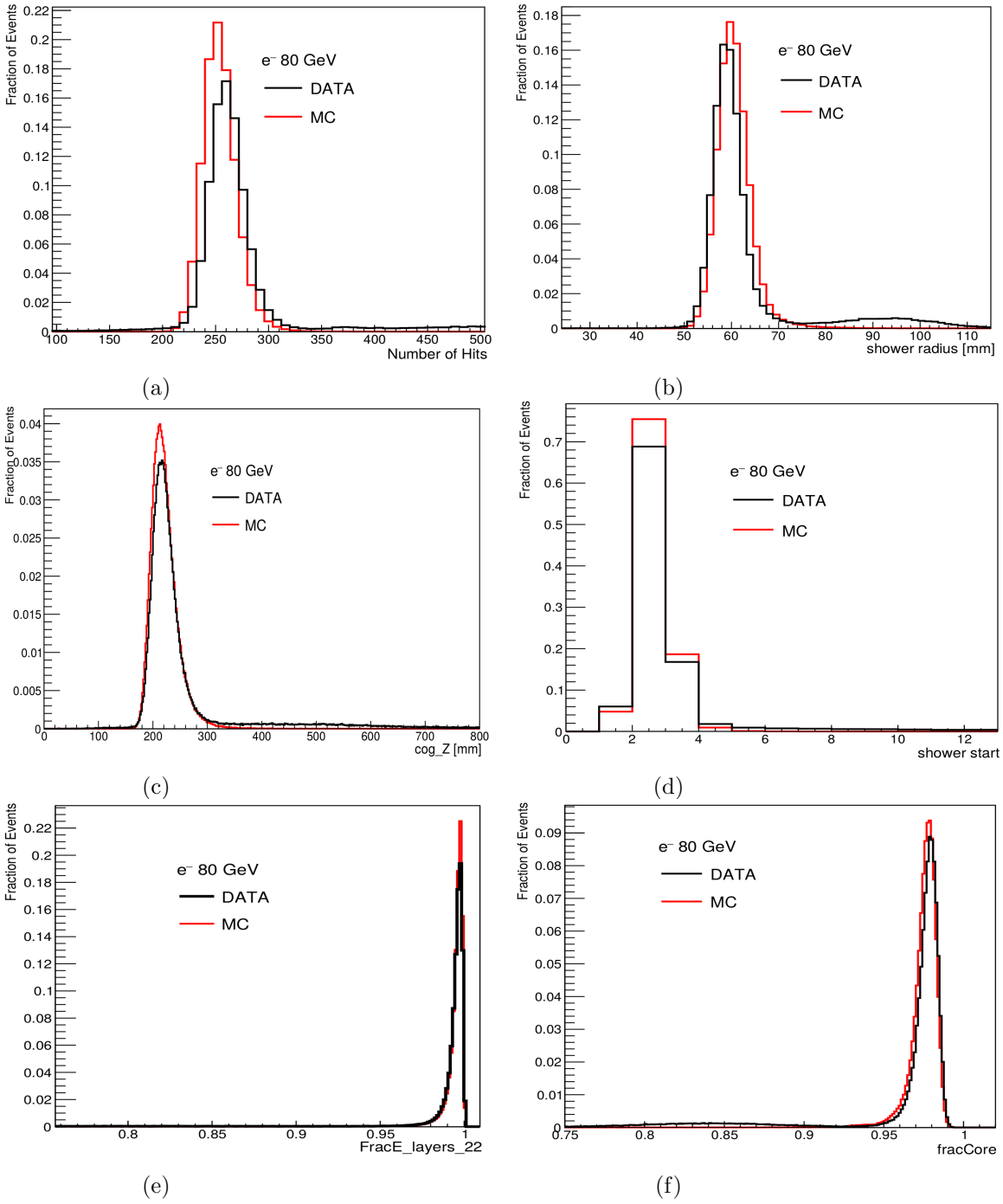

Figure 6.38: Distributions of the Particle ID variables used for the event selection. The variables are number of hits (a), shower radius (b), center of gravity in beamline axis z (c), shower start (d), the fraction of energy in the first 22 layers (e) and the fraction of hits in shower core (f).

Event selection for electrons data : 10 - 100 GeV								
Particle ID							Cut off in CoG X and Y	
Beam Energy	nHits min / max	CoG_Z [mm] min/ max	Radius min / max	st_max	fr_22_min	fr_core_min	CoG_X [mm] min / max	CoG_Y [mm] min / max
10 GeV	44 / 110	110 / 300	27 / 110	6	0.92	0.66	60 / 170	-150 / -60
20 GeV	76 / 162	130 / 320	38 / 80	5	0.92	0.76	90 / 150	-120 / -90
30 GeV	100 / 190	140 / 320	38 / 76	6	0.92	0.8	120 / 150	-120 / -90
40 GeV	125 / 230	148 / 330	42 / 82	6	0.94	0.8	120 / 150	-120 / -90
50 GeV	150 / 250	150 / 330	44 / 80	5	0.95	0.85	120 / 150	-120 / -90
60 GeV	172 / 270	160 / 350	47 / 84	5	0.95	0.85	120 / 150	-120 / -90
70 GeV	185 / 330	160 / 340	49 / 90	6	0.92	0.9	120 / 150	-120 / -90
80 GeV	200 / 360	165 / 350	50 / 94	6	0.93	0.91	120 / 150	-120 / -90
90 GeV	220 / 365	160 / 350	50 / 94	6	0.93	0.92	120 / 150	-120 / -90
100 GeV	240 / 390	160 / 375	55 / 90	6	0.93	0.93	120 / 150	-120 / -90

Table 6.1: Summaries of cut-offs applied on Particle ID variables and on the center of gravity on X and Y. All these cut-offs are estimated by MC and applied on electron data and MC for all the energies.

6.7.3 Hit Energy Spectra

Looking at the hit energy distributions of data and simulation is important to understand the individual response of the detector cells. In this analysis, the hit corresponds to the cell's response identified uniquely by I, J, and K indices. Figure 6.39 shows the comparison of hit energy distribution for data and simulation for different beam energies. As shown in Figure 6.39a, data agree well with MC at 10 GeV, with some fluctuations at high hit energy due to the low statistics. At 50 GeV shown in Figure 6.39b, a tail in high hit energies is seen in the simulation due to the over-saturation correction of data using the high number of effective pixels. However, for 100 GeV, a large tail in data is observed, caused by the under-saturation correction for the hits with high energies (Figure 6.39c).

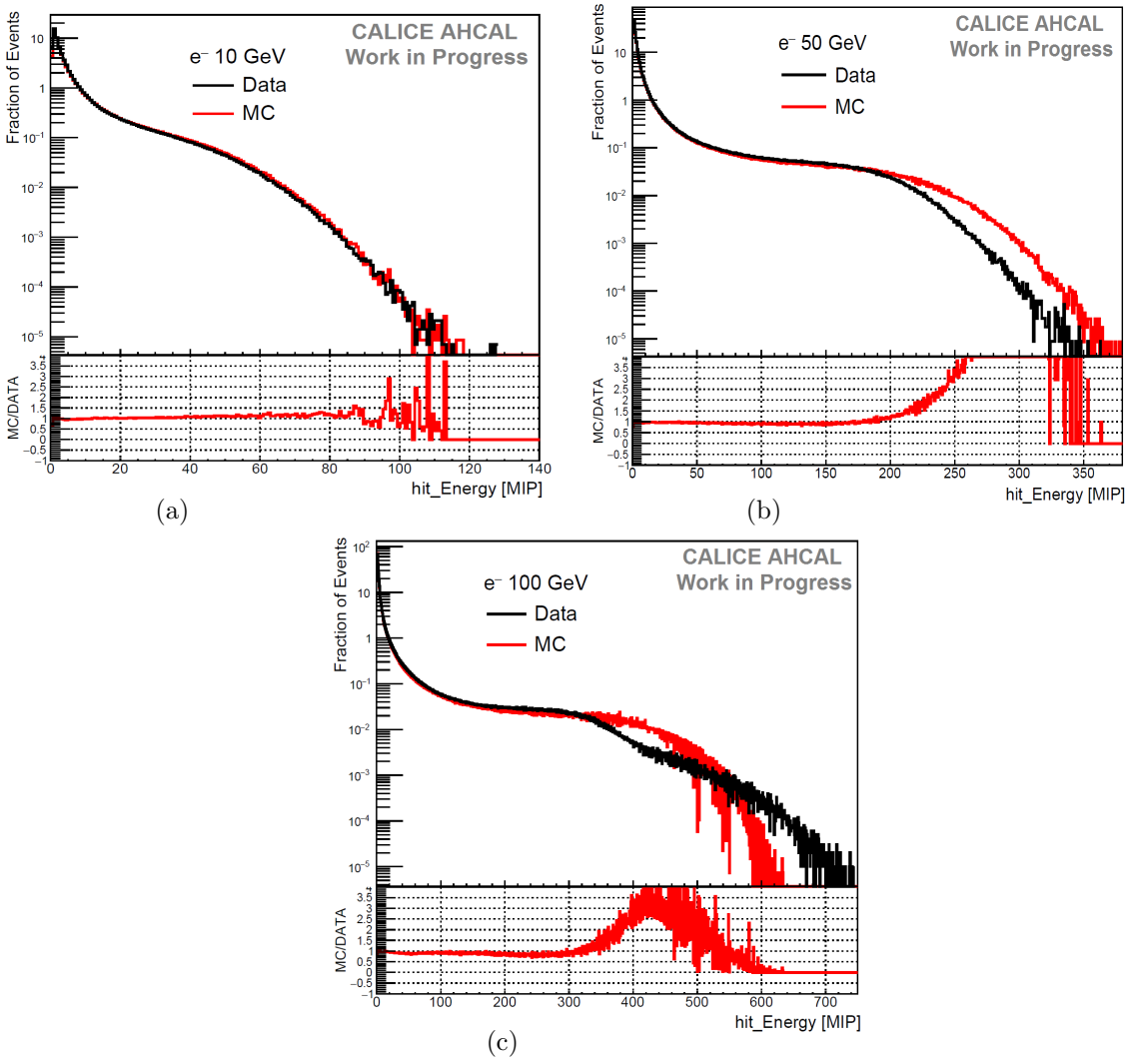

Figure 6.39: Comparison of the hit energy distribution for data and simulation for 10 GeV (a), 50 GeV (b) and 100 GeV (c).

As already explained in section 6.7.1, our limited knowledge of the SiPM saturation leads to a significant disagreement between data and MC. This variation of saturation from SiPM to SiPM is caused either by the SiPM itself or from the optical coupling between SiPM and scintillator tiles.

6.7.4 Longitudinal Shower Profiles

The comparison of the electrons' longitudinal shower profiles between data and simulation provides a good understanding of the electromagnetic shower deposition along the beam direction (z-axis) as well as modeling the detector geometry for the validity of the simulation model. The longitudinal profile of electrons' shower after the event selection for a beam energy of 10 GeV is shown in Figure 6.40, where the shape is well described, indicating the accuracy of the detector geometry in the simulation. As shown in Figure 6.40a, 2 to 10% excess in the mean number of hits per layer is seen in data compared to simulation. A 5% discrepancy after the fifth layer is visible by comparing the mean energy per layer between data and MC, as shown in Figure 6.40b. However, in the first four layers, the mean energy is higher in data than in simulation. As a first assumption, this difference could be caused by the early showering electrons, but no improvement is evident after rejecting these events using the pre-shower layer.

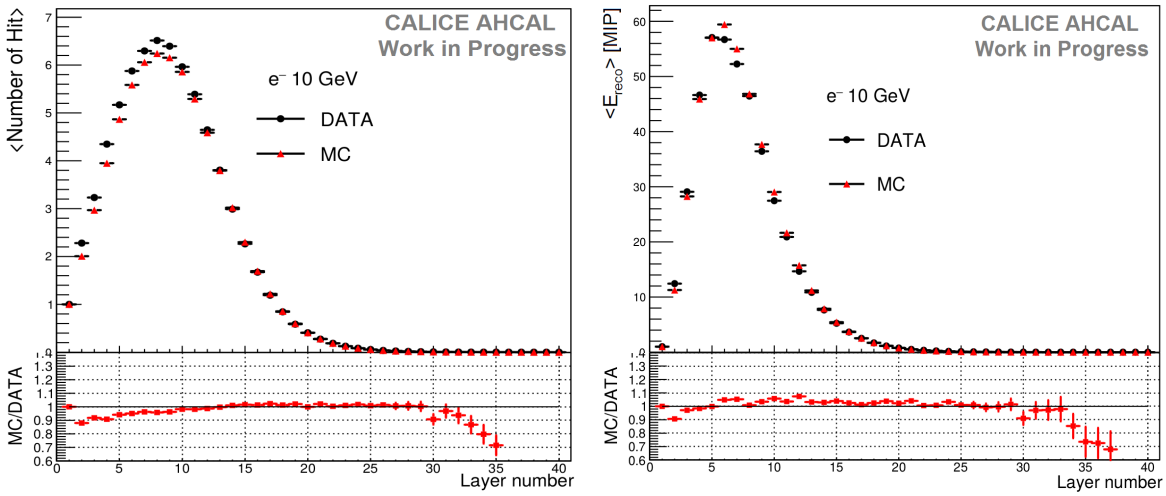

(a) (b)

Figure 6.40: Longitudinal shower profile for 10 GeV electrons for data (black) and simulation (red). a) The mean number of hits per layer. b) The mean energy per layer.

The same comparison of the longitudinal shower profile between data and simulation is made for 50 GeV and 100 GeV electrons, as shown in Figures 6.41 and 6.42, respectively. For both beam energies, higher mean hits per layer can be seen in data than in MC. In contrast, high energy deposition is visible in the simulation due to the over-saturation applied in data. However, in layer eight, where the shower deposits the maximum energy, the data is higher than the MC because of the SiPM saturation fluctuations from channel to channel.

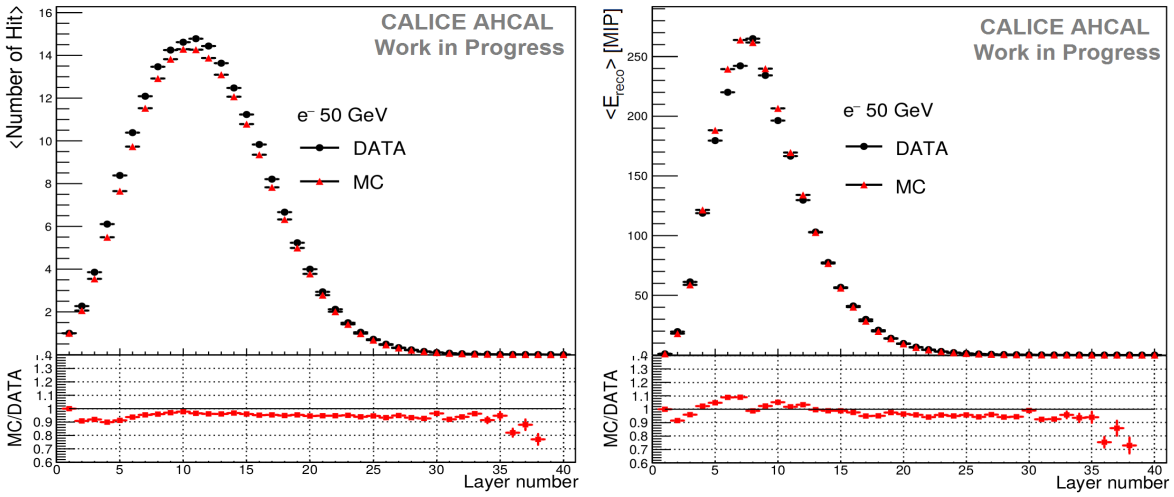

(a) (b)

Figure 6.41: Longitudinal shower profile for 50 GeV electrons for data (black) and simulation (red). a) The mean number of hits per layer. b) The mean energy per layer.

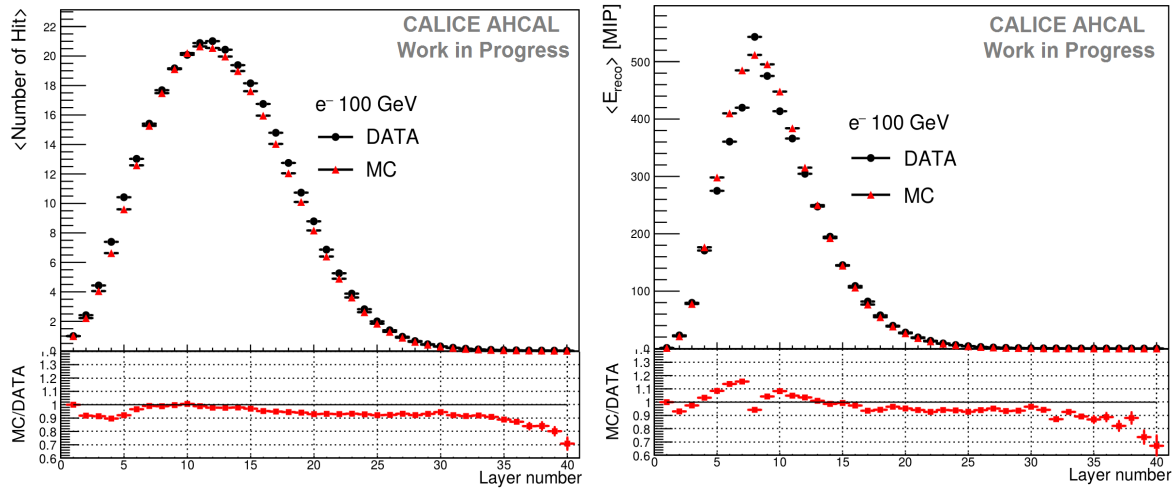

(a) (b)

Figure 6.42: Longitudinal shower profile for 100 GeV electrons for data (black) and simulation (red). a) The mean number of hits per layer. b) The mean energy per layer.

6.7.5 Energy Reconstruction

The comparison of the number of hits and energy sum distributions between data and simulation gives a first hint about the detector's total response. The comparison of the hit distributions of the electromagnetic shower in data and MC are shown for different energies in Figures 6.43a, 6.44a and 6.45a. For all the energies, 5% excess of the number of hits in data than in simulation is visible.

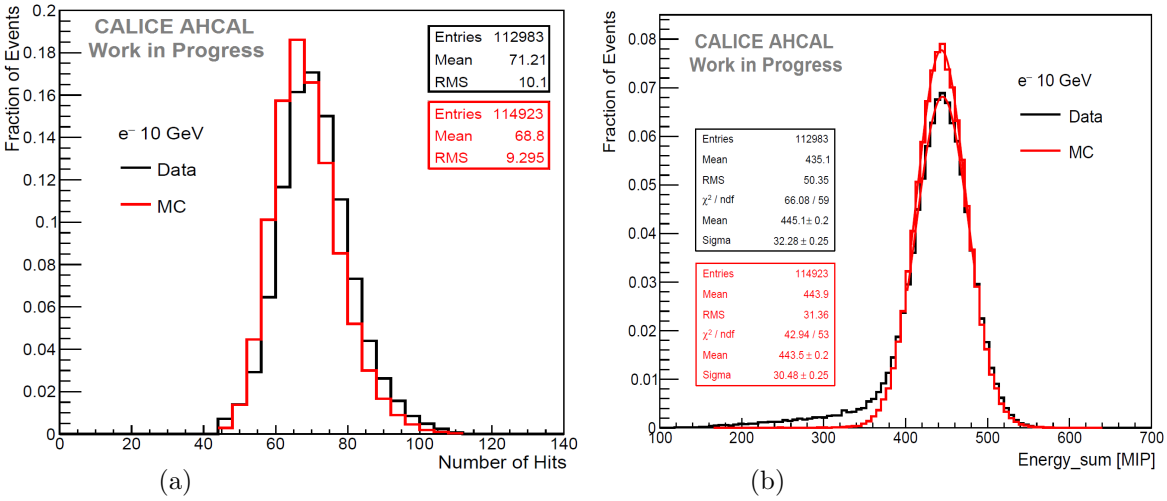

Figure 6.43: Distribution of number of hits (a) and Energy sum distribution (b) per events for 10 GeV electrons. The mean is defined by a Gaussian function fit within $\pm 1.2\sigma$ of a mean defined by an initial fit over the full range. Data in black and simulation in red.

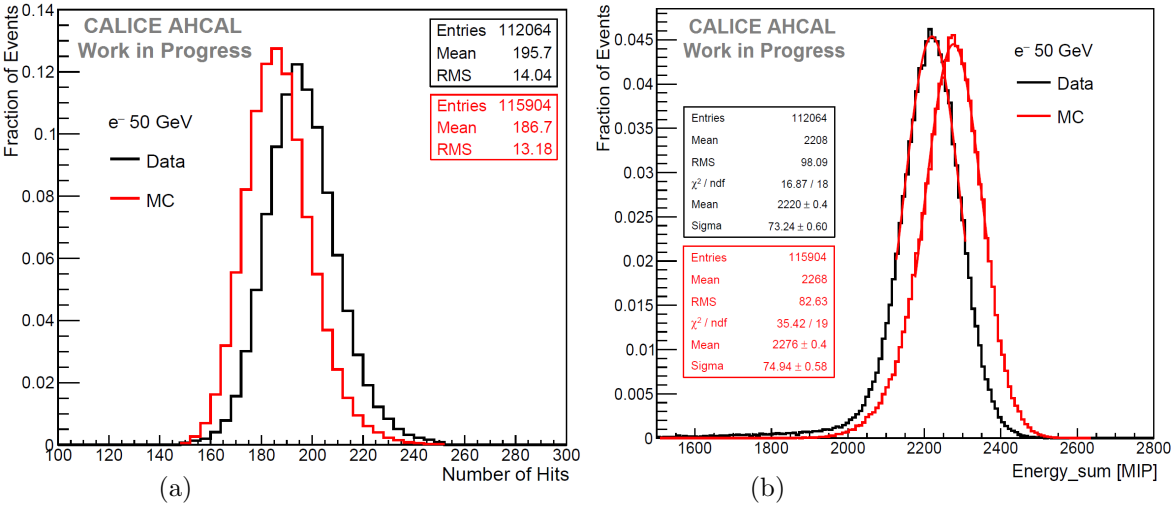

Figure 6.44: Distribution of number of hits (a) and Energy sum distribution (b) per events for 50 GeV electrons. The mean is defined by a Gaussian function fit within $\pm 1.2\sigma$ of a mean defined by an initial fit over the full range. Data in black and simulation in red.

The reconstructed energy of data and simulation is shown for different energies in Figures 6.43b, 6.44b and 6.45b. Comparing simulation to data for all the energies, the mean energy sum in MC shifts to high energy, and this difference scales with the beam energies. For 10 GeV electrons, a large tail towards low energies is visible in the energy sum distribution of data, and it is not fully reproduced by the simulation. However, for 100 GeV, the tail is larger in simulation than the data. This tail causes the disagreement observed in the longitudinal shower profiles in the first five layers between data and simulation.

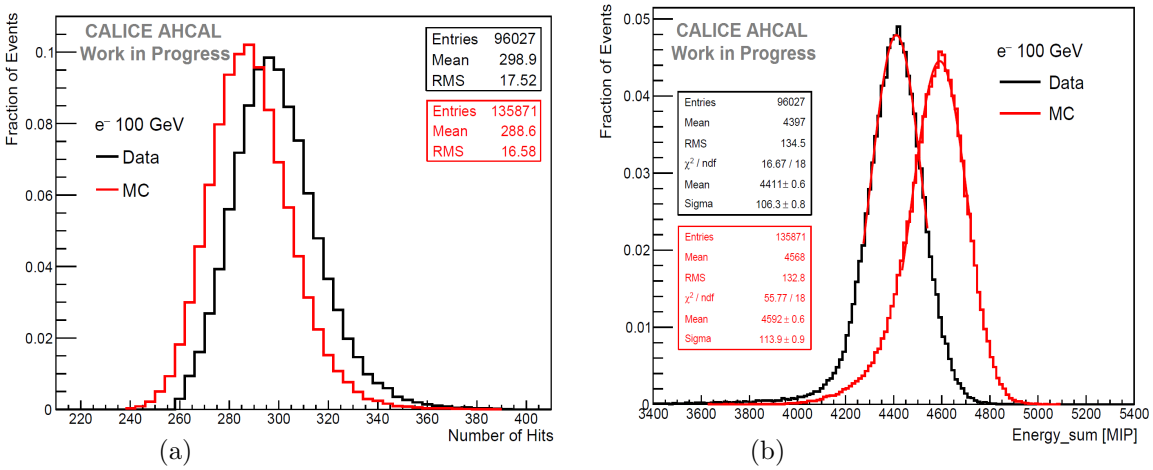

Figure 6.45: Distribution of number of hits (a) and Energy sum distribution (b) per events for 100 GeV electrons. The mean is defined by a Gaussian function fit within $\pm 1.2\sigma$ of a mean defined by an initial fit over the full range. Data in black and simulation in red.

6.7.6 Linearity and Energy Resolution

The linearity of the calorimeter response for an extensive energy range can be a principal feature for testing the detector calibration. Additionally, the high energy deposit in a single tile by electromagnetic shower can provide an accurate check for the non-linearity correction. Figure 6.46 shows the reconstructed energy as a function of the beam momentum for data and simulation. The E_{reco} is the mean energy sum of a Gaussian function fit within $\pm 1.2\sigma$ of a mean defined by an initial fit over the full range. The fit is done only in the central region of the energy sum due to its asymmetry of the distribution. Higher reconstructed energy is predicted in MC than data, with a discrepancy that increases from 1 to 5% with the beam energy. The deviation from the linearity for data and simulation is presented in the residual plot in Figure 6.47a. Generally, the detector provides a linear response with less than 1% deviation at higher energies, and less than 2% at low energies. The width of the

reconstructed energy σ_{reco} as a function of beam momentum is shown in Figure 6.47b. A discrepancy of 1 to 7% on the width is visible between data and MC.

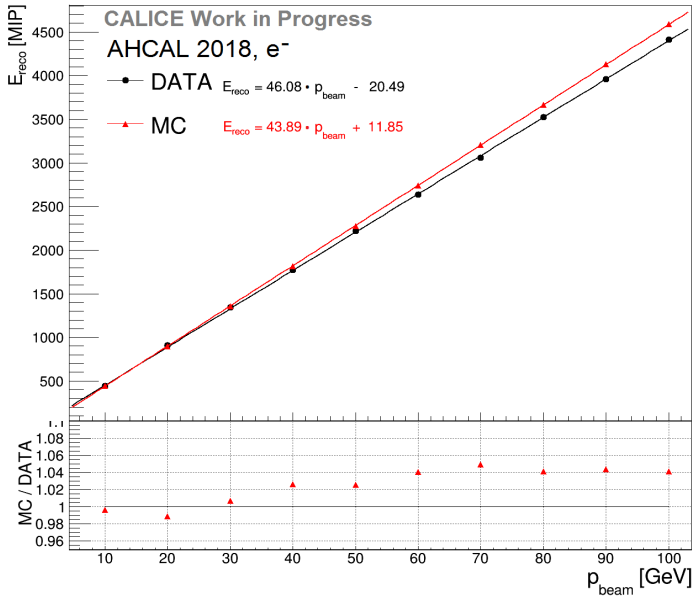

Figure 6.46: Reconstructed energy E_{reco} as a function of beam momentum for data (black) and MC (red). The linearity plots are fitted with linear function.

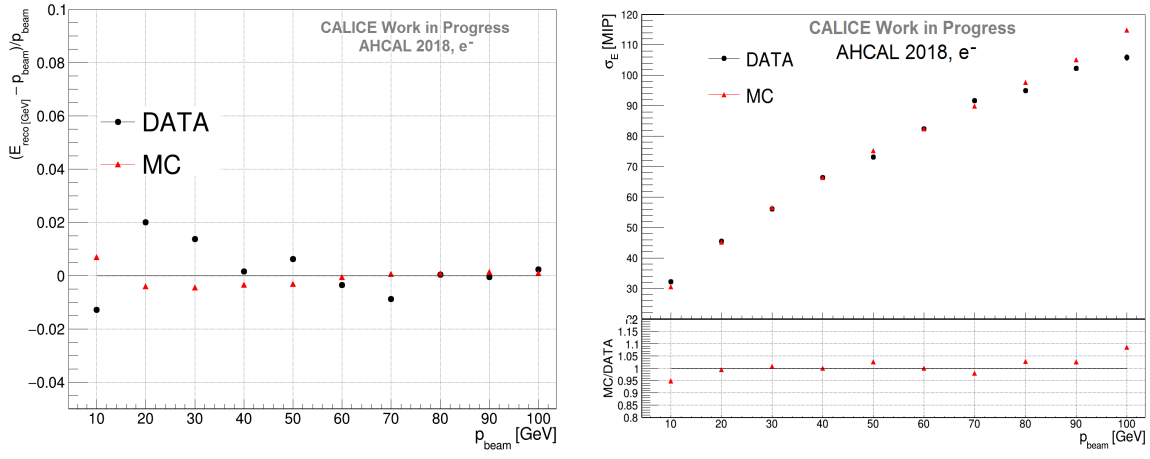

(a) (b)

Figure 6.47: Deviation from linearity (a) and width of the reconstructed energy (b) as a function of beam momentum for data (black) and simulation (red). σ_E is sigma of a Gaussian function fit within $\pm$ 1.2σ of a mean defined by an initial fit over the full range.

The electromagnetic energy resolution is estimated as the ratio of the width and the mean energy sum of a Gaussian function fit within $\pm 1.2\sigma$ of a mean defined by an initial fit over the full range. The electromagnetic energy resolution achieved with the AHCAL is shown

in Figure 6.48, with the fit results of data and simulation. The stochastic term for data is a = (22.58 ± 0.15)%/$GeV^{\frac{1}{2}}$, whereas for simulation it is a = (21.70 ± 0.14)%/$GeV^{\frac{1}{2}}$. The constant term is c = (1 ± 0.05)% for data and c = (1.15 ± 0.04)% for simulation. However, the noise term b for data and simulation is 0. Without including the systematic uncertainties in the energy resolution, data agrees with simulation within 5%. This discrepancy at high energy can be explained by the limited knowledge of the SiPM saturation.

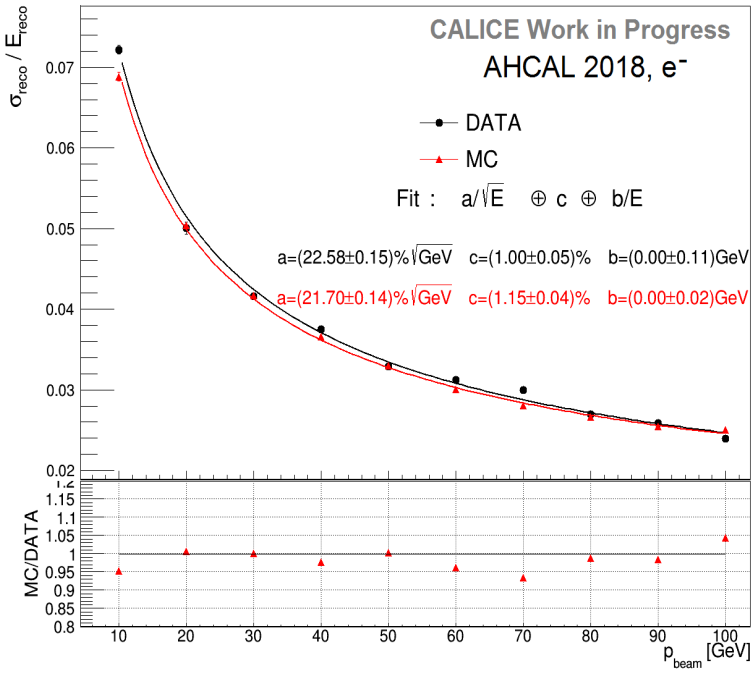

Figure 6.48: The energy resolution as a function of beam momentum for data (black) and simulation (red). Both are fitted with energy resolution function and the results of the fit are displayed in the plot.

6.7.7 Systematic Uncertainties

The systematic uncertainties of the AHCAL detector response are optimized from different calibration parameters such as MIP, Gain, and Inter-Calibration constants. Additionally, the variation of the SiPM saturation from channel to channel is estimated as a systematic uncertainty of the SiPM response. All these systematic uncertainties are computed in the simulation and illustrated in the following sub-sections.

6.7.7.1 Systematic Uncertainty of the MIP calibration constant

As discussed in section 6.5.4, the MIP calibration constant is a factor that converts the energy deposit in ADC counts to MIP unit. The comparison of two muon runs in the beginning and the end of the test beam period is used to estimate the MIP's systematic uncertainty. Figure 6.49a represents the distribution of the most probable value (MPV) extracted from the MIP distribution of all channels of the first run. In contrast, Figure 6.49b represents the MPV distribution over all the channels in the last run. The MPV distribution of both datasets is very narrow, and the mean of Gaussian function fit peaks at ∼1 MIP.

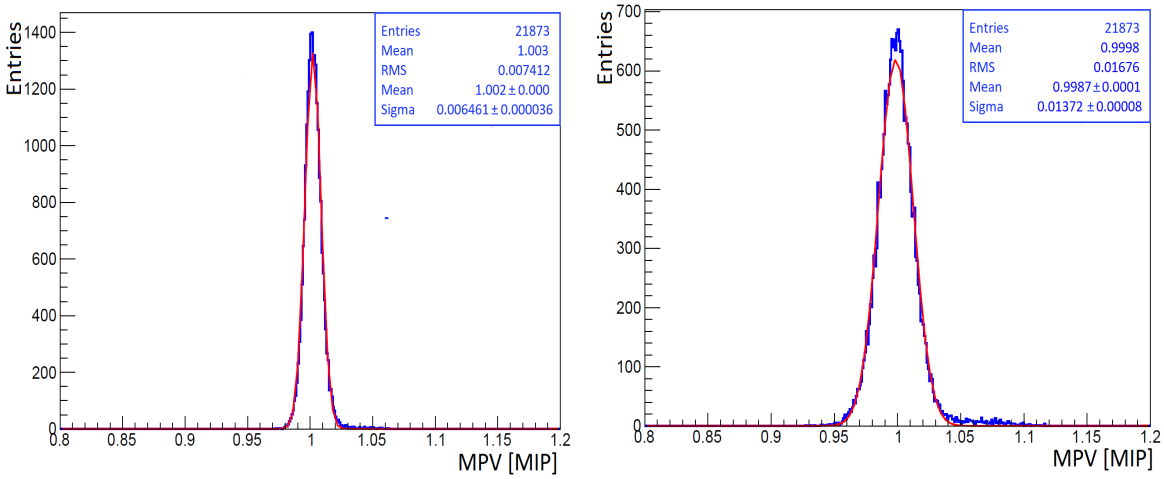

(a) (b)

Figure 6.49: The distribution of Most Probable Value over all the channels for the first (a) and last (b) runs of muon data taking. The MPV is defined by the convoluted Landau and Gaussian function fit of the hit energy deposited by muons [109].

Figure 6.50 represents the ratio distribution of the MPV of the two runs, where the mean of the Gaussian function fit is 1 MIP. The MIP factor of each channel is smeared randomly with Gaussian smearing by 1.5%, given by the RMS of the MPV ratio distribution. Afterward, the energy deposit is calculated with the smeared MIP factor in the digitization, while the calibrated MIP factor is used in the reconstruction. This calculation is done for 10, 40, and 80 GeV electrons, to estimate the systematic uncertainty over the whole energy range.

The comparison of the hits distribution between data and MC with and without the smearing for 10 GeV, 40 GeV and 80 GeV electrons are shown in Figures 6.52a, 6.52c and 6.52e, respectively. By smearing the MIP calibration factor, no variation is visible in the hits distributions. However, a slight variation of the mean and the RMS of the energy sum

distribution is seen. Figures 6.52b, 6.52d and 6.52f show the energy sum distribution with a Gaussian fit result. The fit is done in the central region of the peak within $\pm 1.2\sigma$. The MIP systematic uncertainty in the linearity, shown in Figure 6.51a, is insignificant with less than 0.2%. While the systematic uncertainty in the resolution, shown in Figure 6.51b, variates from 0.5% at low energy to 1.5% towards high energies.

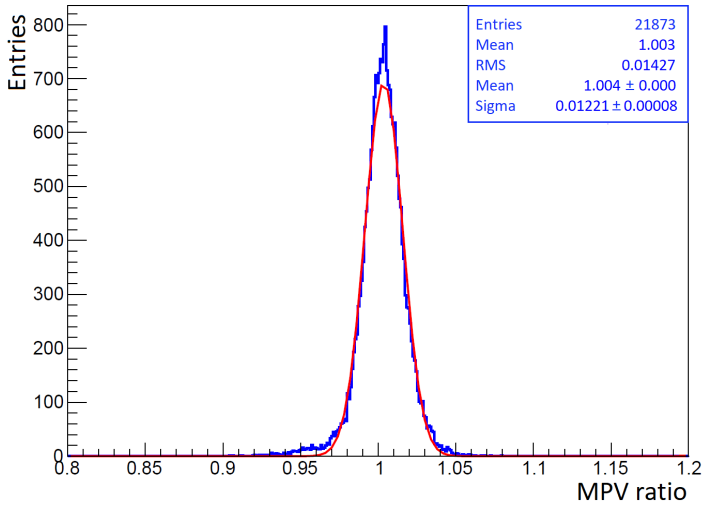

Figure 6.50: Distribution of MPV ratio of the first run over the last run with the Gaussian fit. The mean is ∼1 with an RMS of ∼0.015 [109].

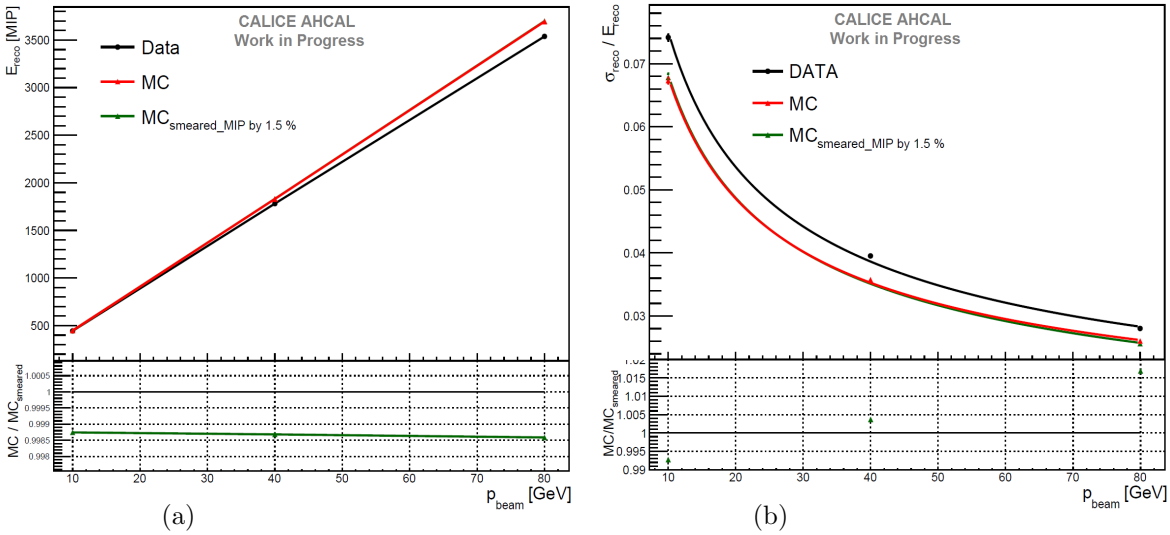

(a) (b)

Figure 6.51: Linearity (a) and energy resolution (b) plots for data (black), MC (red) and MC with smeared MIP (green). E_{reco} is the mean of the energy sum defined by the Gaussian fit within $\pm 1.2\sigma$. σ_{reco} is the RMS of this fit.

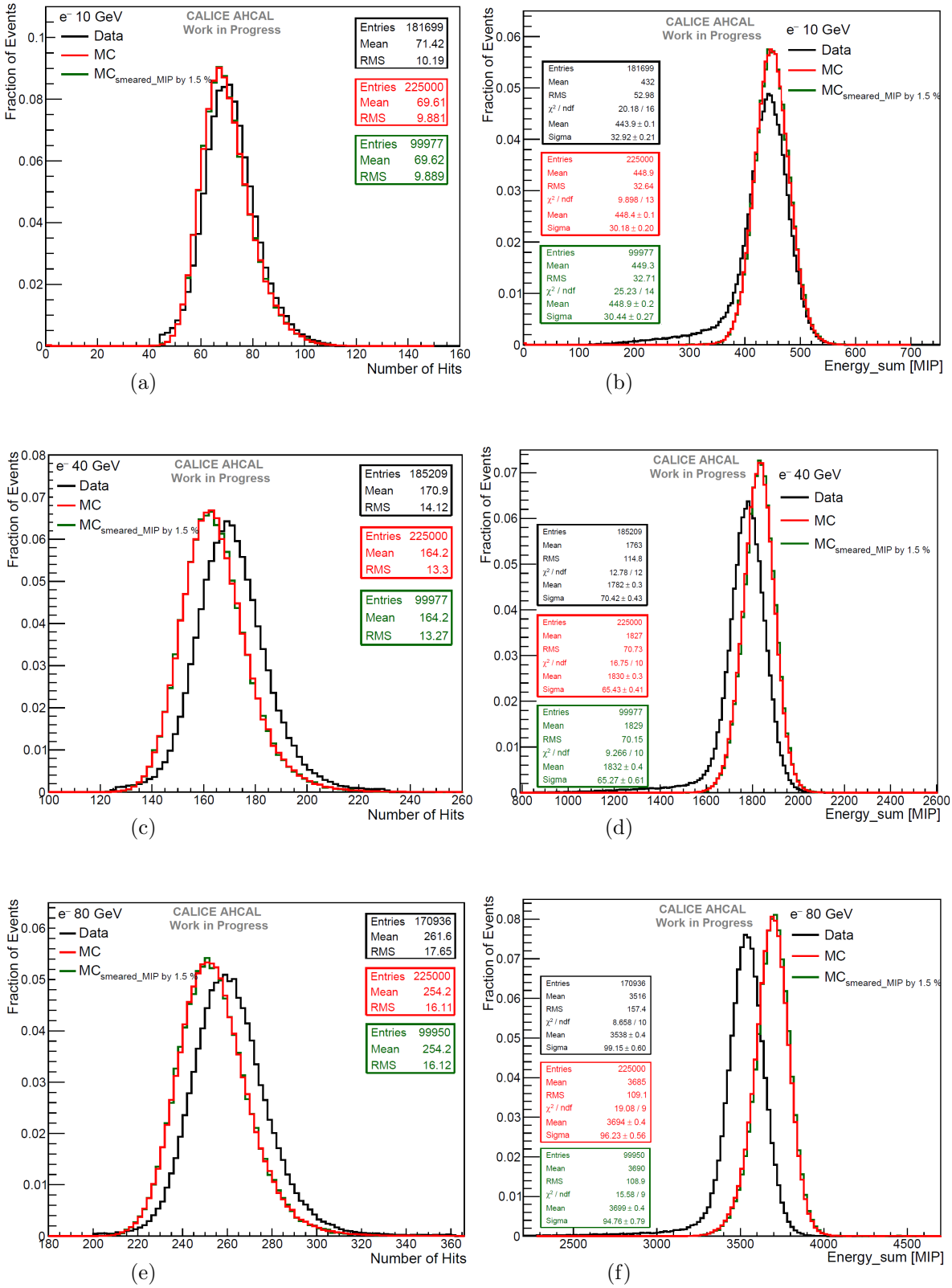

Figure 6.52: Data, MC and smeared (MIP) MC comparison of the hit distributions for 10 GeV (a), 20 GeV (b) and 80 GeV (c) electrons and the energy sum distribution for 10 GeV (b), 40 GeV (d) and 80 GeV (f) electrons. The mean is defined by Gaussian fit within $\pm 1.2\sigma$.

6.7.7.2 Systematic Uncertainty of the Gain

The gain extraction is already discussed in section 6.5.2. Similarly to the MIP factor, the gain systematic uncertainty is calculated by checking the gain stability over two LED runs at the beginning and the end of the test-beam. A variation of 1.5% is given by the RMS of the gain ratio distribution of the two runs. For each channel, the gain constant is smeared with a random Gaussian function with a standard deviation of 1.5%, used for the energy calibration in the digitization. The gain systematic uncertainty is estimated in simulation for 10, 40, and 80 GeV electrons to cover the whole energy range. Figure 6.54 shows the distributions of the hits and energy sum for data, MC, and smeared MC for all the energies, where a very slight variation in the fit parameters of the smeared simulated energy sum is observed compared to MC. As shown in Figure 6.53a, the gain systematic uncertainty in detector linearity is very low with less than 0.2%. However, the uncertainty in the energy resolution variates from 1% to 2%.

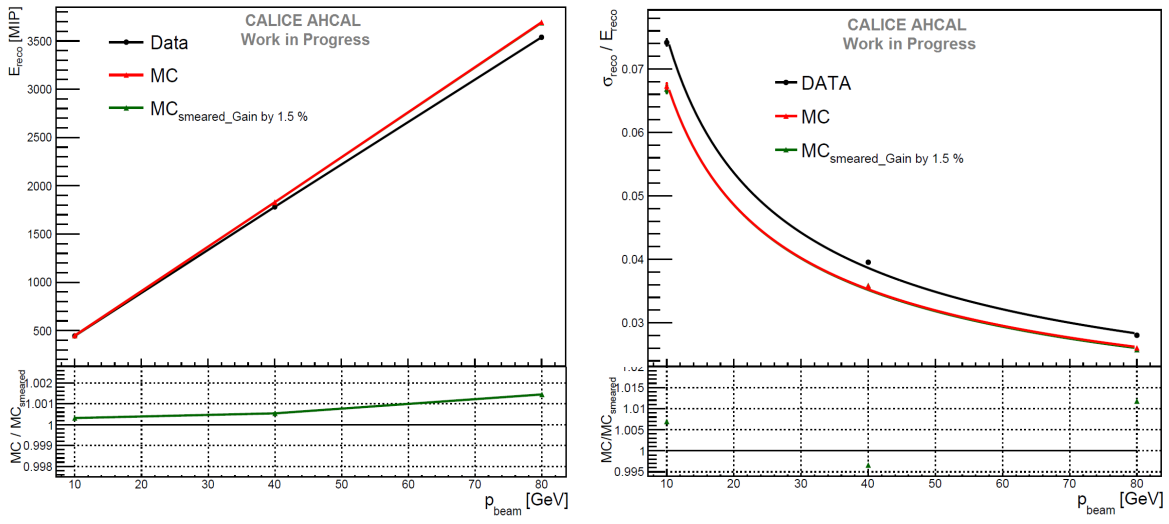

(a) (b)

Figure 6.53: Linearity (a) and energy resolution (b) plots for data (black), MC (red) and MC with smeared Gain (green). E_{reco} is the mean of the energy sum defined by the Gaussian fit within $\pm 1.2\sigma$. σ_{reco} is the RMS of this fit.

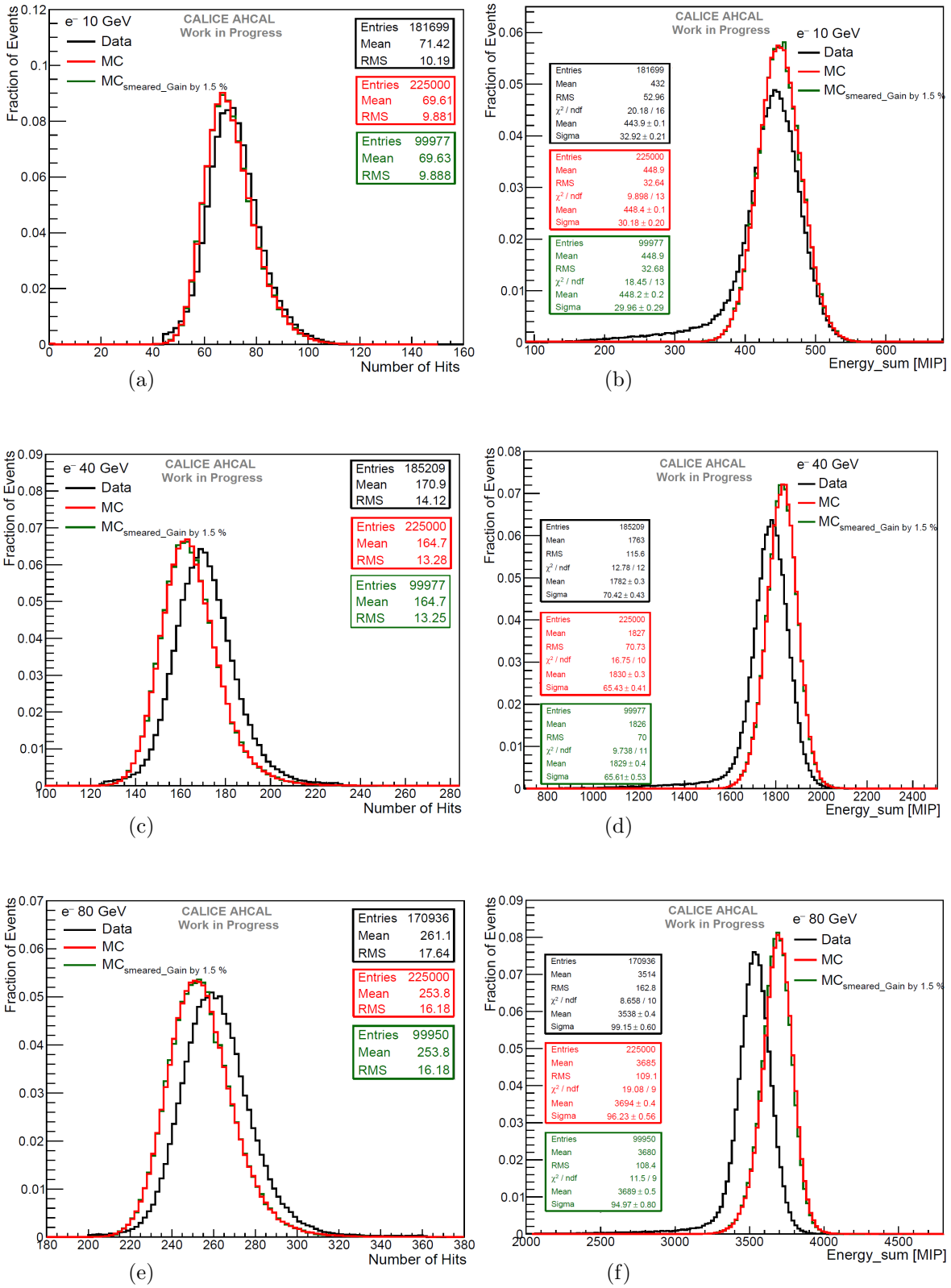

Figure 6.54: Data, MC and smeared (Gain) MC comparison of the hit distributions for 10 GeV (a), 20 GeV (b) and 80 GeV (c) electrons and the energy sum distribution for 10 GeV (b), 40 GeV (d) and 80 GeV (f) electrons. The mean is defined by Gaussian fit within $\pm 1.2\sigma$.

6.7.7.3 Systematic Uncertainty of the High Gain - Low Gain Inter-Calibration

As explained previously in section 6.5.3, two procedures are used to extract the high gain - low gain inter-calibration factor. The systematic uncertainty is estimated with the ratio of the IC factors of the two methods, as shown in Figure 6.55. The ∼1.5% systematic shift of the IC factor is considered as its systematic uncertainty.

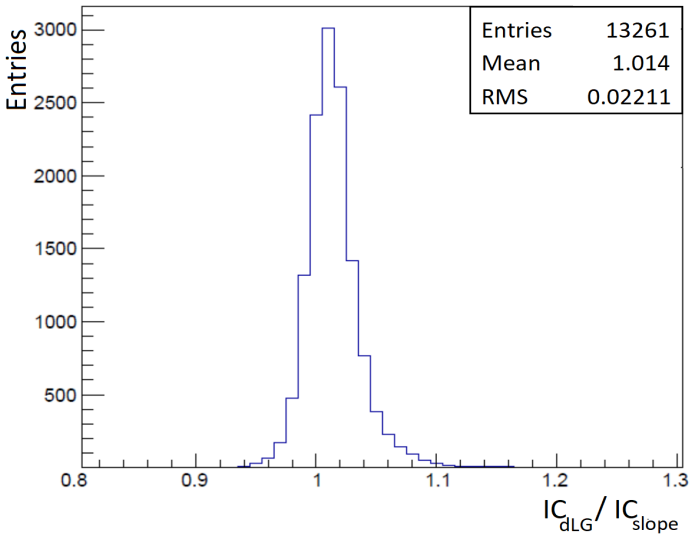

Figure 6.55: The ratio distribution of the IC factor extracted by two procedures [111].

The quantification of the systematic uncertainty of the IC factor is studied in the simulation. In the digitization, each channel's IC factor is smeared with a random Gaussian function by 1.5%. The comparison of the distributions of hits and energy sum between data, MC, and smeared MC, is shown in Figure 6.56. No significant difference is seen in the hits distributions, while a slight variation is visible on the fit parameters of the energy sum. Figure 6.57a shows the comparison of the detector linearity for data and simulation with and without the smeared IC factor. No significant variation is seen in the detector linearity, with a considerable variety of less than 1% at low energy to 6% towards high energy.

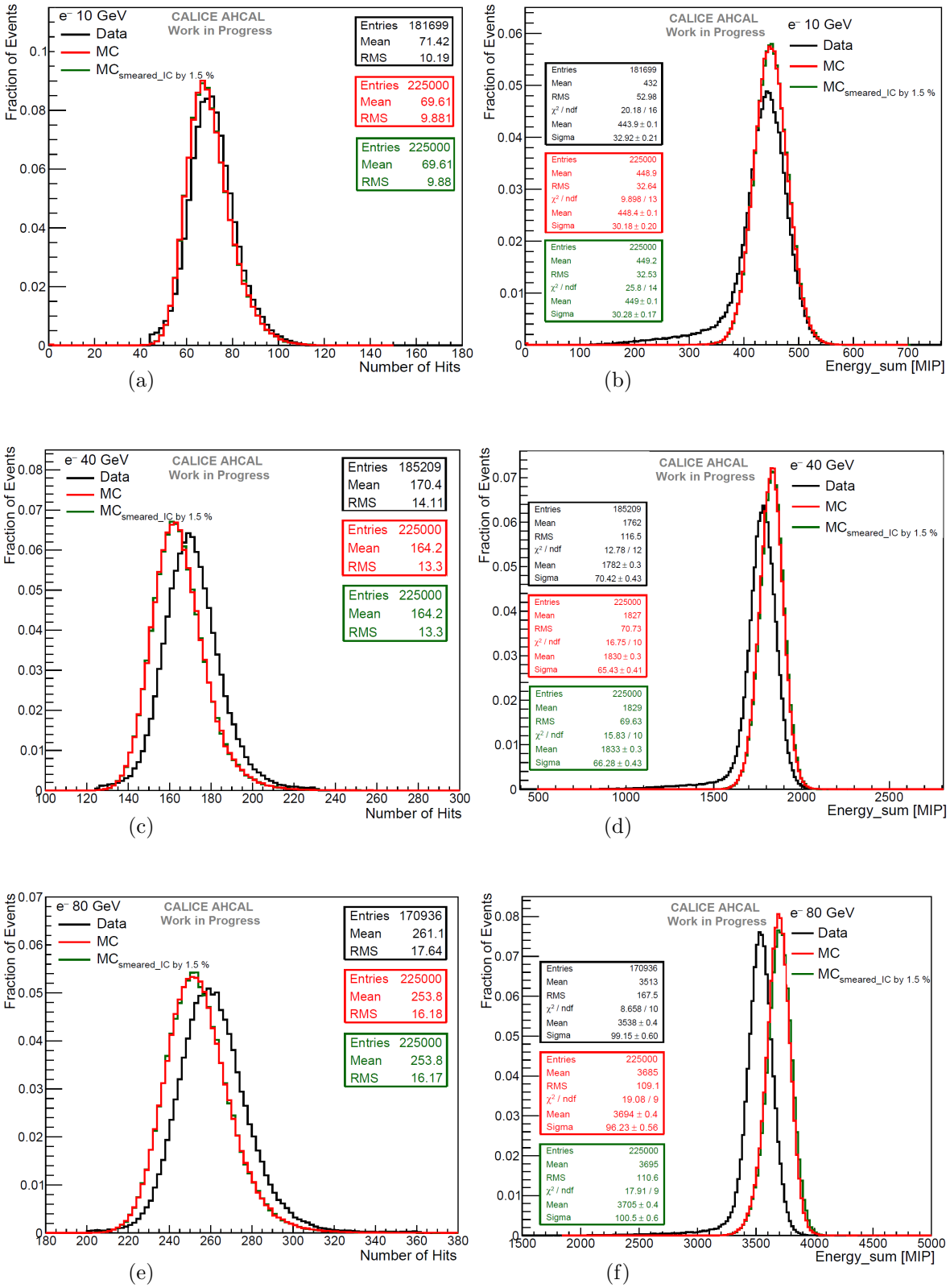

Figure 6.56: Data, MC and smeared (IC) MC comparison of the hit distributions for 10 GeV (a), 20 GeV (b) and 80 GeV (c) electrons and the energy sum distribution for 10 GeV (b), 40 GeV (d) and 80 GeV (f) electrons. The mean is defined by Gaussian fit within $\pm 1.2\sigma$.

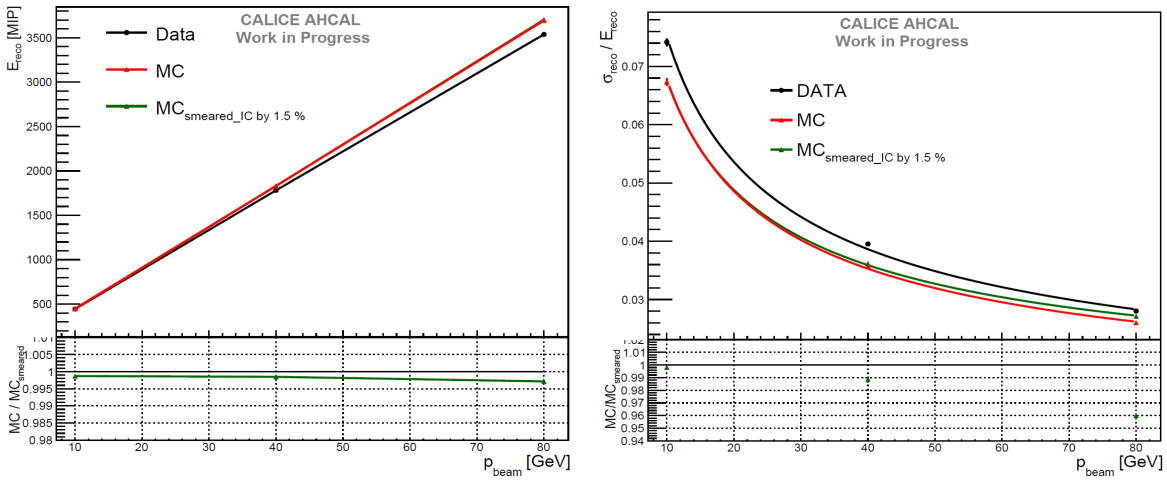

(a) (b)

Figure 6.57: Linearity (a) and energy resolution (b) plots for data (black), MC (red) and MC with smeared IC (green). E_{reco} is the mean of the energy sum defined by the Gaussian fit within $\pm 1.2\sigma$. σ_{reco} is the RMS of this fit.

6.7.7.4 Systematic Uncertainty of the SiPM response

As discussed in section 6.7.1, a variation of the N_{eff} by 100 pixels in the saturation correction of the SiPM is estimated as systematic uncertainty of SiPM response. Therefore, the number of effective pixels 2668 used for the saturation correction is smeared with a random Gaussian function of σ=100 pixels. A comparison of data, MC, and smeared MC is done to estimate the systematic uncertainties for a large energy range. In digitization, the saturation function uses the smeared N_{eff} only for the smeared MC, but a fixed N_{eff} of 2668 is applied to the reconstruction of data and both simulations. The comparison of the hit distributions in MC and smeared MC for 10, 30, 60, and 90 GeV electrons is shown in Figure 6.58. The smearing of the N_{eff} pixels in the MC does not influence the distributions of hits.

The energy sum distributions for data, MC, and smeared MC for different beam energies are shown in Figure 6.59. As expected, for 10 GeV and 30 GeV (Figures 6.59a and 6.59b) the smearing of the N_{eff} pixels does not influence the deposited energy significantly, since the SiPM saturation is not reached at low energy. Figures 6.59c and 6.59d show the energy sum distributions for 60 GeV and 90 GeV with the Gaussian fit parameters, respectively. At high energies, an influence on the energy sum after the smearing of the N_{eff} pixels can be observed. From the fit parameters, the most probable value of the energy sum of the smeared MC is shifted to a lower value while the sigma gets larger, comparing to MC.

As shown in Figures 6.60, a significant effect is visible on the linearity and energy resolution by smearing the N_{eff} pixels. The systematic uncertainty on linearity, shown in Figure 6.60a, varies from less than 1% at low energy to 4% towards high energy. The SiPM systematic uncertainty in the energy resolution varies from 1% to 13%, with a strong dependence on the beam energy. This high uncertainty is caused by the variation of the saturation correction from SiPM to SiPM, which is either over-estimated or under-estimated in the reconstruction.

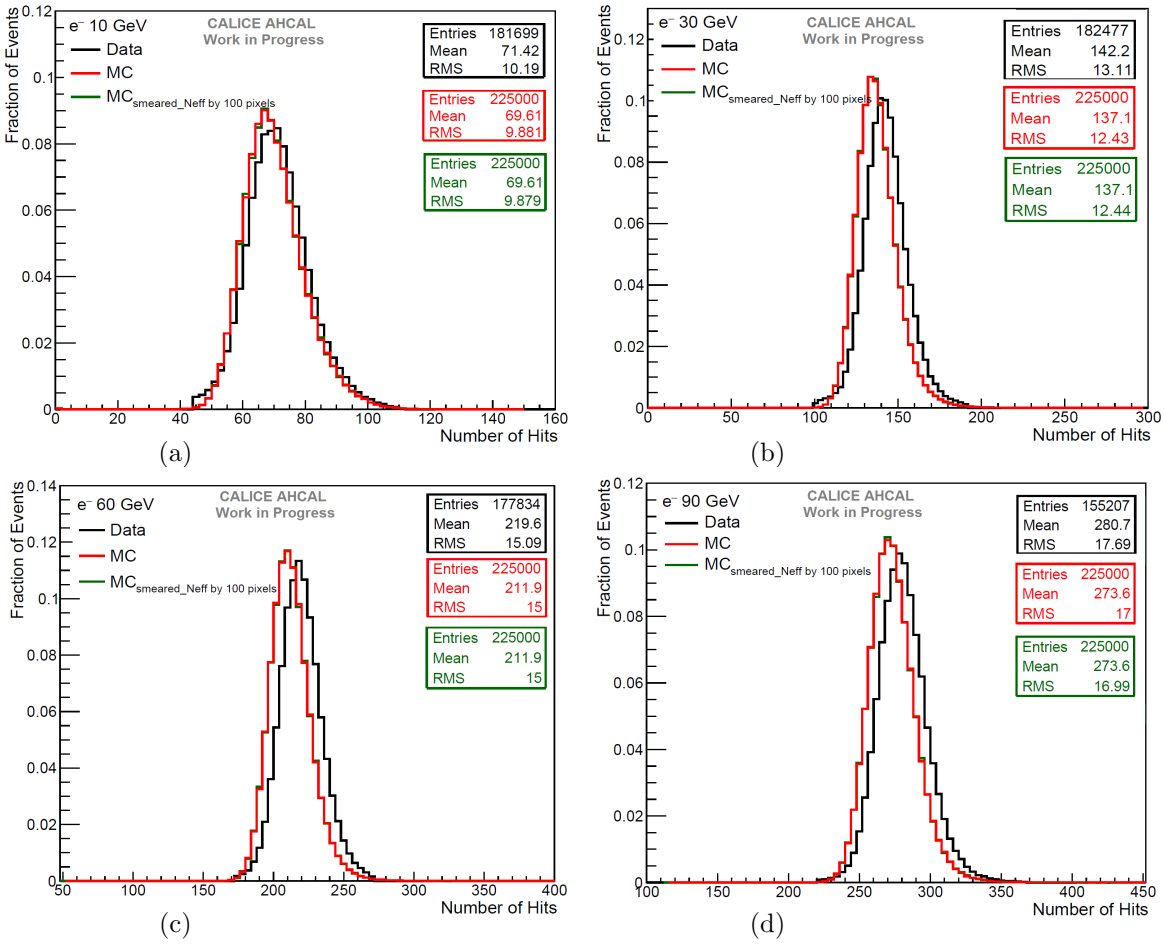

Figure 6.58: Hit distributions for data and MC and smeared (N_{eff}) MC for 10 GeV (a), 30 GeV (b), 60 GeV (c) and 90 GeV (d) electrons.

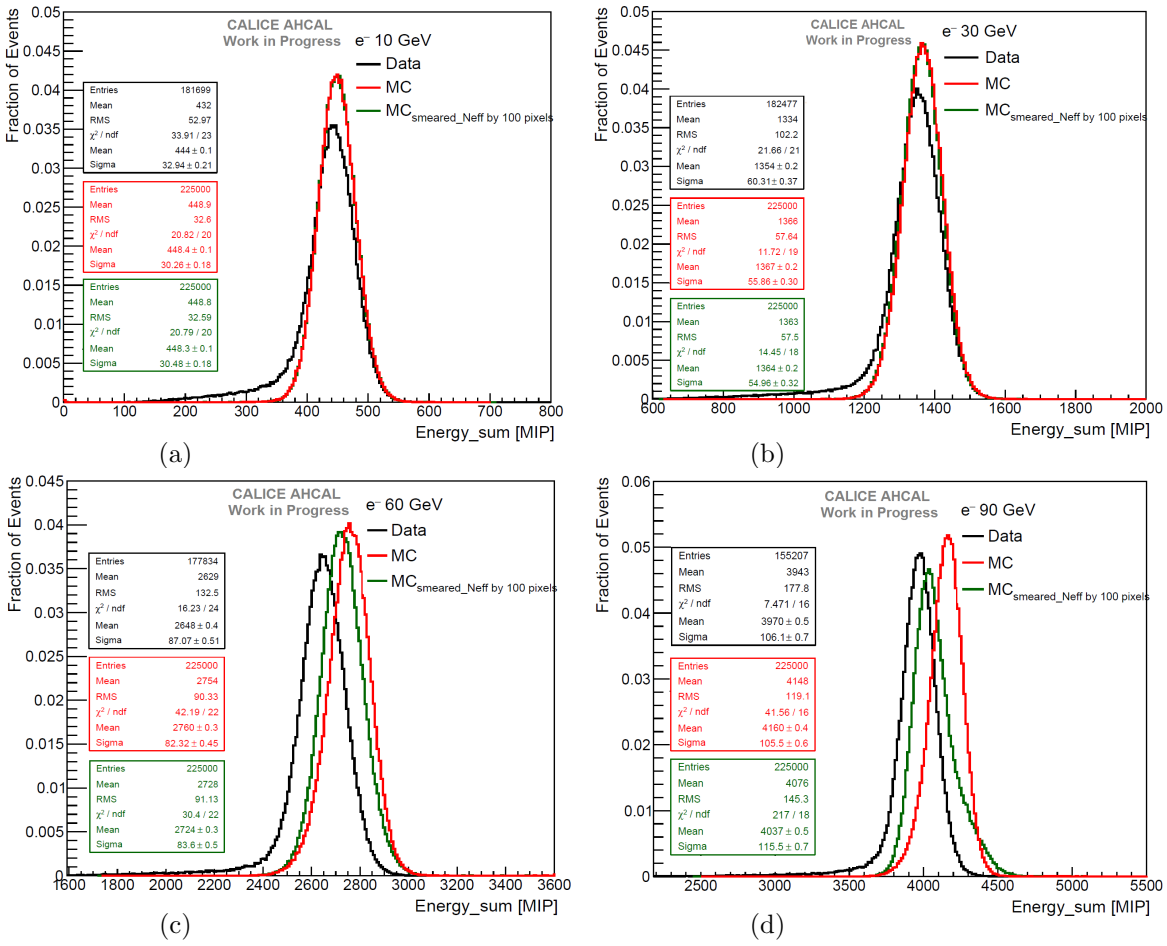

Figure 6.59: Energy sum distribution for data and MC and smeared (N_{eff}) MC for 10 GeV (a), 30 GeV (b), 60 GeV (c) and 90 GeV (d) electrons.

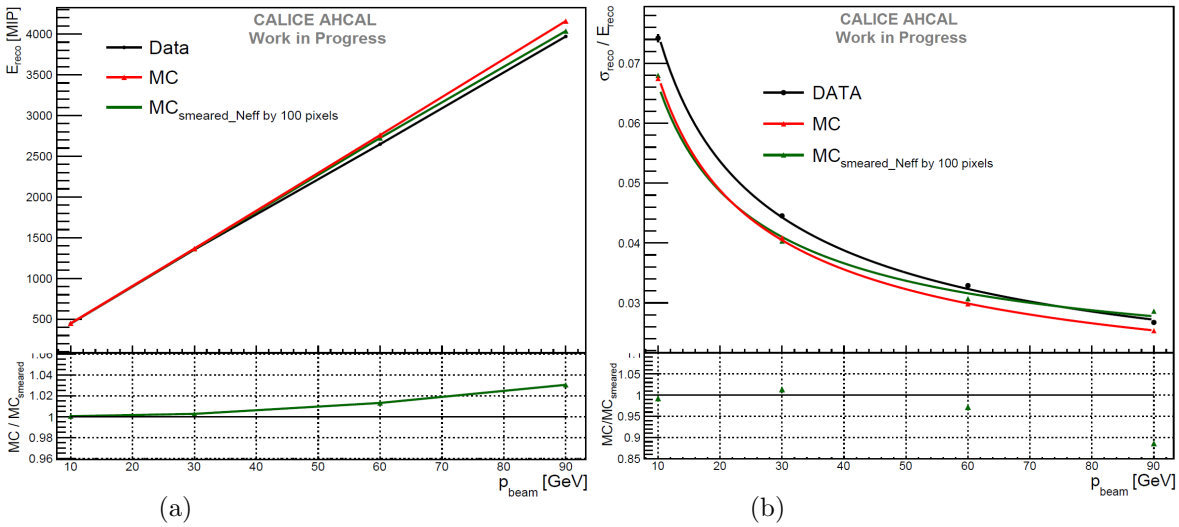

Figure 6.60: Linearity (a) and energy resolution (b) plots for data (black), MC (red) and MC with smeared N_{eff} (green). E_{reco} is the mean of the energy sum defined by the Gaussian fit within $\pm 1.2\sigma$. σ_{reco} is the RMS of this fit.

6.7.8 Results

The results obtained in this chapter characterize most aspects of the performance of the AHCAL detector response to electrons. This analysis is studied with data collected in a well-controlled test beam environment. The obtained results can be a useful reference for the performance of a hadronic calorimeter technology based on the SiPM and scintillator tiles.

The energy calibration is performed successfully with muons and light from the LED monitoring system recorded at the SPS in June 2018. The detector geometry and beamline setup are simulated in similar conditions and environments to provide a reliable comparison between data and MC. The electromagnetic response of the AHCAL to electrons is measured for the energy range from 10 to 100 GeV. A selection of a single-electron shower containing in the detector is performed using a particle identification algorithm, which consists of selecting the desired particle and rejecting all the contaminations. The electrons' longitudinal shower profiles of data agree with the simulation at the level of 5% to 15% depending on the beam energy. This discrepancy can be explained by the variation of the SiPM saturation from channel to channel, which is not yet well understood.

The systematic uncertainties of linearity and energy resolution are studied extensively for different contributions' sources and summarized in Table 6.2, where the domination of the SiPM uncertainty is visible. In these studies, the deposited energy is reconstructed in simulation using the smeared factor of each uncertainty source.

The calorimeter response for electromagnetic showers is expected to be linear to the beam momentum. Figure 6.61 and Figure 6.62 present the reconstructed energy E_{reco} and energy resolution as a function of the beam momentum for data and simulation with the total systematic uncertainty. The total uncertainty is the quadrature sum of all the uncertainty sources. The data agree with MC within a maximum uncertainty of 5% for the linearity and 6% for energy resolution. This difference is mainly due to the saturation of the SiPM, and it is well covered by the total uncertainty in the energy resolution. However, the difference in the linearity at 10 GeV is not yet understood, and it could be a result of the misdescription of the detector material in the simulation. A good experimental electromagnetic energy resolution is achieved by the AHCAL technological prototype with a stochastic term of $a = (22.58 \pm 0.15)\%/GeV^{1/2}$ and a constant term of $c = (1 \pm 0.05)\%$. This result can be compared to the measurement of the ATLAS Tile Calorimeter. This detector is a sampling calorimeter based on plastic scintillator tiles and read out by wave-length shifting (WLS)

fibers and photomultipliers (PMTs). An electromagnetic energy resolution of $\frac{28\%}{\sqrt{E}} \oplus 2.8\%$ is achieved with electrons of an energy range from 10 to 180 GeV [119].

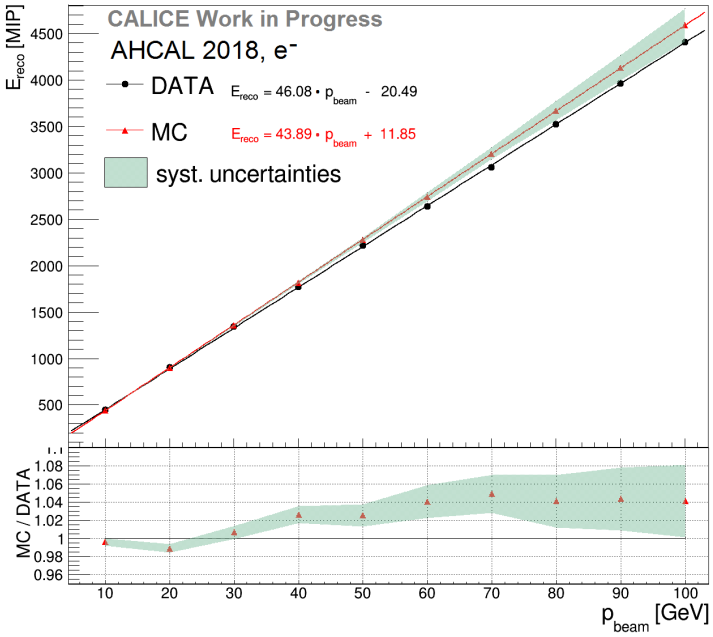

Figure 6.61: The response of the AHCAL prototype to electron as a function of beam momentum for data (black), MC (red). The green band show the overall systematic uncertainties.

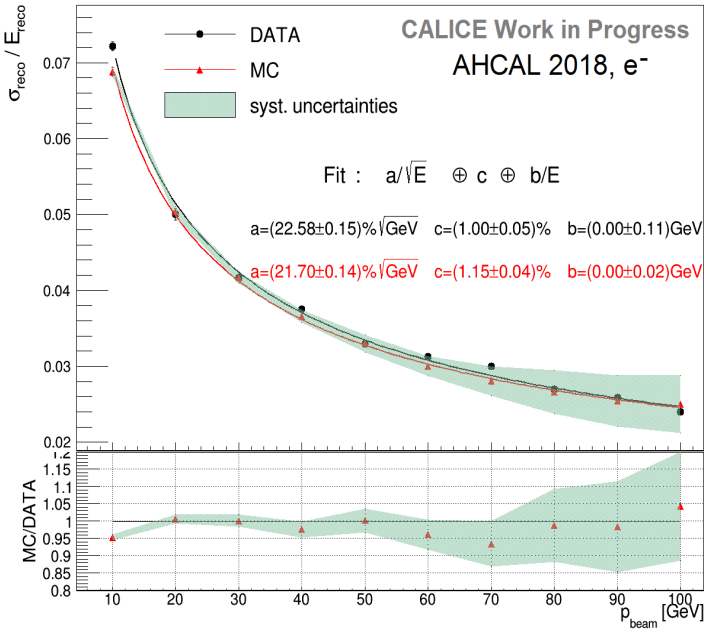

Figure 6.62: Energy resolution as a function of beam momentum for data (black) and simulation (red). Both are fitted with energy resolution function and the fit results are displayed in the plot. The green band corresponds to the total systematic uncertainty.

Systematic Uncertainties for analysis of electrons data			
Source of Uncertainty	Energies	Variable	Uncertainties [%]
MIP Calibration	10 GeV	Linearity	±0.02 (stat) ±0.2 (sys) %
		Resolution	±0.8 (stat) ±0.5 (sys) %
	40 GeV	Linearity	±0.01 (stat) ±0.2 (sys) %
		Resolution	±0.9 (stat) ±0.5 (sys) %
	80 GeV	Linearity	±0.01 (stat) ±0.2 (sys) %
		Resolution	±0.7 (stat) ±1.7 (sys) %
Gain Calibration	10 GeV	Linearity	±0.02 (stat) ±0.2 (sys) %
		Resolution	±0.8 (stat) ±0.5 (sys) %
	40 GeV	Linearity	±0.01 (stat) ±0.5 (sys) %
		Resolution	±0.9 (stat) ±2 (sys) %
	80 GeV	Linearity	±0.01 (stat) ±1.2 (sys) %
		Resolution	±0.7 (stat) ±2 (sys)%
HG-LG Inter-Calibration	10 GeV	Linearity	±0.02 (stat) ±0.2 (sys) %
		Resolution	±0.8 (stat) ±0.2 (sys) %
	40 GeV	Linearity	±0.01 (stat) ±0.2 (sys) %
		Resolution	±0.9 (stat) ±1 (sys) %
	80 GeV	Linearity	±0.01 (stat) ±0.3 (sys) %
		Resolution	±0.7 (stat) ±6 (sys) %
SiPM Saturation	10 GeV	Linearity	±0.02 (stat) ±0.2 (sys) %
		Resolution	±0.8 (stat) ±0.5 (sys) %
	30 GeV	Linearity	±0.02 (stat) ±0.5 (sys) %
		Resolution	±1 (stat) ±2 (sys) %
	60 GeV	Linearity	±0.01(stat) ±1.5 (sys) %
		Resolution	0.8 (stat) ±3 (sys) %
	90 GeV	Linearity	0.01(stat) ±3 (sys) %
		Resolution	0.7 (stat) ±11 (sys) %

Table 6.2: Summary of the systematic uncertainties calculated for electron data. All these uncertainties are calculated in the simulation.

Conclusion

The e^+e^- Linear Collider as the International Linear Collider (ILC) can be a complementary machine for the LHC and can deliver a precise description of new particles' proprieties. To reach these ambitious goals, the ILC requires an unprecedented jet energy resolution of 3-4 % from 50-250 GeV, which can be achieved using Particle Flow Algorithms (PFAs). The PFAs concept combines the measurement of the tracking system and the calorimeters into an optimal jet energy measurement, by reconstructing each particle with the detector that gives the best resolution. However, a very high granular calorimeter is required to distinguish between individual calorimeter clusters.

The CALICE collaboration is developing several calorimeter concepts with unprecedented high granularity, such as the Analog Hadronic Calorimeter (AHCAL). The AHCAL is a simpling calorimeter based on $3 \times 3 \times 0.3\ cm^3$ plastic scintillator tiles as an active material read out by the Silicon Photomultipliers (SiPMs). A former physics prototype of the AHCAL has proven the performance and suitability of such a concept. A second generation technological prototype of 38 layers with 1.7 cm steel absorber ($\sim 4\lambda$) has been constructed and commissioned by several institutes. In addition, the readout of the AHCAL was operated with the power pulsing mode to avoid the extra-cooling system, due to the minimum of unmonitored material in the detector required by the PFA concept.

The first part of this thesis is related to the commissioning procedure of AHCAL boards (HBCUs), where it is essential to understand the behavior of the SPIROC2E ASICs used for the readout. Therefore, a test-board has been designed for the SPIROC2E chip testing to ensure the quality of the recorded data. An automatic test stand has been developed with the same readout components used in the real detector to perform all the tests needed for the characterization of the chip. For each ASIC, a list of tests with individual analyses was measured, such as bias voltage, gain, and TDC measurements. Additional studies were made

to understand the chip behavior such as ADC saturation, gain stability in power pulsing mode, and the pedestal variation from LG and HG outputs. Around 1000 ASICs have been tested at an optimal time of 8 to 10 min per chip with a yield of ∼85 %. The data and analysis results were stored with reference of the chips' serial numbers for further analysis.

The second part of this thesis presents the test beam measurement of the AHCAL with electrons collected in June 2018 at the SPS, CERN. Firstly, the detector was calibrated with LED runs and muon data, where all calibration constants were extracted for 98% of channels, such as pedestal, gain, MIP calibration, and High-Gain Low-Gain inter-calibration. The AHCAL detector was simulated, including a detailed implementation of geometric features and the beamline instruments. The saturation of the SiPM was studied in detail using simulated and measured electron data by varying the number of effective pixels used in the saturation correction functions. A variation of the saturation from SiPM to SiPM was observed, leading to a significant discrepancy between data and simulation at high beam energies. The number of effective pixels of 2668 was used in the saturation correction with an uncertainty of ±100 pixels.

After the calibration validation and the optimization of the simulation's parameters, the electrons' data were analyzed and compared to simulation. This analysis aimed to measure the electromagnetic response and energy resolution of the AHCAL technological prototype for a single electron shower. Therefore, a single electron was selected with the particle identification (PID) algorithm using the simulation. An additional selection was applied to the center of gravity of the shower in the X and Y axis to reduce the transverse leakage. All these selections were optimized in simulation and applied to data and simulation.

The comparison of data and simulation showed a discrepancy of 5% to 15% in the longitudinal shower profile. A remarkable difference in the reconstructed energy between data and simulation was visible, which scales with the beam energy. The AHCAL response for the electromagnetic shower was proven to be linear with the beam momentum with a good agreement to the simulation within 5%. An energy resolution of $\frac{22.6\%}{\sqrt{E}} \oplus 1\%$ and $\frac{21.7\%}{\sqrt{E}} \oplus 1\%$ was achieved in data and simulation, respectively. A good agreement between data and simulation could be seen within 6%. Finally, all systematic uncertainties were studied, where the SiPM uncertainty was dominant. The total systematic uncertainty represented the quadratic sum of all the uncertainties, and covered the discrepancy between data and simulation for most of the energies except fof 10 GeV. This difference at low energy has not been well understood

and could be explained by the misdescription of the detector material in the simulation.

In summary, the calibration parameters and the modeling of the detector configuration were verified with electrons. A good electromagnetic response of the AHCAL was achieved with an agreement to the simulation within the uncertainties. All these results give promising hints to further analysis to study the hadronic response, which is the primary role of the AHCAL.

Acknowledgements

I would like to thank some people without whose help and support it would not have been possible to complete this thesis.

Firstly, I would like to express my sincere gratitude to my advisor Prof. Christian Zeitnitz. Throughout my whole PhD, you supported me with your immense professional knowledge, your kindness and patience. I could not have asked for a better supervisor!

Furthermore, special thanks go to Dr. Katja Krüger for the supervision throughout my analysis. Thank you for all your constructive advices!

I would also like to use this space to send a special thank you to other people who supported me during my doctorate: Mathias Reinecke and Peter Kind for your advices during the hardware part of my thesis, Dr. Felix Sefkow for the opportunity to work close to the AHCAL group at DESY and Dr. Oskar Hartbrich for answering every question during the writing process and proof-reading my thesis.

Thank you also to the hardware ATLAS group at Wuppertal University. Especially Niklaus Lehmann and Tobias Flick for proof-reading and correcting my thesis. Also, thank you to Rizwan for many visits and interesting conversations in my office.

Additionally, with the AHCAL group, I had the opportunity to experience an unforgettable time: Daniel, Olin, Vladimir, Erik, Saiva, Jiri, Amvra, Eldwan, Anna, Phi and Marisol, thank you for many great memories, constructive Physics talks and your friendliness and openness!

I would like to dedicate this thesis to my parents and brother. Without you, I would not be where I am now. Thank you for always believing in me and supporting me with everything you can! A special thank you also goes to my fiancs family! I am happy to be part of such a nice family in Germany! The last thank you goes to Sassi: You are the best thing that happened in my life, and I am very thankful that I can always count on you.

Appendix

.1 Beam profile for all electron data runs used for this analysis

e- data : 10 - 100 GeV					
	run number	X	ΔX	Y	ΔY
10 GeV	61293	124,2	27,8	-103,9	29,8
	61294	125,3	27,8	-103,2	29,2
	61295	125,2	27,8	-103,4	29,5
20 GeV	61296	129,5	19,5	-101,3	20,0
	61297	129,7	19,4	-101,5	20,1
	61298	129,6	19,8	-101,6	20,4
	61299	129,2	19,3	-101,5	21,1
	61300	129,5	19,6	-101,3	21,2
30 GeV	61213	129,3	14,3	-102,5	14,6
40 GeV	61212	128,9	13,0	-102,9	11,6
50 GeV	61214	128,5	11,4	-99.5	9,5
60 GeV	61211	127,7	10,7	-106,0	8,3
70 GeV	61215	128,0	10,1	-104,3	7,1
80 GeV	61210	124,6	10,4	-103,5	6,3
90 GeV	61216	127,1	9,6	-102.2	6,6
100 GeV	61218	126,3	10,2	-101,0	7,4

Table 3: List of electron runs taken at SPS in June 2018 with the beam profile used for the simulation of this thesis

.2 Reconstructed Energy

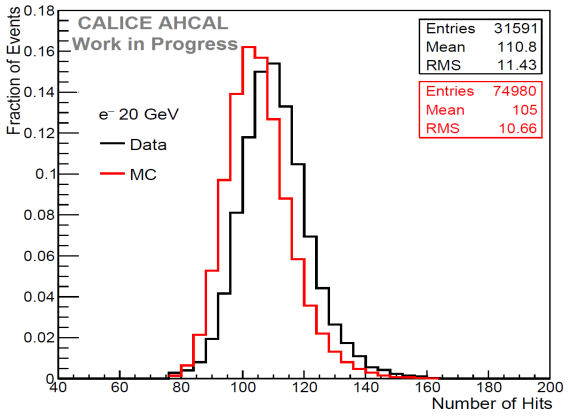

(a)

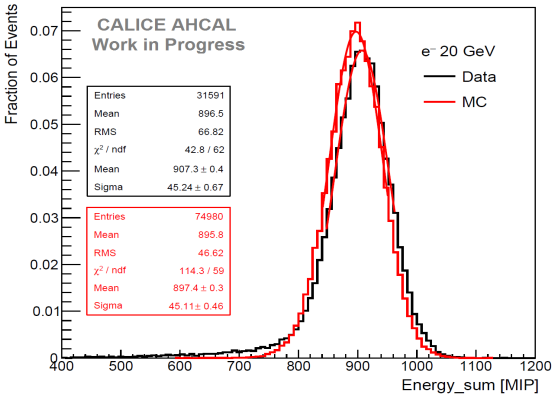

(b)

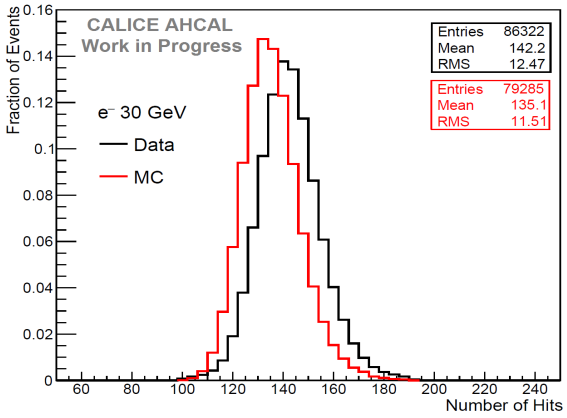

(c)

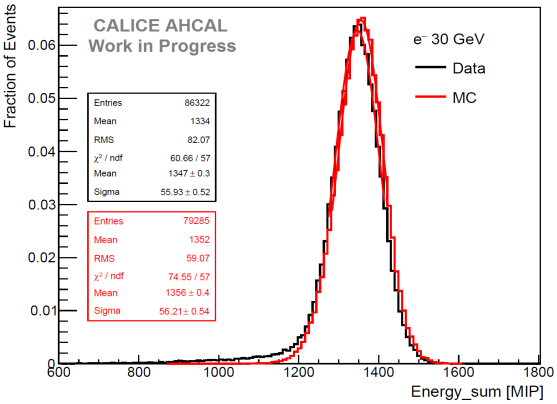

(d)

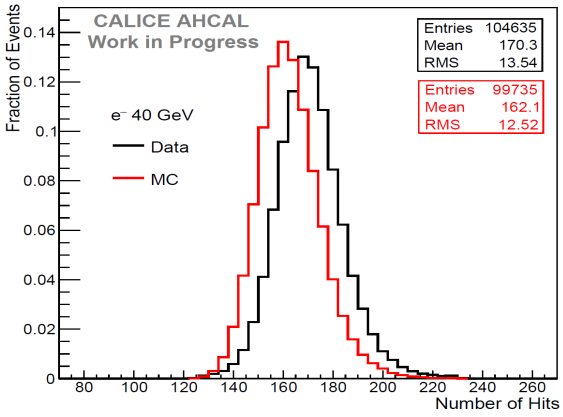

(e)

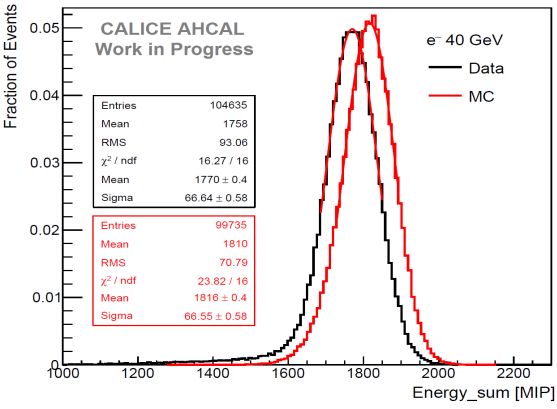

(f)

Figure 63: Hit distributions for Data and MC w/o IC factor smearing for 20 GeV (a), 30 GeV (b) and 40 GeV (c). Energy sum distribution for electron of 20 GeV (b), 30 GeV (d) and 40 GeV (f).

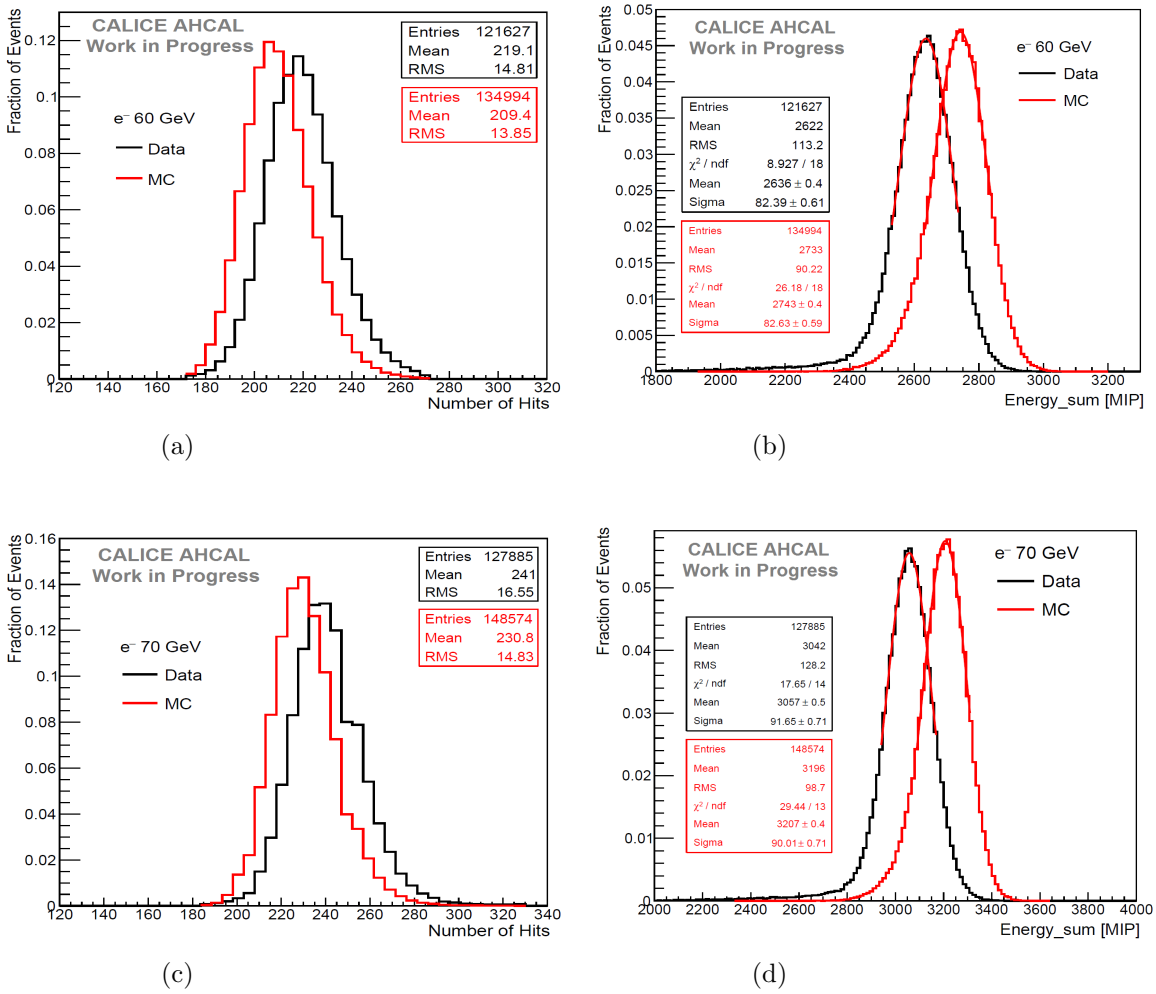

Figure 64: Hit distributions for Data and MC w/o IC factor smearing for 20 GeV (a), 30 GeV (b) and 40 GeV (c). Energy sum distribution for electron of 20 GeV (b), 30 GeV (d) and 40 GeV (f).

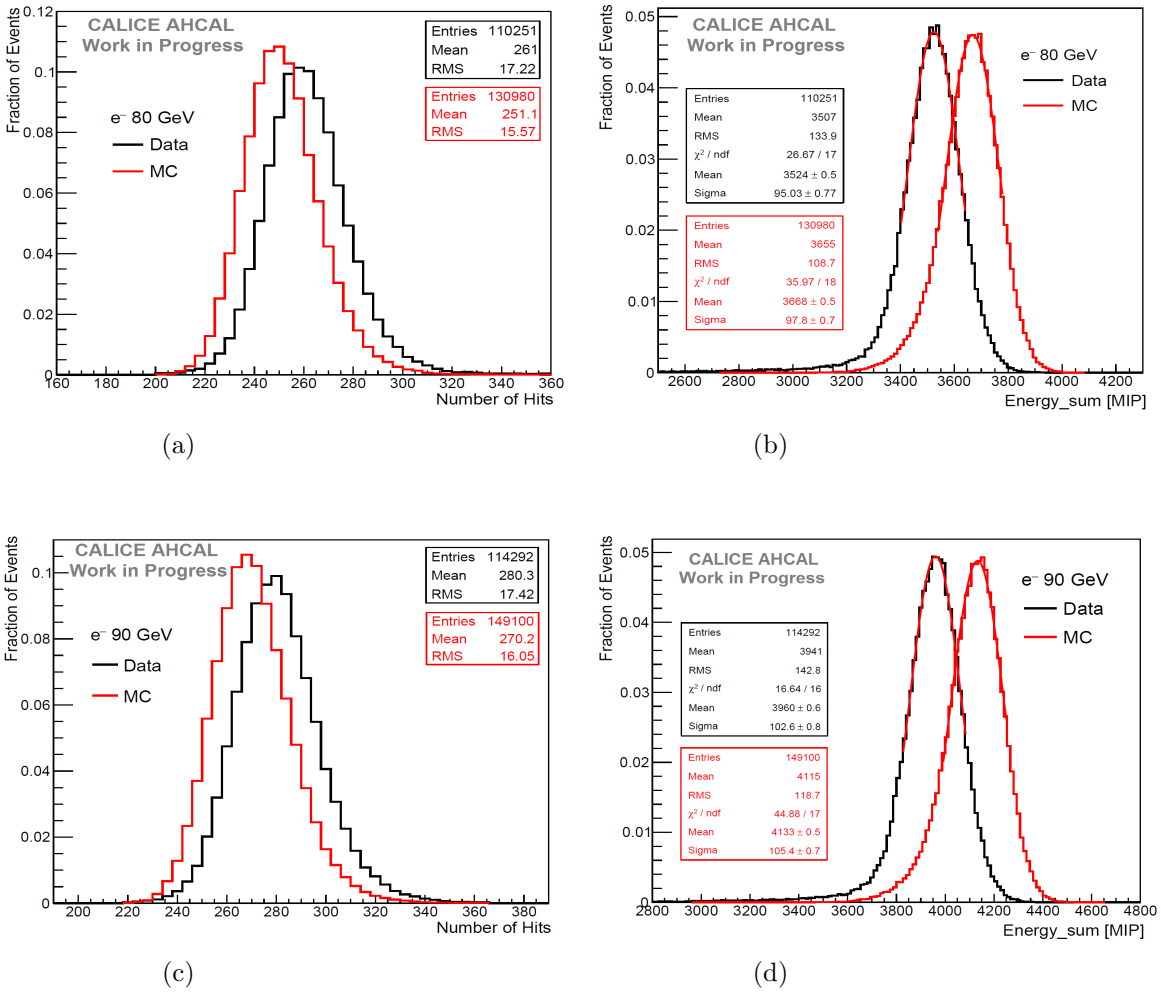

Figure 65: Hit distributions for Data and MC w/o IC factor smearing for 20 GeV (a), 30 GeV (b) and 40 GeV (c). Energy sum distribution for electron of 20 GeV (b), 30 GeV (d) and 40 GeV (f).

.3 Hit energy Spectra

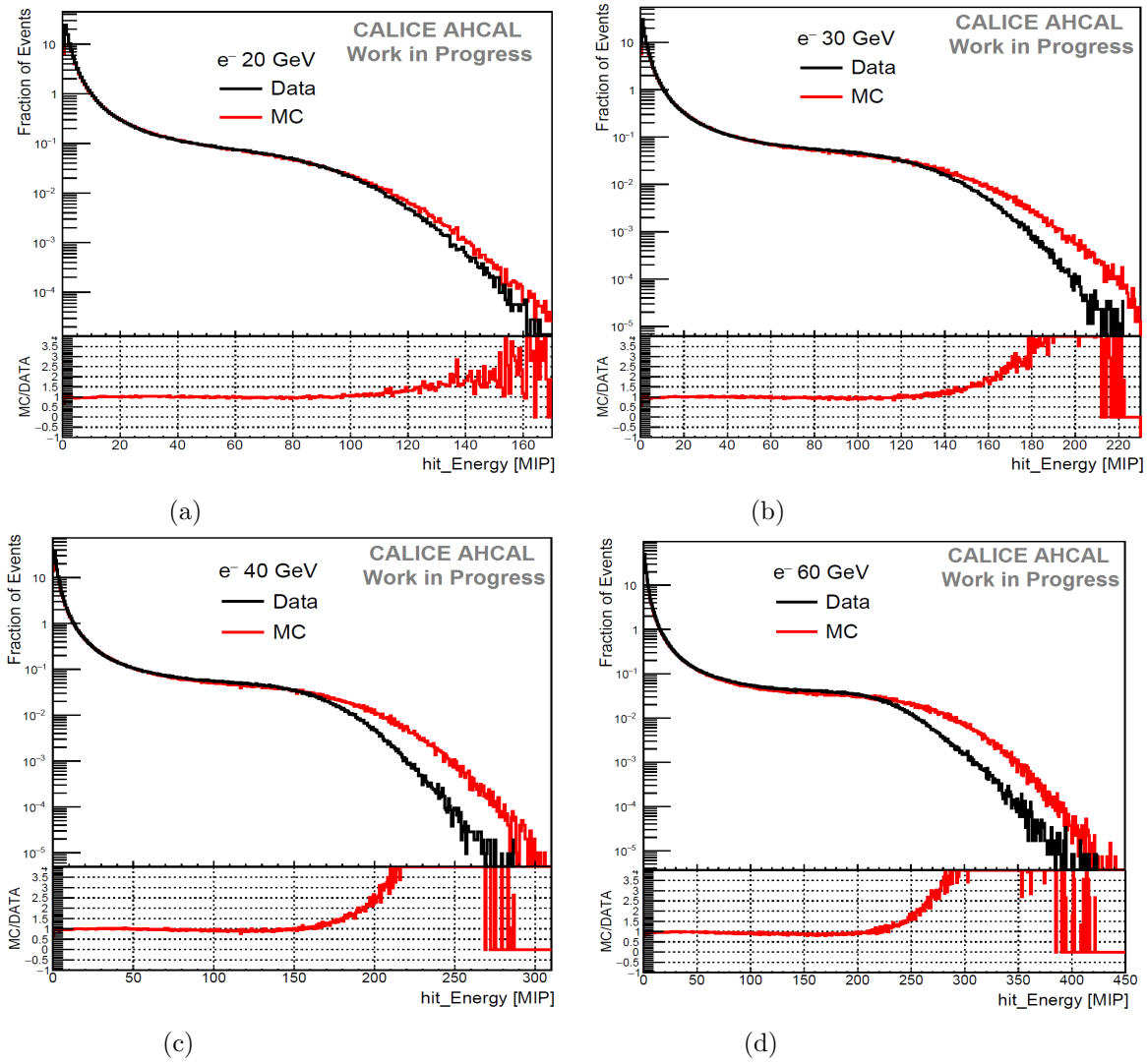

Figure 66: Comparison of the hit energy distribution for data and simulation for 20 GeV (a) , 30 GeV (b) , 40 GeV (c) and 60 GeV (d). The number of effective pixels used in the saturation correction of data is 2668.

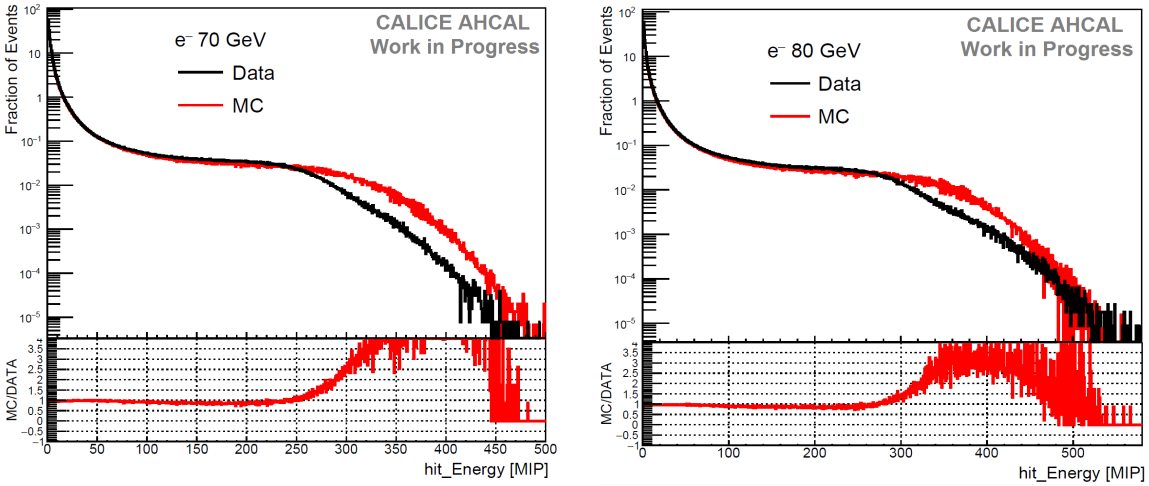

(a)

(b)

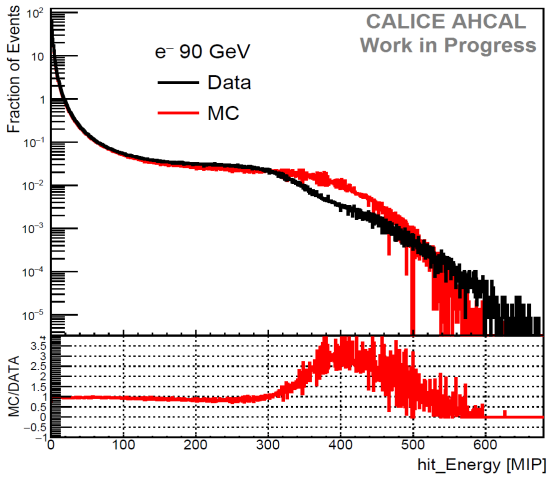

(c)

Figure 67: Comparison of the hit energy distribution for data and simulation for 70 GeV (a) , 80 GeV (b) and 90 GeV (c). The number of effective pixels used in the saturation correction of data is 2668.

.4 Shower profiles

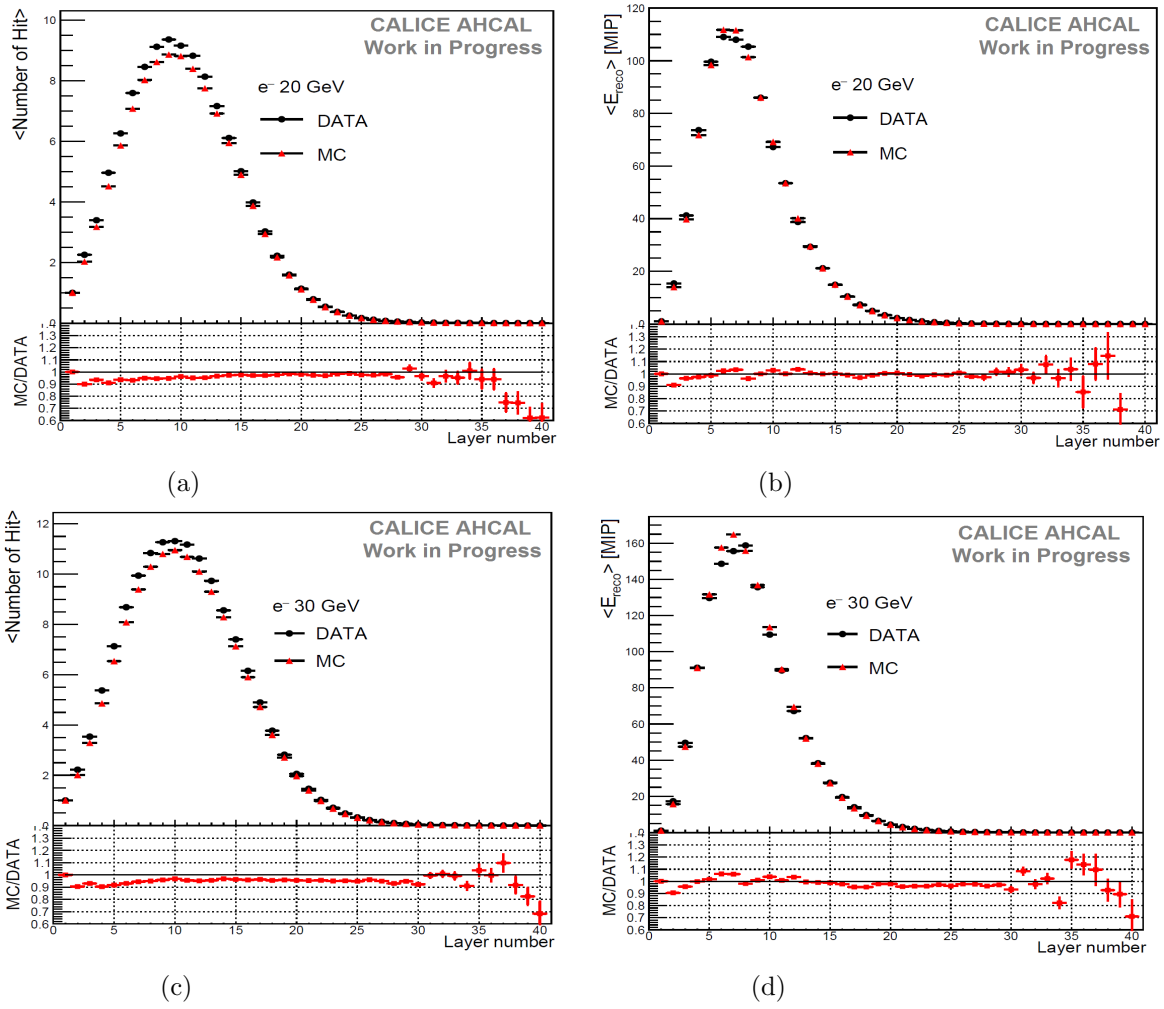

Figure 68: Distribution of mean number of hits per layer for 20 GeV (a) and 30 GeV (b). Distribution of the mean energy per layer for 20 GeV (c) and 30 GeV (d).

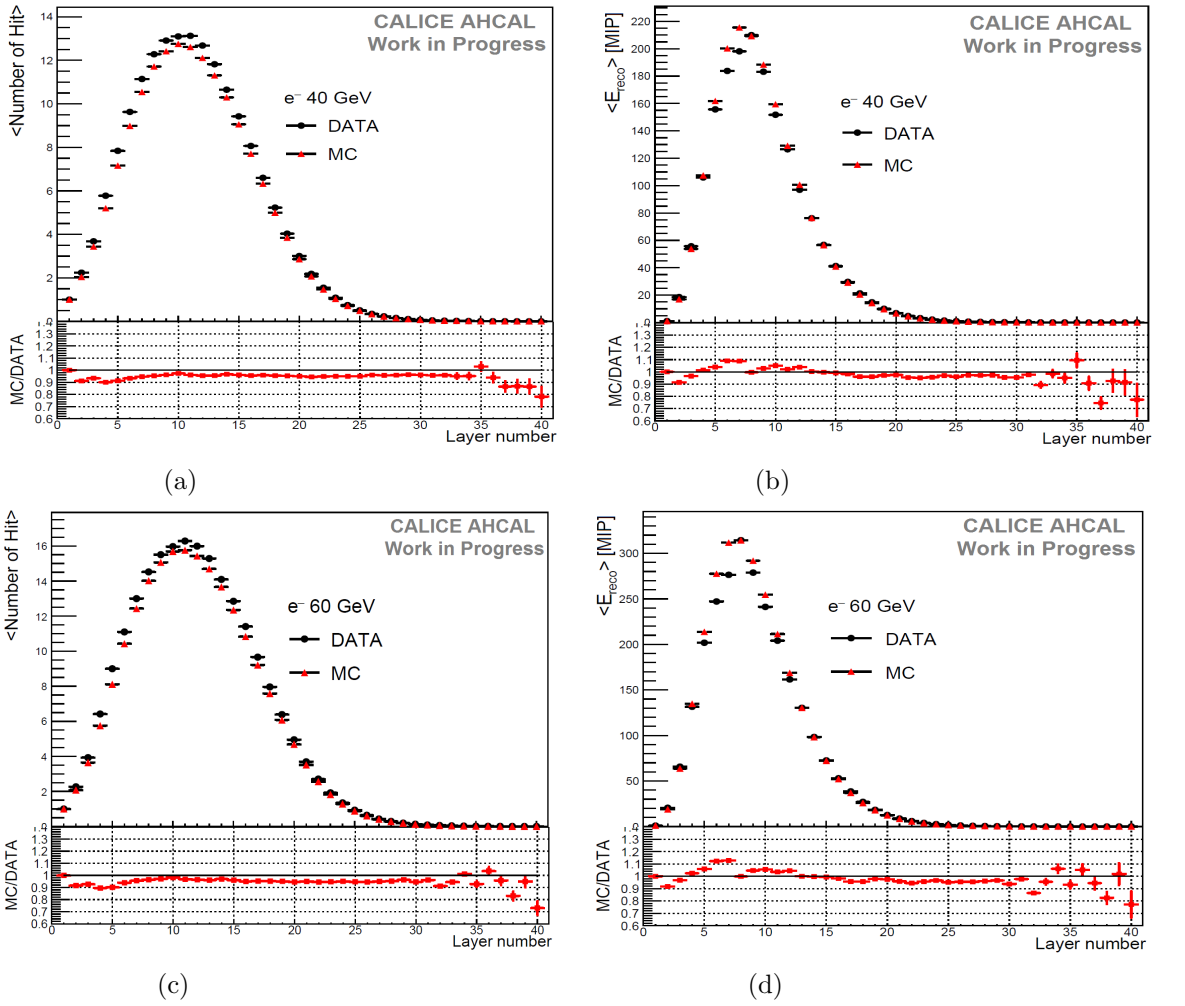

Figure 69: Distribution of mean number of hits per layer for 40 GeV (a) and 60 GeV (b). Distribution of the mean energy per layer for 40 GeV (c) and 60 GeV (d).

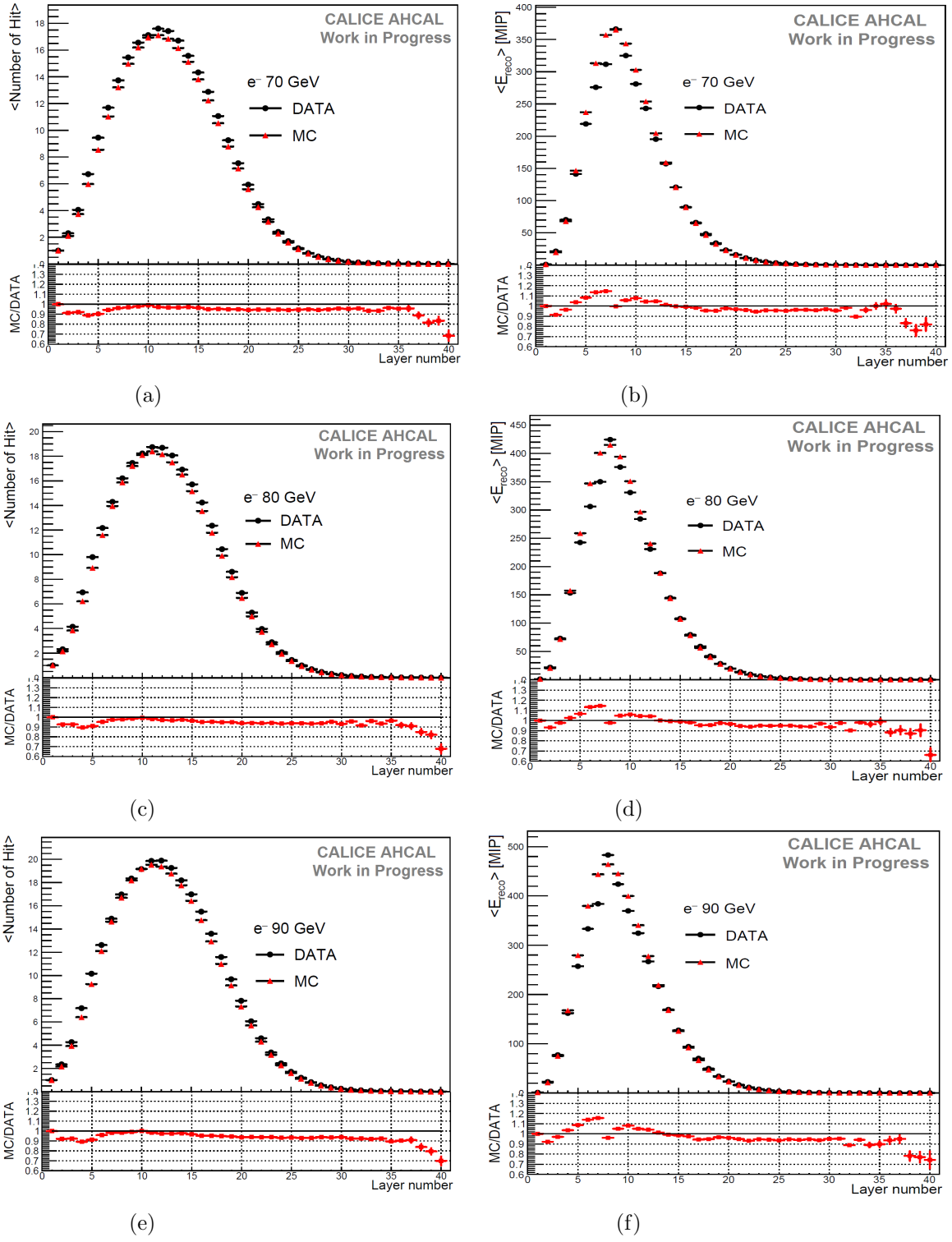

Figure 70: Distribution of mean number of hits per layer for 70 GeV (a), 80 GeV (b) and 90 GeV (e). Distribution of the mean energy per layer for 70 GeV (c), 80 GeV (d) and 90 GeV (f)

Bibliography

[1] CMS Collaboration. Observation of a new boson at a mass of 125 gev with cms experiment at the lhc. *Phys. Lett. B 716 (2012) 30*, pages 30–61, 2012. [arXiv:1207.7235].

[2] ATLAS Collaboration. Observation of a new particle in search for the standard model higgs boson with the atlas detector at lhc. *Phys. Lett. B 716 (2012)*, pages 1–29, 2012. [arXiv:1207.7214].

[3] J. E. Brau T. Behnke, et al. The International Linear Collider Technical Design Report - Volume 1. *kjhk*, pages 30–61, 2013. [arXiv:1306.6327].

[4] M. A. Thomson. Particle Flow Calorimetry and the PandoraPFA Algorithm. *Nucl. Instrum. Meth. A611: 25-40*, 2009. [arXiv:0907.3577].

[5] M. Riordan M. Dresden L. Hoddeson, L. Brown. *THE RISE OF THE STANDARD MODEL*. Cambridge University Press, 1997.

[6] J. Thomson. Cathode Rays, Philos. Mag. 44, 293.

[7] Carl D. Anderson and Seth H. Neddermeyer. Cloud Chamber Observations of Cosmic Rays at 4300 Meters Elevation and Near Sea-Level. *Phys. Rev. 50, 263.*

[8] F. Reines and C. Cowan. The Neutrino. *Nature 178, 446449.*

[9] Martin L. Per1. EVIDENCE FOR, AND PROPERTIES OF, THE NEW CHARGED HEAVY LEPTON. 1977. SLAC-PUB-1923 April 1977.

[10] S. Bilenky. Neutrino oscillations: from an historical perspective to the present status. 2016. [arXiv:1602.00170v1].

[11] G. Barr, R. Devenish, R. Walczak, and T. Weidberg. *Particle Physics in the LHC Era.* Oxford University Press, January 2016.

[12] M Gell Mann. A Schematic Model of Bayrons and Mesons. *Phys. Lette. 8*, pages 214–215, 1964.

[13] G. Zweig. An SU(3) Model for Strong Interaction Symmetry and its Breaking. *CERN Report N. 8419/TH.412*, 1964.

[14] S. Abaci and al. Observation of the Top Quark. *Phys.Rev.Lett.74:2632-2637,1995*, 1995. [arXiv:hep-ex/9503003].

[15] S. L. Glashow. Partial Symmetries of Weak Interactions. *Nucl. Phys. 22*, pages 579–588, 1961.

[16] A. Salam. Electromagnetic and Weak Interactions. *Phys. Lett. 13*, pages 167–171, 1964.

[17] Petter W. Higgs. Broken symmetries and the mass of gauge bosons. *Phys. Lett. 13.16*, pages 508–509, Aug. 1964.

[18] F. Englert and R. Brout. Partial symmetry and the mass of gauge vector mesons. *Phys. Lett. 13.9*, pages 312–323, 1961.

[19] F. Halzen and Alan D. Martin. *Quarks and Leptons: an Introductory Course in Modern Particle Physics*. Wiley, 1984.

[20] ATLAS Collaboration. Measurement of Higgs Boson production and coupling in diboson final states with the ATLAS detector at LHC,. *Phys. Lett. B 726 (2013) 88*, 2013. [arXiv:1307.1427].

[21] CMS Collaboration. Measurement of the properties of a Higgs boson in the four-lepton final state. *Phys. Lett. D 89 (2014) 092007*, 2014. [arXiv:1302.5353].

[22] M. Aicheler et al. A Multi-TeV Linear Collider Based on CLIC Technology : CLIC Conceptual Design Report. *CERN-2012-007*.

[23] F. Richard. From LEP and SLC to ILC. *Lecture*, 2013.

[24] J. E. Brau T. Behnke et al. The International Linear Collider Technical Design Report - Volume 3.1 : Accelerator R&D. 2013. [arXiv:1306.6353].

[25] J. E. Brau T. Behnke, et al. The International Linear Collider Technical Design Report - Volume 4 : Detectors. 2013. [arXiv:1306.6329].

[26] T. Barklow H. Baer, et al. The International Linear Collider Technical Design Report - Volume 2: Physics. 2013. [arXiv:1306.6352].

[27] J. E. Brau T. Behnke, et al. The International Linear Collider Technical Design Report - Volume 3.2 : Accelerator Baseline Design. 2013. [arXiv:1306.6328].

[28] et al. J. E. Brau T. Behnke. The International Linear Collider Technical Design Report - Volume 3.1: Accelerator R&D in the Technical Design Phase. 2013. [arXiv:1306.6353].

[29] Working Group Collaboration. Detector Outline Document for the Large Detector Concept. 2006. hhtp://www.ilcldc.org/documents/dod/.

[30] F. Richard. GLD Dector Outline Document. *Physics/0607154*, 2006.

[31] K. Fuji et al. Physics Case for the International Linear Collider. *In: The European physical journal. C, Particles and fields 75.8*, 2013. [arXiv:1506.05992].

[32] K. Fuji et al. Measurement of the Higgs boson mass and $e^+e^- \to$ ZH cross section using Z $\to e^+e^+$ at the ILC. *Phys. Rev., vol. D94, no 11, p. 113002*, 2016.

[33] M. A. Thomson. Model-independent measurement of the e^+e^- to hz cross section at future e^+e^- Linear Collider using hadronic z decays. *Eur. Phys. J. C76*, Feb 2016.

[34] J. Tian. Study of Higgs self-coupling at the ILC based on the full detector simulation at $\sqrt{s} = 500$ GeV and $\sqrt{s} = 1$ TeV. *High Energy Accelerator Research Organization, KEK, Tsukuba, Japan, LC-REP-2013-003*, April 2013.

[35] M. Kurata et al. The Higgs Self Coupling Analysis Using The Events Containing $H \to WW^*$ Decay. *High Energy Accelerator Research Organization, KEK, Japan, LC-REP-2013-025.*

[36] CMS DO Collaborations ATLAS, CDF. First combination of Tevatron and LHC measurements of the top-quark mass. *Eur. Phys. J. C75*, 2014. [arXiv:1403.4427].

[37] Y. Sudo. Study of Direct top Yukawa Coupling Measurement at the ILC with $\sqrt{s} = 500$ GeV. *presented at Top Physics at Lepton Colliders workshop, Tsukuba, Japan 2016.*

[38] J. Strube T. Price, P. Roloff and T. Tanabe. Full simulation study of the top Yukawa coupling at the ILC at $\sqrt{s} = 1$ TeV. *Eur. Phys. J. C75*, 2015. [arXiv:1409.7157].

[39] Scott Dodelson Csaba Csaki. *PHYSICS OF THE LARGE AND SMALL*. World Scientific Publishing Co. Pte. Ltd, 2009.

[40] B. Rossi. *High Energy Particles*. 1952.

[41] K. A. Oliver and Particle Data Group. Review of Particle Physics. *Chinese Physics C 38*, 2014.

[42] M. Tanabashi et al. (Particle Data Group). *Phys. Rev. D 98, 030001*, (2018)and 2019 update.

[43] M. Livan R. Wigmans. *Calorimetry for Collider Physics, an Introduction*. 2019. p. 39.

[44] R. Wigmans. Calorimetry, Energy Measurement in Particle Physics. *Oxford Science Publications*, 2000. Oxford University Press.

[45] Wingerter-Seez. *Particle Physics Instrumentation, Proceedings of the 2014 AsiaEuropePacific School of High-Energy Physics*. LAPP, CNRS, Paris, France, and Universit Savoie Mont Blanc, Chambry, France.

[46] H. Bethe J. Ashkin. *Experimental Nuclear Physics, ed. E. Segré, J. Wiley, New York*. 1959. p. 253.

[47] Gabriel et al. *Nucl. Instr. and Meth. A338, 336*, 1994.

[48] E. Brianne. Time Development of Hadronic Showers in a Highly Granular Analog Hadron Calorimeter. (2018). PhD Thesis, Universität Hamburg.

[49] V. Ivanchenko et al. Recent Improvements in Geant4 Electromagnetic Physics Models and Interfaces. *in 3th Monte Carlo Conference MC2010, vol.2, (Tokyo, Japan), pp. 898-903*, Oct. 2010.

[50] V. Ivanchenko et al. Progress in GEANT4 Electromagnetic Physics Modeling and Validation. *in CHEP2015*, 2015.

[51] N. Feege. Low-energetic Hadron Interactions in Highly Granular Calorimeter. (2011). PhD Thesis, Universität Hamburg.

[52] N. Stepanov and A. Heikkinen J. P. Wellisch. Bertini intra-nuclear cascade implementation in Geant4.

[53] V. N. Ivanchenko and G. Folger J. P. Wellisch. The Binary Cascade. *The European Physical Journal A-Hadrons and Nuclei, vol.21, pp.407-417,*, Sep. 2004.

[54] G. Folger and J. P. Wellisch. String Parton Models in Geant4.

[55] Bo Andersson. THE FRITIOF DYNAMICS In:2nd International Workshop on Correlation and Fluctuation in Multiparticle Production (IWCF 1997) Jinan, Shandong, China,June 28-July 6, 1987.

[56] E. F. Staubo N. S. Amelin and L. P. Csernai. Semihard collisions in Monte Carlo quark-gluon string model. *Physical Review D46.11*, Dec. 1992.

[57] G. Gustafson B. Andersson and B. Nilsson-Almqvist. A model for low-pT hadronicreactions with generalizations to hadron-nucleus and nucleus-nucleus collisions. *Physics, Section B281.1-2*, Dec. 1987.

[58] Jose Manuel Quesada et al. Recent developments in pre-equilibrium and de-excitation models in Geant4.

[59] B. Hermberg. Measuring Hadronic Jets at the ILC - From Particle Flow Calorimetry to the Higgs Self-Coupling. (2015). PhD Thesis, Universität Hamburg.

[60] The CMS Electromagnetic Calorimeter: overview,lessons learned during Run 1 and futureprojections.

[61] C. W. Fabjan F. Gianotti. Calorimetry for Particle Physics. *Review of Modern Physics, V.75,*, Oct. 2003.

[62] P. Adzic et al. Energy resolution of the barrel of the CMS electromagnetic calorimeter. *JINST 2 P04004*, (2007).

[63] B. Aubert et al. Development and construction of large size signal electrodes for the ATLAS electromagnetic calorimeter. *Nuclear Instruments and Methods in Physics A, Vol. 539*, (2005).

[64] P. Adragna et al. Testbeam studies of production modules of the ATLAS Tile Calorimeter. *Nuclear Instruments and Methods in Physics A, Vol. 606*, (2009).

[65] The CMS Collaboration. Performance of the CMS Hadron Calorimeter with Cosmic Ray Muons and LHC Beam Data on behalf of the ATLAS Collaboration. *INST 5:T03012*, (2010). [arXiv:0911.4991].

[66] J.-C. Brient and H. Videau. The Calorimetry at the Future e+ e- Linear Collider. *Proc. APS/DPF/DPB Summer Study on the Future of Particle Physics (Snowmass 2001)*, Jul. 2001.

[67] V. L. Morgunov. Calorimetry Design with Energy-flow Concept (Imaging Detector forHigh-energy Physics). *in Proc. Tenth International Conference Pasadena, California,*, Mar. 2002.

[68] M. A. Thomson. Particle Flow Calorimetry and the PandoraPFA Algorithm. 2009. [arXiv:0907.3577].

[69] The CALICE collaboration. Design and electronics commissioning of the physics prototype of a Si-W electromagnetic calorimeter for the International Linear Collider. *Journal of Instrumentation, vol. 3, no. 08, p. P08001,*, (2008).

[70] The CALICE Collaboration. Response of the CALICE Si-W electromagnetic calorimeter physics proto-type to electrons, Nuclear Instruments and Methods in Physics Research Section A: Accelerators, Spectrometers, Detectors and Associated Equipment, vol. 608, no. 3, pp. 372 383,. (2009).

[71] C. de La Taille G. Martin-Chassard S. Callier, F. Dulucq and N. Seguin-Moreau. SKIROC2, front endchip designed to readout the Electromagnetic CALorimeter at the ILC,Journal of Instrumentation,vol. 6, no. 12, p. C12040, 2011.

[72] K. Kawagoe and al. Beam test performance of the highly granular SiW-ECAL technologicalprototype for the ILC. [arXiv:1902.00110].

[73] The CALICE collaboration. Construction and Response of a Highly Granular Scintillator-based Electromagnetic Calorimeter.

[74] B. Bilki. Construction and Testing of the CALICE Digital Hadron Calorimeter in Proceedings, International Conference on Calorimetry for the High Energy Frontier (CHEF 2013) : Paris, France, April 22-25,2013,. (2013).

[75] I. Laktineh N. Lumb J.-P. Ianigro, R. Kieffer and M. Bedjidian S. Vanzetto. Glass resistive plate cham-bers for a semi-digital HCAL,Nuclear Instruments and Methods in Physics Research Section A: Accel-erators, Spectrometers, Detectors and Associated Equipment, vol. 623, no.1, pp. 120122,. *1st International Conference on Technology and Instrumentation in Particle Physics*, (2010).

[76] B. Bilki and the CALICE Collaboration. The calice Digital Hadron Calorimeter: calibration and response to pions and positrons. *Journal of Physics: Conference Series, vol. 587, no.1, p. 012038*, (2015).

[77] G. Martin-Chassard F. Dulucq, C. de La Taille and N. Seguin-Moreau. HARDROC: Readout chip for CALICE/EUDET Digital Hadronic Calorimeter.

[78] C G. Baulieu and al. Construction and commissioning of a technological prototype of a high-granularity semi-digital hadronic calorimeter. *Journal of Instrumentation, vol. 10, no. 10, p. P10039*, (2015).

[79] C. Adloff and al. Construction and Commissioning of the CALICE Analog Hadronic Calorimeter Prototype. *JINST 5 (2010) P05004*, 2010. [arXiv:1003.2662].

[80] B. Dolgoshein P. Buzhan and A Ilyin. An advanced study of Silicon Photomultiplier. *ICFA Inst. 23*, 2001. [arXiv:1003.2662].

[81] E. Lozenz D. Renker. Avances in solde state photon detectors. *Journal of Instrumentation 4.04*, 2009. ISSN: 1748-0221.

[82] O. Hartbrich. Scintillator Calorimeters for a Future Linear Collider Experiment. June 2016. PhD Thesis, DESY, Hamburg, ISSN 1435-8085.

[83] Introduction to SiPM. *Technical Note*. `https://www.sensl.com/downloads/ds/TN%20-%20Intro%20to%20SPM%20Tech.pdf`.

[84] W. Shen-R. Stamen P. Eckert, H.-C. Schultz-Coulon and A. Tadday. Characterisation Studies of Silicon Photomultipliers. *Nucl. Instrum. Meth.A 620*, 2010. [arXiv:1003.6071].

[85] B. Dolgoshein. Silicon Photomultipliers in Particle Physics: possibilities and limitation. *Proceedings tp the 42nd Workshop of the INFN ELOISATRON Project, Erice, Italy, World Scientific Publishing Co. Pte. Ltd*, Singapore (2004).

[86] Woo Suk Sul Hyoungtaek Kim and Gyuseong Cho. Characterization of Silicon Photomultipliers at National Nano-Fab Center for PET-MR. *Review of Scientific Instruments 85, 103107*, 2014.

[87] Naomi van der Kolk. SiPM and Scintillator studies. *Talk in the AHCAL Main Metting*, 2015. `https://agenda.linearcollider.org/event/6931/contributions/34071/attachments/28101/42541/AHCALmeeting_12_2015.pdf`.

[88] Naomi van der Kolk. Sipm and scintillator studies. *Talk in the CLICdp Metting*, 2015. `https://indico.cern.ch/event/376800/contributions/1799937/attachments/751409/1030859/CLICdp_NvanderKolk.pdf`.

[89] Felix Sefkow. The new scintillator-SiPM-based analogue HCAL prototype. *Talk in second edition of the CHEF Conerence Lyon*, 2017. `https://indico.cern.ch/event/629521/contributions/2702990/attachments/1533879/2402067/CALICE-AHCAL-CHEF17-FS.pdf`.

[90] Yong Liu and al. A Design of Scintillator Tiles Read Out by Surface-Mounted SiPMs for a Future Hadron Calorimeter. 2015. [arXiv:1512.05900].

[91] Naoki Tsuji "CALICE Collaboration". Performance of alternative scintillator tile geometry for AHCAL. April 2019. [arXiv:1902.05266].

[92] Dulucq F Fleury J-Jaeger J J de La Taille C Martin-Chassard G Bouchel M, Callier S and Raux L. SPIROC (SiPM Integrated Read-Out Chip):dedicated very front-end electronics for an ILC prototype hadronic calorimeter with SiPM read-out. *INST 6 C01098*, 2011.

[93] Omega LAL/IN2P3. `https://portail.polytechnique.edu/omega/fr/omega/omega-en-bref`.

[94] Omega LAL/IN2P3. SPIROC2 User Guide.

[95] L. Emberger. AHCAL Time Calibration, talk in calice collaboration metting at cern. 2019. talk in CALICE Collaboration Metting at CERN.

[96] Jiri Kvasnicka. Data Acquisition System for the CALICE AHCAL Calorimeter. 2017. [arXiv:1701.02232].

[97] Jiri Kvasnicka. AHCAL DAQ. CALICE Collaboration Metting Mainz 2018.

[98] M. Terwort P. Gottlicher, M. Reinkecke. Concept and status of the CALICE AHCAL engineering prototype. *CALICE Collaboration meeting CERN (2011).*

[99] R.Leitner T.Davidek. Parametrization of the Muon Response in the Tile Calorimeter.

[100] NATIONAL INSTRUMENTS. LabVIEW User Manual.

[101] Deutsches Electronen-Synchrotron (desy), hamburg. `https://www.desy.de`.

[102] H. J. Burckhart H. Kvedalen B. Hallgren, H. Boterenbrood. The Embdedded Local Monitor Board in the LHC Front-end I/OSystem. 2001. CERN, NIKHEF-H Amsterdam.

[103] https://www.xilinx.com/products/silicon-devices/soc/zynq-7000.html.

[104] Lourdes Urda Gmez. First Results from new SPIROC2E ASIC. 2016.

[105] http://sba.web.cern.ch/sba/BeamsAndAreas/H2/H2_presentation.html.

[106] N. Abgrall. NA61/SHINE facility at the CERN SPS beam and detector system. *JINST 9 P06005*, 2014. [arXiv:1401.4699].

[107] Sefkow and Frank Simon "CALICE Collaboration". A highly granular SiPM-on-tile calorimeter prototype. April 2019. [arXiv:1808.09281].

[108] S. Huck. CALICE Collaboration meeting "Utrecht" 2019. `https://agenda.linearcollider.org/event/8109/contributions/43656/attachments/34451/53137/SaivaHuck_CALICEMeetingUtrecht.pdf`.

[109] D. Heuchel. Pedestal, MIP and Iter-Calibration. *CALICE Collaboration meeting "CERN" 2019*. `https://agenda.linearcollider.org/event/8213/contributions/44354/attachments/34779/53694/DH$_calice_9_19_ahcal_$calibration_v2.pdf`.

[110] O. Pinto. Gain and Saturation Calibration. *CALICE Collaboration meeting "CERN" 2019*. `https://agenda.linearcollider.org/event/8213/contributions/44355/attachments/34782/53701/Gain_saturation_CALICE_CERN_20190930.pdf`.

[111] Y. Sudo. HG/LG Inter-Calibration and Gain Stability. *CALICE AHCAL main meeting "DESY" 2018*. https://agenda.linearcollider.org/event/8082/contributions/43029/attachments/34071/52425/HGLGIC_main_meeting.pdf.

[112] C. Grefe P. Mato" M. Frank, F. Gaede. DD4hep: A Detector Description Toolkit for High Energy Physics Experiments. *Journal of Physics: Conference Seires, vol. 513 no. 2*, 2014.

[113] A. Agostinelli and al.". Geant4: a simulation toolkit, Nuclear Instruments and Methods in Physics Research Section A: Accelerators, Spectrometers, Detectors and Associated Equipment. 2003.

[114] Liu Linghui. Private communication.

[115] F. Gaede. Marlin and LCCD: Software tools for the ILC. *Nucl. Instrum. Meth., vol. A559, pp. 177180*, 2006.

[116] S. Krause. *CALICE Collaboration meeting "Mainz" 2019*. https://agenda.linearcollider.org/event/7798/contributions/40980/attachments/32814/49927/CALICE2018$_SiPM_Response_Krause_v4.pdf.

[117] Sascha Krause. SiPM Response. *CALICE Collaboration Meeting Mainz 2018*, 2018.

[118] V. Bochamikov. Particle Identification and topological analysis in 2018 AHCAL test beam data. *CALICE Collaboration meeting "CERN" 2019*. https://agenda.linearcollider.org/event/8213/contributions/44343/attachments/34812/53758/VBocharnikov_CALICE_meeting_CERN.pdf.

[119] Testbeam studies of production modules of the ATLAS Tile Calorimeter.